université PARIS-SACLAY

Study of the Galactic Center and Search for Dark Matter with the H.E.S.S. Inner Galaxy Survey

Étude du centre galactique et recherche de matière noire avec la H.E.S.S. Inner Galaxy Survey

Thèse de doctorat de l'université Paris-Saclay

École doctorale n°576, Particules, Hadrons, Énergie et Noyau : Instrumentation, Imagerie, Cosmos et Simulation (PHENIICS)
Spécialité de doctorat : Astroparticules et Cosmologie
Graduate School : Physique, Référent : Faculté des sciences d'Orsay

Thèse préparée dans l'unité de recherche **Département de Physique des Particules** (Université Paris-Saclay, CEA), sous la direction d'**Emmanuel MOULIN**, Directeur de recherche

Thèse soutenue à Paris-Saclay, le 23 Septembre 2022, par

Alessandro MONTANARI

Composition du jury

Tiina SUOMIJARVI Professeur, Université Paris-Saclay (IJCLab)	Présidente
Alessandro DE ANGELIS Professeur, University of Padova	Rapporteur & Examinateur
Jacques DUMARCHEZ Directeur de recherche, Université Paris Cité (LPNHE)	Rapporteur & Examinateur
Nathalie BESSON Directrice de recherche, CEA (IRFU/DPhP)	Examinatrice
Antoine KOUCHNER Professeur, Université Paris Cité (APC)	Examinateur
Emmanuel MOULIN Directeur de recherche, CEA (IRFU/DPhP)	Directeur de thèse

THESE DE DOCTORAT
NNT : 2022UPASP098

université PARIS-SACLAY

ÉCOLE DOCTORALE
Particules, hadrons, énergie et noyau : instrumentation, imagerie, cosmos et simulation (PHENIICS)

Titre: Étude du centre galactique et recherche de matière noire avec la H.E.S.S. Inner Galaxy Survey

Mots clés: Astrophysique des hautes énergie, Astronomie gamma, Matière noire, Emissions diffuses, Astroparticule, Centre Galactique

Résumé: L'astrophysique des très hautes énergies (THE, $E \geq 100$ GeV) a été pionnière dans l'étude des processus non thermiques qui accélèrent des rayons cosmiques (RC) au sein d'objets galactiques et extragalactiques. L'une des régions les plus prometteuses est le Centre Galactique (CG), peuplée par de nombreuses émissions THE, comme l'émission étendue de bulles de Fermi (BF) détectée par *Fermi*-LAT aux énergies du GeV. Les rayons gamma THE sont des messagers remarquables pour rechercher la mystérieuse matière noire (MN). Parmi les candidats particules MN figurent les particules massives à faible interaction (WIMP), qui peuvent s'auto-annihiler et produire des rayons gamma aux TeV dans des régions denses de l'Univers, comme le CG. D'autres cibles sont les sous-halos MN, prédits dans les galaxies de type Voie lactée par des simulations cosmologiques de formation de structures. Le système stéréoscopique à haute énergie (H.E.S.S.), un réseau de 5 télescopes atmosphériques imageurs Cherenkov (IACT), détecte photons aux TeV. H.E.S.S. observe la région du CG dans des conditions uniques grâce à sa localisation dans l'hémisphère sud. La première partie de la thèse introduit des notions sur l'astrophysique THE, le réseau H.E.S.S., les candidates MN et les méthodes d'analyse statistiques utilisées. Pour ce dernier, nous décrivons les tests statistiques de log-vraisemblance (LLRTS) et les premiers résultats d'une nouvelle méthode des réseaux neuronaux bayésiens sur la discrimination spectrale et spatiale d'un signal faible en présence d'un fond dominant non trivial. La deuxième partie porte sur la région CG au THE. La Inner Galaxy Survey (IGS), un ensemble d'observation H.E.S.S. du CG, est décrit en détail. L'étude des incertitudes systématiques qui affecte les données IGS et l'effort en cours pour construire des modèles de brui de fond sont largement présentés. Avec les données IGS, nous recherchons l'émission à la base des BF et, pour la première fois, elle est détectée jusqu'à $\sim$ 2 TeV avec signification intégrée de 9.2 σ. Nous montrons les flux observés différentiels d'énergie et des limites supérieures. À 1 TeV, le flux mesuré des BF est de $\sim 1.2\times10^{-9}$ TeVcm^{-2}s^{-1}sr^{-1}. D'un ajustement conjoint des données Fermi et H.E.S.S., nous pouvons déterminer la coupure d'énergie sur le spectre des photons. Des analyses supplémentaires pour inclure les incertitudes systématiques sont en cours. La troisième partie rapporte de nouveaux résultats sur la recherche MN. En utilisant l'ensemble de données IGS, nous dérivons 95% C.L. limites supérieures observées et attendues sur la section efficace d'annihilation des WIMPs ($\langle\sigma v\rangle$), avec le LLRTS et pour nombreux canaux d'annihilation. Pour le canal $\tau^+\tau^-$, nos limites atteignent 1.2×10^{-26} cm^{3}s^{-1} pour une masse de MN de 0.7 TeV, défiant les valeurs attendues pour le MN thermique. À 1.5 TeV MN, nous améliorons de 1.6 les résultats précédents H.E.S.S.. Pour les canaux testés, ce sont les limites les plus contraignantes aux TeV. Nous étudions également les incertitudes systématiques et sur le choix du profil MN. Une autre recherche est effectuée vers les candidats sous-halo MN, les objets de Fermi non identifiés (OFNI), sélectionnés dans le catalogue Fermi 3FHL sans contrepartie astrophysique conventionnelle. Les limites supérieures sur le produit entre $\langle\sigma v\rangle$ et le J-factor sont calculées. L'émission d'ovnis en terme de MN est exclue jusqu'à $\sim$ 300 GeV. La portée en termes de sensibilité du signal MN avec la génération actuelle d'IACT dans la région CG est étudiée avec un jeu de données IGS fictif, les rendements de rayons gamma de pointe pour le flux de photons MN attendu et pour la distribution MN dans le CG, y compris la rétroaction baryonique et les calculs cinématiques stellaires. La sensibilité dérivée ne peut pas sonder le Higgsino MN thermique mais exclut le Wino et le Quintuplet MN thermique aux TeV. La sensibilité de notre analyse est robuste face à plusieurs sources d'incertitudes que nous avons explorées.

université PARIS-SACLAY

ÉCOLE DOCTORALE
Particules, hadrons, énergie et noyau : instrumentation, imagerie, cosmos et simulation (PHENIICS)

Title: Study of the Galactic Center and Search for Dark Matter with the H.E.S.S. Inner Galaxy Survey

Keywords: High-Energy astrophysics, Gamma-ray astronomy, Dark Matter, Diffuse emissions, Astroparticle physics, Galactic Center

Abstract: Very high energy (VHE, $E \geq 100$ GeV) astrophysics pioneered the study of non-thermal processes describing cosmic rays (CRs) accelerated by galactic and extragalactic objects. CRs can be investigated by observing the Galactic Center (GC), which hosts many VHE sources and emissions, like for instance the Fermi Bubbles (FBs) found by *Fermi*-LAT in the GeVs. VHE photons can be used to study the still mysterious Dark Matter (DM). Among the best DM particle candidates are the weakly interacting massive particles (WIMPs), which if massive enough can self-annihilate and emit TeV gamma-rays from dense regions of the Universe. The most promising target to search for DM is the GC. Other ones are DM subhalos, predicted in Milky-Way-like galaxies by cosmological simulations. The High Energy Stereoscopic System (H.E.S.S.), an array of 5 Imaging Atmospheric Cherenkov Telescopes (IACT), observes VHE photons between around 50 GeV and tens of TeV. It can observe the GC region thanks to its ideal position in the southern hemisphere. The future array of IACTs, the Cherenkov Telescope Array, will push the boundary of the sensitivity in the TeV energies. The first part of the thesis introduces fundamental concepts on VHE astrophysics, on H.E.S.S., the supposed nature of DM and the statistical methods used in this work. We describe the log-likelihood-test-statistics (LLRTS) and results from a novel Bayesian neural network framework on the spectral and spatial discrimination of a weak signal in the presence of a non-trivial dominating background. The second part of the thesis focuses on the GC region at VHE. The Inner Galaxy Survey (IGS), a 6-years H.E.S.S. observational dataset of the GC is described in detail. The study of the systematics affecting it and the ongoing effort to build background models from extra-galactic observations and run-wise simulations of the IGS are extensively presented. With the IGS, we search for the low-latitude FBs emission in the region of interest defined by the Fermi analysis. For the first time, the FBs are detected up to $\sim$ 2 TeV and an integrated significance of 9.2 σ. We show observed flux points and upper limits. At 1 TeV, the FBs are measured at $\sim 1.2\times10^{-9}$ TeVcm^{-2}s^{-1}sr^{-1}. From a joint fit of the Fermi and H.E.S.S. analyses, we could obtain the energy cutoff on the photon spectrum, however more effort to include all the systematics is ongoing. The third part reports new results on DM search. Using the IGS dataset, we derive 95% C.L. observed and expected upper limits on the WIMPs annihilation cross-section ($\langle\sigma v\rangle$), with the LLRTS and for several annihilation channels. For the $\tau^+\tau^-$ annihilation channel, our limits reach 1.2×10^{-26} cm^{3}s^{-1} for a DM mass of 0.7 TeV, challenging the expected values for thermal DM. At 1.5 TeV DM mass, we improve the limits of 1.6 with respect to previous H.E.S.S. results. For the tested channels, these are the most constraining limits for TeV DM masses. We also investigate limits uncertainties due to the choice of the DM profile and the systematics. Another search for DM signal is performed towards DM subhalo candidates, the selected unidentified-Fermi-objects (UFOs) in the 3FHL Fermi catalog with no conventional astrophysical counterpart. We derive upper limits on the product between $\langle\sigma v\rangle$ and the J-factor. The DM UFOs emission is excluded down to $\sim$ 300 GeV. The reach in term of DM signal sensitivity with the current generation of IACTs in the GC region is investigated using a mock IGS dataset, the state of the art gamma-ray yields for the expected DM photon flux and for the DM distribution in the GC, including baryon feedback and stellar kinematic computations. New limits are derived for model-independent DM searches. The derived sensitivity cannot probe thermal Higgsino DM but excludes thermal Wino and Quintuplet DM. We widely explore how the evaluation of different uncertainties can affect the final results. The sensitivity of our analysis is robust against several sources of uncertainties.

Irfu - CEA Saclay

Institut de recherche
sur les lois fondamentales
de l'Univers

"Considerate la vostra semenza:
fatti non foste a viver come bruti,
ma per seguire virtute e canoscenza"

Dante, Divina Commedia, "Inferno", canto XXVI, vv. 118-120

Acknowledgments

This period has been a very memorable part of my life. I will never forget these years, especially because I have to say many thanks to very important people.

The first thanks go to Emmanuel, my PhD thesis supervisor. He has been a great teacher, a great motivator, and a great scientist to me. I am grateful for the work done together, the time spent making science and understanding the Universe. In these years, I really understood that being a researcher is a privilege. I am happy to have learnt from you and I think I am now closer to the path of the researcher.

Then I say thanks to my PhD thesis jury, for the thorough scientific discussion that enriched my work.

I also want to thank my colleagues at the Very-High-Energy Astrophysics working group at IRFU, because I strongly believe that results to be proud of are always obtained with a great team. Thanks a lot for always being friends and scientific references during these years. Thanks to the PhD students and postdocs, Halim, Valentin, Federica, Hector and Atilla, for the fun moments, with beers or weird ski lessons, during the collaboration meetings or the conferences.

A big thank you goes to all the H.E.S.S. colleagues, from the IT and Operations departments and the astrophysics working groups. They make all this work possible.

Thanks to Denys, Dorit, Dmitry, Fabian, Nick, and Oscar for the great collaboration, and for making the exchange between theory and experiment possible and our results ready for the papers.

Thanks to my other friends in Paris: Syrielle, Irene, Martin, Mariagiovanna, Simone, Amelie, and Hyunwoo. You have been my home and my flatmates during these crazy years. I owe you a lot and I love you a lot. I will always come back to you, in some ways.

Thanks to my friends in Italy. Even though we had very few chances to meet during these years, you are one of my reference points when I need to remind myself how wonderful my life is.

Then I say thank you to my family. You gave me the freedom to choose what I want to do for my life and always supported me. This is not to be taken for granted and thanks to your love, I feel proud of myself and privileged to have the good fortune of studying the Universe for a living.

There is another important person that I want to thank. Alix, even though I cannot talk Astrophysics with you, you are among the most inspiring people that

I have in my life. You are a wonderful human being and I am extremely grateful of having shared these years with you.

The last thanks go to my grandparents. They are my roots. They made their life through very hard periods, after the World War II, to let us savor the taste of freedom. I owe them the opportunity to study and discipline my mind. A special thought goes to my departed grandmother, who loved me without any restrain. I will always be thankful for having a childhood with her.

Contents

List of Tables

List of Figures

Synthèse en français

Introduction L'astrophysique des très hautes énergies (THE, $E \geq 100$ GeV) a ouvert la voie à l'étude des processus non thermiques, les plus violents de l'Univers. Les rayons cosmiques (RC) qui sont accélérés par des objets galactiques comme les restes de supernova et les trous noirs ou des objets extragalactiques comme les noyaux galactiques actifs, émettent des rayons gamma. L'origine et les mécanismes d'accélération des RC sont encore largement débattus. L'une des régions du ciel les plus prometteuses pour ces investigations est le Centre Galactique (CG), où une émission diffuse de rayons gamma TeV a été détectée à proximité du trou noir supermassif central Sagittarius A*. Cette détection était considérée comme un indice pour un objet accélérant des protons jusqu'à des énergies PeV, c'est-à-dire un Pevatron. Plus récemment, des photons accélérés jusqu'à 1.4 PeV ont été collectés à partir de 12 autres sources. Le satellite *Fermi*-LAT a détecté une émission THE étendue au-dessus et au-dessous du Plan Galactique, les Bulles de Fermi (BF). Cette émission est plus brillante aux basses latitudes et ne montre aucun indice de coupure d'énergie dans l'analyse de Fermi, ouvrant ainsi la question de ce qui peut être fait aux énergies du TeV.

La physique fondamentale au-delà du modèle standard de la physique des particules peut être étudiée avec les rayons gamma THE. La Matière Noire (MN) imprègne 85% du contenu en matière de l'Univers. Néanmoins, sa nature laisse encore perplexe de nos jours. Parmi les meilleurs candidats pour expliquer la MN se trouvent les particules massives non baryoniques qui peuvent interagir gravitationnellement et par la force faible avec la matière standard. Ces particules sont connues sous le nom de particules massives à faible interaction (WIMPs). Lorsque des WIMPs suffisamment massifs sont considérés, ils peuvent s'auto-annihiler dans des régions denses de l'Univers. Ce processus d'annihilation peut produire des rayons gamma TeV. La région la plus prometteuse pour détecter le signal MN est le CG. D'autres cibles prometteuses sont les galaxies satellites sphéroïdales naines de la Voie lactée et les sous-halos MN, qui devraient être hébergées par des galaxies de type Voie lactée par les simulations cosmologiques. Ces cibles sont dominées par le MN et dépourvues de gaz, elles pourraient donc être utilisées pour rechercher une confirmation d'un éventuel signal MN du CG. De nombreux programmes d'observation sont dédiés à l'étude de la physique fondamentale et à la recherche de signal MN.

Les rayons gamma THE peuvent être observés par les télescopes d'imagerie atmosphérique Cherenkov (IACT). Le système stéréoscopique à haute énergie (H.E.S.S.) est un réseau de 5 IACT collectant des rayons gamma dans la gamme d'énergie comprise entre environ 50 GeV et des dizaines de TeV. La région CG peut être observée par H.E.S.S. grâce à sa position idéale dans l'hémisphère sud. L'observation de cette région du ciel est vraiment prometteuse pour la détection du signal MN pour la gamme de masse qui ne peut pas être sondée par les collisionneurs et pour essayer de caractériser l'émission des BF. De nombreuses contraintes importantes sur les propriétés du TeV MN ont été dérivées des observations de la région CG et de certains candidats sous-halo MN. Le futur réseau d'IACT, le Cherenkov Telescope Array (CTA), poussera la sensibilité dans la gamme d'énergie TeV et permettra de contraindre encore plus les paramètres spatiaux MN.

Cette thèse de doctorat décrit le vaste programme d'observations de la région CG avec H.E.S.S., comment cet ensemble de données est utilisé pour l'étude de certaines émissions importantes dans la région et les recherches de signal MN du halo interne de la Voie lactée et de certains candidats sous-halo MN . Des nouveautés dans les méthodes statistiques utilisées pour démêler les signaux faibles dans un ensemble de données dominé par un arrière-plan non trivial sont également présentées. Des études sur la portée finale de la sensibilité aux signaux de matière noire de la région du centre galactique avec la génération actuelle d'IACT sont rapportées.

La **première partie** de la thèse introduit des notions fondamentales sur l'astrophysique THE, la H.E.S.S. réseau de télescopes, les méthodes statistiques utilisées dans ce travail et la nature du MN. Des concepts sur l'astrophysique de la production de rayons gamma par les mécanismes d'accélération des rayons cosmiques sont rapportés dans le **Chap. 1**. Les H.E.S.S. télescopes et une description succincte des techniques de détection, d'observation et de mesure du bruit de fond sont donnés au **Chap. 2**. Dans **Chap. 3** le paradigme MN, les meilleurs candidats pour MN et la distribution MN sont rapportés. Nous présentons également un rapport concis du signal attendu pour la détection indirecte de MN et des cibles de rayons gamma THE les plus prometteuses. Enfin, les méthodes statistiques et les tests de performance permettant de caractériser les résultats et les incertitudes sont présentés au **Chap. 4**. Des méthodes plus classiques avec l'application de statistiques de test de log-vraisemblance ainsi que de nouveaux cadres de réseaux de neurones bayésiens sont présentés et appliqués pour la discrimination d'un signal faible en présence d'un bruit de fond non trivial.

La **deuxième partie** de la thèse porte sur la région CG au THE. Nous utilisons **Chap. 5** pour une présentation générale du ciel THE dans le CG. Nous introduisons d'abord brièvement les observations du CG à plusieurs longueurs d'onde. Nous décrivons ensuite de manière concise les sources astrophysiques TeV connues peuplant le CG et l'émission THE étendue qui ont été détectées dans la région. Nous concluons le chapitre avec quelques sections sur les débits THE mesurés à

partir du CG, en nous concentrant sur les BF. Au **Chap. 6**, l'Inner Galaxy Survey (IGS) est présenté, à partir des objectifs scientifiques de ce programme étendu d'observations. Nous décrivons ensuite l'ensemble de données d'observation avant l'avènement de la H.E.S.S. phase II, lorsque le réseau était composé uniquement des quatre petits télescopes, et après celui-ci, avec le réseau complet de cinq télescopes. Les paramètres de la prise de données, tels que les angles de zénith et de décalage des observations et les cartes du ciel en excès et en signification, pendant l'IGS sont affichés. Deux sections détaillées sont ensuite consacrées à la description de l'étude de la systématique affectant l'ensemble de données IGS et à la procédure que nous mettons en œuvre pour construire des modèles de fond à partir d'observations extra-galactiques et de simulations par exécution de l'ensemble de données IGS. La deuxième partie se conclut par le **Chap. 7**, où nous présentons la recherche de l'émission des BF à basse latitude avec H.E.S.S.. Les BF étaient déjà détectés par *Fermi*-LAT comme une structure à double lobe au-dessus et au-dessous du CG. Nous utilisons l'ensemble de données IGS et une région d'intérêt définie à partir du modèle spatial *Fermi*-LAT des BF pour dériver de nouvelles contraintes sur l'émission aux énergies du TeV, où l'expérience satellite ne peut pas observer les photons et ne peut détecter aucun indice de coupure sur le GeV spectre.

La **troisième partie** rapporte des nouvelles sur la recherche de signal MN. Dans **Chap. 8** nous montrons de nouveaux résultats pour les limites de la section efficace d'annihilation pondérée en vitesse des WIMPs auto-annihilants. Pour cela, nous supposons des modèles standard de spectres MN et de distribution MN dans le CG et nous obtenons de nouvelles limites à partir de l'ensemble de données IGS. Une autre recherche de signal MN est présentée au **Chap. 9**. Dans ce cas, nous utilisons un ensemble de données d'observations vers des candidats subhalo MN, des objets sélectionnés sans contrepartie astrophysique conventionnelle dans le 3FHL *Fermi*-LAT catalog de sources à hautes énergies. Nous appelons ces objets des objets de Fermi non identifiés (OFNI). La sélection a été effectuée pour trouver les meilleurs candidats sous forme de sous-halos MN et facilement observables avec H.E.S.S.. Dans le dernier chapitre, *i.e.* **Chap. 10**, nous explorons quelques perspectives sur la détection de signaux MN avec la génération actuelle d'IACTs et en particulier avec H.E.S.S.. Pour ce travail, nous avons créé un jeu de données fictif de mesures imitant l'état actuel des observations de la région CG avec l'IGS. Nous utilisons des calculs de rendement de rayons gamma de pointe pour les spectres de photons attendus à partir des profils de distribution MN et MN annihilants dans le CG. Nous calculons les limites de sensibilité dans divers canaux, nous testons également la portée de H.E.S.S. pour les mesures de photons émis par le MN s'annihilant dans les canaux de neutrinos. Enfin, nous calculons les limites des candidats canoniques WIMP tels que le Wino, le Higgsino et le Quintuplet, montrant quelles sont les réalisations possibles avec la génération actuelle d'IACT.

Le **Chapitre 1** donne un aperçu de l'astrophysique des rayons gamma THE et des processus connexes. Plusieurs objets de l'Univers accélèrent les rayons cosmiques chargés par des processus d'interaction leptonique et hadronique qui peuvent alors produire des rayons gamma à THE, utilisés pour l'étude de l'Univers non thermique. Des expériences spatiales et terrestres ont été construites selon différentes techniques de détection pour détecter ces rayons gamma. Les concepts fondamentaux de l'Univers non thermique, les mécanismes d'accélération des CRs et de production de rayons gamma sont expliqués succinctement dans **Sec. 1.1**, **1.2** et **1.3**. Les accélérateurs TeV CRs sont présentés dans **Sec. 1.4**. Les expériences qui observent le ciel gamma pour une détection directe ou indirecte sont présentées dans **Sec. 1.5**. Enfin, la physique fondamentale qui peut être étudiée avec l'astrophysique des rayons gamma est brièvement rapportée dans **Sec. 1.6**.

Le **Chapitre 2** présente l'expérience H.E.S.S.. Elle part du concept de gerbe atmosphérique de particules et de lumière Cherenkov produite dans l'atmosphère par les rayons gamma THE en interaction avec celle-ci, en **Sec. 2.1**. Ensuite, **Sec. 2.2** montre quelques brefs détails sur le réseau de H.E.S.S. cinq-télescopes, comme la configuration et les phases de l'expérience. Les procédures d'identification et de sélection des événements sont présentées dans **Sec. 2.3**. Les méthodes utilisées pour l'observation et la mesure du bruit de fond sont présentées dans **Sec. 2.4**. **Sec. 2.5** présente les fonctions de réponse de l'instrument (IRF), telles que la surface effective de l'instrument, la définition du seuil d'énergie et les résolutions énergétique et angulaire. Enfin, le chapitre se termine par la **Sec. 2.6** pour la description des méthodes de reconstruction des événements mesurés en phase I ou en phase II de l'instrument H.E.S.S..

Le **Chapter 3** concerne le paradigme MN. Dans **Sec. 3.1**, nous résumons les éléments de preuve de l'existence de MN dans l'Univers, la densité thermique des reliques de particules froides de MN et le modèle standard ΛCDM de Cosmologie . Nous introduisons ensuite les candidats théorisés pour expliquer le MN dans **Sec. 3.2**. **Sec. 3.3** est dédié à une brève explication des théories alternatives au modèle ΛCDM. Les techniques de détection, détections directes et indirectes et recherche de collisionneur sont présentées dans **Sec. 3.4**. Les profils de distribution MN attendus et théorisés selon les modèles actuels et la mesure de la cinématique stellaire sont présentés dans **Sec. 3.5**. Des cibles prometteuses pour la recherche de signal MN sont résumées dans **Sec. 3.6**. Le flux attendu de photons gamma du signal d'auto-annihilation MN est expliqué dans **Sec. 3.7**. Les différentes caractéristiques caractérisant un spectre de rayons gamma provenant de l'annihilation MN sont présentées dans **Sec. 3.8**.

Le **Chapitre 4** est dédié à une description détaillée des méthodes statistiques que nous utilisons dans ce travail. La première partie montre les méthodes basées sur les statistiques de test, où la fonction de vraisemblance de Poisson et la statistique de test du rapport de vraisemblance sont présentées dans **Sec. 4.2**. Ces

méthodes sont utilisées pour les recherches de signaux MN, vers les OFNIS et dans le jeu de données IGS, et pour étudier l'émission des BF. Un exemple d'utilisation de ces méthodes pour le calcul de limites sur un paramètre libre du modèle choisi pour la description de l'émission est donné dans **Sec. 4.4**, avec un jeu de données fictif d'observations qui est défini dans **Sec. 4.3**. Les manières possibles d'inclure les incertitudes systématiques dans les limites finales sont présentées dans **Sec. 4.5**. Les performances de notre framework pour reconstruire un faux signal avec une valeur injectée du paramètre libre sont montrées dans **Sec. 4.6**. Cette première partie se conclut par une synthèse et des perspectives. La deuxième partie du chapitre se concentre sur la description des méthodes basées sur le réseau de neurones bayésien, où nous montrons comment nous avons testé un cadre BNN pour apprendre la forme spectrale du signal et la proportion spatiale lorsqu'une émission dominante de fond non triviale est présente. Les bases des réseaux de neurones sont présentées dans **Sec. 4.8**. Nous introduisons ensuite le mélange dit additif, pour indiquer la composition des émissions de signal et de fond dans un espace de paramètres spatio-spectraux. Cela se fait dans **Sec. 4.9**. Les expériences que nous avons poursuivies sont montrées dans **Sec. 4.10** et les résultats finaux, où nous montrons que notre modèle est capable de récupérer la forme spectrale du signal et sa proportion spatiale, sont présentés dans **Sec. 4.11**. Nous concluons le chapitre par un résumé des méthodes basées sur les réseaux de neurones, avec également quelques perspectives possibles sur la façon dont ce pipeline peut être appliqué pour démêler un signal MN faible en présence d'un bruit de fond non trivial. Au moment de la rédaction, les résultats obtenus avec les cadres de réseaux de neurones bayésiens ont été soumis à ICLR2023 [64].

Le **Chapitre 5** est une description générale de la région CG à THE. Nous commençons par un bref résumé des observations du CG à plusieurs longueurs d'onde en **Sec. 5.1**. Ensuite, **Sec. 5.2** présente les sources astrophysiques TeV observées dans la région. Les émissions étendues mesurées au THE sont présentées dans **Sec. 5.3**. Le chapitre se termine par **Sec. 5.4**, qui concerne les débits sortants mesurés à partir de la région CG à THE, avec un accent particulier sur la structure des BF à double lobe, qui est encore contrainte par H.E.S.S. dans ce travail.

Le **Chapter 6** décrit en détail le grand ensemble de données d'observations de la région du CG recueillies entre 2014 et 2020, l'ensemble de données dit Inner Galaxy Survey (IGS). Dans un premier temps, **Sec. 6.1** se concentre sur les objectifs scientifiques de l'enquête et présente en détail les positions de pointage choisies au fil des années. Le jeu de données d'observation est décrit dans la **Sec. 6.2**, avec le résumé des observations du CG pendant la phase I de la H.E.S.S. et pendant la phase II, qui inclut l'IGS. Les paramètres de la prise de données sont présentés dans **Sec. 6.3**, où les distributions d'angle de zénith et de décalage et les cartes de signification et de ciel en excès sont indiquées. L'étude systématique réalisée pour avoir une estimation de l'incertitude systématique affectant un ensemble de données aussi large est présentée dans **Sec. 6.4**. Les modèles de fond que

nous construisons avec des observations extra-galactiques et des simulations par exécution de l'ensemble de données IGS mesuré sont présentés dans **Sec. 6.5**. L'étude approfondie de la systématique affectant cet ensemble de données est présentée en détail et quelques résultats généraux en sont dérivés. Cette enquête a été adaptée à cet ensemble de données et aux analyses présentées dans ce travail, mais les concepts généraux peuvent être appliqués pour comprendre les incertitudes systématiques dans d'autres analyses. Nous finalisons le chapitre avec quelques conclusions et la perspective de ce que l'ensemble de données IGS peut être utilisé.

Dans le **Chapitre 7**, nous montrons les résultats de la recherche de l'émission des BF avec le jeu de données IGS. Les BF sont une structure géante à double lobe s'étendant jusqu'à $\sim 55^{\circ}$ au-dessus et au-dessous de la région CG. Cette émission a déjà été détectée par le *Fermi*-LAT jusqu'à des énergies de centaines de GeV. Dans l'analyse de Fermi, l'émission semble plus brillante et plus dure aux basses latitudes galactiques, où nous avons le pic d'exposition avec l'ensemble de données IGS. De plus, le spectre de Fermi ne montre aucune indication de coupure, que nous pourrions rechercher aux énergies TeV avec H.E.S.S.. Dans **Sec. 7.3**, nous résumons brièvement comment le jeu de données IGS peut être utilisé pour la recherche de l'émission des BF à basse latitude au TeV. Dans **Sec. 7.2**, nous définissons la région d'intérêt (ROI), appelée plus tard la région *ON*, que nous utilisons pour rechercher l'émission. Pour cela, nous prenons le gabarit spatial de l'analyse de Fermi. Nous utilisons le modèle spatial pour définir notre retour sur investissement, en considérant les pixels avec une luminosité de surface supérieure à 8,5 et en supposant que le modèle spatial est indépendant de l'énergie. Dans la même section, nous expliquons comment nous avons utilisé la méthode *Reflected Background* pour mesurer le bruit de fond résiduel dans la région d'intérêt, en utilisant les régions *OFF* réfléchies par la région ON par rapport à la position de pointage. Nous dérivons ensuite des distributions de comptage d'énergie, où nous collectons les photons mesurés dans les régions ON et OFF dans des bacs d'énergie. Dans la même section, nous expliquons également toutes les coupes d'analyse appliquées et les régions d'exclusion utilisées pour masquer les sources astrophysiques THE connues dans le CG. Dans la même section, nous dérivons l'excès de signification dans les mêmes cases d'énergie utilisées pour les distributions dans la région ON, en suivant la procédure Li&Ma définie dans le chapitre où nous présentons les méthodes statistiques. Un net excès positif est visible dans les intervalles de basse énergie, depuis le seuil d'énergie à 300 GeV jusqu'à environ 2 TeV. La signification intégrée au-dessus du seuil d'énergie est de 9.2 σ. Dans **Sec. 7.4**, nous montrons quelques tests de performance, où nous essayons de récupérer un signal injecté dans notre jeu de données avec le framework TS. Ceci est fait pour évaluer la sensibilité de notre instrument pour récupérer un signal des bulles à l'ordre du flux détecté dans l'analyse *Fermi*-LAT. Dans **Sec. 7.5**, nous montrons le H.E.S.S. spectre dérivé

pour l'émission des BF avec des points de flux observés différentiels d'énergie et des limites supérieures de flux. Les résultats finaux ont été recoupés avec deux chaînes d'analyse alternatives, produisant les mêmes résultats. L'excès aux basses énergies se confirme et on peut tracer des points de flux dans les quatre premières tranches d'énergie, depuis le seuil jusqu'à environ 2 TeV. À 1 TeV, l'émission de BF est mesurée par H.E.S.S. à $\sim 1.2 \times 10^{-9}$ TeV cm^{-2} s^{-1} sr^{-1}. Dans la même section, nous expliquons comment nous avons inclus les incertitudes systématiques estimées au chapitre 6 dans le spectre final. A partir d'un ajustement conjoint des résultats spectraux de Fermi et H.E.S.S., nous pouvons obtenir la coupure d'énergie sur le spectre photonique, $E_{\rm coupure} = 1.4$ TeV. De plus, nous dérivons des contraintes sur les caractéristiques des spectres d'éventuelles populations de particules mères pour l'émission des BF. En considérant des modèles leptoniques simples, la limite de coupure est de 4.7 TeV. Pour les modèles hadroniques simples, la limite de coupure est de 11.2 TeV. Nous tenons à souligner que ces résultats ont été dérivés pour l'analyse principale où l'étude approfondie des incertitudes systématiques n'a pas encore été incluse. Les résultats ne sont donc qu'une possibilité, car ils changeront lorsque l'effort en cours sera inclus. Le chapitre se termine dans **Sec. 7.6** avec quelques perspectives sur d'éventuels travaux futurs pour la caractérisation de l'émission des BF et l'inclusion de plusieurs études encore en cours sur la systématique affectant l'analyse. Au moment de la rédaction, les résultats obtenus sur les FB sont en préparation pour une soumission à *Nature* d'ici quelques mois [140].

Le **Chapitre 8** montre les résultats de la recherche de signaux d'annihilation MN de la région CG avec l'ensemble de données IGS. Nous commençons dans **Sec. 8.2** avec un résumé sur la façon dont l'ensemble de données IGS peut être utilisé pour rechercher MN. La procédure de mesure de l'émission de fond est présentée dans **Sec. 8.2**, où nous définissons la ROI et les régions d'exclusion, nous expliquons comment la méthode du fond réfléchi a été appliquée et nous montrons la distributions de comptage d'énergie pour les régions ON et OFF. Dans la même section, nous montrons des cartes du ciel d'importance excessive et excessive pour l'ensemble de données IGS. Nous montrons ensuite à quoi ressemblerait le signal attendu de MN, avec des spectres théoriques de photons aux énergies TeV provenant de l'auto-annihilation de MN, et quelle distribution de MN attendue dans le CG nous supposons pour l'analyse. Puisque nous n'avons observé aucun excès significatif dans les distributions de comptage d'énergie, nous calculons les limites supérieures à 95% C.L. sur la section efficace d'annihilation moyennée en vitesse $\langle \sigma v \rangle$ des particules WIMPs MN, le paramètre libre sur nos modèles supposés. Le calcul est effectué avec le cadre LLRTS précédemment défini. Plusieurs canaux d'annihilation pour les WIMP sont testés, avec un rapport de branchement de 100%, ce qui signifie que deux WIMP s'annihileraient complètement dans le canal mentionné. Nous adoptons un profil de distribution cuspy MN au centre de notre Galaxie. Les limites par rapport à la masse MN sont

présentées dans **Sec. 8.3**, comme les limites supérieures observées calculées avec les distributions ON et OFF et les limites supérieures attendues où 300 réalisations de Poisson sont obtenues à partir des mesures OFF, indépendamment pour les distributions ON et OFF. Pour les limites attendues, des valeurs moyennes, 1 et 2σ sont extraites des distributions des limites obtenues avec les réalisations pour chaque valeur de la masse. Dans toutes les limites, l'incertitude systématique affectant l'ensemble de données IGS est incluse en tant que paramètre de nuisance gaussien. Dans la même section, nous montrons également la comparaison de nos limites avec d'autres expériences. Notre dérivation apporte les limites les plus contraignantes dans la gamme de masse du TeV, ouvrant la voie aux analyses avec observations CTA. Pour les WIMP qui s'annihilent dans le canal d'annihilation W^+W^- , nos limites atteignent 3.7×10^{-26} cm^{3}s^{-1} pour une masse de particule MN de 1,5 TeV. Dans le canal $\tau^+\tau^-$, les limites atteignent 1.2×10^{-26} cm^{3}s^{-1} pour une masse de particule MN de 0.7 TeV, traversant les valeurs $\langle\sigma v\rangle$ attendues pour les particules MN s'annihilant avec une section efficace thermique-relique. A 1.5 TeV de masse de MN, nous obtenons un facteur d'amélioration de 1.6 par rapport aux résultats précédents obtenus avec H.E.S.S. en 2016. De plus, nous montrons comment nos limites se dégraderaient en supposant d'autres profils de MN cœur ou cuspy. L'impact de l'incertitude systématique sur les limites est expliqué en détail dans **Sec. 8.4**. Nous concluons avec des perspectives possibles à partir des observations futures de la région CG dans **Sec 8.5**. Les résultats présentés dans ce chapitre ont été publiés dans *Physical Review Letters* [7].

Dans **Chapter 9** nous recherchons le signal d'annihilation MN à partir d'une sélection d'une poignée d'OFNIS. Nous introduisons d'abord pourquoi les sous-halos MN sont prédits par des simulations cosmologiques dans **Sec. 9.2**. Dans **Sec. 9.3**, nous montrons les quatre objets Fermi non identifiés sélectionnés pour l'analyse H.E.S.S. du catalog Fermi 3FHL. Dans la même section, nous expliquons l'analyse des données de Fermi des OFNIs sélectionnés et comment ils peuvent être modélisés avec des modèles de matière noire. Ensuite, l'ensemble de données d'observation H.E.S.S. et l'analyse sont présentés dans **Sec. 9.4**. Dans cette section, nous présentons les cartes du ciel en excès et en signification, la méthode que nous avons utilisée pour la mesure du bruit de fond et les distributions d'énergie des événements obtenues, construites à partir des régions ON et OFF. Puisqu'aucun excès significatif n'a été observé ni dans le FoV ni aux positions OFNI, nous avons dérivé 95% C.L. limites supérieures des paramètres libres pour le modèle supposé de MN auto-annihilant. Le calcul et quelques détails supplémentaires sont présentés dans **Sec. 9.5**. Puisqu'aucune mesure cinématique stellaire n'est disponible pour ces objets, les paramètres libres pour cette analyse sont $\langle\sigma v\rangle \times J$. Le dernier terme décrit la distribution de MN dans l'objet observé, et dans ce cas ne peut pas être calculé. Nous dérivons des limites supérieures sur ce produit, à la fois pour chaque ensemble de données individuel et pour l'ensemble combiné. Pour cette combinaison, nous testons deux méthodes : au niveau du

comptage et au niveau de la fonction de vraisemblance. Le second est démontré comme le plus sensible aux fluctuations des jeux de données individuels, donc celui choisi pour ne pas perdre d'informations. En supposant un MN thermique, nous pouvons dériver des limites supérieures sur le facteur J uniquement. Ensuite, des limites peuvent être obtenues à partir de simulations cosmologiques à N corps. Nous discutons de cela et de l'incertitude liée dans **Sec. 9.6**. L'émission d'OFNIs est exclue à partir de MN jusqu'à $\sim$ 300 GeV, avec le jeu des limites issues de nos observations H.E.S.S. et des simulations cosmologiques à N corps. Nous concluons avec quelques perspectives pour d'éventuelles observations futures des OFNIs en **Sec. 9.7**. Les résultats présentés dans ce chapitre ont été publiés dans *The Astrophysical Journal* [10].

Le **Chapitre 10** montre l'étude sur la portée de sensibilité de la génération actuelle d'IACT aux signaux d'annihilation de MN, en utilisant des ensembles de données fictifs d'observations CG. Pour ces études, nous calculons le flux attendu de photons provenant de l'annihilation du MN en utilisant le rendement de rayons gamma de l'art. Nous montrons cela dans **Sec. 10.1**, avec une brève description des spectres des candidats MN canoniques tels que le Wino, le Higgsino et le Quintuplet et les dérivations les plus avancées pour la distribution MN dans le CG région, compte tenu de la rétroaction du baryon et de nouvelles mesures stellaires. Ensuite, **Sec. 10.2** présente comment nous avons traité les émissions connues de THE dans la région CG, qui sont un fond irréductible. Nous montrons dans la même section comment le retour sur investissement est défini et les taux de bruit de fond et de signal attendus dans la région. Nous présentons également les méthodes statistiques classiques qui sont ensuite utilisées pour la dérivation de la sensibilité. L'ensemble de données utilisé pour le calcul des limites est obtenu à partir du fond résiduel attendu des rayons cosmiques, qui est modélisé avec les paramètres obtenus à partir de la mesure des expériences CR. Nous ajoutons également certaines émissions conventionnelles connues, comme le PeVatron, l'émission BFs et le signal pulsar milliseconde d'un modèle spatial de renflement CG stellaire. Les limites sont indiquées dans **Sec. 10.3**, pour plusieurs canaux d'annihilation, pour les candidats MN canoniques considérés dans ce travail et pour les canaux neutrinos. La MN constituée de Winos est exclue pour toutes les distributions de MN que nous utilisons dans ce chapitre jusqu'à 10 TeV. Le niveau de sensibilité actuel ne peut pas sonder la masse thermique pour le Higgsino MN. Cependant, le niveau de section efficace théorique du Higgsino peut être atteint par la sensibilité du courant pour des masses d'environ 6.5 TeV, due à la résonance induite par Sommerfeld. La sensibilité actuelle exclut les valeurs thermiques pour Quintuplet DM. Les incertitudes systématiques et la manière dont elles peuvent affecter les limites finales sont explorées dans **Sec. 10.4**. Ici, nous montrons les incertitudes théoriques données par la différence des rendements gamma et des profils de distribution MN. L'incertitude sur la mesure du bruit de fond est introduite comme paramètre gaussien de nuisance. Enfin, nous testons le pouvoir

de reconstruction de notre cadre lorsque nous modifions les modèles générant notre émission de fond et injectons un faux signal MN dans notre jeu de données fictif. Nous concluons avec des perspectives futures possibles dans **Sec. 10.5**. Au moment de la rédaction, les résultats présentés dans ce chapitre ont été soumis à *Physical Review D* [282].

Conclusion Une étude de la région du Centre Galactique et plusieurs analyses pour la recherche de signal de matière noire à Très Haute Énergie, utilisant des jeux de données H.E.S.S. , sont présentées dans cette thèse.

Des méthodes statistiques appropriées pour la recherche d'un signal faible dans des ensembles de données dominés par le fond sont expliquées. Des modèles plus classiques, comme le cadre largement connu de log-vraisemblance-rapport-test-statistiques sont utilisés pour les analyses présentées dans ce travail. Une nouvelle approche basée sur les cadres de réseaux de neurones bayésiens est introduite et appliquée sur un ensemble de données synthétiques avec un signal injecté et un arrière-plan non trivial. Nous montrons comment ce cadre peut récupérer la description spatiale et spectrale du signal lorsque le fond est dominant. Les efforts en cours visent à appliquer cette architecture sur des jeux de données astrophysiques réels, par exemple la recherche de signal MN.

Le halo intérieur de la Voie Lactée est un environnement plein de possibilités pour tester l'astrophysique à Très Haute Énergie. Poussée par cela, la H.E.S.S. Collaboration a observé de manière approfondie les quelques degrés intérieurs autour du centre galactique avec le réseau complet de cinq télescopes. Cet ensemble de données, connu sous le nom d'Inner Galaxy Survey, se compose de 6 ans de données de haute qualité pour un total de 546 heures en temps réel, collectées entre 2014 et 2020. Il est décrit en détail, en mettant l'accent sur les détails de l'exposition et les paramètres de la prise de données. Les travaux en cours pour le développement de modèles de fond pour ces observations du centre galactique, utilisant des observations extra-galactiques et des simulations par séquences de l'ensemble de données Inner Galaxy Survey, sont introduits.

L'une des émissions importantes dans le halo intérieur de la Voie lactée est celle des bulles de Fermi. Cette émission de bulles à double lobe, détectée aux basses latitudes par le satellite *Fermi*-LAT , est analysée à partir des observations de l'Inner Galaxy Survey. Nous présentons l'analyse H.E.S.S. pour dériver le spectre des bulles et nous montrons les points de flux détectés pour des énergies comprises entre 300 GeV et $\sim$ 2 TeV. À 1 TeV, l'émission de BF est mesurée par H.E.S.S. à $\sim 1.0 \times 10^{-9}$ TeV cm^{-2} s^{-1} sr^{-1}. Les contraintes sur les populations de particules mères générant l'émission de BF peuvent être obtenues avec cette analyse. Les lois de puissance de coupure exponentielle sont testées pour les modèles leptoniques et hadroniques, mais les résultats ne peuvent pas définir de manière significative une valeur pour la coupure d'énergie, par conséquent, seules des limites inférieures peuvent être énoncées. En H.E.S.S., des études dédiées sont en cours pour approfondir les incertitudes systématiques et mieux contraindre

l'émission pour des énergies supérieures à 2 TeV.

Le Centre Galactique est également la cible la plus prometteuse pour la recherche de signaux d'annihilation MN puisqu'il est le plus proche et qu'il devrait héberger une grande quantité de matière noire. Les observations IGS sont utilisées pour dériver les limites les plus contraignantes, pour les canaux d'annihilation explorés dans ce travail, sur $\langle \sigma v \rangle$ des particules de matière noire pour les particules MN de masses TeV. En considérant le canal $\chi\chi \rightarrow W^+W^-$, nos limites atteignent 3.7×10^{-26} cm^{3}s^{-1} pour une masse de particule MN de 1.5 TeV. Dans le canal $\tau^+\tau^-$, les limites atteignent 1.2×10^{-26} cm^{3}s^{-1} pour une masse de particule MN de 0.7 TeV, traversant les valeurs $\langle \sigma v \rangle$ attendues pour les particules MN s'annihilant avec une section efficace thermique-relique. A 1.5 TeV de masse MN, nous obtenons un facteur d'amélioration de 1.6 par rapport aux résultats précédents de l'analyse H.E.S.S. en 2016. Des cibles complémentaires pour la recherche de signaux DM sont les sous-halos DM candidats.

Nous avons effectué une analyse sur une sélection de ces sous-halos parmi les sources de haute énergie du catalog 3FHL *Fermi*-LAT sans autre contrepartie astrophysique. Pour cette recherche, les limites supérieures du signal de matière noire sur le produit des paramètres libres $\langle \sigma v \rangle \times J$, à la fois pour chaque ensemble de données individuel et pour celui combiné sont dérivées. L'émission d'OFNIs en terme de MN a été exclue jusqu'à 300 GeV de l'analyse H.E.S.S. . En supposant un MN thermique, nous pouvons dériver des limites supérieures sur le facteur J uniquement.

La portée en terme de sensibilité avec la génération actuelle d'IACTs, et en particulier avec H.E.S.S., au signal d'annihilation des particules de matière noire est exposée dans ce travail. Pour cette étude, nous utilisons un jeu de données fictif des observations de l'Inner Galaxy Survey, créé à partir du fond résiduel attendu des rayons cosmiques et du fond conventionnel comme les émissions d'une population de milli-pulsar dans le renflement galactique, les BF et le Pevatron dans le Centre Galactique. L'état de l'art des rendements gamma pour le calcul des flux de photons attendus de MN annihilant est utilisé. Une nouvelle dérivation de la distribution MN dans le CG, y compris la rétroaction du baryon et les calculs cinématiques stellaires, a été appliquée. Des limites ont été dérivées pour les recherches MN indépendantes du modèle. La sensibilité aux candidats MN canoniques tels que le Wino, le Higgsino et le Quintuplet est explorée. La matière noire théorique de Wino est exclue jusqu'à 10 TeV. Le niveau de sensibilité actuel atteint la section efficace théorique de Higgsino pour des masses de l'ordre de 6.5 TeV, du fait de la résonance induite par Sommerfeld. La sensibilité actuelle exclut les valeurs thermiques pour Quintuplet DM. Nous explorons largement comment l'évaluation des différentes incertitudes peut affecter les résultats finaux.

Ce travail apporte de nouvelles informations importantes sur une nouvelle approche pour le démêlage d'un signal dans un ensemble de données dominé par l'arrière-plan avec une architecture de réseau de neurones bayésien. Le H.E.S.S. IGS,

qui constitue les observations les plus sensibles disponibles à ce jour de la région du CG aux énergies du TeV, est présenté en détail. La recherche du signal BF montre la capacité de contraindre cette émission étendue avec H.E.S.S.. De nouvelles limites importantes sur $\langle \sigma v \rangle$ des particules MN sont obtenues avec l'IGS et les observations H.E.S.S. des candidats subhalo MN. Enfin, des repères ont été établis sur la sensibilité aux signaux de matière noire pour la génération actuelle d'IACT.

Introduction

The study of non-thermal processes in the Universe, the most violent ones, has been pioneered by Very High Energy astrophysics (VHE, $E \geq 100$ GeV). Galactic objects, like supernova remnants and black holes, or extra-galactic ones, like the active galactic nuclei, accelerate cosmic rays which emit gamma-rays, photons at energies higher than the MeV energies. The mechanisms responsible for the origin and the acceleration of cosmic rays are still widely debated. The Galactic Center is one of the most promising regions in the sky for these investigations. A diffuse TeV gamma-ray emission has been detected close to the central supermassive black hole Sagittarius A*. This detection has been claimed as a hint for a proton accelerator up to PeV energies, *i.e.* a Pevatron. More recently, other 12 sources have been identified with photons of energies up to 1.4 PeV. An extended Very-High-Energy emission has been detected by the *Fermi*-LAT experiment above and below the Galactic Plane, the Fermi Bubbles. This emission is brighter at low latitudes and shows no hint for an energy cutoff in the Fermi analysis, thus opening the question of what can be done at TeV energies.

Very High Energy gamma-rays are a laboratory for the study of fundamental physics beyond the standard model of particle physics. 85% of the matter in the Universe is dark. The nature of this elusive component is still puzzling. Among the best candidates to describe dark matter are non-baryonic massive particles which can interact gravitationally and through the weak force with the standard matter. These particles are known as weakly interacting massive particles (WIMPs). When WIMPs massive enough are considered, they can self-annihilate in dense regions of the Universe producing TeV gamma-rays. The most promising region to observe signals from annihilating dark matter is the Galactic Center and the few degrees of sky around it. Alternative targets are dark matter subhalos, which are predicted to be hosted by Milky-Way-like galaxies by cosmological simulations. These targets are dominated by the presence of dark matter and host no gas, therefore could be a clear confirmation of an eventual dark matter signal detected in the Galactic Center.

Imaging Atmospheric Cherenkov Telescopes (IACT) can observe Very-High-Energy gamma-rays. The High Energy Stereoscopic System (H.E.S.S.) is an array of 5 IACTs observing gamma-rays in the energy range between around 50 GeV and tens of TeV. The Galactic Center region can be observed by H.E.S.S. at high sensitivity,

thanks to the ideal position of the array in the Southern hemisphere. This region of the sky is promising for observations because of possible dark matter signals in the masses range which cannot be probed by the colliders. Many important constraints have been derived on dark matter and Very-High-Energy emissions with observations of the Galactic Center region and dark matter subhalo candidates. The future array of IACTs, the Cherenkov Telescope Array (CTA), will push the sensitivity in the TeV energy range to study even deeper these emissions.

Since the Galactic Center region is one of the most promising laboratories for studying Very-High-Energy astrophysics, what can we do with H.E.S.S. observations of it?

In this PhD thesis, I describe the extensive program of observations of the Galactic Center region with H.E.S.S., the Inner Galaxy Survey. This dataset is used for the search for the Fermi Bubbles emission and for dark matter annihilation signals from the inner halo of the Milky Way. Other searches for dark matter signals are presented with observations towards dark matter subhalo candidates. Novelties on Bayesian Neural Network frameworks for the discrimination of a weak signal in a background-dominated dataset are discussed. Studies on the final reach in sensitivity to dark matter signals from the Galactic Center region with the current generation of IACTs are presented.

The **first part** of the thesis is introductory. The fundamental concepts on Very-High-Energy astrophysics, the H.E.S.S. telescopes array, the statistical methods used in this work and the nature of dark matter are presented. **Chapter 1** shows concepts on the astrophysics of gamma-rays production through the acceleration mechanisms of cosmic rays. The H.E.S.S. telescopes and a concise description of the detection, observation and background measurement techniques is made in Chapter **Chapter 2**. The dark matter paradigm, the best particle candidates for dark matter and the current understanding of the expected dark matter distribution in the Galactic Center region are reported in **Chapter 3**. The expected signal for indirect detection of dark matter and of the most promising Very-High-Energy gamma-ray targets are also presented. In the last chapter of the first part I answer the question: which new advanced statistical methods can we apply to the study of a weak signal? **Chapter 4** shows the statistical methods and performance tests for characterizing the results and the uncertainties. Classical methods with the application of log-likelihood-test-statistics as well as Bayesian Neural Network frameworks are presented and applied for the discrimination of a weak signal in the presence of non trivial background. The Bayesian Neural Network frameworks are a novel approach that can be applied on astrophysical datasets. At the moment of the writing, the results obtained with our Bayesian Neural Network framework have been submitted to ICLR2023 [64].

In the **second part** of the thesis, the Galactic Center region at Very-High-Energy is explored. **Chapter 5** is an introduction. A brief description of the Very-High-Energy sky in the Galactic Center region is given here. First, the observations of the

Galactic Center at multi-wavelengths are introduced. The known TeV astrophysical sources populating the Galactic Center and the extended Very-High-Energy emissions that have been detected in the region are described. The chapter is concluded with a brief report on the Very-High-Energy outflows measured around the Galactic Center. In this, I also introduce the Fermi Bubbles, the double-lobe structure detected by the *Fermi*-LAT satellite at GeV energies. This emission shows no hing for a cutoff up to $\sim$ TeV and it is brighter in the inner halo of the Milky Way. The Inner Galaxy Survey is presented in detail in **Chapter 6**. I first introduce the scientific goals of this extended program of observations. This dataset can be used to search for dark matter annihilation signals from the Galactic Center region and for the Fermi Bubbles emissions, given that the exposure of the Survey is higher in the region where the latter is expected to show at TeV energies. The observational dataset before the advent of H.E.S.S. phase II, when the array was composed by only the four small telescopes, and after it, with the full five-telescopes array is described. A detailed presentation is given about the parameters of the data taking of the Survey, such as the zenith and offset angles of the observations and excess and significance sky maps. Two extensive sections are then dedicated to the description of the study of the systematics affecting the dataset and the procedure that I am implementing to build background models from extra-galactic observations and run-wise simulations of the Inner Galaxy Survey observational runs. The second part concludes with **Chapter 7**, where I present the search for the low-latitude Fermi Bubbles (FBs) emission with H.E.S.S.. *Fermi*-LAT already investigated the low-latitude Bubbles, but what can we achieve with H.E.S.S. observations? For this search, I use the Inner Galaxy Survey dataset and define a region of interest from the *Fermi*-LAT spatial template of the Bubbles to derive new constraints on the emission at TeV energies, where the satellite experiment cannot observe photons and cannot detect any hint for a cutoff on the GeV spectrum. I show the results of the detection of the Bubbles with H.E.S.S.. With these constraints, new limits can be derived on the models of the parent particle populations that can explain the emission. However, several systematic uncertainties affecting the analysis are still being studied. At the moment of the writing, the results shown in this chapter are being prepared for a submission to *Nature* within a few months [140].

The new results for the search of dark matter annihilation signals with H.E.S.S. are reported in the **third part** of this work. I already introduced how the Inner Galaxy Survey is used to search for the Fermi Bubbles, but how can it be used to obtain new constraints on dark matter signals? In **Chapter 8**, I show new results for the limits on the velocity-weighted annihilation cross section of self-annihilating WIMPs with the Inner Galaxy Survey observations. The obtained limits are the most constraining ones in the TeV mass range for the tested annihilation channels. This work includes the estimate of the systematic uncertainties affecting the Inner Galaxy Survey dataset in the final limits. The results shown in this chapter

have been published in *Physical Review Letters* [7]. **Chapter 9** presents another search for dark matter annihilation signals. In this case, candidate dark matter subhalos are observed by H.E.S.S.. The selection of the candidates was performed among the sources with no conventional astrophysics counterparts in the 3FHL *Fermi*-LAT catalog of sources at high energies. We call these objects unidentified-Fermi-objects. The selection has been performed to find the best candidates as subhalos and easily observable with H.E.S.S.. Our analysis excludes the emission detected from the unidentified-Fermi-objects as from dark matter. To obtain the final limits, a joint fit of H.E.S.S. and *Fermi*-LAT data analyses is performed. Using cosmological N-body simulations, more stringent constraints can be obtained on the sources. The results shown in this chapter have been published in *The Astrophysical Journal* [10]. The last chapter, *i.e.* **Chapter 10**, explores the reach in terms of sensitivity to dark matter annihilation signals with the current generation of IACTs and in particular with H.E.S.S.. For this work, I have created a mock dataset of measurements mimicking the current status of observations towards the inner halo of the Milky Way with the Inner Galaxy Survey. I use state of the art gamma-ray yield computations for the expected spectra of photons from annihilating dark matter and dark matter distribution profiles in the Galactic Center. Sensitivity limits are obtained in several channels for model-independent dark matter annihilation. The reach of H.E.S.S. for measurements of photons emitted from dark matter annihilating in neutrino channels is also tested. Finally, limits are computed for WIMPs canonical candidates such as the Wino, Higgsino and Quintuplet, showing what are the possible achievements with the current generation of IACTs. At the moment of the writing, the results shown in this chapter have been submitted to *Physical Review D* [282].

Part I

Very-High-Energy Astrophysics

Chapter 1

Astrophysics at TeV energies

Contents

In this chapter, the astrophysics and the underlying processes regarding Very-High-Energy (VHE, $E \gtrsim 100$ GeV) gamma rays will be succinctly introduced. The acceleration of cosmic rays in the Universe is induced by various mechanisms. Very-High-Energy gamma rays can be produced through leptonic and hadronic particle physics processes. These gamma rays are used to study phenomena, amongst the most violent, in the non-thermal Universe. In Sec. 1.1, we introduce the fundamental concepts for the model of the non-thermal Universe. Sec. 1.2 and Sec. 1.3 are devoted to the presentation of the acceleration mechanisms of cosmic rays and the subsequent production of gamma rays. In Sec. 1.4, some of the astrophysical accelerators of cosmic rays are presented. Sec. 1.5 introduces the main instruments that observe the non-thermal VHE Universe via the direct or indirect detection of gamma rays. In Sec. 1.6, we present how Very-High-Energy gamma-ray detection can be used to study some forefront topics of fundamental physics. General and detailed reviews of High Energy Astrophysics can be found in Refs. [252, 329].

1.1 Preamble

The thermal radiation is the light emitted by the Sun, the stars and the light bulbs, and more generally by matter in thermal equilibrium. The continuum black-body spectrum is characteristic of the thermal radiation and follows the Stefan-Boltzmann law ($E \propto T^4$). The wavelength and frequency ν of this radiation depends on the temperature of the body emitting it ($\nu \propto T$). The frequency is larger as the object is hotter. Light at the highest energy is not produced thermally because there is no object hot enough to produce this. Photons of this light are commonly known as gamma-rays and are the results of non-thermal processes implying particle interaction with ambient medium or fields. The temperature of the source does not influence or characterize the non-thermal radiation. VHE gamma-ray astronomy studies the non-thermal Universe, which relates to processes of extreme particle acceleration. These processes can take place in astrophysical environments such as black holes, explosion or merging of massive stars.

1.2 Cosmic-ray acceleration processes

1.2.1 Spectra of cosmic rays

Cosmic rays (CRs) is the name associated with high-energy protons, electrons/positrons and atomic nuclei moving through space at nearly the speed of light. These can be emitted by the Sun, from outside of the Solar System in our own galaxy or from distant galaxies as well. A shower of secondary particles is produced by the impact of cosmic rays with Earth's atmosphere. Victor Hess and Domenico Pancini

excluded the terrestrial origin of the radiation coming from the showers generated by cosmic rays after the observation of electroscopes discharging spontaneously in the air. Pancini and Hess studied this radiation: Pancini found that the radiation decreases in deep waters [298] and Hess showed that it increases with altitude [199]. Millikan introduced the term *cosmic rays* for this extraterrestrial radiation in 1928 [275].

CRs have been observed in wide energy range and they can be classified as low-energy (LE) in the $E < 50$ MeV energy range, high-energy (HE) for the range between 50 MeV and 100 GeV, VHE for energies between 100 GeV and 100 TeV, ultra-high-energy (UHE) for energies above 100 TeV and up to 100 PeV and finally extremely-high-energy (EHE) at energies above 100 PeV. In Fig. 1.1, we show the measured power-law like CR spectrum [94]. Some features are distinguishable: a modulation at low energies due to Solar wind activity, the "knee" at energies of about 10^{15-16} eV with a spectral index change, and the "ankle" at 10^{18-19} eV with a spectrum change. The rate of detection of CRs drastically decreases with increasing energy. Below the knee, the CR spectrum shows an index of ~ 2.7, which then changes to ~ 3.3 between the knee and the ankle and it goes to ~ 2.6 above the ankle. Galactic origins are assumed for CRs at LE and HE, while those above the ankle have likely extragalactic origins because they are accelerated to such high energies by extragalactic sources like active galactic nuclei. A transition between the Galactic and extragalactic CRs is expected in the intermediate energy range. At VHE, CRs get to Earth with a rate of 1 particle/$(\mathrm{m}^2\mathrm{yr})$. Above 10^{20} eV, no detection of CRs was expected because EHE CRs can efficiently interact with the Cosmic Microwave Background (CMB) radiation through processes $\gamma_{\mathrm{CMB}} + p \to p + \pi^0$ or $\gamma_{\mathrm{CMB}} + p \to n + \pi^+$ and loose energy. This is known as the Greisen–Zatsepin–Kuzmin (GZK) cutoff [295]. EHE CRs were detected by Auger, and this puts a limit on the distance of their source of about 50 Mpc[1], called the GZK horizon, such that the probability that CRs survive during the travel is larger.

1.2.2 First and second-order Fermi acceleration processes

The acceleration of charged particles happens when they interact with irregularities of a magnetic field. The concept of the CR acceleration process was introduced by Enrico Fermi in the '50s. He developed the second order Fermi acceleration mechanism [170].

Clouds in the interstellar medium perfectly ionized are perfect conductors. They show irregularities in the magnetic field distribution if they are initially magnetized. An incoming relativistic particle with an incoming velocity $\simeq$ c, enters the cloud which moves with velocity u. The particle then moves randomly inside the cloud and interacts with it. It is reflected off with increased energy because of

[1]A parsec is defined as 3.26 light-years. Proxima Centauri, the nearest known star to Earth other than the sun is about 1.3 parsecs away (approximately 4.25 light years) [288].

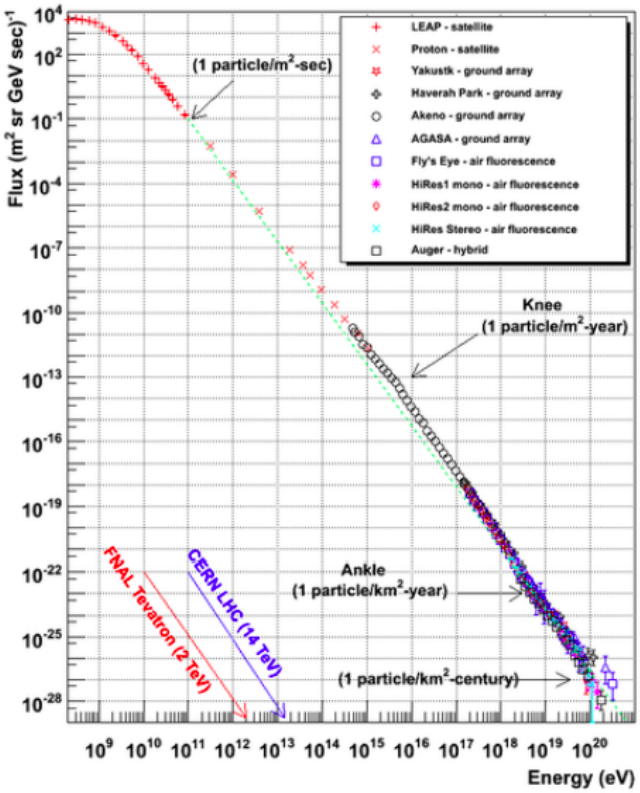

Figure 1.1: The CR spectrum spanning energies from 10^8 to 10^{21} eV. The features known as the *knee* and *ankle* are highlighted. The rate of CRs for different energies are given. A power-law with index ~ 2.7 is shown in green. Figure extracted from Ref. [94].

elastic diffusion on magnetic structures. The cloud is acting as a magnetic mirror: it accelerates head-on particles and decelerates head-back ones. The particle can gain, on average, an energy $\langle \Delta E/E \rangle = 8/3(u/c)^2 = 8/3\beta^2$ [170]. This mechanism is second order because the gain per reflection depends on β^2. However, the whole detected CR spectrum cannot be explained with this theory. In fact, this mechanism cannot explain particles accelerated above the GeV energies. A linear gain with u/c would explain the spectrum more efficiently since $u/c << 1$. A sketch of the second order Fermi acceleration mechanism is shown in the left panel of Fig. 1.2.

To solve the problems connected to the second order acceleration, the latter was revisited in the '70s and the first order Fermi acceleration mechanism was developed. This mechanism is known as diffusive shock acceleration [50, 67]. The acceleration happens because of the interaction of a relativistic particle with a strong shock wave at supersonic velocity. Particles are present both in the front and the back of the shock which propagates in the interstellar medium. Since

they cross the shock from both directions, the particles are scattered isotropically. In the gas rest frame, a shock wave approaches upstream with speed u_1 and the velocity of the gas beyond the shock is $u = u_1 - u_2 > 0$, with u_2 being the velocity of the gas in the shock wave rest frame. A relativistic particle crossing the shock upstream with speed v and angle θ with respect to the direction of the shock wave benefits from a small increase of energy $\Delta E = E(u/v)\cos\theta$ and is scattered behind the shock. At each passage, the average gain through the shock front is $\langle \Delta E/E \rangle \simeq u/c$. At rest with the gas downstream, the gas is approaching the shock to the front with approaching speed u. So the same small increase of energy is transmitted to a particle crossing the shock front downstream. Therefore, a particle crossing the shock several time will benefit from many energy increase. The collisions are always head-on and there is no lost of energy by crossing. Considering a full upstream-downstream-upstream passage, an average gain is of $\langle \Delta E/E \rangle = 4/3(u/c) = 4/3\beta$, *i.e.* it increases linearly with β. After n cycles in the acceleration region, the probability that the particle does not escape is of P^n = ($1 - \langle \Delta E/E \rangle$)^n. The number of particle after n cycles, starting with the initial number N_0, will be $N_n = N_0 P^n$. After n cycles, the energy of the particles is $E_n = E_0(1 + \langle \Delta E/E \rangle)^n = E_0 \epsilon^n$. Therefore $N/N_0 = (E/E_0)^{\ln P/\ln \epsilon}$. The particles spectrum can then be approximately written to $dN/dE \propto E^{-1+(\ln P/\ln \epsilon)}$. Considering $\ln P/\ln \epsilon \simeq -1$, gives a spectral index ~ 2 at the source. Then, the diffusion of the CRs through the medium produces a softer spectrum, with an index of 2.3-2.7, far from the accelerators. A sketch of the first order Fermi acceleration mechanism is shown in the right panel of Fig. 1.2.

Figure 1.2: Sketch of the second and first order Fermi acceleration mechanisms in the left and right panels, respectively. Figure extracted from Ref. [254].

1.3 Production mechanisms of gamma rays

The production of VHE gamma-rays can happen through the acceleration of electrons and positrons via leptonic processes, or protons and nuclei via hadronic ones [329]. Depending on the energy range which is considered, the relevance of the given acceleration process changes. The range of energies up to tens of keV is dominated by the Synchrotron radiation, while the GeV energy range is populated mainly by photons from the bremsstrahlung process. In the GeV-TeV energy

range, the Inverse Compton Scattering becomes the dominant process together with pion decay. We present briefly each mechanism in what follows. More detailed reviews can be found in Refs. [95, 252].

1.3.1 Leptonic processes

The interaction of a charged particle with an electromagnetic field produces **Synchrotron radiation**. The acceleration produces radial movement of the particle which moves in a spiral trajectory around the lines of the magnetic field. We show in Fig. 1.3 the production of synchrotron emission by a fast electron that is bent in a magnetic field. This radiation covers a wide range of energies from radio to X-rays in the electromagnetic spectrum and is polarized. The energy of the synchrotron radiation emitted by relativistic electrons moving in a typical galactic magnetic field is expressed as:

$$E_{\rm syn} \simeq 0.05 \left(\frac{E_{\rm e}}{\rm TeV}\right)^2 \left(\frac{B}{3\ \mu{\rm G}}\right) \text{ eV}. \tag{1.1}$$

The term $E_{\rm e}$ is the energy of the incident electron with respect to the lines of the galactic magnetic field. A parent population of electrons following the spectral power law $dN_e/dE_e \propto E_e^{-\alpha}$, with α index of the power law, result in a gamma-ray spectrum of $dN_\gamma/dE_\gamma \propto E_\gamma^{-(1+\alpha)/2}$. In the left panel of Fig. 1.3, we show a sketch for the Synchrotron radiation.

When a particle, mainly an electron or a positron, decelerates due to the deflection of a Coulomb field of an atomic nucleus the **Bremsstrahlung**, or braking radiation, is produced. The incoming electron loses energy, which is converted into a continuum spectrum of photons. Above a few tens of MeV, the Bremsstrahlung is the dominating radiating process for electrons/positrons. For muons, it dominates above a few hundreds of GeV because the radiation is inversely proportional to the mass of the incoming particle, therefore muons lose energy slower than electrons. The interaction of electrons with energy E with atoms and molecules can trigger the production of gamma-rays of frequency up to $\nu = E/h$. On average, the energy of the gamma-ray is about 1/3 of the energy of the accelerated particle, *i.e.* $\langle E \rangle_\gamma = \langle E \rangle_e / 3$. Therefore, electrons accelerated up to tens of TeV can produce gamma-rays at TeV. Dense environments are better to host this process because high density of atomic nuclei can favor the deceleration of the particles. The central panel of Fig. 1.3 shows a sketch for the Bremsstrahlung.

The interaction between an accelerated electron and a low energy photon is known as the **Inverse Compton Scattering** (ICS). This process consists of the cooling of a relativistic electron which transfers energy to photons. In the right panel of Fig. 1.3, we show a sketch of how the energy of the electron is lost in

the interaction where the photon gains it. The maximum frequency in the observer frame is $\nu/\nu_0 \simeq 4\gamma^2$, with γ the Lorentz factor. The spectrum is peaked towards the average frequency, and that can be seen from the average frequency $\langle\nu\rangle/\nu_0 \simeq 4/3\gamma^2$. Considering the interaction between a charged particle with energy $E_{\rm e}$ and mass m with a target photon of energy E, happening in non-relativistic regime ($E << m^2$), the cross section of the ICS interaction is close to the Thompson one, *i. e.* $\sigma_{\rm ICS} = \sigma_{\rm T}(1 - 2\kappa_0)$, with $\kappa_0 = E/m^2$. The Thompson cross section is $\sigma_{\rm T} \simeq 6.65 \times 10^{-25} cm^2$. The scattered photon in this regime has an energy $E_\gamma \simeq E^2/m^2$. The ICS cross section changes in the ultra-relativistic Klein-Nishina regime ($E >> m^2$) to $\sigma_{\rm ICS} = 3/8\sigma_{\rm T}\kappa_0^{-1}{\rm ln}(4\kappa_0)$. In this case, the photons produced can have the same energy as the initial electron. From a parent particle population of electrons with a spectrum following $dN_{\rm e}/dE_{\rm e} \propto E_{\rm e}^{-\alpha}$, gamma-ray spectra following $dN_\gamma/dE_\gamma \propto E_\gamma^{-(1+\alpha)/2}$ and $dN_\gamma/dE_\gamma \propto E_\gamma^{-(\alpha+1)}{\rm ln}(\kappa_0 + const)$ are produced in the Thompson and Klein-Nishina regimes, respectively.

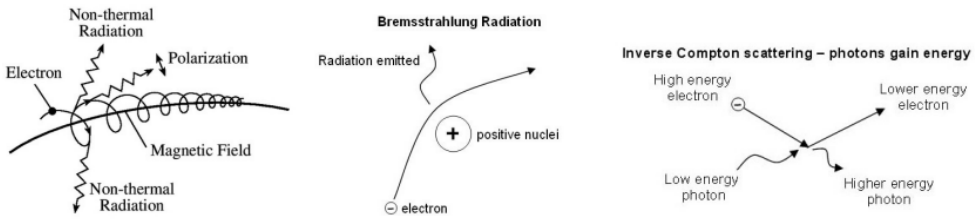

Figure 1.3: Leptonic mechanisms for the production of VHE gamma-rays. *Left panel:* Synchrotron radiation production through interaction of a charged particle with a magnetic field. Figure extracted from Ref. [239]. *Central panel:* Bremsstrahlung process producing gamma-rays when an electron breaks in the electric field of a positively charged nucleus. Figure extracted from Ref. [219]. *Right panel:* Inverse Compton Scattering producing VHE gamma-rays when a very energetic electron is scattered against a low energy photon and their energy is exchanged. Figure extracted from Ref. [219].

1.3.2 Hadronic processes

The interaction of accelerated protons with the interstellar gas produces neutral pions. Subsequently, pions decay into photons [346]. We show in Fig. 1.4 a sketch of the accelerated protons interacting with a proton in the interstellar medium. This ends up producing charged and neutral pions in the fractions of 1/3 of neutral pions π^0 and 2/3 of charged pions π^+ and π^- [223]. Hadronic photoproduction, given by the interaction of accelerated protons with photons is also relevant for the production of pions. Muons and subsequently neutrinos are produced from charged pions, while pairs of gamma-rays are produced from the decay of neutral pions, in the process $\pi^0 \rightarrow \gamma + \gamma$, with a 98.8% branching ratio and a lifetime of

τ_{π^0} = 8.4$\times 10^{-17}$ s. TeV gamma-rays are produced most efficiently by this process. The distribution of gas which is the target for the incident protons is traced by the gamma-ray emission. The energy threshold of this interaction is at $2m_{\pi^0} \simeq 270$ MeV. The maximum of the gamma-ray spectrum at $E_\gamma = m\pi^0/2 \simeq 67$ MeV is a specific feature of this emission. From an initial spectrum of the parent particle population of protons following $dN_{\rm p}/dE_{\rm p} \propto E_{\rm p}^{-\alpha}$, a gamma-ray spectrum following $dN_\gamma/dE_\gamma \propto E_\gamma^{-\alpha+0.1}$ is produced due to a slight dependence of the inelastic pp interaction with energy [223]. A clear signature of proton acceleration by an astrophysical object would be a joint detection of neutrinos from charged pion decay and gamma-rays from neutral pion decay.

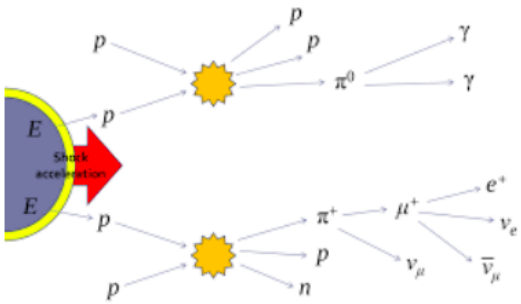

Figure 1.4: Accelerated protons interacting with the photons of the interstellar medium producing pions. Charged pions decay into muons and the corresponding neutrinos, while the neutral ones produce a pair of gamma-rays.

1.3.3 Dark matter decay and annihilation processes

The phenomena involving DM interactions such as the self-annihilation of dark matter (DM) particles or their decay can produce gamma-rays. The latter can be the result of primary or secondary processes. We keep the description of the production of gamma-rays through DM annihilation and the expected gamma-ray spectrum for Sec. 3.8.

1.4 Some astrophysical accelerators of cosmic rays

The explosion of a star more massive than 8 times the Sun into a supernova results in a **Supernova Remnant** (SNR) [119]. A supernova explosion is the last burst of life of a very massive star. The core of the star, once the outer layers have been expelled through the supernova explosion, implodes into a white dwarf, a neutron star or a black hole. The difference between the three depends on whether the star has a mass below 10 (it becomes a white dwarf), between 10

and 29 (it becomes a neutron star) or above 30 solar masses (it becomes a black hole). When the star turns into a white dwarf, it then accretes mass until the collapse. The remnant structure is made out of expanding material ejected during the explosion that creates a shock front. The shock of SNR can accelerate cosmic rays that then produce gamma-rays [180]. The CR acceleration is driven by about 10% of the energy of the explosion. The first SNR detected in VHE gamma-rays by H.E.S.S. is SNR RXJ1713.7-3946 [34].

Short and intense jets of gamma-rays from extragalactic processes are known as **Gamma-Ray Bursts** (GRBs). These phenomena are transient and among the brightest ones in the Universe. The explosion of a very massive star into a black hole or the merging of two neutron stars (or a neutron star and a black hole) can produce GRBs. The detection of prompt GRBs gamma-rays has been performed by *Fermi*-LAT up to about 50 GeV. Their luminosity is about 10^{52-54}erg/s. In the keV-MeV energy range, hundreds of GRBs have been detected [86]. MAGIC detected a prompt emission of GRBs above 300 GeV [259]. A longer-lived emission, the afterglow, is produced after the first gamma-ray jet by the interaction of the ejecta and the interstellar medium. H.E.S.S. detected also for the first time VHE gamma-rays from a GRB afterglow above 100 GeV [328].

A compact region at the center of a galaxy with very high luminosity over some portion of the electromagnetic spectrum can be an **Active Galactic Nuclei** (AGN). AGN can be powered by a supermassive black hole at the center of the galaxy. These black holes have masses up to a billion times the mass of the Sun. In optical and X-rays, an accretion disk of gas is visible rotating around them. Gamma-rays in highly collimated relativistic jets are also produced by AGNs [93]. The object is known as a blazar if the jet is pointing towards Earth (at an angle smaller than $\sim 20°$). Hundreds of these are detected at GeV energies and tens at TeV. The main processes producing gamma-rays in this case are ICS on synchrotron electrons. The synchrotron self-Compton process is a standard interpretation for AGN spectra [262]. The role of hadronic processes in the emission is not yet settled. The protons can be accelerated by the jets up to EeV energies. Among the brightest blazars spectra are the flares from PKS 2155-304 [37].

Massive stars with nuclei between 1.5 and 2.9 solar masses exploding in supernovae can then produce **Pulsars** (PSR) [197]. Later, the winds generated by the pulsar can power a **Pulsar Wind Nebulae** (PWN). After the ejection of the outer layers, the remaining core can be a neutron star with high rotation rate. Charged particles are accelerated by the strong magnetic field which traps them in beams and then ejects them by the poles. Since the emitted jets are periodically observed by Earth giving the effect of pulsations, the objects are called pulsars. The typical periodicity of the pulsation is of the order of the second. The Vela Pulsar is one of the most energetic gamma-ray emitting PSR [189]. H.E.S.S. recently detected TeV events from the Vela Pulsar [162]. The particles following the lines of the magnetic field around the PSR are not ejected in the beams but rotate with

the neutron star itself. However, at a large enough distance the particles cannot rotate with the star anymore otherwise they would be forced to go faster than the speed of light. The particles therefore escape the PSR at this distance, which is known as the light cylinder [266]. These particles are then injected in the interstellar medium and form the so-called pulsar wind nebula. Once outside the light cylinder, particles can be accelerated through shock waves in the medium via ICS, which can effectively produce gamma-rays [63]. The Crab Nebula is the most observed PWN in VHE gamma-rays [32] and was also used as a standard candle for measurements in Very-High-Energy astrophysics.

1.5 Gamma-ray experiments

1.5.1 Space-based experiments

The direct detection of gamma-rays is performed by experiments carried on satellites, which are outside Earth's atmosphere. They can detect gamma-rays from a few MeV up to about a hundred GeV because of the small size, which reflects their acceptance in the order of ~ 1 m^2. Their duty cycle is almost 100% since they are always observing and do not suffer the alternation of day and night. They can benefit of modest angular resolution around 0.15°-0.35°, very good energy resolution $\sim 10\%$ E and a wide field of view (FoV) > 2 sr. Currently operating gamma-ray telescopes are the *Fermi*-LAT and AGILE. AGILE (Astro-Rivelatore Gamma a Immagini Leggero) was launched in 2007 [30]. The satellite is equipped with a Gamma-Ray Imaging Detector (GRID) which covers the 30 MeV-50 GeV energy range, the silicon X-ray detector SuperAGILE covering the range between 18 and 60 keV, the non-imaging gamma-ray scintillator detector Mini-Calorimeter (MCAL) covering the range of 350 keV-100 MeV. It is equipped with an anticoincidence detector that acts as a veto. *Fermi*-LAT is located on the Fermi Gamma-ray Space Telescope observatory, formerly known as the Gamma-ray Large Area Space Telescope (GLAST) [171]. The *Fermi*-LATenergy range covers 20 MeV-300 GeV, reaching an energy resolution lower than 10%. It can cover a field of view wider than 2 sr and affording an angular resolution lower than 0.15° for energies larger than 10 GeV [171]. The Large Area Telescope Instrument is shown in Fig. 1.5. The experiment contains an anticoincidence detector, a tracker and a calorimeter. The detector discriminates against the background and it acts as a veto. This part of the detector flashes when CRs pass in. The gamma-rays are then converted to electron and positron pairs by the tungsten foils located in the tracker. They are finally stopped by the iodide calorimeter which can then measure the total energy of the initial gamma ray.

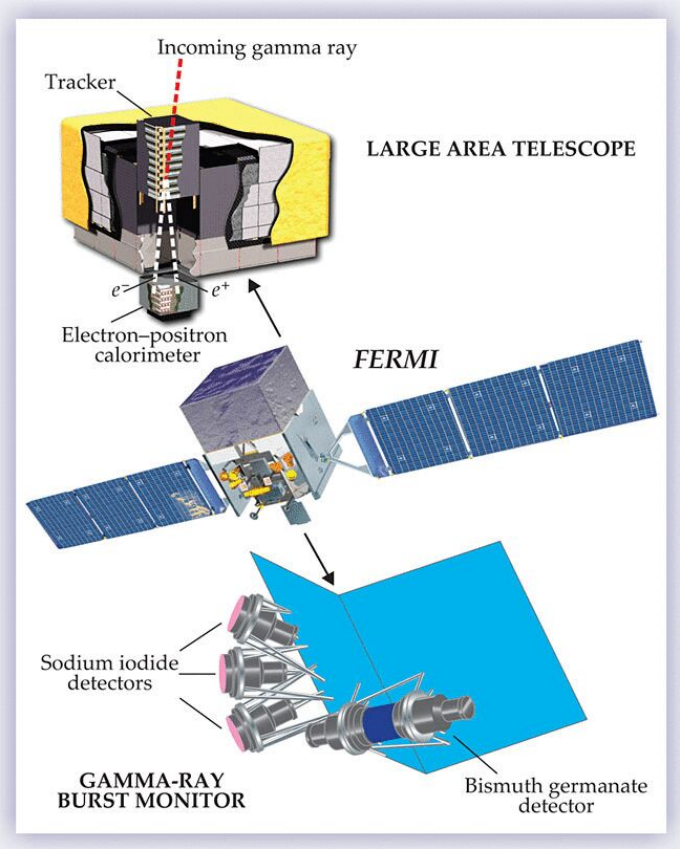

Figure 1.5: The *Fermi*-LAT space telescope and its instruments: the Large Area Telescope and the Gamma-ray Burst Monitor. Figure extracted from Ref. [151].

1.5.2 Ground-based experiments

Water tanks experiments

The secondary charged particles of the shower produced by the primary gamma-rays interacting with the atmosphere are detected by water tanks experiments. Since the particle shower develops quite rapidly in the atmosphere and the target/charged particles are mostly in the core of the particle shower, these experiments are located at the highest altitude possible, to probe the shower core. While the charged particles in the shower travel inside the water tanks, they produce Cherenkov light detectable with photomultipliers (PMTs). Then, the energy and direction of the primary incoming gamma-ray can be reconstructed. The spatial distribution of their hits in the tanks array is used to discriminate between gamma-rays and CRs. The large surface of the tanks based experiments allows the detec-

tion of photons at VHE energy, with best sensitivity beyond the TeV. These experiments benefit from modest energy resolution $\sim$ 50% E, good angular resolution of 0.2-0.8°, pretty large FoV $\sim$1 sr and long duty cycle $\sim$ 90%. The two main water tank gamma-ray observatories are the HAWC (High Altitude Water Cherenkov observatory) [193] and the Water Cherenkov detector facility part of the LHAASO experiment [160]. The LHAASO Water Cherenkov Detector Array (WCDA) facility is a close-packed surface with water Cherenkov detectors with a total area of about 78,000 m^2. It is built at 4410 meters of altitude in the Sichuan province of China. The layout of LHAASO is shown in Fig. 1.6. More details can be found in Ref. [250].

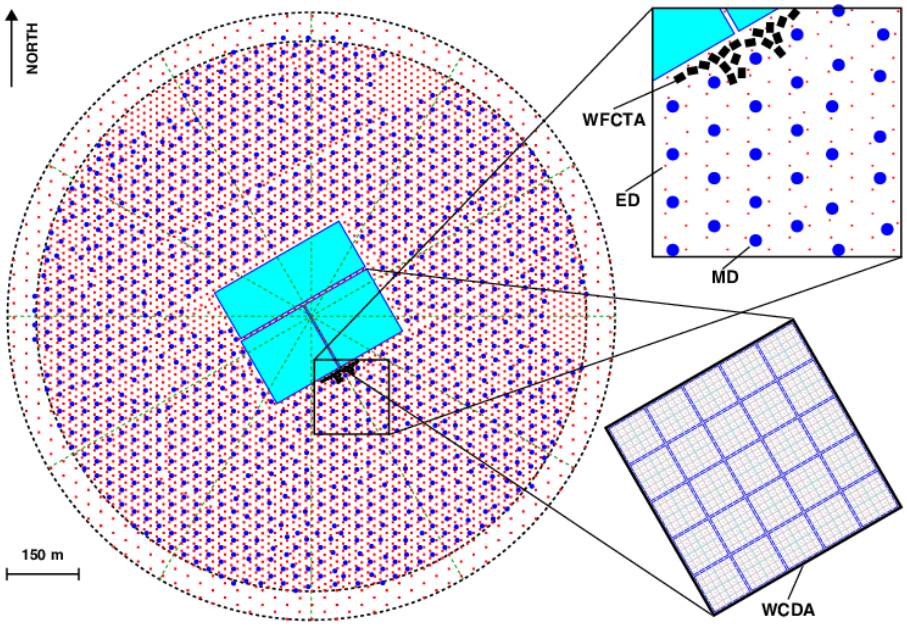

Figure 1.6: The layout of the LHAASO experiment with all the facilities composing it. The zoomed portions of the layout show the WCDA, some electromagnetic particles (ED) and muon (MD) detectors and the wide field-of-view air Cherenkov telescopes array (WFCTA) Figure extracted from Ref. [250].

Ground-based Atmospheric Cherenkov telescopes

The indirect detection of VHE gamma-rays is performed by ground-based imaging atmospheric Cherenkov telescopes (IACTs). The gamma-rays interact with the molecules of the atmosphere and trigger a shower of charged particles that produce Cherenkov light. IACTs are sensitive to gamma-rays between tens of GeV and about a hundred TeV. They benefit from excellent energy resolution $\sim$10% E and angular resolution of < 0.1°. However, the IACTs duty cycle is short, *i.e.* 10$-$15% because no observations are performed during day time. Moreover, since the FoV is modest, $\sim$ 5°corresponding to $\sim 10^{-1}$ sr, observations with IACTs

are pointed. We present more details about the detection technique with IACTs in Chap. 2. The main currently operating IACTs are H.E.S.S.(The High Energy Stereoscopic System) [138], MAGIC (Major Atmospheric Gamma-ray Imaging Cherenkov telescope) [260] and VERITAS (Very Energetic Radiation Imaging Telescope Array System) [361]. We summarize the main characteristics of these arrays of telescopes in Tab. 1.1. On the MAGIC site in La Palma, the telescope FACT (First G-APD Cherenkov Telescope) [169] was mounted in 2011 to test a new technology that will be applied for CTA (Cherenkov Telescope Array), the future of the Cherenkov Telescopes array. FACT camera uses Geiger-mode avalanche photodiodes (G-APDs) instead of the usual photomultiplier tubes. The avalanche photodiodes are more robust, can work at lower voltage and can detect photons with better efficiency. These pixels have also been tested when hit by strong moonlight, with the goal to provide a longer duty cycle which is crucial for the detection of transient emission.

Name	Hemisphere	Altitude [m]	Number of telescopes	Mirror area [m^2]	Number of pixels	FoV [deg.]	E_{thr} [TeV]
H.E.S.S.	South	1800	4+1	108/600	960/2048	5/3.2	0.1/0.03
MAGIC	North	2225	2	234	574	3.5	0.06
VERITAS	North	1275	4	106	299	3.5	0.1

Table 1.1: Main characteristics of the three currently operating arrays of IACTs: H.E.S.S., MAGIC and VERITAS.

1.6 Very-High-Energy gamma rays as messengers

In this Section we will briefly present which fundamental physics subjects can be investigated with VHE gamma-rays.

Very-high-energy gamma-rays can be used to search for DM signals. We present more details about this with H.E.S.S. observations in Part III of this work.

The Universe is considered opaque to photons, because the latter travel in the medium, interact with background light and create pairs of electrons and positrons. Therefore, photon absorption due to the interaction with background radiation can be studied too. Gamma-rays in the GeV-TeV energy range can be absorbed by the **Extragalactic Background Light** (EBL), whereas ultra-high-energy gamma-rays (> 100 TeV) could interact also with the Cosmic Microwave Background (CMB). The attenuation of the gamma-ray spectrum is of a factor $\exp(-\tau(E, z))$, which depends on the energy of the gamma rays and the distance of the source z by the optical depth $\tau(E, z)$. According to standard EBL models, such as the Franceschini one from Ref. [177], the optical depth of gamma-rays with energy 10 TeV is about 0.5 for sources located at redshift z = 0.01 (corresponding to a distance of about 45 Mpc) and it increases up to 100 for sources as far as z = 1 (about 3 Gpc).

The speed of light can vary with energy due to the modification of the photon dispersion relation as predicted by some quantum gravity models. **Lorentz Invariance Violation** (LIV) is studied with the observations of VHE transient short-lived phenomena like GRBs, flares of AGNs or PSRs. LIV signatures could be found in time lags between two energy ranges or deviations from the standard spectra, besides the corrections that need to be taken into account for the interaction of the photons with the EBL. H.E.S.S. studied LIV with observations on PKS 2155-304 [98] and Mrk 501 [253] flares.

Hypothetic black holes formed in the very early Universe, known as **primordial black holes** (PBH), can give distinct VHE signatures. These are formed just after the Big Bang in very dense regions and not from collapse of massive stars, forming astrophysical black holes. The mass range of PBH can span a wide range, from the Planck mass to thousands of solar masses. The search for gamma-ray flares with duration from several microseconds to several seconds can probe evaporation of PBH with m$\sim 10^{15}$ g. This reference mass is used because all PBHs roughly lighter than this value would have completely evaporated in the present Universe [191]. H.E.S.S. set constraints on the PBH evaporation rate [354].

Gamma-rays are the result of radiative processes of VHE CRs. Therefore the study of the sources accelerating CRs at TeV-PeV energies can bring new information on the processes of the acceleration of particles, on the objects accelerating the CRs up to the knee and the very **origin of Galactic cosmic rays**. These sources can be related to SNR, PSR, AGNs and supermassive black holes. In this context, H.E.S.S. [18] and LHAASO [111] have been reporting measurements of gamma-rays at hundreds of TeV.

Chapter 2

The H.E.S.S. observatory

Contents

This chapter is dedicated to explain how the H.E.S.S. (High Energy Stereoscopic System) experiment works. The photons produced by the Cherenkov showers, the result of Very High Energy primary photons interacting with the atmosphere, are detected by the H.E.S.S. array. We explain the mechanism at the base of the production of the Cherenkov light, then the technique used for the detection of VHE light and the standard methods adopted for the background rejection. At the end of the chapter we also discuss the performance of the array. Sec. 2.1 is dedicated to the description of the atmospheric showers of particles. We describe one of the experiments in this field, the H.E.S.S. array of Cherenkov telescopes in Sec. 2.2. Sec. 2.3 and Sec. 2.4 are dedicated to the description of the events selection techniques and observation methods, respectively, used in H.E.S.S.. The instrument response functions (IRFs) and sensitivity of the instrument are explained in Sec. 2.5. The event reconstruction techniques used during the different phases of H.E.S.S. are described in Sec. 2.6. Finally, Sec. 2.7 briefly describes the H.E.S.S. data taking monitoring day shift, for which I have been recently nominated part of the supervising team.

2.1 Atmospheric showers of particles

When an incident primary particle interacts with the Earth atmosphere, a shower of secondary particles can be produced in the latter. From the primary particle's nature, the interactions that the former undergoes in the atmosphere may differ. This results in particle showers with specific features [79].

2.1.1 Creation of particle showers

Electromagnetic shower

The electromagnetic shower produced in the atmosphere consists of a cascade of photons, electrons and positrons. The shower is initiated by a primary particle which is either a photon or an electron/positron. A gamma-ray interacting with matter produces an electron-positron pair. Then, radiation is emitted by the electron and the positron. The former is composed by other gamma-rays that are due to the bremsstrahlung interaction close to atomic nuclei. The development of the shower is due to the repetition of these processes and contains positrons, electrons and photons. If the primary particle possesses enough energy, the processes can be propagated. With enough energy the pair production can start, if the primary particle is a photon, or the energy can be irradiated through the bremsstrahlung, if the initial particle is a CR electron. The propagation of the shower is halted when the photons have not enough energy left to keep producing pairs or other energy loss mechanisms other than bremsstrahlung (e.g. *ionization*) start developing. This happens after the threshold in energy at $E_{\rm thr}$ =

800 MeV$/(Z+1)$. Through the radiation length X_0, we can define the distance traveled by the shower, *i.e.* the length or depth of it. The former is characteristic of every material. For a photon, the length is defined as the distance on which 7/9 of the initial energy of the photon $E_{\gamma,0}$ is lost. For an electron, it corresponds to the distance for which the electron has lost all but 1/e of its energy. The photons travel slightly deeper in the atmosphere. An approximate definition of the depth is

$$X = X_0 \frac{\ln(E_{\gamma,0}/E_{\rm thr})}{\ln 2}. \tag{2.1}$$

The width of the shower evolves as a function of the electron multiple scattering. The largest part of the shower never leaves a region of twice the Molière radius $R_{\rm M}$. The latter is the radius of the cylinder that, on average, contains 90% of the energy in the shower initiated by the incident particle on the atmosphere. It is defined as $R_{\rm M} = 0.0265\ X_0(Z+1.2)$ and it is characteristic of the material. The sketches of electromagnetic and hadronic showers are shown in Fig. 2.1.

Hadronic shower

The development of the showers created by the interaction of hadrons with the atmosphere is more complicated and is the result of nuclear interaction and decay. The showers also include sub-components: *(i)* hadronic ones from nuclear fragments, *(ii)* the nuclear interaction of CR hadrons with the atmosphere produces kaons and charged pions that can decay into muons and corresponding neutrinos and *(iii)* the muons decay in electrons, producing photons and possibly sub-showers. The various interactions taking place make the hadronic shower wider than the electromagnetic one. Moreover, it shows sub-showers induced by high-momentum particles created in inelastic collision, and thus these ones can be highly displaced from the shower axis. The nuclear interaction length λ is used to define the depth of the shower. The former is the mean path that a hadron travels in a material before undergoing inelastic nuclear interaction. In the air, $\lambda > X_0$, so the starting point of the hadronic showers is deeper in the atmosphere compared to the electromagnetic ones. A sketch of a hadronic shower is shown in the right panel of Fig. 2.1.

2.1.2 Cherenkov light emission

Cherenkov light is produced by charged particles traveling through a medium at relativistic velocities. This emission appears when the particle travels in a medium with refractive index n such that its speed v is larger than the speed of light in the same material, ***i.e.,*** $v > c/n$**.** The speed of light in the material, given by $u = c/n$, is smaller than the particle speed v, ***i.e.*** $v > u$. The light is emitted in a cone with angle α such that

$$\cos\alpha = \frac{u}{v}. \tag{2.2}$$

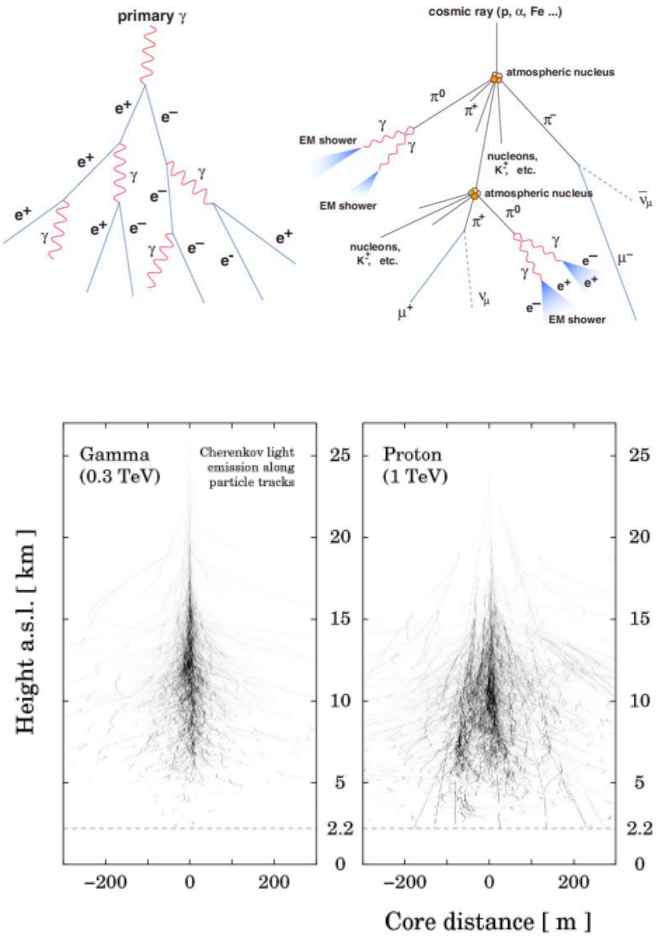

Figure 2.1: Sketch of an electromagnetic (left) and hadronic showers (right) in the top panels. Top panels are extracted from Ref. [305]. The development of a simulated electromagnetic shower initiated by a 300 GeV gamma-ray in the atmosphere is shown in the bottom left panel. The bottom right panel shows the development of a simulated hadronic shower initiated by a 1 TeV CR proton. The interaction of the proton is deeper and the produced shower is wider, with subshowers displaced from the core of the shower. Bottom panels are extracted from Ref. [79].

The maximum value of the angle is such that $\cos(\alpha_{\rm max}) = \frac{1}{n}$. If the incident particle is energetic enough, electrons and positrons can get to relativistic velocities such that Cherenkov light is produced [363]. For the shower with electrons, the energy threshold is $E_{\rm thr} = y_{\rm thr} m_{\rm e} c^2$, where $y_{\rm thr} = [1 - 1/n^2]^{-1/2}$. In the atmosphere, the threshold assumes the value of $\sim$20 MeV at 10 km altitude, without

considering the attenuation. VHE gamma rays are not directly detected (they do not reflect on mirrors), they are observed through the Cherenkov light produced in the shower they initiated. The latter peaks at around 400 nm, covering the wavelengths between 300 and 700 nm. The maximum intensity of the Cherenkov light corresponds to the peak of sensitivity of PMTs. However, optical light emitted from stars is in this range of wavelengths. Therefore, this has to be considered as a background for the detection of the Cherenkov light. For a VHE gamma ray with a primary interaction depth of 10 km, the light pool produced by the shower on the ground has a diameter of about 250 m if the scattering of electrons is included. The ground-based Cherenkov telescopes that are situated inside the pool are designed to detect the Cherenkov photons, as shown in Fig. 2.2.

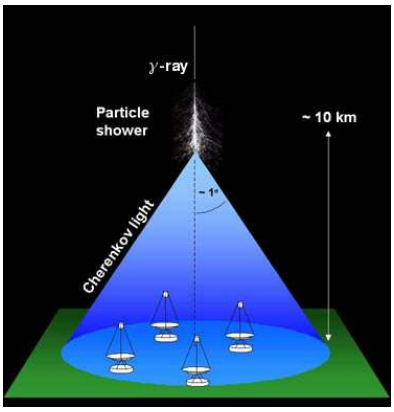

Figure 2.2: Sketch of Cherenkov light emitted by an electromagnetic shower in the atmosphere. Four IACTs are placed inside the cone of the Cherenkov light.

The Cherenkov photons get to the ground in a few ns. This happens right after their first production in the shower, therefore is crucial to equip the telescopes with PMTs with GHz acquisition electronics in the cameras of the telescopes. The geometry of the electromagnetic shower and the image produced on the focal plane of the camera, when the image is reflected on the mirror of the telescope, are shown in Fig. 2.3. The parameters describing the shower can be reconstructed through the Cherenkov light detected by each PMT of the camera. Camera images of particle showers initiated by a muon, a hadron and a photon are shown in Fig. 2.4. Through the spatial and temporal analysis of the camera images we can recover pieces of information like the energy, the direction and the nature of the primary particle, interacting with the atmosphere.

2.2 The High Energy Stereoscopic System

The acronym H.E.S.S. indicates the High Energy Spectroscopic System, consisting of an array of five IACTs. Four of the telescopes are of smaller size and are visible

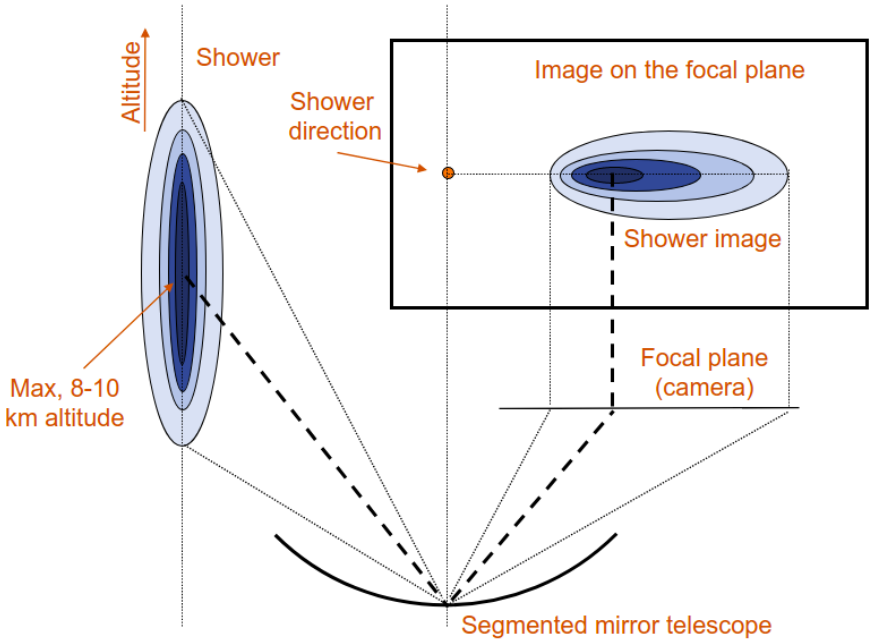

Figure 2.3: Image of an atmospheric shower of Cherenkov light on the focal plane of the camera of an IACT. The image on the focal plane is shown after reflection on the mirror of the telescope.

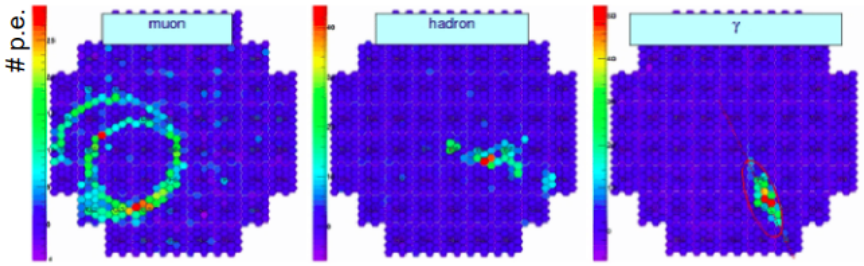

Figure 2.4: Images of atmospheric showers in the camera. From left to right, showers induced by a muon, a hadron and a photon are shown, respectively.

in Figure 2.5 at the corners of a square of 200 m size. They stand at each cardinal point. The fifth larger telescope is at the center of the square. The location site of the instrument is in the Namibian region of Khomas Highland, at geographic coordinates 23°16'17" S and 16°30'00" E, on a plateau at 1800 m of altitude above the sea level. The dry climate, mild temperature and reduced luminous pollution have been considered for the choice of this region. The H.E.S.S. array stands in a unique position in the Southern hemisphere and this makes it the best among the currently operating IACTs to observe the Galactic plane and, in particular, the

Galactic Center region at VHE. The H.E.S.S. Collaboration consists of more than 260 researchers from 13 countries and 40 institutes.

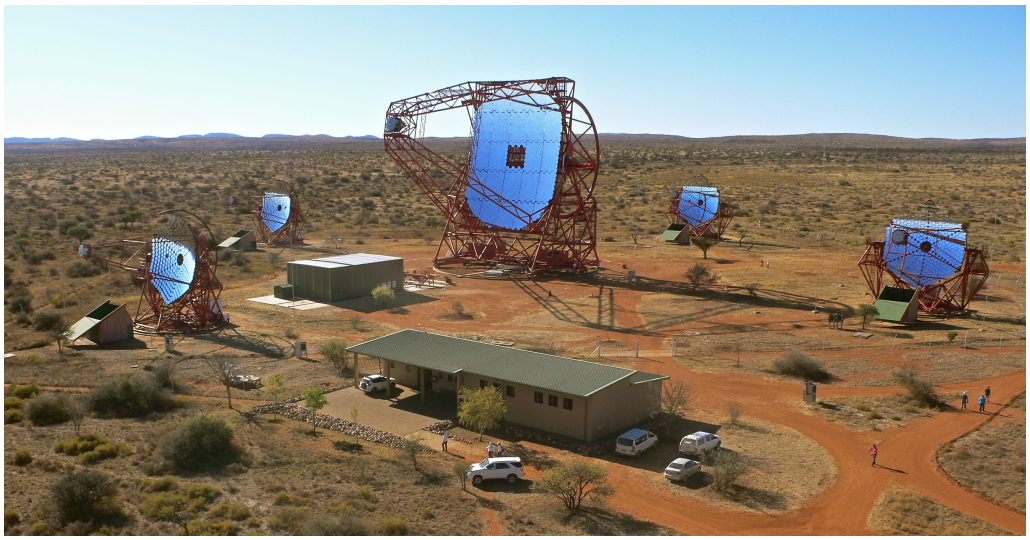

Figure 2.5: The H.E.S.S. array of IACTs. The phase one small telescopes CT1-4 are visible at the corners of the array. The large phase two telescope CT5 is at the center. Figure extracted from Ref. [138].

The first phase of the experiment started in 2003 with the four small telescopes [207]. The small telescopes are known as CT1-4 and each one of these is built over a metallic rotating structure that can move in the azimuth and zenith directions (Alt-Az mount). The structure supports a camera and a Davies-Cotton mirror of diameter 12 m [242].

In each of the small telescopes, the mirror is a group of 382 smaller circular mirrors, whose area sums to 108 m^2 [80, 144]. For construction, all the facets are at the same focal length f. This results in a discontinuous surface. The focal length is 15 m and the focal ratio f/d is 1.2. Given the way in which the mirror tiles are aligned, the focus is positioned at the camera. In the Cherenkov light wavelength range, the reflectivity is better than 80%. The fast drive in the mount of the mirror controls the movement of the telescopes in altitude and azimuth. The drive is supervised by servo-controlled AC motors and backup battery-driven DC motors. To move the telescope, the system can reach a speed of 100° per minute. A stability within 0.15 mrad rms is reached over the full range covered in altitude. This is guaranteed by the support of the mirror.

At the focal point position of each telescope, a camera is mounted. In each camera, 960 photomultipliers (PMTs) are mounted with a field of view (FoV) of 0.16° (3 mrad) each. Each PMT is identified as a pixel. The total FoV is of 5° in diameter. Winston cones are applied on the front of each PMT, in order to decrease the dead zones, increase the surface dedicated to light collection and focus the

light onto the active area of the PMT. The pixels are grouped by 16 into 60 drawers. Triggering and readout of the events is completed with electronics integrated into the camera body. For a single telescope, the average trigger rate is 200-300 Hz. The effective pixel coincidence window is $\sim$ 1.5 ns.

In 2014, the second phase of the data taking of the experiment started, with the addition of the fifth larger telescope completely built in 2012. This telescope is known as CT5 [236]. It has a diameter of 28 m, for a total area of 614 m^2 of mirrors. The whole shape of the mirror is parabolic, considering the 875 hexagonal mirror facets. The focal length is 36 m. CT5 is shown in Fig. 2.5, at the center of the array. The drive that moves along the azimuth can reach a peak positioning speed of 200° per minute, whereas the elevation one 100° per minute. About 1 mm of displacement accuracy is obtained. The pixels of the camera are again hexagons, counting 128 pieces. A total of 2048 PMTs are equipped with Winston cones. The diameter of the camera is 2 m, covering a FoV of 3.2° on the sky. The integration time for the effective signal is 16 ns. The typical rate for a mono trigger of CT5 is 1.5 kHz.

The small telescopes' cameras had the electronics upgraded in 2015-2016, to improve the overall performances of the array [183]. The upgrade reduced the dead time of the stereo mode, the failure rate due to aging of the system and improved the general performances. The upgrade of the electronics was based on the NECTAR readout chips [290]. The readout time was reduced from 450 μs to 15 μs in order to work in stereoscopic mode, in coincidence with CT5 at higher trigger rate. A renovation of cabling scheme, power supply and pneumatics have also been performed.

2.3 Event identification and selection

2.3.1 Definition of the trigger systems and data quality cuts

Events are selected at a low level and a significant part of the background can be rejected (around 95%). To do so, three thresholds have been defined. First, the number of photoelectrons in a single pixel is counted. This threshold ($S1$) defines a pixel that triggers but rejects the electronic noise and pedestal. The second threshold ($S2$) is defined according to the number of nearby pixels that are triggered in the same sector of the camera. This threshold identifies the telescope that are triggered. The last threshold ($S3$) is the number of telescopes that are triggered, and is defined as the stereoscopic one. For the H.E.S.S. I phase, $S1$ was fixed to 4 photoelectrons per pixel, $S2$ was defined as 3 pixels per sector and $S3$ as 2 telescopes.

The identification of the primary particle is based on the shape of the shower. For instance, a muon shower shows a ring-like signature on the camera. Moreover, this shower is rarely seen in more than one telescope [359] because it is

produced by particles with high momentum in hadronic showers far away from the shower core. These particles are isolated and requiring stereoscopy can efficiently reject them. The reconstruction of shape and direction of the shower is improved by applying the stereoscopy in the array of telescopes, as shown in Fig. 2.6. The direction of the shower is reconstructed by taking the intersection of the directions prolonged from the major axes of the images of the shower reconstructed in each telescope.

Further quality cuts are added after the triggering. The pixels that are not used in each camera, because they are either broken or turned off due to the presence of bright stars, cannot exceed 10%. The global trigger rate must be above 70% of the average of the list of observations (*run list*, with a single observation of 28 minutes named *run*). The variation of the trigger rate between the small telescopes has to be less than 10%. A weather station and an infrared LIDAR monitor the sky conditions to detect clouds. This is done because conditions like high humidity, temperature or presence of clouds can strongly alter the trigger rate or show inhomogeneities in the FoV [157].

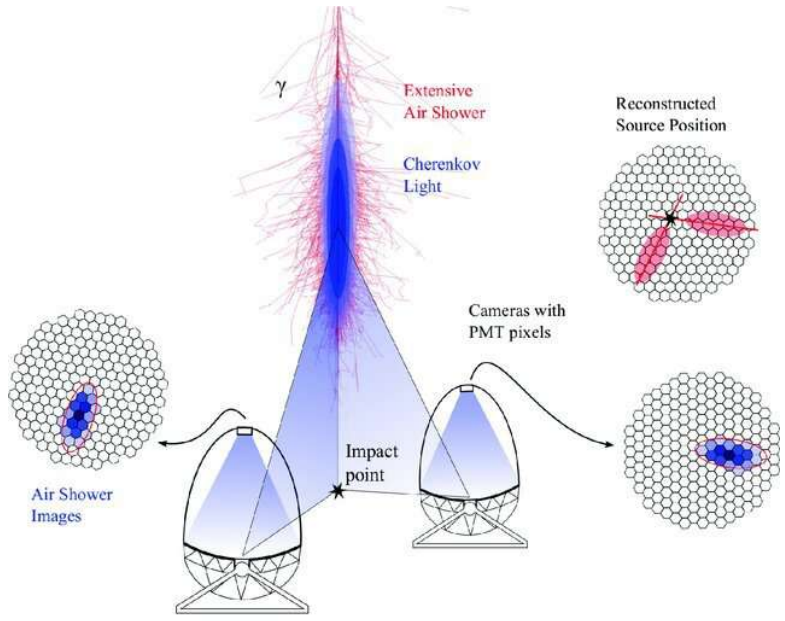

Figure 2.6: Sketch of the reconstruction through the stereoscopy technique with two telescopes showing the images of the air shower in the cameras of telescopes and the reconstructed source position.

2.3.2 Development of telescope-wise data quality cuts

Quality cuts on the selection of data at low-level are crucial to distinguish whether an observational run can be used for data analysis or not. These cuts can be used, for instance, to monitor whether the trigger rate of each individual telescope is at the right level. Another example is the amount of deactivated pixels during a run for bright objects inside the FoV. Setting an adequate threshold on the number of deactivated pixels can determine whether a run can be used for data analysis or not. The cuts can be also used to visualize whether the subsystems of the telescopes were within some standard quality criteria during the observations. However, the latter may not be the same for all telescopes involved in the observations because for instance, many of the subsystems, like the Camera or the Radiometer measuring the temperature of the Camera of the telescopes, are not the same for all telescopes. Due to this reason, at the time of the writing, I have been involved in the development of telescope-wise data-quality-cuts to improve the low-level monitoring of the subsystems of the telescopes. The goal is to implement different cuts for each of the five telescopes and for each subsystem, in order to have a precise screening of the status of the subsystems during the observations. This will also help to more accurately address any possible arising issue, knowing that the subsystems have specifically tailored quality criteria. These cuts are in development in the H.E.S.S. database [136].

2.3.3 Calibration of the instrument

The analysis is performed in different steps, including the calibration, the parametrization of the image and the reconstruction of an event. Then the properties of the primary particle are determined. To reconstruct the signal amplitude, several parameters are needed. The ratio between the gains at low and high level in the amplification channels are considered first. Then the value of the pedestals in the two channels. The gain in both channels is considered after. The final parameter considered is the coefficient of flat-field in each pixel, which is necessary to obtain an uniform output over the camera. To calibrate the instrument, dedicated runs are performed to measure these parameters. Through this step, the photoelectron signal is properly converted into ADC counts. Calibration is done once that the broken pixels are detected and excluded. Ref. [243] shows more details on the calibration of CT1-4 upgraded cameras. The same, but for the camera in CT5, is shown in Ref. [117]. Through the instrument calibration, the night sky background (NSB) can be measured. The latter is produced by bright light spots or diffuse optical light, for instance star light, light from the planets and zodiacal light. When no Cherenkov light is measured, the NSB measured in the PMTs dominates the electronic noise. For measurement at large Galactic latitudes, it represents a single-photoelectron rate of about 40-100 MHz, whereas up to 400 MHz can be reached in the vicinity of the Galactic center. The NSB strongly affects the width

of the pedestals and therefore the energy threshold [153].

2.3.4 Analyses chains for the reconstruction of the events

The step after the calibration consists in reconstructing the image of the showers on the cameras. Depending on the reconstructed characteristics of the shower, events are classified as either gamma-like or hadron-like. The events are extracted from the runs that satisfy the selection criteria previously mentioned. Two main chains exist for the H.E.S.S. selection and data analysis.

Hillas parameter reconstruction

The first-developed chain is based on the moments of the image of the shower on the camera, since the gamma-ray showers show an almost elliptical shape in the camera. This first chain is known as *HAP* [139]. The geometrical parameters are known as the Hillas parameters [202, 201]. The latter are:

- the RMS of the signal on the axis perpendicular to the main one of the ellipse (the image on the camera), also called *width*;
- the RMS of the signal along the main axis: the *length*;
- the center of gravity;
- the orientation of the ellipse;
- the angular distance between the pointing position of the telescope and the expected position of the target.

Semi-analytical shower modeling

The *Model*++ analysis chain was also developed [153]. This analysis chain is used for the main analyses of all the studies presented in this work. The distribution of the Cherenkov light on the camera is simulated for the comparison to the actual distribution of the measured Cherenkov light in each pixel through a χ^2. The particle distribution parameterization used to build a model of the electromagnetic shower is built with KASKADE [230]. The parameterization is built in longitude, latitude and angles coordinates. It also accounts for the depth of the interaction, the collection efficiency and other factors like the atmospheric conditions affecting the atmospheric absorption. In addition, the NSB is considered on a pixel-by-pixel basis for building the model [153]. Broken and inactive pixels are also taken into account. Several parameters can be considered to estimate the distribution of the Cherenkov photons in the camera:

- how the shower developed in longitudinal coordinates;

- how charged particles are developed in the same coordinates;
- the energy of electrons/positrons initiating the shower;
- how they are positioned with respect to the pointing position of the telescope;
- the rate at which Cherenkov photons are produced;
- the spatial distribution of the latter with respect to the electrons;
- the opacity of the atmosphere.

The detector is simulated using SMASH [188], to account for instrumental features that include the collection efficiency and reflectivity of the mirrors, the Winston cones, the geometry of the telescopes, the photoelectrons-to-ADC counts conversion, response function, the integration window, and the local and central trigger systems. Simulations at different conditions are performed for gamma, electrons, protons and nuclei. The former includes different zenith angles, impact distance and energy bins. The images of the Cherenkov light in the camera, that are obtained by the simulations, and the shower development are stored through *lookup tables*. To compare the measured and the simulated showers, a maximum likelihood test is computed on a pixel-by-pixel basis. The log-likelihood function for the test is taken as: $\ln\mathcal{L}(x|\mu) = P(x|\mu, \sigma_{el}, \sigma_{\rm NSB})$ and it represents the probability that a signal x is observed in a pixel where the expected intensity is μ. This assumes that the width of the electronic background and NSB are $\sigma_{\rm el}$ and $\sigma_{\rm NSB}$, respectively. The total likelihood is the sum over all pixels $N_{\rm pixel}$. Through the comparison of measured and simulated showers, we can tag gamma-like and hadron-like events. The quality of this comparison is evaluated through parameters known as the mean scale shower goodness (MSSG) [153]. This shows the agreement between the gamma-ray shower templates and the measurement in the pixels, knowing the electronic background and the NSB. To define the MSSG, we consider the difference between the log-likelihood function and the Monte Carlo simulations predicted likelihood, *i.e.* $\ln\mathcal{L}(x_i, \mu_i)$ and $\langle\ln\mathcal{L}|_{\mu_i}\rangle$, respectively. The MSSG is written as:

$$\text{MSSG} = -2\frac{\sum_i[\ln\mathcal{L}(x_i, \mu_i) - \langle\ln\mathcal{L}|_{\mu_i}\rangle]}{\sqrt{2\ d.o.f.}}. \tag{2.3}$$

The number of degrees of freedom d.o.f. is $N_{\rm pixels}$=6 obtained from the difference in number of parameters used to compute the two likelihood functions [153]. The index i indicates the ith pixel. In Fig. 2.7 we show how the reconstructed event distribution and simulated one behave as a function of the shower goodness parameter for excess photons measured towards a target. A standard cut can be applied to remove 95% of the background events and retain 70% of photons. The

events from the background that are identified as gamma-like events are known as the *residual background*. The latter can be measured and we describe different techniques in the following sections. The reconstruction of the shower is done directly through geometrical reconstruction of the main axis. The geometrical intersection of planes is applied. The energy of the shower is obtained from the image intensity. All the parameters are recovered through an evaluation of a likelihood function in each pixel. Then the comparison with the simulated shower is applied and the parameters of the real shower are recovered.

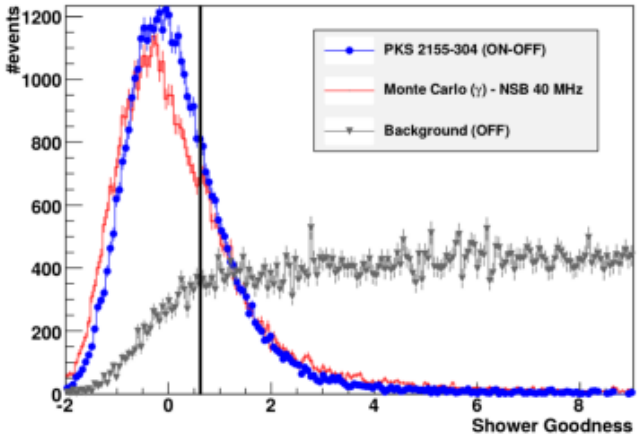

Figure 2.7: Distribution of events versus shower goodness for observation of the target PKS 2155-304. The measured events are given as the blue distribution, whereas the simulated ones are shown in red. The background is the gray distribution. The black vertical line shows the cut at MSSG = 0.6. Figure extracted from Ref. [153].

2.4 Observation methods and measurement of the background

2.4.1 Characteristics of the observations

One year of observations with the H.E.S.S. telescopes consists of about 1300 hours, which results in about 15% duty cycle. This amount includes observations in presence of Moon light [141]. In the past, this was not the case and a duty cycle of $\sim$ 12% was reached. Observations with the Sun are not possible, because of the too large luminosity. Therefore, it is required that the latter is at least 18° below the horizon. The available observing time is distributed among all the targets that have been chosen for the yearly observations after the proposals evaluation. To

observe, a low zenith angle is always preferred, with only few cases of zenith angle above 60°.

A single observation is named a run and has a length of 28 minutes. Different strategies for the observations can be applied. At first, the observation should be chosen as a pointed one, as part of a survey or as a transient observation. The former is the observational strategy for a specific object, targeted in advance and observed taking into account the visibility of the region above the horizon, better if close to zenith to reach the lowest energy threshold. The survey defines the observation of a large region, which is scanned during several runs thanks to a series of predefined pointing positions. This observational strategy is scheduled in advance, too. Observation of transient phenomena like GRBs, gravitational waves (GW) or flares from blazar are targeted when another experiment sends an alert. This observational strategy cannot be pre-scheduled. The observations of transient phenomena are mainly pointed, except for the case of GW for which a specific technique is adopted [334].

For the pointed observations, the telescope is pointed close to the chosen target, which position is referred to as the pointing position. The latter can be defined in different ways. The available background measurement techniques are dependent on the pointing mode and are explained in the next section. The new observation mode normally used is the *wobble* one. To cover the observations with the *wobble*, more than one pointing position is defined around the target position. The positions are taken at a distance called the observational *offset*. Usual choice for the *wobble* mode is to cover four perpendicular pointing positions at an offset of 0.7° around the target for point-like source searches, which are useful for the measurement of the background affecting the observations.

2.4.2 Background measurement techniques

The measurement of the background depends on the observation mode. The simplest approach is to define an *OFF* region to measure it, opposed to the *ON* one where the signal should be measured. This is used for standard pointed observations. Signal and residual background observations are on the same field of view.

When the *wobble* method is applied for the observations, the *Wobble Ring Background* and *Wobble Multiple OFF* modes are applied. For brevity, we will refer to these as *Ring Background* and *Multiple OFF*. For the first one, an annulus is defined on the observed sky, including the ON region where the signal is searched for. In this region, outside a circular mask excluded around the target position to avoid signal contamination, the residual background is measured. When another astrophysical object appears in the FoV, it is excluded from the ring. In the second technique, the background is measured in circular regions of the same dimension of the signal region, such that they lie in the annulus on which the target is

searched for. For these modes, the acceptance of the camera, that degrades radially from the center of the camera, is now the same for signal and background regions, when azimuthal symmetry is assumed. Moreover, the techniques assure to measure both signal and background during the same observation, in the same FoV and therefore under the same observational conditions. Both techniques are shown in Fig. 2.8. The signal region, the ON, is represented in orange while the background OFF region is given in gray. The excluded region is shown in blue.

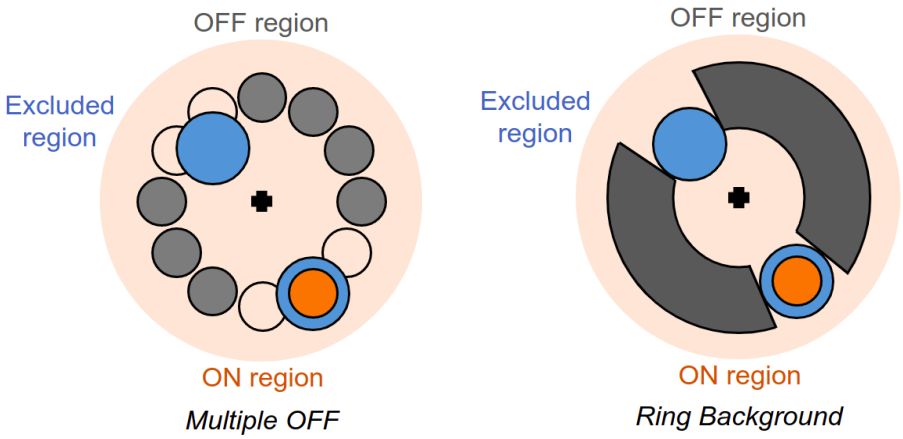

Figure 2.8: Techniques used to measure background known as the *Wobble Multiple OFF* and *Wobble Ring Background* on the left and right, respectively. The signal region (orange) is on the target and the pointing position is shown by the black cross. The regions for the measurement of background and the excluded regions are shown in gray and blue, respectively.

2.5 Instrument Response Functions and Sensitivity of H.E.S.S.

2.5.1 Effective Area

The effective area of the telescope corresponds to the portion of a plane surface, taken perpendicularly to the direction of maximum radiation, through which the major part of the radiation is collected. The area depends on the event energy and so varies along the energy range which is covered by the instrument. This behavior also depends on the offset and the zenith angles under which the observation is performed [153]. It is also connected to the optical efficiency of the telescopes, which correlates to the muon efficiency [116]. More details on the behavior of the effective area as a function of the zenith angle are given in Ref. [68]. In Fig. 2.9, we show the effective area for the M++ analysis chain for three different sets of cuts:

standard, faint and loose. The effective area can be obtained for hard cuts too. The area for the Hillas analysis is shown as well for two thresholds on the photoelectrons (p.e.), 60 p.e. and 200 p.e., the latter being the one most used in the literature. Above 10 TeV, a smaller effective area is obtained in M++ with respect to the Hillas one. However, it is then comparable to the one for Hillas 60 for lower energies and better than the latter at hundreds-GeV energy range. The effective area is also strongly affected by the radial distance from the center of the camera [75]. A relative rate of 70% at 1.5° is reached and a negligible degradation in the inner 1° is maintained.

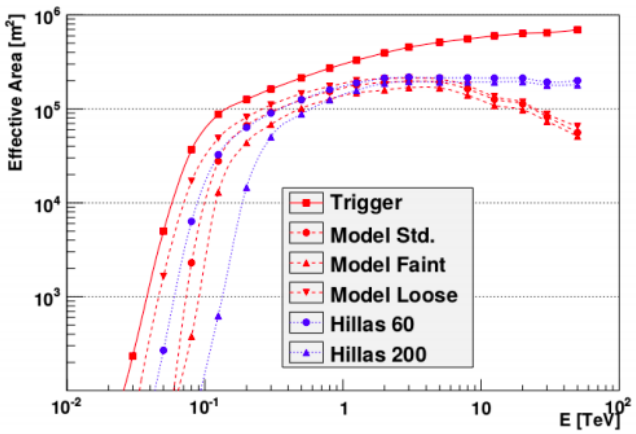

Figure 2.9: Effective areas for the H.E.S.S. instrument as a function of the energy, compared for the analysis chains Model++ (red dots) and Hillas (blue dots), for different selection cuts. Figure extracted from Ref. [153].

2.5.2 Energy range and threshold

The energy range covered by the H.E.S.S. instrument depends on the energy and the dispersion of the Cherenkov shower. First, the primary gamma-ray has to be energetic enough to produce Cherenkov light from the shower, then the shower has to be energetic enough to produce enough Cherenkov light detectable by the cameras and the shower has to be not too spread (*i.e.* not too energetic because this would create too many subshowers or pairs of particle-antiparticle) to be almost fully contained in the FoV of the telescope(s). The observation conditions impact the development of the shower. For instance, the zenith angle affects the threshold in energy over which photons can be collected. Indeed, observations at a large zenith angle mean that the showers are crossing a thicker layer of the atmosphere. Therefore, only the most energetic showers can reach the telescopes under these observation conditions. The effective energy threshold is set following a usual criterion of taking the value of energy corresponding to the 10% of the

maximum effective area. The threshold is defined after the application of the cuts on the parameters of the reconstructed shower. For the CT1-4 configuration, the threshold is 160 GeV for observations at zenith, and degrades to 220 GeV at zenith 30°, 400 GeV at zenith 45° and 1.2 TeV at zenith 60°. The higher threshold is the main reason for which observations at small zenith angles are preferred unless it is necessary to observe in diverse conditions.

2.5.3 Energy and angular resolutions

For the definition of the energy resolution we consider the RMS of the $\Delta E/E = |E_{\rm reco} - E_{\rm true}|/E_{\rm true}$ distribution [153]. It expresses the probability to recover a mean energy E for an event with true energy $E_{\rm true}$. The energy resolution for the H.E.S.S. experiment in almost all the energy range is around 10% and it never gets larger than 15% or lower than 5%, as shown in Fig 2.10. The former is improved when more telescopes are considered in the stereo mode and it is almost stable with offset and zenith angle variations. The bias of the reconstructed energy is around 5% in the whole sensitivity range. The bias grows near the energy threshold, due to effects of the trigger, up to 20%. Also, a high resolution is crucial to distinguish peculiar narrow spectral features. When CT5 is considered alone, a resolution of 30% is reached in the hundreds-of-GeV energy range.

The 68% containment radius of the point spread function (PSF) is considered as the angular resolution [153]. For events reconstructed with the Model++ chain, it is lower than 0.1° for the whole energy range. It does not show a strong dependency with the zenith angle. It stabilizes at 0.06°(at 68% C.L.) for gamma-rays in the TeV energy range. When more ($>$2) telescopes are considered in the stereo mode, the angular resolution can be improved. A good angular resolution allows morphological studies of extended sources and diffuse emission. In Fig. 2.11, we show that Model++ has a better angular resolution than Hillas. The resolution for the latter degrades significantly at large zenith angles due to the reconstruction technique.

2.6 Reconstruction configurations and sensitivity

After the advent of the H.E.S.S. II array, including the small and the big telescopes, the data can be observed and reconstructed with three main techniques. When only CT5 is used to reconstruct gamma-like events in a single-telescope mode, the configuration is called *CT5 Mono* configuration, where the best event reconstruction with the array configuration with only the 28-m diameter telescope is chosen. The reconstruction of the events with the large telescope and at least one of the small telescopes in the reconstruction of the event is called *CT1-5 Stereo* configuration, where at least two telescopes of the array were required to trigger the same shower event and the best shower event reconstruction is chosen between

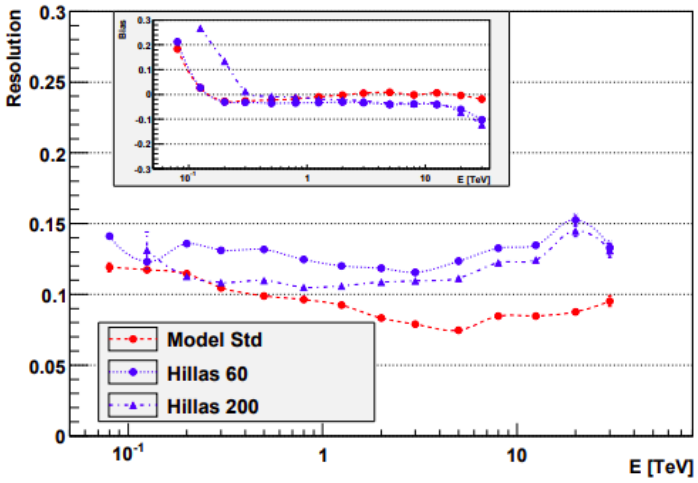

Figure 2.10: Energy resolution and bias for the H.E.S.S. experiment are shown as a function of the energy, for the Model++ and Hillas analysis chains as red and blue dots, respectively. A few percent is reached for the energy bias. A value of 10% E is maintained for the energy resolution in Model++ throughout the whole energy range. Figure extracted from Ref. [153].

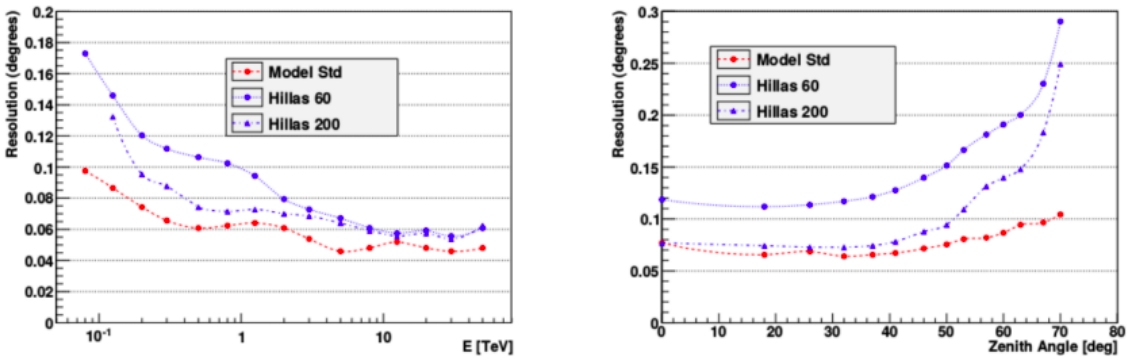

Figure 2.11: *Left panel:* Average angular resolution for the H.E.S.S. experiment for the two analysis chains, as red dots for Model++ and as blue dots for Hillas. *Right panel:* Angular resolution as a function of energy and as a function of the zenith angle is shown in the left and right panels, respectively. Figure extracted from Ref. [153].

an array configuration with only the four 12-m diameter telescopes and the one with the five telescopes. When the large telescope is not used at all, the *CT1-4 Stereo* is used for the reconstruction. In this case the best event reconstruction with the array configuration with only the four 12-m diameter telescopes is chosen. We show these three configurations in Fig. 2.12. An additional reconstruction class is the *Combined* configuration, in which the best reconstruction of the event

between *CT1-4 Stereo*, *CT1-5 Stereo* and *CT5 Mono* is chosen.

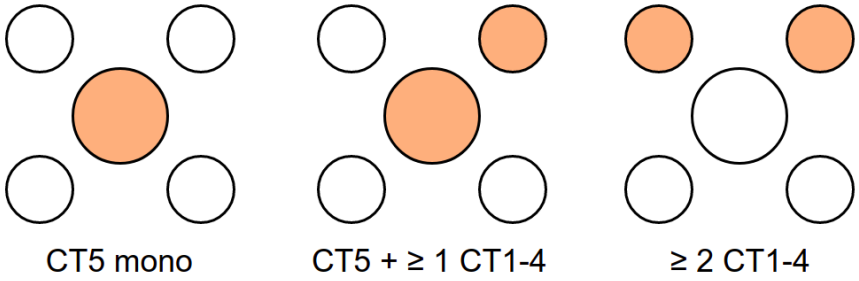

Figure 2.12: The reconstruction configurations in the H.E.S.S. II phase. *CT5 Mono*, *CT1-5 Stereo*, and *CT1-4 Stereo* are shown respectively in the left, central and right panels of the figure.

The performances of observations with the full five-telescopes array vary with the chosen reconstruction configuration [209]. We show the behavior of the effective areas as a function of the energy for the four configurations previously mentioned in the left panel of Fig. 2.13. The analyses that include CT5 have larger acceptance below a few hundred GeV. For these, a lower energy threshold can be adopted. This is due to the large size of the big telescope, which makes it more sensitive to low energies. Events below 100 GeV cannot be detected with only CT1-4. The configuration with only the latter has the largest energy threshold. The Combined configuration has the overall best acceptance. A clear estimate of the performance of an IACT can be obtained through its flux sensitivity. In 25 hours of observations, the H.E.S.S. array reaches the sensitivity of about 1% of the Crab nebula flux for observations taken at the zenith angles of a point-like source. Slightly larger or smaller sensitivity can be obtained for diverse reconstruction algorithms. Energy differential flux sensitivity of H.E.S.S. is shown in the right panel of Fig. 2.13. Here, the same behavior shown by the effective area for the different configurations is found. Below 300 GeV, the reconstruction with CT5 provides the best sensitivity. *CT5 Mono* and *Combined* analyses are also sensitive below 100 GeV. The *CT1-5 Stereo* configuration provides the overall best sensitivity. However, the best compromise to have good sensitivity that covers the largest range possible is given by the *Combined* configuration. Above 3 TeV, the sensitivity is expected to degrade more quickly for the *CT5 Mono*.

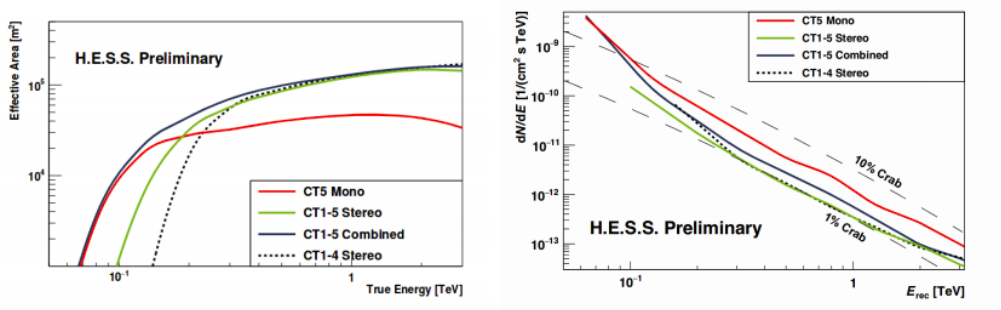

Figure 2.13: The effective area, also known as acceptance, and sensitivity per reconstruction type of the H.E.S.S. II experiment is shown in the left panel. The effective area is displayed for an observation at $\theta_{\mathrm{zenith}} = 20°$, $\theta_{\mathrm{offset}} = 0.7°$ and muon efficiency of 70%. The comparison is shown for the *CT1-4 Stereo* (black dotted), *CT1-5 Stereo* (green), *CT5 Mono* (red) and *Combined* configurations (black). The effective area as a function of E_{reco} energy after selection cuts is shown in the left panel. The differential flux as a function of energy is shown in the right panel, where the 1% and 10% of the Crab nebula flux are also shown and black long-dashed lines. Figure extracted from Ref. [209]

2.7 Monitoring of the data taking quality - the *H.E.S.S. day shift*

The monitoring of the quality of the data taking is performed by the H.E.S.S. Collaboration every day during the shift periods. In the last few years, a new way of monitoring has been developed - the *day shift*. Day shifters can monitor the subsystems of the telescopes the day right after each observational night, with no need of being on site. The day shift task consists in reviewing the subsystems of all the five telescopes, checking the level of the parameters characteristics of the latter and preparing a report for troubleshooting potential issues by contacting the experts directly [137]. The day shift task is important to gain efficiency on the observation time, to solve problems as soon as possible and constantly supervise the quality of the data taking. During my PhD, I have participated in three day shifts. At the moment of the writing, I have been nominated part of the group of people supervising the day shifters. I have been involved in each day shift, by supervising the shifters and cross-checking the quality of the data taking and addressing the expert to efficiently monitor the quality of the H.E.S.S. observations.

Chapter 3

The Dark Matter mystery

Contents

There are plenty of pieces of evidence on the existence of dark matter (DM) in our Universe. Nevertheless, its nature is still a mystery. In this chapter, we present an overview of the paradigm commonly accepted to explain dark matter. From cosmological measurements, 24% of the Universe is made of dark matter. 85% of the total content of matter in the Universe is made of dark matter. Measurements of astrophysical phenomena at the galaxy scale can be explained through the adoption of the dark matter paradigm. For instance, the rotation curve of galaxies and cluster dynamics. Many extensions of the Standard Model of particle physics include new elementary particles which can explain a new kind of invisible matter. These new exotic particles are known as weakly interacting massive particles (WIMPs). Many techniques have been deployed to search for dark matter. Indirect search of dark matter covering the TeV mass range is of particular interest for this work. A possible dark matter signal depends on the underlying mechanism of the self-annihilation process that yields the final gamma-ray spectra and on how dark matter is distributed in the observed targets. The strength of the searched signal depends on all of this.

In Sec. 3.1 we explain the pieces of evidence for the existence of dark matter. Some particle candidates for the explanation of the latter are presented in Sec. 3.2. Alternative theories to the standard model of cosmology are given in Sec. 3.3. The techniques used for the detection of DM are presented in Sec. 3.4 and the expected distribution of DM in our Galaxy is presented in Sec. 3.5. The targets that can be used to detect signals of DM in gamma-rays are introduced in Sec. 3.6. The expected flux of gamma-rays from self-annihilating dark matter particles is explained in Sec. 3.7. Finally, we dedicate Sec. 3.8 for the description of the annihilation spectra.

3.1 Observational evidence of Dark Matter

3.1.1 Evidence from astrophysics

The missing mass

Observing objects in gravitationally bound systems provided the first historical evidence of the necessity of DM to explain the standard model of Cosmology. The measured velocity of these objects diverge from what is expected when only gravitational interaction within visible objects is taken into account. Fritz Zwicky observed individual galaxies in the Coma cluster and measured the velocity dispersion, in the '30s [373]. He demonstrated, applying the virial theorem, that the observed rotation curve could not be explained by the gravitational potential of the visible galaxies. The mass inferred from the luminosity of the galaxies was 400 times smaller than the mass expected for the cluster. "Dark matter" was used to name this apparently "missing mass", to explain the invisible, *i.e.* non-luminous,

mass. Vera Rubin and Kent Ford also measured rotational curves of galaxies in the 70's [327], confirming the hypothesis of this missing part of matter. Through their measurement of the Andromeda galaxy, they showed that the velocity of the stars in the galaxy does not follow the Kepler's law $1/\sqrt{r}$ behavior. In fact, they showed that the velocity profile behaves like a constant to the outer parts of the galaxy. Under the validity of the Newtonian gravity, this implies that there must be additional invisible matter, a DM halo, that extends as $1/r^2$ from the center of the galaxy. Fig. 3.1 shows the two theorized components following the two behaviors, marked as the "disk" and "halo" lines. To compute the galaxy rotation curves in the inner part, data from the stellar population is used. The outer part is obtained through measurements of the Doppler shift of the 21-cm emission line of neutral hydrogen and can therefore cover faint regions beyond the disk at several tenths of kpc. An example of the rotation curve of the galaxy NGC 3198 is shown in Fig. 3.1 [360]. The curve is shown as a function of the distance from the center of the galaxy. The curve obtained from only visible matter is shown as "disk". The "halo" curve is obtained through the contribution of the DM halo.

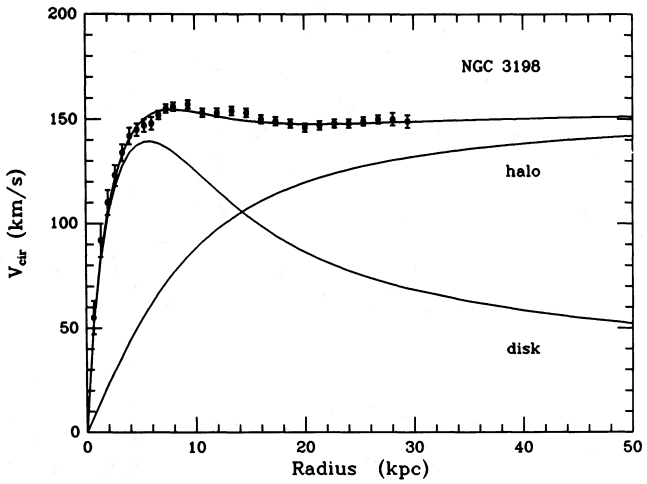

Figure 3.1: Measured rotation curve of the galaxy NGC 3198. Measured points are shown as dots, together with contribution from the visible matter and the DM halo. Figure taken from Ref. [360].

Gravitational lensing

Strong lensing Gravitational lensing provides an additional astrophysical evidence of the existence of DM [267]. Lensing implies distortion of the background light, due to the deformation of space-time due to gravitating mass. The deformation produces a lens effect on the background galaxies, similarly to optical refraction. This effect is shown in the left panel of Fig. 3.2, in the observations of the Abel

1689 cluster with Hubble [293]. The light coming from the background is significantly bended, which cannot be explained through the potential generated by the visible mass.

Figure 3.2: *Left panel*: Image of the gravitational lensing of the Abel 1689 galaxy cluster as observed with the Hubble telescope. The galaxies in the background are distorted by the DM halo of the cluster. Figure extracted from Ref. [293]. *Right panel*: The Bullet Cluster as composite image of the merger 1E0657-558. Credit: X-ray: NASA/CXC/CfA/ Ref. [264]; Lensing Map: NASA/STScI; ESO WFI; Magellan/U.Arizona/ Ref. [132]; Optical: NASA/STScI; Magellan/U.Arizona/ Ref. [132].

Bullet cluster One of the most convincing pieces of evidence for the existence of DM are the collisionless DM halos in the cluster merger E0657-558. This episode is known as the Bullet Cluster [132, 264]. In the right panel of Fig. 3.2, the composite X-ray and optical image of the Bullet Cluster are shown. Ordinary matter is represented in magenta. The mass distribution is estimated through the weak lensing of light passing close to a massive object. The mass distribution from weak lensing is shown in blue. This is dominated by the DM. The hot gas of the two mergers lags behind the subcluster galaxies and interacts, while the DM component in the two mergers is ahead of the collisional gas and coincident with the collisionless galaxies. The measurement of the Bullet Cluster has been used for constraints on the self-interaction cross-section of DM down to $\sigma/m < 1$ cm^{2}g^{-1} [265].

3.1.2 Evidence from cosmology

The standard model of Cosmology

Einstein's equation of General Relativity governs the standard model of Cosmology together with Friedmann-Lemaître-Robertson-Walker metric and Hubble's discovery of the expansion of the Universe [229, 178, 245, 325]. The model can be used to explain the thermal history of the Universe from the Big Bang, the relic background radiation, the abundance of elements and the formation of structures at large scale. In Refs. [306, 83], extended reviews of the model can be found. Homogeneity and isotropy are fundamental characteristics of the Universe. This is

known as the cosmological principle. Distribution of galaxies on a large scale confirms the homogeneity. Isotropy can be explained through the observations and measurements of Cosmic Microwave Background (CMB) measurements.

The Friedmann equations [178, 325, 245] are derived under the hypotheses already mentioned and the relationship between the energy content and the geometry of the Universe [167]. The equations are

$$\begin{aligned} \left(\frac{\dot{a}}{a}\right)^2 &= \frac{8\pi G}{3}\rho - \frac{k}{a^2} \\ \frac{\ddot{a}}{a} &= -\frac{4\pi G}{3}\left(\rho + \frac{3p}{c^2}\right) + \frac{\Lambda c^2}{3}. \end{aligned} \tag{3.1}$$

The term G is the Newtonian gravitational constant, k is the curvature of the Universe, $a(t)$ is the scale factor specifying how the Universe expands and Λ represents the vacuum energy enabling an accelerated expansion of the Universe. The latter is referred to as the cosmological constant. The curvature of the Universe can be -1 for an open hyperbolic space, 0 for a flat space and +1 for a closed spherical space. The sum of the energy densities of the Universe is expressed by $\rho = \rho_{\rm m} + \rho_{\rm r}$, including matter and radiation densities. The pressure is encoded in the term p. The Hubble parameter is $H(t) = \dot{a}(t)/a(t)$ and is included in the first equation. Assuming a flat Universe, the critical density $\rho_{\rm c} = 3H^2/8\pi G$ is equaled by the total density $\rho_{\rm tot}$, which is constituted by the density of matter and radiation plus the density of the vacuum, *i.e.* $\rho_{\rm tot} = \rho + \rho_\Lambda$, with $\rho_\Lambda = \Lambda/8\pi G$. Each component density ρ_i is a fraction of the critical density in terms of the density parameter $\Omega_i = \rho_i/\rho_{\rm c}$. The first Friedmann equation can be rearranged with the present values of the density parameters, *i.e.* using the relic density of matter, radiation and vacuum energy:

$$\frac{H^2(z)}{H_0^2} = \Omega_{\rm r}(1+z)^4 + \Omega_{\rm m}(1+z)^3 + \Omega_{\rm k}(1+z)^2\Omega_\Lambda. \tag{3.2}$$

The curvature term is given by $\Omega_{\rm k} = -k/H_0^2$ and the scale factor is related to the redshift in $a(t) = 1/(1+z)$. It can be measured with cosmological probes that that most of the matter is not made of baryons but of cold DM, *i.e.* $\Omega_{\rm m} = \Omega_{\rm b} + \Omega_\chi$, Ω_χ being much larger than $\Omega_{\rm b}$. In this case, the DM is a particle-like component. The cosmological model standardly accepted, which includes dark energy and DM, takes the name of Lambda-cold-dark-matter (ΛCDM) model.

Cosmological measurements

Cosmic Microwave Background A plasma of photons and baryons in thermal equilibrium permeated the early Universe. Free electrons could move in this environments. Neutral hydrogen formed at the recombination epoch, when the

Universe cooled down to temperatures $\sim$ 3000 K. Most of this primordial production of neutral hydrogen was in excited states and the transition to the bound state caused the emission of photons. The Universe was then transparent and the photons could propagate freely. The decoupling era was reached and the photons, fossil light of the Big Bang, constitutes the so-called Cosmic Microwave Background (CMB). The latter was accidentally detected in 1964 by a radio telescope at Bell Labs [308]. The relic temperature of the Universe is given by today's CMB measurements, T = 2.725 K. Anisotropies in the CMB were detected by measurements performed in the '90s [337]. The latter obtained a level of anisotropy of 16 ± 4 μK. Baryon density can be derived by the direct correlation with respect to the CMB temperature. The CMB map is covered in cold spots for areas with high density, whereas warm ones are in places of under-densities. In Fig. 3.3, we show the power spectrum of CMB temperature as a function of the multipole moment. Compression peaks are the odd ones and are provoked by the radiation pressure and baryon gravitational potential, instead decompression driven only by pressure produces the even peaks. Large baryon density would mean height increasing of the odd peaks with respect to the even peaks. Therefore, a measurement of $\Omega_{\rm b}$ is provided by the relative amplitude between the second peak and the first one.

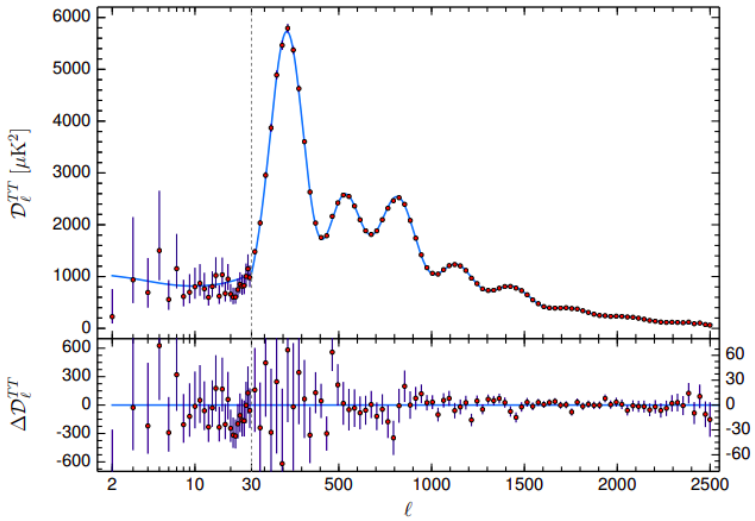

Figure 3.3: CMB angular power spectra as a function of the multiple moment derived from Planck 2018 measurements. The (ΛCDM) predictions are fitted too. Figure extracted from [309].

Baryonic Acoustic Oscillations The photon-baryon fluid detectable today shows anisotropies in the CMB that are mostly explained by the baryon acoustic oscillations (BAO). Relativistic acoustic waves were formed in the early Universe's pri-

mordial plasma, due to the interactions between baryonic gravitational potential and radiation pressure. From the overdensities' positions, the baryon-photon fluid propagated outward as an expanding spherical shell at the speed of sound, due to the influence of radiation pressure. At the recombination epoch, the acoustic waves froze, when the baryons were not anymore under the influence of radiation pressure. This means that the spherical baryonic shells stayed standing around the central DM overdensities. The comoving radius of the baryons' shell is not very different from the comoving sound horizon at recombination $r_{\rm s}$. With this, BAOs can be used as standard rulers for the horizon size and therefore for the geometry of the Universe. Baryonic and DM density evolve together, driven by gravity. Moreover, a separation of $r_{\rm s}$ is more likely between nowadays observed galaxies. This corresponds to a peak at $r_{\rm s}$ in the density profile of the matter. Measuring one single object in the sky is not enough to obtain the BAO scale. The density profile results from many perturbations, *i.e.* is a measurement of statistical correlation between the position of large scale structures in the Universe. If no DM existed, no characteristic correlation scale would exist nowadays due to the complete removal of the perturbations. For a BAOs review, Ref. [54] can be consulted.

Type Ia Supernovae Type Ia supernovae present homogeneity and high luminosity of the peak magnitudes. A map onto a standard object can be obtained considering that these objects are not identical but constitute a family. They can therefore be used as standard candles because their behavior depends only on the local physics and they are expected to be independent of environment and evolution. Then, their distance is the factor influencing their apparent magnitude. Their redshift is caused by the expansion of the Universe and the distance of their host galaxy must be known [345] to measure it. Through this measurement, $a(t)$ can be constrained and one can then put constraints on the relic densities in the ΛCDM model.

Big Bang Nucleosynthesis To determine the abundance of baryons, we need to consider the process of primordial nucleosynthesis [135], or Big Bang nucleosynthesis. The latter is the process responsible for the creation of the chemical elements at early phases of the Universe after the Big Bang. Nuclear reactions formed mainly the light elements in the first tens of minutes of the Universe, while the latter was still hot. These elements, ^{4}He, D, ^{3}He and ^{7}Li, abundances are fixed to values widely accepted ^{4}He/H $\sim$ 0.1, ^{3}He/H $\sim$ D/H $\sim 10^{-5}$ and ^{7}Li/H $\sim 10^{-10}$. Light elements' abundance depends on the ratio of baryon-to-photon η, constrained in a range of $5.1\times10^{-10}<\eta<6.5\times10^{-10}$ [357]. Baryonic matter's abundance correlates to η and it is shown to be five times smaller than the DM abundance. The former is measured to be $\Omega h^2 = 0.0224 \pm 0.0001$[1] [309]. It accounts

[1] A common practice is to introduce the dimensionless Hubble constant, usually denoted by h and commonly referred to as "little h" [149]. Then, the Hubble constant is written as $H_0 = h\times100$ km s^{-1} Mpc^{-1}.

for about 5% of the critical density of the Universe. The other 95% to complete the density of the Universe is constituted by 70% of dark energy and by 25% of DM. The nucleosynthesis of the baryons is one of the main proofs of the validity of the ΛCDM model [155].

Structure Formation The hierarchical formation of structures is due to the amplification of primordial density fluctuations which grow as a consequence of the expansion of the Universe [317]. On the experimental point of view, measuring the distribution of luminous objects in the Universe can be used to describe the formation of large scale structures and find a relation between the latter and the characteristics of the observed objects. The distribution of matter in regions of the sky can be mapped by surveys that combine measurement of the redshift and the angular position of astronomical objects. A statistically representative volume of the Universe was mapped by the 2dF Galaxy Redshift Survey (2dFGRS)[356] at the Anglo-Australian Telescope. The survey revealed the optically luminous galaxies in that volume. More recently, the most detailed three-dimensional map of a third of the sky was produced by the Sloan Digital Sky Survey (SDSS) [358], using multi-spectra with deep multi-color images in ultraviolet, green, red and infrared. Observed structure distribution and simulated one from the growth of the cosmic fluctuations in the near-uniform early Universe can be compared. An analytical treatment of gas dynamics, radiative cooling, photoionization, recombination and radiative transfer cannot be made in the model. Thus, complex N-bodies numerical simulations in a large box of space are performed to study the formation of structures. The initial conditions of the Universe set nearly uniform matter density with small inhomogeneities. The measured CMB temperature power spectrum is used to simulate perturbations accordingly. Then, the equations explaining the expansion of the Universe, all matter gravity, baryonic gas pressure forces and dark energy are injected. Simulations include baryons only since recently, however there is still no consensus on how to include their physical processes in the simulations. The evolution of the system and gravity makes the fluctuations develop. DM halos and galaxies are formed in regions with high initial density because matter collapses in them. More details on the simulations of the formation of large scale structures, clusters and groups of galaxies and their evolution can be found in Ref. [342, 340]. Other times, the filaments become more prominent and clusters form at the intersections between them. At lower redshifts, below 1, the growth of structures slows down. This is due to gravity becoming subdominant and dark energy dominating the acceleration. The formation of low mass objects happens first and then they merge into bigger ones. From simulations we can see that hot DM would not explain the distribution of the nowadays observed galaxy-scale structure. Only cold DM was included in the initial simulations of structure formation. These predicted very cuspy profiles, which were in tension with some observations at galactic scales. When baryons are included, the inner part of the halos tends to flatten. We show in Fig. 3.4 part of the 2dFGRS and

SDSS maps in the left and top panels, respectively. Surveys produced by the Millennium simulations are shown in the opposite panels [174]. These are built with semi-analytic techniques to simulate the dark matter distribution and the structure formation, and match the geometry and magnitude limits obtained from the experimental surveys. A non-baryonic dark matter can be included in the matter content to obtain striking agreement between the simulations and the measurements. Fluctuations from baryonic-only matter would not allow to reproduce the evolution and the formation of the observed structures from the early Universe to today. The simulations also show prominent structures (see bottom panel) like the observed Sloan Great Wall (visible in the top panel of Fig. 3.4).

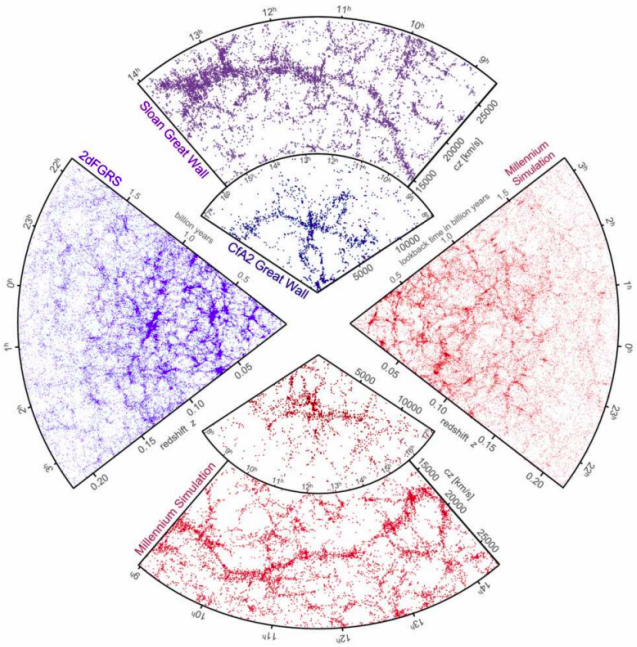

Figure 3.4: The left panel shows the map of a part of the 2dF Galaxy Redshift Survey. The top one shows a part of the Sloan Digital Sky Survey. Maps obtained for the corresponding portions of the sky with the Millenium simulations are shown in the right and bottom panels. Figure extracted from Ref. [340].

3.1.3 Thermal relic density of cold Dark Matter particles

At the beginning of the history of the Universe, when the latter starts to expand, all the particles composing it are in thermal contact with the others and evolve with time [76]. The thermal contact is maintained until the epoch in which the number density of the particles n starts decreasing. This reduces the interaction rate $\Gamma = n\sigma v$, which depends on the particle velocity v and its cross section σ.

The decrease is what is expected from the Boltzmann equation. While the Universe keeps expanding, particle annihilation does not work efficiently anymore for scales below the Hubble parameter (which has dimension of 1/time). This epoch is named as the freeze-out, where the decoupling happens, *i.e.* particles do not interact in the time scale of expansion of the Universe $\sim H^{-1}$. This moment represents the time from when the abundance of the decoupled particles does not change anymore, *i.e.* it freezes to the relic density. Particles with different masses decouple at different epochs, because they undergo different interaction processes. The relic density for cold (*i.e.* non-relativistic) DM particles can be given approximately by [222]:

$$\Omega h^2 \sim \frac{3 \times 10^{-27} \mathrm{cm}^3 \mathrm{s}^{-1}}{\langle \sigma v \rangle}. \tag{3.3}$$

The relic density values for each component are provided from recent Planck measurements [309], and are summarized in the Tab 3.1. From Eq. 3.3, the measured $\Omega_{\mathrm{CDM}}\mathrm{h}^2$ value implies that the value of the thermal relic cross section, *i.e.* the thermally averaged velocity weighted annihilation cross section for DM that was produced in the thermal early Universe, is equivalent to $\langle \sigma v \rangle \sim 3 \times 10^{-26} \mathrm{cm}^3 \mathrm{s}^{-1}$.

Parameter	symbol	value
Hubble constant	$\mathrm{H}_0 = 100\ h$ [km s^{-1} Mpc^{-1}]	67.4 ± 0.5
Cold DM density	$\Omega_{\mathrm{CDM}} h^2$	0.120 ± 0.001
Baryon density	$\Omega_{\mathrm{b}} h^2$	0.0224 ± 0.0001
Matter density	$\Omega_{\mathrm{m}} = \Omega_{\mathrm{b}} + \Omega_{\chi}$	0.315 ± 0.007
Curvature	Ω_k	0.001 ± 0.002
Vacuum energy density	$\Omega_\Lambda h^2$	0.3107 ± 0.0082
Cosmological constant	Λ [eV^2]	$(4.24 \pm 0.11) \times 10^{-66}$

Table 3.1: Latest values of the cosmological parameters from Planck measurements [309].

3.2 Candidates to explain Dark Matter

Even though the nature of DM is still a mystery we are showing in the next sections two of the main categories for DM candidates: Weakly Interacting Massive Particles (WIMPs) and non-WIMPs candidates.

3.2.1 Non Weakly Interacting Massive Particles particles

Axions and axion-like particles

To solve the problem of absence of CP violation in strong interaction, axions were first introduced as particles. They are predicted in QCD from non-zero quark masses. In the pseudo-Nambu-Goldstone theory, axions are classified as bosons and arise from the solution to the strong CP problem found by Peccei and Quinn [304]. Following this solution, a U(1) approximate global symmetry is introduced. The latter is broken at a scale f_{a}, located at around 10^{12} GeV. The coupling to standard matter behaves as $\propto 1/f_{\mathrm{a}}$ for axions. The latter are good candidates for DM because they are neutral, weakly-interacting bosons. They are very light, however, a population of non-relativistic, therefore cold, axions can be produced when out of equilibrium [166]. The spontaneous high scale breaking of an approximate U(1) symmetry can also generate axion-like particles (ALPs). The latter are not linked to the QCD theory, therefore the mass and coupling to standard matter of these particles are independent parameters and cannot be very well constrained with experiments. For a review of the search for axions and ALPs, [152] can be consulted.

Neutrinos

For hot DM, the standard left-handed neutrinos were postulated as candidates up to a few eV in the late '70s [318]. Assuming Universe composed by hot DM, a top-down formation scenario with superclusters formed first and fragmented then into smaller structures is implied. However, the measured distribution of galaxies cannot be reproduced by this scenario, hence the latter is considered obsolete nowadays. Neutrinos are wiped off before being able to form the large scale structures if a bottom-up formation scenario is assumed. If the neutrino oscillations are accounted for with a regular Dirac mass term added in the standard model (SM), right-handed neutrinos are needed. Sterile neutrinos, interacting only via gravitational effects and not via weak interaction (this explains the name "sterile"), are hypothetical leptons [278]. Apart from the three left-handed SM active neutrinos interacting with W and Z bosons, right-handed sterile neutrinos not interacting with the electroweak bosons are present as four or more states. The mass of these states can hypothetically be between 1 eV and 10^{15} GeV. At eV masses, the sterile neutrinos are tested for the detection of neutrino oscillation anomalies. At GeV-TeV masses, the former serve as tests for the baryogenesis theories. Sterile neutrinos at keV masses are good candidates for warm DM. All the previous cases are discussed in Ref. [272, 278]. With the latter, the formation of large scale structures could be explained [164].

3.2.2 Weakly Interacting Massive Particles

The DM particles should respect the following characteristics: non-baryonic, electromagnetically neutral, color neutral(-ish), massive (*i.e.* showing gravitational effects), living for a lifetime larger than the age of the Universe, reproducing the relic density measured with observations and sustaining the formation of the observed structures. One of the compelling candidates which is respecting these characteristics are Weakly Interacting Massive Particles (WIMPs). The latter interact via gravity and any other force (or forces), which may not be part of the Standard Model itself, with intensity as weak or weaker than the weak nuclear force. Moreover, these are favored by a supersymmetric (SUSY) extension of the standard model (SM) [294]. The relic density of DM is reproduced naturally by WIMPs and this is often known as the WIMP miracle. According to SUSY, each particle has a supersymmetric partner, differing by a half-integer spin. A supersymmetric fermion exists for each boson and vice versa. Each quark has a supersymmetric squark. Candidates for WIMPs can be taken from the superpartners of the bosons. In SUSY, the proton decay happens through the process $p \rightarrow e^{+}\pi^{0}$ with a timescale which is rejected by observations. This problem is surpassed with a new discrete symmetry, the R-parity defined by $R = (-1)^{2S+3B+L}$, which is conserved and prevents the proton from decaying. S is the spin, B the baryon number and L the lepton number of a particle. SM particles have $R = 1$, while their superpartner particles in SUSY have $R = -1$. As a consequence of R-parity, the lightest supersymmetric particle (LSP) is stable and it cannot decay into SM particles with an opposite parity. This makes the LSP a good candidate for WIMPs. In particular, the lightest neutralino, which is the lightest mixture between fermionic partners of the neutral Higgs boson and neutral electroweak gauge bosons. The Higgsino is the superpartner of the Higgs boson. The superpartners of the electroweak bosons are the Wino for the *W* boson and the Bino for the gauge boson of the U(1) gauge field corresponding to weak hypercharge. Neutralinos are Majorana fermions, so they can self-annihilate because no distinction can be made with the antiparticle. They interact with the weak vector bosons. Heavy neutralinos can result in the lightest neutralino through *Z* boson decay. The latter is then visible in a detector, and corresponds to a missing momentum in the final state of the interaction. The mass of the WIMP candidates can be constrained by the thermal relic density. To reproduce the relic density and thermal relic cross section, the needed mass is usually referred to as the thermal mass. For a pure Wino candidate, the latter is expected to be 2.9 ± 0.1 TeV, for pure Higgsino is 1.0 ± 0.1 TeV. Another possible state for WIMP dark matter is the 5 representation of SU(2), the Quintuplet, for which the thermal mass is expected to be 13.6 ± 0.8 TeV[204, 101, 277, 129]. This mass range can be probed by gamma-ray telescopes through indirect search for DM. Particles in the Kaluza-Klein theory (KK) are alternative candidates to SUSY particles. These particles are theorized for a multidimensional Universe [225], where the 4-dimensional Universe is a brane embedded in a 3 +

δ + 1-dimension space-time called bulk. The states that propagate through the small extra dimensions are the KK particles and are partners of SM particles like in SUSY, but in this case with the same spin. Similarly to the case of R-parity in SUSY, a new discrete KK-parity is introduced. The Lightest KK particle (LKP) is a good DM candidate in alternative to the LSP [234].

3.2.3 Primordial black holes as dark matter

Primordial black holes (PBHs) have been studied since the '60s [370]. The former are black holes formed via the collapse of the large overdensities present in the early Universe. It was realized that PBHs are potential candidates to explain dark matter [194, 120]. They are non-baryonic since they are created before matter-radiation equality. They could evaporate via the Hawking radiation [196, 195], however PBHs with initial mass $M_{PBH} \gtrsim 10^{14}$ g have a lifetime longer than the age of the Universe [299, 255]. Considering PBH on cosmological scales, they would behave like DM particles but on galactic or smaller scales, the granularity of the PBHs can produce observable effects. Interest on PBH was generated in the late '90s by the MACHO collaboration's 2-year results on observations of microlensing on the Large Magellanic Cloud. Significantly more events were observed than what expected from known stellar populations. The found excess consisted with roughly half of the Milky Way (MW) halo corresponding to 0.5 $M_\odot$ compact objects. On these, astrophysical compact objects were excluded by arguments connected to the baryon budget [173]. With later observations, the allowed halo fraction decreased [45]. Many of the ideas and models for explaining DM with PBHs date back to this time. When LIGO-Virgo discovered the gravitational waves in 2016 from Solar mass black holes [5], a new large wave of interest in PBH DM arose from the possibility that these BHs could be primordial rather than astrophysical [90, 131]. The abundance of PBHs has been later significantly refined. New constraints have been obtained, whereas some existing ones have been weakened or removed. Theoretical calculations on the mechanisms for the PBH formation have also been significantly improved. A comprehensive review of PBH as DM can be found in Ref. [112]. For a detailed review on observational constraints over non-evaporated PBHs, see Ref. [232]. H.E.S.S. searched for bursts of γ-rays in TeV with timescales of a few seconds, which is what is expected from the PBHs evaporation in the final stage, in Ref. [355].

3.3 Alternative theories to Lambda-CDM

Some issues are present for small scale structures, even though the ΛCDM probes successfully most of the cosmological and astrophysical measurements by postulating the existence of DM. For instance, the small size scale measured DM density may not be explained at the center of the galaxies [331]. Understanding how to

include baryons in the simulations may weaken the disagreement, however their treatment is still under debate. Moreover, from N-body cosmological simulations many small-scale substructures in the DM halos and satellite galaxies are predicted. Measurements disagree with this prediction because they count a number of dwarf galaxies about an order of magnitude smaller than in the simulations [106]. Many ultra-faint dwarf galaxies have been detected in the last few years, therefore it is possible that these small halos exist and are not easy to detect. Maybe because the lightest halo is not massive enough to trigger star formation. On the other hand, halos may have been wiped out by tides due to the interaction with more massive halos. Due to the difficulties that the ΛCDM faces at the galaxy scale, some theories have been developed to exclude DM from the Universe formation scenario but still explain some of the observations, in particular the dynamics of stars in galaxies. Following these theories, Newton's law of gravity should be modified [274]. The theories are usually referred to as MOND (Modified Newtonian Dynamics) [274]. MOND theories are limited at galaxy clusters and cosmological scales even though they can well explain some effects at Galactic scales. Many of these theories have been ruled out by recent studies of gravitational waves and the precise measurement of the speed of light [100].

3.4 Detection techniques for Dark Matter

3.4.1 Direct search

When a DM particle χ directly interacts with a particle X of the standard model through a process $\chi \mathrm{X} \rightarrow \chi \mathrm{X}$, we consider these phenomena like direct DM searches. In the latter, the recoil of the nucleus of a target material with which galactic WIMPs undergo elastic scattering is the measured quantity. The rate of how much signal can be observed is dependent on the mass of the DM particle and the interaction cross section between DM particles and the target. Other important parameters to consider are the local DM density and velocity distribution in the Milky Way, the latter known with large uncertainties. The spectrum in energy for the nuclear recoil is $dR/dE_{\mathrm{R}} \sim R_0/(E_0 r)e^{-E_{\mathrm{R}}/E_0 r}$ [246]. The recoil energy and kinetic energy of the incoming DM particle are E_{R} and E_0, respectively. The event rate per unit mass and the total one are R and R_0, respectively. The kinematic factor r depends on the masses of the target nucleus m_{T} and of the DM particle m_{DM} as $r = 4m_{\mathrm{T}}m_{\mathrm{DM}}/(m_{\mathrm{T}}+m_{\mathrm{DM}})^2$. The DM signal rate can be constrained through the measurement of R at E_{R}. The former is contained in R_0 and, when fixing m_{DM}, can be used to obtain limits on the elastic-scattering cross section of DM off nucleons. An expected recoil energy of $\sim$ 1-100 keV can be obtained with the assumption of a Galactic velocity of the order of 10^{-3} c and DM masses between 10 GeV and 1 TeV. Then, about 1 event keV^{-1}kg^{-1}d^{-1} is the expected differential rate at Earth [246]. A major difficulty arises for direct detection because the recoil event is very rare.

Another challenge is to gain sensitivity on low-mass DM by lowering the threshold. The background rejection can be performed on electrons recoil from gamma-ray background external to the target, contamination signals inside the detector and elastic scattering on electrons of neutrinos coming from the Sun. To discriminate these signals, the pulse shape is usually analyzed. In addition, the nuclear recoil from fission should be discriminated. However, this is more difficult and sometimes irreducible. Other difficult background signals are alpha particles recoil, interaction between atmospheric muons and neutrons or neutrinos undergoing coherent scattering with nuclei. Background from external radiogenic and cosmogenic signals are partially rejected through shields and placing the detectors in underground laboratories. Moreover, low-background materials are also fundamental to improve the rejection. The requirements for the detectors are large mass target nuclei, low threshold in E_{R}, low background and good discrimination between nuclear and electron recoils. The already built detectors make use of different materials and target nuclei, apply a variety of detection techniques and cover different DM mass ranges. For instance, large targets with low background are obtained with noble liquid targets, whereas low E_{R} threshold and high energy resolution are reached with cryogenic crystal targets. The scintillation is at the base of most of the experiments of direct detection. Alternative techniques are also ionization and low temperature photon techniques, or combinations of them. Darkside and XENON use liquid argon and xenon and apply both ionization and scintillation techniques. DAMA/LIBRA uses scintillator with NaI(Tl), SuperCDMS and EDELWEISS are detectors with cryogenic germanium and silicon and CUORE uses bolometers with tellurium. Experiments like DAMA/LIBRA look for an annual modulation of the count rate, due to the variation of the distance between the center of the Milky Way and the detector. Thus, this technique depends on the motion of the Earth around the Sun. When the relative velocity reaches a peak in June, peaks in the counts are expected too. DAMA observed a significant signal [78], which was however strongly constrained by other experiments. In Fig. 3.5, we summarize the actual constraints on the spin-independent WIMP-nucleon cross section from direct DM search. Constraints from observations are challenging the coherent elastic neutrino-nucleus scattering cross section, the so-called neutrino floor [97]. This background is irreducible for DM detection, however some models below can be tested with indirect detection. More details on the DM searches with direct detection can be found in Ref. [374].

3.4.2 Creation at colliders

To search for DM at colliders, DM particles are produced through interaction of SM particles which are accelerated in a process XX $\rightarrow \chi\chi$. Run 3 at LHC, and collisions between protons (pp) at a center of mass energy of 13.6 TeV, could reach the statistics and luminosity to obtain very constraining limits on DM searches.

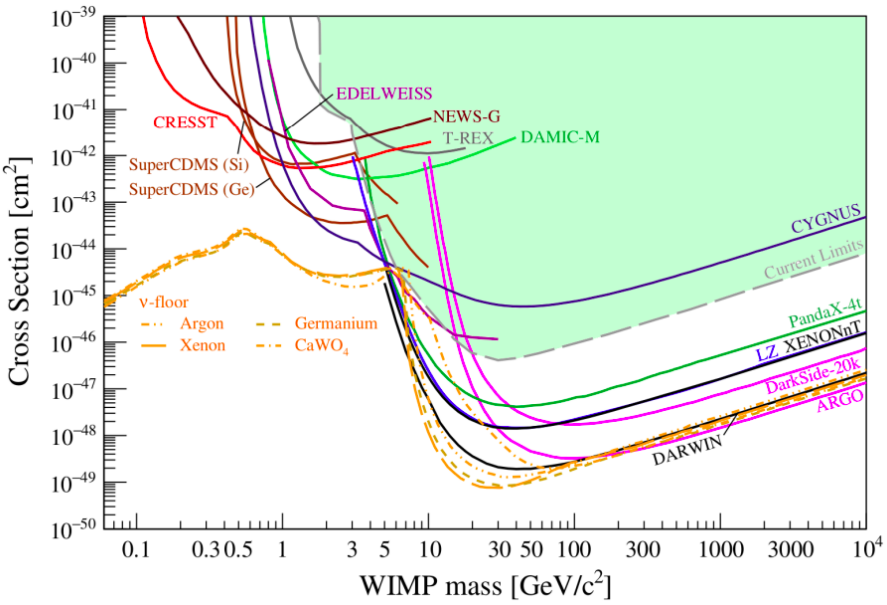

Figure 3.5: Summary on the constraints from direct detection on the spin-independent WIMP-nucleon elastic cross section. The green-shaded region shows the parameter space excluded by the current sensitivity including all the experiments. Colored lines are the sensitivities for either future or upgrades of the already existing experiments. The neutrino floor is shown by the orange-dashed line, corresponding to the neutrino-nucleus elastic cross section. Figure extracted from Ref. [87]

So far, no DM particle candidate was detected and stringent limits have been obtained for some DM models. Through pp collisions, the produced DM particles are not observed directly, however the missing energy can be used as the smoking gun signature [176]. For theories beyond the Standard Model (BSM), a single DM particle and no additional BSM particle are considered. Then, mediators for the interaction between SM and DM particles like the Z boson or the Higgs boson are assumed. Models with new BSM particles as mediators, like heavier versions of SM particles, are more complex. When the considered mediator is heavy, in comparison to the collision energy, DM and SM matter interactions are contact-like and simplified-models can be used. The latter rely on effective field theories (EFTs) [248], reducing the assumptions on the properties of the DM, like on the coupling with SM particles. Otherwise, some simplified models can be developed by knowing that the mediator will likely decay into SM partons that created it. The models describe the visible physics in the final state and not the additional visible physics at energies higher than the collider scale [15]. For specific channels, less simplified models can be used, with the additional information on the specific features and signatures. At LHC, there are some benchmark channels for DM search:

(i) production via *Z* boson and invisible decay that shows very large missing transverse momentum and eventually a single photon from initial state radiation (ISR), (ii) production via the Higgs boson and decay into a pair of *Z* bosons that then decay invisibly, (iii) more general heavy-invisible-particles decays with mediation of *Z* or Higgs bosons with signatures on the missing energy and ISR, like mono-jet and mono-Higgs, (iv) mediators production together with two top or bottom quarks resulting in multi-jets besides missing energy, (v) more complex specific channels of production of SUSY particles and missing transverse momentum and (vi) vertexes for displaced decay of long-lived particles (LLP) or more complex signatures due to LLP decay, happening only in the external sub detectors (calorimeters and muon spectrometers). Possible discovery of DM on only colliders cannot be claimed without confirmation from direct or indirect searches, however new BSM particles can be discovered. We show in Fig. 3.6 a summary of the constraints obtained with the ATLAS and CMS experiments on specific models for DM. As a comparison, constraints from direct DM searches are shown. More details in DM searches at colliders can be found in Ref. [103].

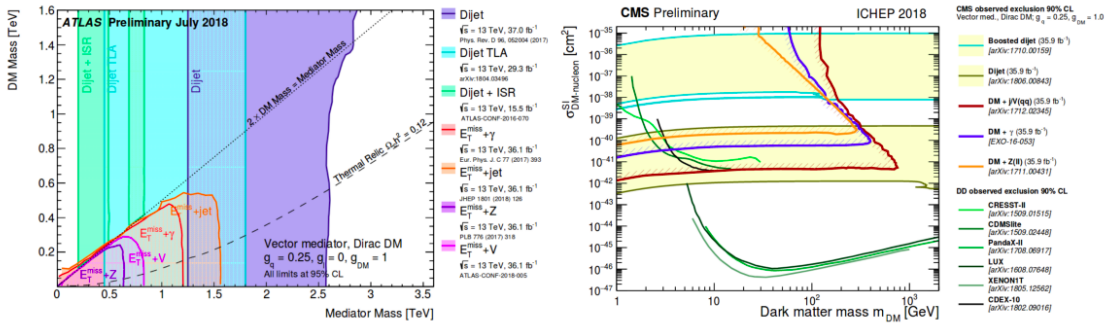

Figure 3.6: Summary for the search of DM at colliders with specific models for ATLAS and CMS. *Left panel*: 95% C.L. ATLAS constraints in the DM mass vs mediator mass region. Combinations of masses consistent with the relic DM density measurements are given by the dashed line. *Right panel*: 95% C.L. CMS constraints on the DM-nucleus cross section, spin-independent and as a function of DM mass. Constraints from direct searches are also shown. Figures extracted from Ref. [103].

3.4.3 Indirect search

The detection of secondary SM particles produced by the self-annihilation of DM in a process $\chi\chi \rightarrow$ XX is what is referred to as indirect search. X can be a photon, a neutrino, a hadron, a lepton or an electroweak boson. For the different final states, instruments have been built to detect the products. When gamma-rays are considered as final states, the advantage is that they are not deviated by magnetic

fields. Therefore, they come directly from their source and the telescopes can be pointed towards the most DM-dense regions of the Universe. However, a large astrophysical background has to be dealt with. Moreover, interaction with EBL attenuates the gamma-ray spectrum, therefore gamma-rays up to redshift z=1 can be used. More details about indirect search of DM with gamma-ray telescopes are given in the following. Neutrinos, as gamma-rays, do not deviate from the direction of their source and they do not undergo many interactions, thus probing up to far distances. Only weakly interactions with matter happen, this is why indirect search with neutrino telescopes are performed with under-water and under-ice large size experiments such as ANTARES and IceCube. This makes sure that no background sources are producing the detected muons, which are then produced by cosmic neutrinos. Prompt DM annihilation can produce neutrinos, which can also be obtained as a secondary product from the decay of leptons (and antileptons) in the final state. DM annihilation also produces couples of gauge bosons, the latter decaying into leptons and finally into neutrinos. Where the neutral Z gauge boson is produced, direct decay into neutrinos can happen. Multiple scattering of solar nuclei and DM is a clean channel for indirect search of DM with neutrinos. Inside the Sun, the DM captured particles annihilating producing SM particles, subsequently decaying into neutrinos. Then, neutrinos escape the Sun and get to the Earth detectors [26, 2]. However, neutrinos are really difficult to detect. Indirect searches can be performed by satellite experiments like AMS and PAMELA, detecting charged CRs. In these cases, the flux of electrons, protons and their antiparticles is measured. Charged CRs are deviated by the Galactic magnetic field at GeV energies, therefore they show an isotropic distribution and cannot be used to get information about the direction of their source, unless very local ones are measured. Therefore, an overall excess of positrons and antiprotons with respect to those derived by standard astrophysical processes is searched. The low background is an advantage of searching for antimatter. PAMELA measured an excess of positrons [27]. This was later confirmed by AMS-02 [31], with better precision and for a wider range of energies. These measurements can be interpreted as a DM signal [320], but also by standard astrophysical processes happening for acceleration of CRs in pulsars [335]. A DM hypothesis should be confirmed by other experiments and measurements of the flux of antiprotons and gamma-rays. An excess of antiprotons has been observed in measurements with AMS [150]. The latter can be a hint for DM with mass of $40-130$ GeV and thermal annihilation cross section. These results are however affected by uncertainties on the propagation of CRs through the ISM. In Fig. 3.7, we show a summary for constraints derived with indirect DM search through detection of secondary SM particles. More details on indirect DM search can be found in [143].

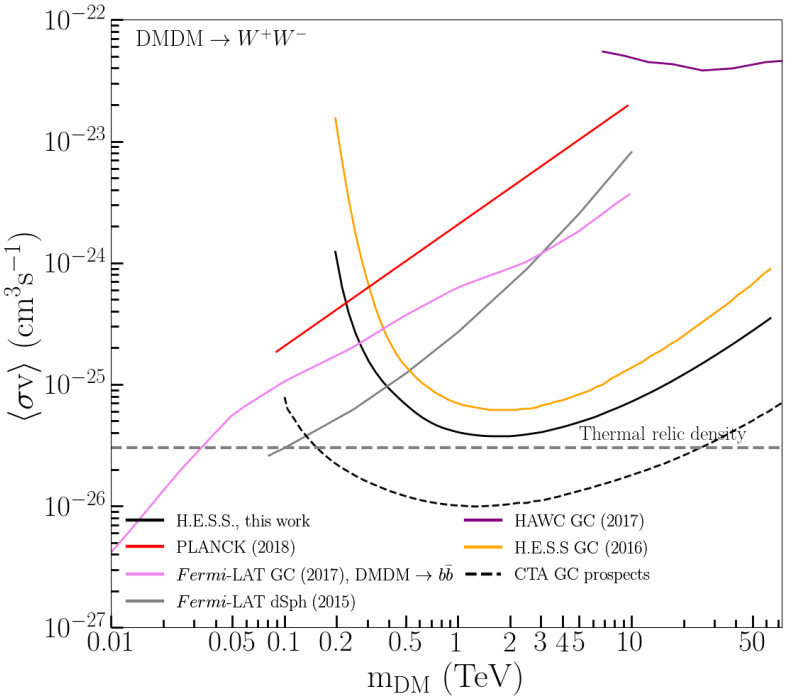

Figure 3.7: Summary of constraints on WIMP self-annihilation cross section from indirect detection techniques. The thermal relic cross section is indicated by the gray line, which represents the natural annihilation scale for thermally produced WIMPs. Figure extracted from Ref. [7].

3.4.4 Complementarity of the detection techniques

The various techniques to detect DM are becoming more and more complementary in such a way that now each individual technique is improving its chance to detect or tightly constrain the dark matter parameter space in the GeV mass range. Masses at TeV cannot be probed by colliders due to the limited energy at the center-of-mass. The same is true for direct detection because the DM particles with large masses are much less dense. Therefore, indirect detection is the preferred channel to probe TeV mass regime. The challenging region of the neutrino floor now starts to be approached by direct detection constraints. On the other hand, the contamination from standard astrophysical emission is a problem for indirect detection. The local DM density is affected by an uncertainty of a factor of two, however the DM density distribution of the observed target is known with limited certainty. Fundamental properties like the spin and the couplings can be understood with production of DM particles at colliders. The former are, for instance, not accessible by indirect detection. However, if a DM particle candidate were discovered at a collider, confirmation from indirect/direct detection techniques would be needed to confirm that the DM permeating the Universe is

actually made of the new particle. To compare the three techniques for the detection, the underlying DM interaction should be known in order to explain the results. In a model-dependent way, this is done through effective field theories (EFTs) and simplified models [273]. When the center-of-mass energy for the interaction is small compared to the mediator mass, the EFT framework can be used. The mediator mass is integrated out leaving the DM particle as the only degree of freedom. Simplified model approaches are applied when the EFT framework cannot be used, as often happens at LHC. The former also includes the mediator properties in the calculations. Specified Feynman diagrams are used for simplified models, with assumptions on the nature of the mediator and its couplings to DM and SM particles. From the constraints in the parameter space of the mediator mass vs DM mass, which can be derived at colliders, constraints on the DM annihilation cross section or DM-nucleon scattering cross section can be derived without any further assumption [142]. We show in Fig. 3.8, results obtained by CMS. The interpretation is done through a simplified model including a pair of Dirac fermionic DM particles coupling to a mediator in the final state. The mediator can be vector, axial-vector, scalar or pseudoscalar. In the left panel, the comparison between direct detection and collider searches with the assumption of a scalar mediator, is shown. For masses lower than 10 GeV, the collider constraints surpass the direct detection ones by orders of magnitude. The comparison between indirect detection and collider searches is done in the right panel, assuming a pseudoscalar mediator. In this case, the constraints from collider searches reach 200 GeV and the indirect detection constraints become more relevant in the same region. Constraints on the DM annihilation cross section $\langle \sigma v \rangle$ can be translated on the EFT scale M_*, with EFTs theories [273]. M_* expresses the strength of the interaction as a function of the DM mass. Given the different possible mediators, four cases are considered: scalar ($\mathcal{O}_S$), pseudo-scalar ($\mathcal{O}_P$), vector ($\mathcal{O}_V$) or axial-vector ($\mathcal{O}_A$) operator. The operators $\mathcal{O}_P$ and $\mathcal{O}_A$ are suppressed by the spin of the target nucleus or the scattering momentum exchange. $\mathcal{O}_P$ and $\mathcal{O}_S$ are suppressed through a Yukawa coupling respecting the principle of minimal flavor violation. Indeed, the indirect detection constraints are suppressed by $\mathcal{O}_S$, the direct detection ones are suppressed by $\mathcal{O}_P$ and both are suppressed by $\mathcal{O}_A$. For $\mathcal{O}_V$, there is no suppression of the interactions. Collider constraints are also weakened by $\mathcal{O}_S$ and $\mathcal{O}_V$. The complementarity between indirect, direct and collider techniques is shown by Fig. 3.9. In this, we are showing CTA forecast limits on M_* as a function of the DM mass at the GC [273], together with LUX [42] and XENON [46], and ATLAS [1] constraints for the different operators. Overlapping regions of the parameter space are covered by the techniques, therefore the combination of them probes a larger region than the one covered when a single technique is used. For the scalar case, the constraints from direct detection are the strongest in the full mass range. For all the mediators, constraints from the indirect searches cover higher masses than the collider searches. For the axial-vector operator, the indirect searches sur-

pass the other techniques in the TeV mass range. For the pseudo-scalar scale, the constraints from the indirect searches are the strongest, however not reaching the value predicted for the relic density. The three experimental approaches are shown in Fig. 3.10, where the possible DM detection channels are represented schematically for the coupling of SM and DM particles through an unknown interaction.

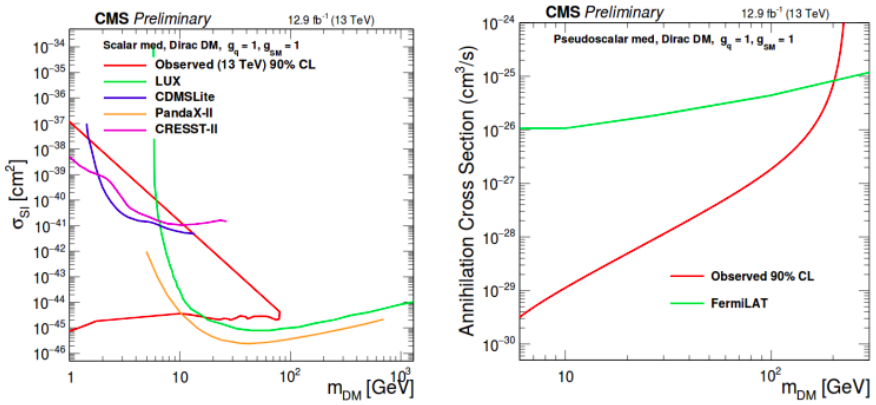

Figure 3.8: Simplified models for the comparison of DM detection techniques. *Left panel*: comparison of direct detection and searches at collider assuming a scalar mediator. The constraints are for spin independent DM-nucleon scattering cross section versus DM mass. *Right panel*: comparison of indirect detection and searches at collider assuming pseudoscalar mediator. The constraints are for the DM annihilation cross section vs DM mass. Figure extracted from Ref. [273].

3.5 Density distribution of Dark Matter at Galactic scale

The proportion of DM signals to be detected is given by the magnitude of the DM density, which is therefore very important to be estimated around the target of interest. To model the DM halos, we can use different parameterizations which can be divided in two macro categories: cuspy and cored density profiles. Most massive galaxies show cuspy profiles, which can form in places like the Milky Way central region, due to the strong gravitational potential of the central supermassive black hole Sgr A*. The two most known cuspy profiles are the Einasto [341] and NFW [292] ones. Einasto parameterization writes as:

$$\rho_{\mathrm{E}}(r) = \rho_s \exp\left[-\frac{2}{\alpha_{\mathrm{s}}}\left(\left(\frac{r}{r_{\mathrm{s}}}\right)^{\alpha_{\mathrm{s}}} - 1\right)\right] \tag{3.4}$$

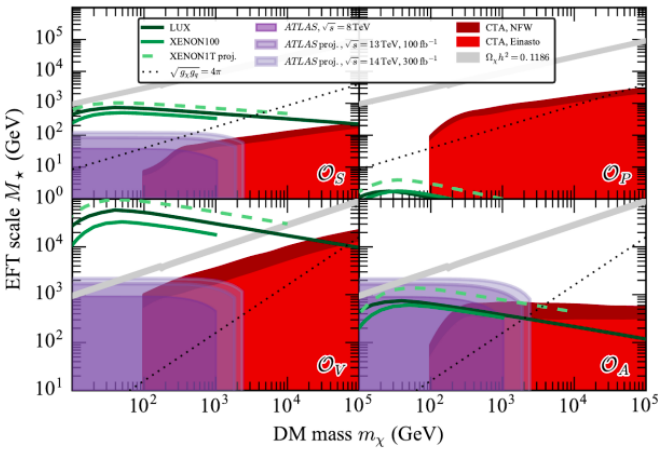

Figure 3.9: Lower limits on the scale M_* for the EFT theories as a function of the DM mass. The comparison is between indirect, direct and collider searches. Figure extracted from Ref. [273].

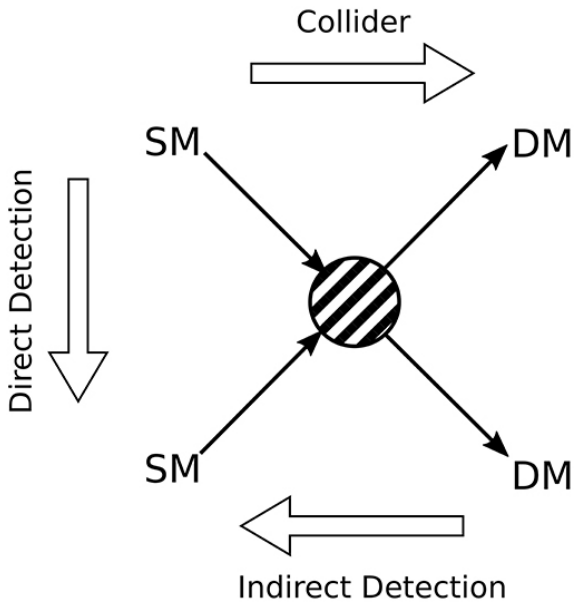

Figure 3.10: The three experimental approaches for the possible DM detection channels represented schematically with the coupling of SM and DM particles through an unknown interaction, shown as the dash-shaded circle. Figure extracted from Ref. [263].

and the NFW writes as:

$$\rho_{\rm NFW}(r) = \rho_{\rm s}\left(\frac{r}{r_{\rm s}}\left(1+\frac{r}{r_{\rm s}}\right)^2\right)^{-1}. \tag{3.5}$$

In the equations, r is the distance from the center of the galaxy, $\rho_{\rm s}$ is the critical density at the position of the Sun, $r_{\rm s}$ is the scale radius for the slope change in the profile. The steepness of the profile is given by α. The NFW profile degenerates at r=0, while $\rho_{\rm E}(0)$ is finite. Many galaxy rotation curves suggest that the central DM halo is flat. For small mass galaxies, a central cored profile can be present. Main models for the latter are the Burkert [107] and the isothermal [89] profiles. The Burkert parameterization writes as:

$$\rho_{\rm B}(r) = \rho_0 \frac{r_{\rm c}^3}{(r + r_{\rm c})(r^2 + r_{\rm c}^2)} \tag{3.6}$$

and the isothermal one writes as:

$$\rho_{\rm Iso}(r) = \rho_0 \left(1 + \left(\frac{r}{r_{\rm c}}\right)^2\right)^{-1}. \tag{3.7}$$

ρ_0 is defined as the density inside the core, while $r_{\rm c}$ represents the radius of the core. From cuspy profiles, cored ones can be obtained by the following modeling:

$$\rho_{\rm E-NFW,core} = \begin{cases} \rho_{\rm E-NFW}(r) & \text{for } r > r_{\rm c} \\ \rho_{\rm E-NFW}(r_{\rm c}) & \text{for } r \leq r_{\rm c} \end{cases} \tag{3.8}$$

These parameterizations are derived from N-body simulations and observations of the kinematic of stars and gas. Nevertheless, the baryonic component is not included in these profiles because much more sophisticated N-body simulations are required for the inclusion [165]. Another component which can alter the DM density profile through tidal stripping or disruption is the interaction with other halos. The smallest one can be disrupted by the interaction [307]. We show examples for the DM density profiles in Fig. 3.11. For the regions close to the GC, the cuspy profiles are 3 or 4 orders of magnitude larger than the cored profiles. The GC dynamics can be reproduced by several DM profiles, because the gravitational potential is actually dominated by stars and gas. The search for DM signal is largely affected by the wide uncertainties on the Galactic halo profile. Therefore also the obtained constraints on the annihilation cross section can vary by many orders of magnitude as a consequence of the assumed DM density distribution.

3.6 Gamma-ray targets for Dark Matter search

When looking for DM, targets with very dense DM halos or clumps need to be observed. These dense regions can host the decay or annihilation of the relic DM particles producing the detectable gamma-ray signal. More details on the characteristics of the expected flux of gamma-rays from DM annihilation are given later. Here, we briefly explain what DM dense regions are.

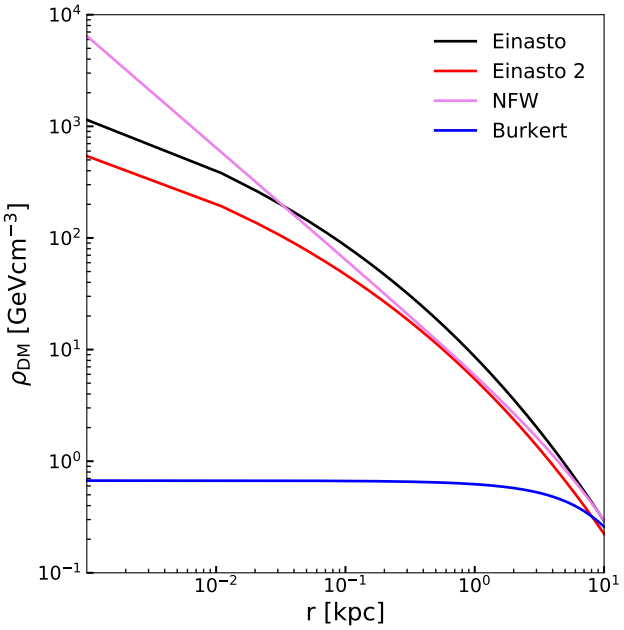

Figure 3.11: DM distribution in the GC region for two examples of the Einasto (black and red lines), NFW (pink line) and Burkert (blue line) profiles.

The Galactic Center (GC) is about 8.127 kpc away [185] from the solar system and is the closest target to detect DM signal. It is expected to contain a large amount of DM, as it was explained in the previous section. When assuming a standard NFW profile, the integrated square density of DM along the line of sight within 1° region around the GC is $\log_{10}(J/\text{GeV}^2\text{cm}^{-5})$ = 21.0. The J-factor represents the distribution of dark matter in an astrophysical system and determine the strength of the signal of DM distribution from the observed target. It will be explained in Sec. 3.7. Therefore, the largest gamma-ray signal from DM is expected from this region. However, the several regions that are present in the regions and emitting in VHE (see Chap. 5) make the expected background not easy to model. This region was observed for a large amount of hours by H.E.S.S. and *Fermi*-LAT, resulting in the strongest constraints so far on DM annihilation. We explain more about the DM search towards the inner halo of the Milky Way with the Inner Galaxy Survey dataset in Chapter 8. *Fermi*-LAT also measured an excess in GeV gamma-rays from the GC region that could be explained as from DM annihilation [237], however explanations from more standard astrophysical sources are more plausible [115], when DM is not detected towards other cleaner environments, *e.g.* dwarf galaxies. There are also studies relating the TeV gamma-ray flux observed by H.E.S.S. towards Sgr A* to DM signal [115]. A *Fermi*-LAT observation claimed a hint of DM signal with DM mass of 130 GeV near the GC [351], which was later

rejected by H.E.S.S. [6].

DM subhalos are predicted of various sizes in the main DM halos by cosmological simulations. From Earth, gamma-rays produced by the halos that are inside the Milky Way are potentially detectable. Small halos do not have large sufficient gravitational potential to accumulate enough matter and ignite star formation, thus they may not shine in gamma-rays unless through DM annihilation signals. Some of the subhalos could be close enough to Earth and made of a relevant DM density such that can be detected. However, their position is completely unknown. Therefore, pointing observations is not the ideal strategy. The observations in wide-field with *Fermi*-LAT revealed a population of sources with no counterpart at other wavelengths, the unidentified Fermi objects (UFOs). These are favorable candidates for DM subhalos [226], and have been targeted by H.E.S.S. observations and we show the results of this analysis in Chap 9.

Dwarf galaxies in the Local Group satellites of the Milky Way (dSphs) are the most DM-dominated objects of the Universe, located not too far from Earth (25 to 250 kpc away). They do not ignite star formation and are almost devoid of gas. This makes them a clean environment for observations in gamma-rays and DM annihilation can be easily associated with an emission from dSphs. Moreover, they are close targets with an expected large signal as compared to other targets such as the galaxy clusters. The J-factor of dSphs, integrated in a region of 0.5°, is of the order of $\log_{10}(J/\text{GeV}^2\text{cm}^{-5})$ = 18.0-19.0. Thus, dSphs are very promising targets for unambiguous detection of DM signals and have been targeted by observations with IACTs. DM search with H.E.S.S. have been performed towards a selection of dSphs and the results are shown in [14].

Galaxy clusters are the largest systems dominated by DM and gravitationally bound. About 80% of their mass is DM [220]. However, they are very far from the Solar system. The J-factor, integrated in a region of 1° is of the order of $\log_{10}(J/\text{GeV}^2\text{cm}^{-5})$ = 16.0-17.0. Nevertheless, they have been used to derive constraints a few orders of magnitude fainter than the ones from GC observations. They are however very promising targets for DM decay [21], for which very large volumes mean more efficient searches, because they present a very large mass, 10^{14}-10^{15} times the mass of the Sun. The decay produces electrons and positrons that undergo ICS and lose energy much faster than they can diffuse out of the system, being therefore a source of gamma-rays before escaping.

A possible detected DM signal must be strong and distinguishable for background emissions. So DM is better searched for in targets with large DM content, which are close by and present low astrophysical background from standard astrophysical sources. Since the GC is the closest to the observers, it is also the most promising target. Unambiguous detection is also possible in other promising targets such as subhalos and dwarf galaxy satellites of the Milky Way, because they show the lowest possible background at a relatively small distance from the observer.

3.7 Expected flux of gamma rays from annihilating Dark Matter

DM annihilation in DM dense environments can produce gamma-rays that are detectable by the IACTs. However, the expected flux of gamma rays is dependent on the assumptions made on the annihilation processes and how the DM is distributed in the target. The flux of gamma-rays writes as:

$$\frac{d\Phi_\gamma}{dE}(E,\Delta\Omega) = \underbrace{\frac{1}{4\pi}\frac{\langle\sigma v\rangle}{m_{\rm DM}^2}\sum_i Br_i\frac{dN_i}{dE}(E)}_{\text{particle physics}} \times \underbrace{J(\Delta\Omega)}_{\text{astrophysics}} . \tag{3.9}$$

The particle physics information on the properties of the DM particles is contained in the first term: the mass $m_{\rm DM}$, the thermally averaged velocity weighted annihilation cross section $\langle\sigma v\rangle$, the spectrum from annihilation dN/dE_i for a specific channel i and the corresponding branching ratio Br_i. The astrophysics information about the DM distribution around the target is encoded in the second term of the equation. This quantity is represented by the *J*-factor, which is computed as the integral of the square of the DM density over the line of sight *los* and the solid angle $\Delta\Omega$. The J-factor is given by:

$$J(\Delta\Omega) = \int_{\Delta\Omega}\int_{\rm los}\rho^2(r(s,\theta))dsd\Omega. \tag{3.10}$$

When signals from DM decay are searched, the J-factor is substituted by the D-factor, $D = \int_{\Delta\Omega}\int_{\rm los}\rho(r(s,\theta))dsd\Omega$. The J-factor can be computed as average over an integration region $\Delta\Omega$:

$$J = \frac{2\pi}{\Delta\Omega}\int d\theta\ \sin\theta\ J(\theta) \quad \text{for a disk } \Delta\Omega = 2\pi\int_0^{\theta_{\rm max}} d\theta\ \sin\theta$$

$$J = \frac{4}{\Delta\Omega}\int d\theta\ \sin\theta\ J(\theta) \quad \text{for an annulus } \Delta\Omega = 2\pi\int_{\theta_{\rm min}}^{\theta_{\rm max}} d\theta\ \sin\theta$$

$$J = \frac{2\pi}{\Delta\Omega}\int\int dldb\ \cos b\ J(\theta,b,l) \quad \text{for a } b\times l \text{ region } \Delta\Omega = 4\int_{b_{\rm min}}^{b_{\rm max}}\int_{l_{\rm min}}^{l_{\rm max}} db\,dl\ \cos b. \tag{3.11}$$

The term θ represents an annular radius and l and b are the longitude and latitude coordinates. To estimate the number of gamma-rays that the telescope observes,

we need to consider the actual flux of gamma-rays $d\Phi_\gamma/dE$, the characteristics of the detector and the information about the observation. Therefore, by the convolution of the differential flux with the detector effective area $A^\gamma_{\rm eff}$ and with the energy resolution $G(E)$, and integrating over time of observation $T_{\rm obs}$ and energy ΔE we obtain the number count of gamma-rays as:

$$N_{{\rm S},\gamma} = T_{\rm obs} \int_{\Delta E} \frac{d\Phi_\gamma}{dE}(E, \Delta\Omega) A^\gamma_{\rm eff} G(E) {\rm d}E. \tag{3.12}$$

The instrument response functions such as the effective area and the energy resolution depend on the observation conditions (*e.g.* zenith angle and *offset* of the observations), as well as on the energy. This was already explained in Sec. 2.5.3.

3.8 Annihilation spectra

3.8.1 Signal from continuum

Several final states of particles are allowed from the annihilation of DM, in the context of particle physics. From tree-level annihilation, leptons, quarks or bosons can be produced, assuming large enough mass of the DM particles to produce them. From final state particles, gamma-rays can then be produced from decay or hadronization. The part of the spectrum of gamma-rays obtained by these processes is known as the continuum. Since the annihilation of cold DM is assumed at rest, the spectrum will present a cutoff at $m_{\rm DM}$. The shape of the spectrum for lower energies changes according to which particles are present in the final state. We show in Fig. 3.12 continuum spectra for annihilation in some channels, for particles of $m_{\rm DM}$ = 10 TeV, computed from Ref. [124]. We also show comparison spectra from a gamma-ray yield from a more recent study [55]. We will show more details about this in Chap. 10. Leptonic spectra are steeper close to $m_{\rm DM}$, thus the maximum of the spectra is close to the latter. For bosonic and quark channels, the maximum of the spectra appears at about $m_{\rm DM}/10$. In the channel $\tau^+\tau^-$, features from both hadronic and leptonic channels are present and the peak is close to $m_{\rm DM}/3$. It also results in the strongest signal at the peak. In the following, we consider 100% branching ratio in each single channel, referring to the XX channel (X can then be X = $W, Z, b, t, e, \mu, \tau, H$. However, branching ratios are dependent on the mass and spin of the particle X and on the choice of dark matter particles. Therefore for each candidate and combination, there can be different models producing different branching ratios.

3.8.2 Signal from mono-energetic line

Final annihilation of DM particles can also directly produce photons, but not at the tree-level. Two photons production can happen through loops. The cross section

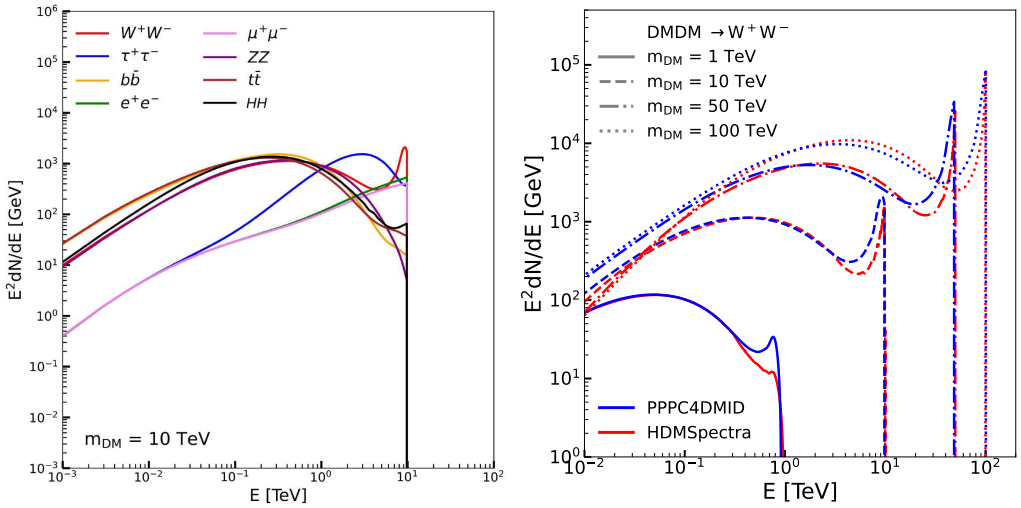

Figure 3.12: Spectra of photons expected from DM particles self-annihilating in the XX channels with X = $W, Z, b, t, e, \mu, \tau, H$. *Left panel*: comparison of spectra extracted from `PPPC4DMID` in Ref. [124] for the annihilation channels used in this work. *Right panel*: comparison of spectra for annihilation of DM in W^+W^- for the two gamma-ray yields used later, `PPPC4DMID` and `HDMSpectra` from Ref. [55].

of this process scales with the square of the electroweak coupling $\alpha_{\rm EW}^2$ and it is suppressed. For the WIMP mass in the TeV range, the signal is 10^2-10^4 smaller than the continuum [319]. The photon spectrum that is obtained from prompt annihilation is referred to as the gamma line. The latter is a monoenergetic line, behaving as a Dirac delta function at the mass of DM $\delta(E - m_{\rm DM})$. In a realistic case, an instrument with finite resolution can detect a spread line, which can be modeled through a Gaussian function with width equal to the energy resolution. This line is the sharpest and clearest signal from DM annihilation. However, it is also the most difficult to detect due to the small expected cross section and the strong sensitivity to fluctuations in the dataset. At the same time, this channel would show the most unambiguous DM detection, since it cannot be mimicked by any other standard astrophysical process.

3.8.3 Astrophysical and particle physics enhancement

Some additional photons can be produced by processes that are enhancing the DM signal. The main contributions among these particle physics processes are the electroweak (EW) corrections and the Sommerfeld enhancement. The spectra shown before already take into account the EW corrections. The ICS with the ambient radiation in the ISM (like for instance the CMB) can happen for states containing light leptons [127]. The spectra obtained from Ref. [124] do not contain the photons from ICS. The main astrophysical contribution to the enhancement

of the DM signal comes from the presence of subhalos

Sub-halos are substructures inside the main DM halo and are predicted by the simulations (see Sec. 3.6). The standard expected DM signal is obtained from the smooth distribution of DM in the host halo, but subhalos could boost this signal [279]. The central cusp of these halos is much steeper than the one in larger halos. Then, the total J-factor for the DM signal is obtained by the sum of the smooth distribution of the main halo and the distributions of the subhalos. The substructures contribute more in the outer part of the main halo than in the inner one. However, whether the gamma-ray signal is really boosted by the subhalo distributions is still under debate [122].

Electroweak corrections consist in possible production of additional radiation when the DM particles with mass larger than the EW scale (≥ 100 GeV) annihilate into a couple of charged particles [123]. When an additional photon is obtained by one of the particles out of the interaction vertex, we are talking about final state radiation (FSR). Instead, when virtual exchanged particles produce a photon we are talking about virtual internal bremsstrahlung (VIB). At larger DM masses, the intensities of these emissions increase. These two phenomena contribute in the addition of sharp line-like features at the end of the spectrum, near $m_{\rm DM}$. The W boson channel spectra show these important features, which are visible in the spectrum in Fig. 3.12.

The Sommerfeld effect is a classical quantum effect that happens for low velocity regimes, when two initial state DM particles exchange the mediation of the interaction for many times before the annihilation takes place [339]. Since this process happens at non-relativistic velocities, it can be hosted by DM halos where the DM particles move with relative velocities of the order of $\beta = v/c = 10^{-5}$ (v = 10 km s^{-1}). Particles interact with a Yukawa-like potential $V(r) = -(\alpha/r)\exp(-m_{\rm V} r)$, exchanging a vector boson of mass m_V, with α being the coupling constant. The enhancement of a factor $S(\beta, m_{\rm DM}, m_{\rm V})$ is applied on the initial value of the thermal relic cross section $\langle\sigma v\rangle_0$ to obtain the value $\langle\sigma v\rangle = S(\beta, m_{\rm DM}, m_V)\langle\sigma v\rangle_0$. Depending on the relative velocity β [240] three regimes can be defined as shown in Fig. 3.13. At large velocities, with $\beta >> \alpha$, no enhancement is present, *i.e.* $S(\beta, m_{\rm DM}, m_V)$ = 1. This regime is shown by and considered for $\beta = 10^{-1}$. At intermediate velocities, when $\sqrt{\alpha m_{\rm V}/m_{\rm DM}} \ll \beta \ll \alpha$, the enhancement scales as 1/v and $S(\beta, m_{\rm DM}, m_V) \simeq \pi\alpha/\beta$ independently on the masses. This regime is given by the green line for $\beta = 10^{-2}$ and shows no resonance. At small velocities, when $\beta \ll \sqrt{\alpha m_V/m_{\rm DM}}$, some resonance happens due to the presence of bound states, as shown by the yellow, magenta and purple lines ($\beta = 10^{-3} - 10^{-5}$). The enhancement depends on the particle mass and scales $\propto 1/\beta^2$. For the very small velocities expected in the DM halos, the increasing of the relic cross section can be up to a factor 10^5 due to resonances. The position of the resonances is given by the mass of the DM and of the mediator $m_{\rm V}$, *i.e.* the strength of the coupling between mediator and DM particle. Small DM masses produce the largest resonances. Large

m_{V} shifts the resonances to larger m_{DM}.

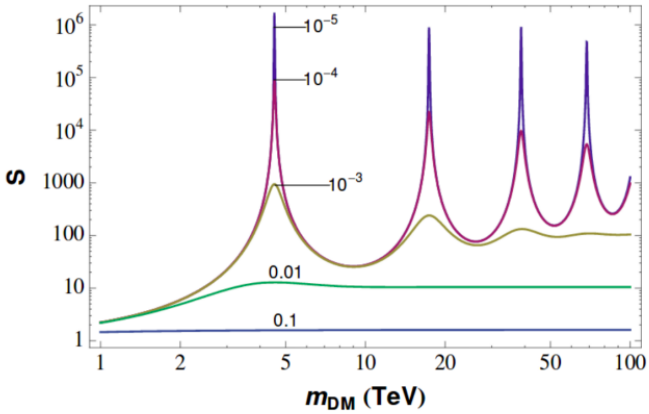

Figure 3.13: Sommerfeld effect induced intensity for DM annihilation into the channel W^+W^- mediated by the Z boson. The intensity is shown as a function of the DM mass. Relative DM velocities in the range of 10^{-1}-10^{-5} are considered for the shown effect. Figure extracted from Ref. [240].

Chapter 4

Statistical methods for Dark Matter and outflows searches

Contents

Summary

A common approach for the search of VHE emissions is to apply the log-likelihood ratio test statistics (LLRTS) on the measured dataset. Sec. 4.1 introduces the concepts explained in the chapter. Then the part dedicated to the TS technique is organized as follows: the Test Statistics and the likelihood function are defined in Sec. 4.2, we define the framework in which we build the mock dataset in Sec. 4.3, we then explain the derivation of limits on the free parameters of a model for the searched emission in Sec. 4.4, we show how to include possible sources of uncertainties in the likelihood function in Sec. 4.5, we briefly discuss how to reconstruct a fake injected signal in Sec. 4.6 and we conclude with some perspectives in Sec. 4.7.

Another approach for disentangling weak signals from the background emission consists of the application of machine-learning-based methods such as neural networks (NNs). We show in the second part of the chapter how Bayesian Neural Networks (BNNs) can be used to disentangle the signal from a non-trivial background. The part dedicated to the BNN approach is organized as follows: Sec. 4.8 is an introduction on Neural Networks and the transformed Bayesian Neural Networks that we are using, Sec. 4.9 shows the additive mixture of synthetic signal and background that we want to study with our framework, some experiments are shown in Sec. 4.10 and the results are given in Sec. 4.11, we conclude with some outlook in Sec. 4.12. The results obtained with our Bayesian Neural Network framework, at the moment of the writing, have been submitted to ICLR2023 [64].

4.1 Introduction

In VHE astrophysics we search for weak phenomena/signals in datasets including either a modeled or measured background. This chapter presents two approaches that can be used to search for weak signals in the presence of a non-trivial background emissions.

Within the LLRTS approach, the phenomena can be modeled through random processes. Therefore, probability density functions are needed to characterize the observed events. Then the LLRTS technique can be used to disentangle the signal emission from the background one. The first part of this chapter is dedicated to explaining the LLRTS approach. We define the likelihood function for Poisson probability density functions together with the TS that can be used for detection or derivation of limits in the works presented in later chapters. This method is later applied to the searches for DM and the Fermi Bubbles' TeV emissions and to measuring/constraining the parameters used to model the searched emissions. To better show how the methods can be applied, we provide examples with a mock dataset of 500 hours of observation of the Galactic Center region with the full five-telescopes H.E.S.S. array. With this dataset, we search for VHE signal of DM self annihilation, deriving constraints on the annihilation cross section of the DM particles. The results obtained with the TS framework are shown in the first part of this chapter

Machine-learning-based methods can be used as predictive models to search for weak emissions in background dominated regions relaxing the a-priori assumptions on the knowledge of the background emission. The second part of this chapter is dedicated to show how Bayesian Neural Networks (BNNs) can be used to disentangle the signal from a non-trivial background. We first recap the basics of the NNs that we are using, then we explain how we combine them to learn a model of simulated emission which is defined over spatial and spectral coordinates. We also show experiments that we performed on the simulated synthetic dataset and we conclude with future foreseen improvements and applications for dark matter searches. The results obtained with the BNN framework are shown in the second part of the chapter.

4.2 Test-Statistics-based methods

In order to search for an emission in a dataset, we first define a model with which the former can be described. Then, one can define a methodology to detect or set limits on the values of free parameters of the model. These limits can be computed through test statistics. In this section, we define the main components of the *Log-Likelihood Ratio Test Statistics* (LLRTS) technique. This method is commonly applied for analyses of H.E.S.S. datasets and the search of outflows or DM signals.

4.2.1 The likelihood function

When the model of the searched emission is defined, we use the likelihood function to derive or measure constraints on the chosen free parameter of the model. One can start by considering an observed dataset $\mathcal{O}$. We can write the probability density function of the dataset as $f(\mathcal{O}, \theta)$. The set θ includes all the parameters that determine the density function. If the dataset $\mathcal{O}$ is constituted by the observed values x_i, we can write the probability density functions for each of the values as $f(x_i, \theta)$. In this case, the set of parameters θ determines the individual functions. Under the assumption of homogeneously and independently distributed observed values, *i.e.* $\mathcal{O} = \{\mathrm{x}_i\}_{i=1}^{n}$, the likelihood function of the whole dataset writes as:

$$\mathcal{L}(\theta, \mathcal{O}) = \prod_{i=1}^{n} f(x_i|\theta) \tag{4.1}$$

The logarithm of this function can be extracted to obtain the log-likelihood:

$$\ln \mathcal{L}(\theta, \mathcal{O}) = \sum_{i=1}^{n} \ln f(x_i|\theta) \tag{4.2}$$

Therefore, the probability that the event x_i is observed for a model that depends on θ is given by the likelihood function, which is a function of the parameters θ.

4.2.2 The log-likelihood ratio test-statistics

The hypothesis of the new searched phenomenon is defined as $H_1(\theta_1)$, depending on the set of parameters θ_1 that characterizes the searched emission. Then, the latter is compared to a null-hypothesis $H_0(\theta_0)$, being it the hypothesis with only background emission and depending on the set θ_0. To state that the searched signal has been found, the hypothesis H_1 has to be more likely than H_0. The probability that the latter is true is obtained by the comparison of two likelihood functions built under the two hypotheses. Therefore, we define a test statistics TS to assess which hypothesis is more compatible with the data. The LLRTS is defined as:

$$TS = -2\ln \lambda(\theta) = -2\ln \frac{\mathcal{L}(\theta_1, \mathcal{O})}{\mathcal{L}(\theta_0, \mathcal{O})}. \tag{4.3}$$

In the limit of high statistics, the TS follows a χ^2 distribution [365]. Therefore, assuming one free parameter in the model used for the hypothesis H_1, the 95% C.L. limits on the latter can be derived by taking its value corresponding to TS = 2.71, for a one-sided likelihood and one degree of freedom between the two hypotheses. Similarly, TS = 3.84 corresponds to 99% C.L. limits. TS values for

other C.L. can be derived by considering values of the χ^2 for different degrees of freedom, when the limit of high statistics is considered.

4.2.3 Profiling likelihood technique

In this work, we applied the *full profiling* definition of the TS. A detailed description of this definition is provided in Ref. [147]. Then, the ratio of the likelihood functions for the H_1 and H_0 hypotheses is defined as:

$$\lambda(\theta) = \frac{\mathcal{L}(\widehat{\widehat{\theta}}_1, \mathcal{O})}{\mathcal{L}(\widehat{\theta}_0, \mathcal{O})} \tag{4.4}$$

with θ_1 and θ_0 the sets of parameters for the hypotheses H_1 and H_0. This definition is valid for $0 \leq \widehat{\theta} \leq \theta$. The term $\widehat{\widehat{\theta}}$ is computed from a conditional maximization of the likelihood function, therefore it depends on θ. Instead, $\widehat{\theta}$ is derived from a non-conditional maximization of the likelihood function and does not depend on θ.

In cases where $\widehat{\theta} < 0$, the *hybrid profiling* definition can be applied. In this case the ratio of the likelihood functions is defined as:

$$\lambda(\theta) = \frac{\mathcal{L}(\widehat{\widehat{\theta}}_1, \mathcal{O})}{\mathcal{L}(\widehat{\widehat{\theta}}_0(0), \mathcal{O})}. \tag{4.5}$$

A *simplified* definition, with no profiling of the likelihood, can be adopted. In this case the the ratio of the likelihood functions is defined as:

$$\lambda(\theta) = \frac{\mathcal{L}(\widehat{\theta}_1, \mathcal{O})}{\mathcal{L}(\widehat{\theta}_0, \mathcal{O})}. \tag{4.6}$$

In case of *discovery* we can write:

$$TS = \lambda(0). \tag{4.7}$$

This implies rejecting the hypothesis of background-only emission [147]. To define a discovery we need to take into account the significance of the excess in the observed signal. We will present more details about how to derive the significance of the excess in Sec. 4.4.2.

The *full profiling* approach is the most robust one and permits to obtain the best constraints, however the hypotheses needed for this approach may not be easily satisfied when a very small signal is searched for. This can be especially true for regions like the GC, where the residual background can be contaminated and difficult to estimate. Moreover, high fluctuations are present in the measurements in this region. In later chapters, the full profiling approach is used for the analyses presented in this work.

4.2.4 Binned Likelihood technique

The analyses that are presented in this work are built on massive datasets. Therefore, an un-binned likelihood, *i.e.* event-by-event, approach is not applicable. Thus, the analyses are performed with binned datasets. As a consequence, the likelihood function which is used for the derivation of constraints on the parameters of the tested model is binned. Spectral bins are defined on the energy range in which the instrument is sensitive. Spatial bins are usually defined on the region of the sky where the events are measured. One example is the search for dark matter annihilation signals in the dataset of H.E.S.S. observations towards the Galactic Center region. For this analysis, spatial and spectral bins are used for the likelihood function to better exploit the morphology of the expected dark matter signal. The binned likelihood function is therefore built as $\mathcal{L}_{i,j}$, for the ith spatial and jth spectral bins. To obtain the limits for the tested hypothesis, the total likelihood function is obtained through the product of the binned function over all the bins: $\mathcal{L} = \prod_{i,j} \mathcal{L}_{i,j}$.

4.2.5 Combination of likelihood functions

Multiple astrophysical objects or regions of the sky can be used for the measurement or derivation of constraints on the same searched model. Therefore a total likelihood function is defined for each of the dataset, for each object as it was explained in the previous section. Limits on the model of the searched emission can be obtained with each individual dataset or the likelihood functions of the datasets can be combined in a combined likelihood function to obtain combined limits with the TS. The combination of the datasets can be performed when no significant overall excess is found anywhere in the FoV in none of the individual datasets nor in the stacked datasets. The combined likelihood function is then defined as: $\mathcal{L}_{\rm comb} = \prod_{k=1}^{\rm N_{targets}} \mathcal{L}_k$, where $\mathcal{L}_k$ is the total likelihood computed for the target and the dataset k. The constraints obtained with the combined likelihood function are obviously stronger than the constraints obtained with the functions for the individual datasets because of the larger statistics.

Two approaches can be utilized for the combination of the functions. One approach consists in the sum of the statistics obtained either in all the individual datasets or in datasets from different instruments. The total number of measured events can be obtained for each energy bin i and spatial bin j by summing the events over the k dataset. The same procedure is applied for the derivation of expected events from background and from the signal emission. Then the total likelihood is built as the product over the likelihood functions for each energy and space bin $\mathcal{L}_{\rm comb} = \prod_{i,j} \mathcal{L}_{i,j,\rm tot}$. In this case, for each spatial and spectral bin, the subscript *tot* indicates that the likelihood function is obtained with the sum of the events in the bins, over the dataset. However, combining $\mathcal{L}_{i,j,\rm tot}$ produces loss of information. In fact, when the combination includes some datasets with

many more events than some other in the combination, the possible fluctuations due to different statistics are smoothed out. This can be avoided when the combination is performed at another level. The total likelihood function can be built as previously mentioned for each dataset k: $\mathcal{L}_k = \prod_{i,j} \mathcal{L}_{i,j,k}$. Then the combined likelihood function is obtained through the product of the functions over the index k, *i.e.* $\mathcal{L}_{\rm comb} = \prod_{k=1}^{\rm N_{targets}} \mathcal{L}_k$.

More details on the combination of likelihood functions and limits derivation from several datasets are provided in Sec. 9.5.3 and Sec. 9.5.4. In these sections, quantitative examples on the derivation of TS profile from the two likelihood combination approaches are also provided for one of the analyses shown in this work.

4.3 Mock data framework

In VHE astrophysical analyses we search for an emission in a defined region of interest (ROI), referred hereafter to as the *ON* region. A widely used approach is to measure the background in a control region, the so-called *OFF* region. Methods for the definition of the OFF region have been already shown in Sec. 2.4.2 and others will be introduced later to explain more in detail how events in the OFF regions are measured. The ROI for the example shown in this chapter is defined from a standard definition for the search for DM signal from the region around the center of the Milky Way - the Galactic Center (GC) region. It is considered as a circular region of 3° radius, which is split in rings of width 0.1°. The rings are considered from inner radius of 0.3° up to 2.9°, centered on the GC. More details about this way of defining the ROI are provided in Sec. 8.2.

Then ON and OFF events can be measured, collected independently and binned in energy to build event energy distributions for the ON and OFF regions, respectively. For the example shown in this chapter, we build a mock dataset from Poisson realizations of the real residual-background measurements obtained with observations of the GC region that the H.E.S.S. Collaboration performed in the last years. More details on the observed dataset and on the analyses performed with it are given later in Chap. 6. We make independent realizations for the ON and OFF simulated distributions, using the OFF events measured in each energy bin of the measured distributions. Therefore, the mean of the Poisson probability function is set to $N_{\rm OFF}$. These realizations are computed for each observational *run* in the dataset. Moreover, the obtained simulated distributions are re-scaled assuming 500 hours of homogeneous observations of the inner halo of the Milky Way, spanning Galactic latitudes from b=-3° up to b=6°and in Galactic longitudes of l $\leq |4|^\circ$, with the full-five telescopes H.E.S.S. array.

Fig. 4.1 shows an example of the event distributions used in the first part of this chapter for ROI 22 in black and red, respectively. Statistical error bands at 1σ are shown too. The two distributions show the standard power-law like behavior expected from measurements of the residual-background. However, above $\sim$ 10

TeV, the number of measured events stays constant. This is due to the population of events measured and reconstructed in the configuration *CT1-4 Stereo*, because the four small telescopes of the H.E.S.S. array are more sensitive to high energies for the reconstruction of events. The reconstruction modes have been already presented in Sec. 2.6. More detail on how the event distributions are built with the standard measurement methods used for analysis of H.E.S.S. datasets are provided later in Sec. 8.2 and Sec. 7.3.

4.4 Limit computation on the free parameters

Once our event energy distributions are defined, we can search for the expected emission in the region of interest. If no significant excess is found in the ON region w.r.t. the OFF region, we can apply the LLRTS procedure with the distributions and derive limits on the parameters for the model of DM self-annihilating in the W^+W^- annihilation channel and following an Einasto density profile (more details are provided in Sec. 3.5).

As was previously described, an hypothesis with a model for the searched emission can then be tested against the hypothesis of background only. To do this, one can define the likelihood function and the test statistic. Limits on the free parameters of the assumed model can then be derived. In the next sections we explain in detail how this is implemented.

4.4.1 Poisson probability function

To test emission models against background only hypotheses in VHE gamma-ray datasets, we have to deal with counting problems. To treat the latter, we define Poisson distributions of counts x_i. We then define the measured number of photons in the ON and OFF regions as $N_{\rm ON}$ and $N_{\rm OFF}$, respectively. Then, to search for dark matter annihilation signals, we expect to measure $N_{\rm S}$ signal photons and $N_{\rm B}$ background photons from residual background in the ON region. $N_{\rm S}$ is derived from Eq. 3.12 (more details on the derivation are provided in Sec. 3.8). The measured photons $N_{\rm ON}$ are distributed according to a Poisson function with mean $N_{\rm S}+N_{\rm B}$. If a leakage of signal photons is expected in the OFF region, $N'_{\rm S}$ signal photons and $\alpha N_{\rm B}$ background photons should be measured. The term α indicates the ratio between the solid angle size in the sky of the OFF and ON regions. Therefore, the $N_{\rm OFF}$ photons are distributed as a Poisson function with mean value $N'_{\rm S}+\alpha N_{\rm B}$. Having defined the distribution functions, we can then write the likelihood function as:

$$\mathcal{L}(N_{\rm S}, N_{\rm B}|N_{\rm ON}, N_{\rm OFF}, \alpha) = \frac{(N_{\rm S}+N_{\rm B})^{N_{\rm ON}}}{N_{\rm ON}!} e^{-(N_{\rm S}+N_{\rm B})} \frac{(N'_{\rm S}+\alpha N_{\rm B})^{N_{\rm OFF}}}{N_{\rm OFF}!} e^{-(N'_{\rm S}+\alpha N_{\rm B})}. \quad (4.8)$$

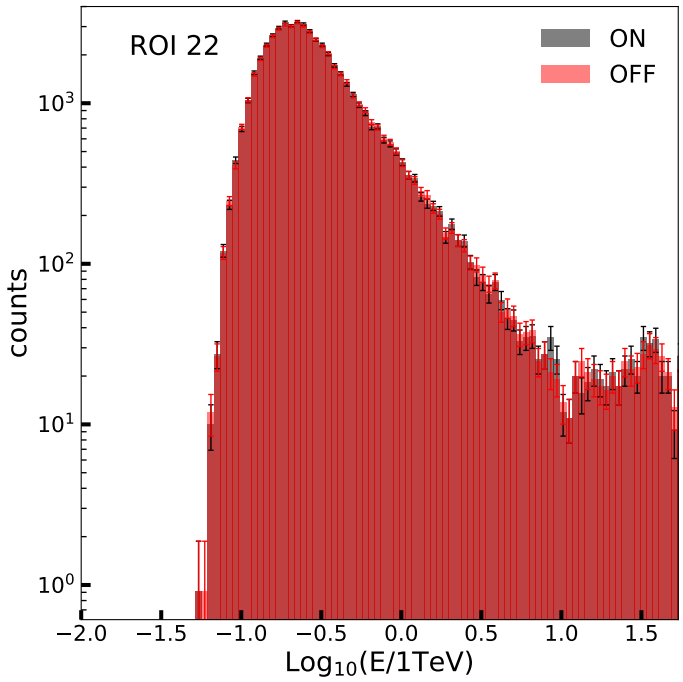

Figure 4.1: Event energy distributions for one of the region of interest (ROI 22) defined for the search of DM annihilation signals in the GC region. The ON and OFF distributions are obtained from 100 Poisson realizations of the OFF measured distribution in order to mimic two independent measurements in absence of signal. The steady number of events above $\sim$ 10 TeV is due to the realizations of populations of events measured by the four small telescopes and reconstructed in the *CT1-4 Stereo* configuration.

In the *full profiling* approach, we can redefine the TS that we have introduced in Sec. 4.2.3. In $TS = -2\ln(\lambda)$, we consider:

$$\lambda(N_{\rm S}) = \frac{\mathcal{L}(N_{\rm S}, \widehat{\widehat{N_{\rm B}(N_{\rm S})}})}{\mathcal{L}(\widehat{N_{\rm S}}, \widehat{\widehat{N_{\rm B}(N_{\rm S})}})}. \tag{4.9}$$

The equation is valid for $0 \leq \widehat{N_{\rm S}} \leq N_{\rm S}$. $\widehat{N_{\rm B}}$ is a non-conditional maximization so it does not depend on $N_{\rm S}$, which is maximized independently. Therefore, we obtain $\widehat{N_{\rm B}} = N_{\rm OFF}/\alpha$ and $\widehat{N_{\rm S}} = N_{\rm ON} - N_{\rm OFF}/\alpha$. When $\widehat{N_{\rm S}} < 0$ (expectation can be negative because fluctuations can produce negative values), the TS needs to be defined as the *hybrid profiling approach*. Instead for $\widehat{N_{\rm S}} > N_{\rm S}$, TS$\equiv$0. $\widehat{\widehat{N_{\rm B}(N_{\rm S})}}$ is obtained from the conditional maximization $\mathrm{d}\mathcal{L}/\mathrm{dN_B} = 0$ and it corresponds to the best estimate of the background for a given signal $N_{\rm S}$.

4.4.2 Significance of the measured excess

The measured events in the ON and OFF regions are compared to search for an excess in the signal region with respect to background. Following Ref. [247], the significance of the excess can be computed as:

$$S = \textit{sign}\ \sqrt{2}\left\{ N_{\rm ON} \ln\left[\frac{1+\alpha}{\alpha}\left(\frac{N_{\rm ON}}{N_{\rm ON}+N_{\rm OFF}}\right)\right] + N_{\rm OFF}\ln\left[(1+\alpha)\left(\frac{N_{\rm OFF}}{N_{\rm ON}+N_{\rm OFF}}\right)\right]\right\}^{1/2} \quad (4.10)$$

where the sign is negative in case $N_{\rm OFF} > N_{\rm ON}$ and negative significance is then computed. To consider an observed excess in gamma-ray astrophysics as significant, S above 5σ has to be obtained.

4.4.3 Computation of observed and expected limits

As was shown in Eq. 3.12, the expected number of events from self-annihilating DM particles depends on the velocity-weighted annihilation cross section $\langle\sigma v\rangle$. We keep as free parameter in the equation $\langle\sigma v\rangle$ and fix the other parameters in the model, like the DM mass $m_{\rm DM}$, the annihilation channel and the J-factor value for the DM distribution. Therefore, by using Eq. 4.8 and the LLRTS procedure we can compute upper limits on $\langle\sigma v\rangle$. This is done for a DM particle of mass $m_{\rm DM}$ that produces an annihilation spectrum dN/dE and for the DM distribution described by the J-factor J.

Upper limits (U.L.) at 95% C.L. are then obtained, as a function of $m_{\rm DM}$, by using the events for the computation of the terms $N_{\rm ON}$, $N_{\rm OFF}$ and $N_{\rm B}$. The 95% C.L. U.L $\langle\sigma v\rangle$ corresponds to TS = 2.71. All the values of $\langle\sigma v\rangle$ for TS larger than 2.71 are excluded at 95% C.L..

We show here results for the derivation of expected upper limits. A refined estimate for expected limits is obtained through the Poisson realizations of the measured background event distributions, as previously explained. The expected distributions are shown in Fig. 4.1.

For each of the realization of ON and OFF distribution, the computation of the 95% C.L. upper limits with the LLRTS procedure is performed. To obtain the mean expected limits, the mean of the distribution of $\langle\sigma v\rangle$ values obtained through the realizations is extracted. The containment bands at 68% and 95% C.L. are obtained by the standard deviation of the same distribution. We show one example of the latter for of the log-values of $\langle\sigma v\rangle$ obtained with the realizations in Fig. 4.3. The mean of the distribution is -25.26, with standard deviation 0.08. Expected limits and containment bands derived with this procedure are shown in Fig. 4.2. The expected limits are shown as the black solid line. The containment bands are shown as the green and yellow shaded areas for the 68% and 95% C.L., respectively.

Expected limits and containment bands can also be computed through an alternative method, the Asimov dataset [147]. This can be used to quickly explore

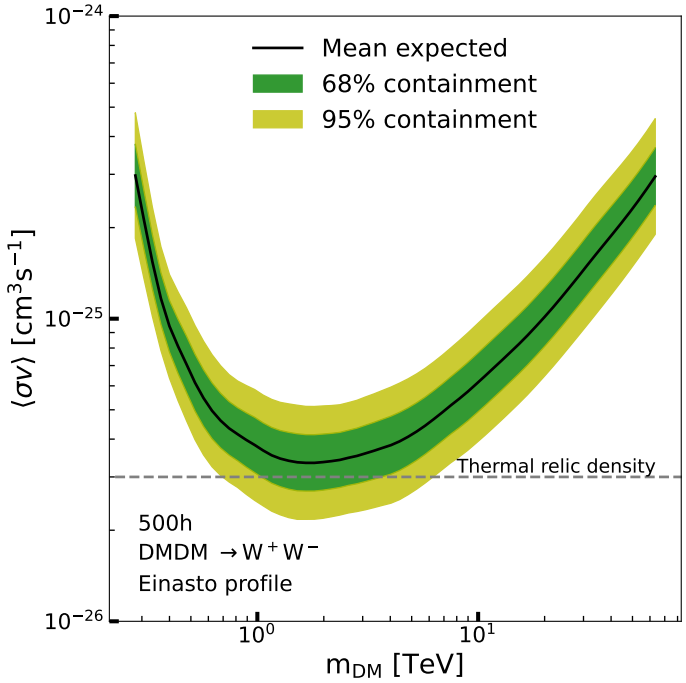

Figure 4.2: Limits on $\langle \sigma v \rangle$ for DM particles annihilating in the W^+W^- channel and for DM distributed in the target as an Einasto profile. H.E.S.S. II like event distributions are obtained as mock dataset from realizations of an observed H.E.S.S. II dataset, with events reconstructed in the *CT1-5 Stereo* configuration. Expected limits (black solid line) are obtained from 100 realizations of the background. 68% and 95% containment bands are shown and are obtained from the standard deviation for distributions like the one shown in Fig. 4.3.

the sensitivity of the experiment to DM in an annihilation channel. The Asimov dataset is an artificial dataset which reproduces the real parameter values when the estimators in the LLRTS are evaluated. Setting the partial derivatives of the Likelihood function, with respect to the parameters, equal to 0 gives the results for the estimators. Data counts in the Asimov dataset correspond to the result of a very-large-statistics Monte Carlo realization and therefore coincide with the mean expectation of the corresponding actual measurements. For this setup, we fix $N_{\mathrm{ON}} = N_{\mathrm{OFF}}$ in Eq. 4.8, corresponding to no excess. For a likelihood function defined by a Poisson function $\mathcal{L}(\lambda|d) = \frac{\lambda^d}{d} exp(-\lambda)$, using the Asimov dataset consists in setting d equal to the mean λ and calculating the limit from this. This avoids making realizations on d, calculating $\overline{\lambda}_{95\%}$ and taking the mean for each one. This consists in computing the TS as $TS = (\Phi^{-1}(0.95) \pm N)^2$, where Φ is the cumulative distribution function of a standard normal distribution, with mean $\mu = 0$ and width $\sigma = 1$. To compute the containment bands, we add N. The usual LLRTS for $TS = 2.71$ is given by $N = 0$, which results in the mean expected limits.

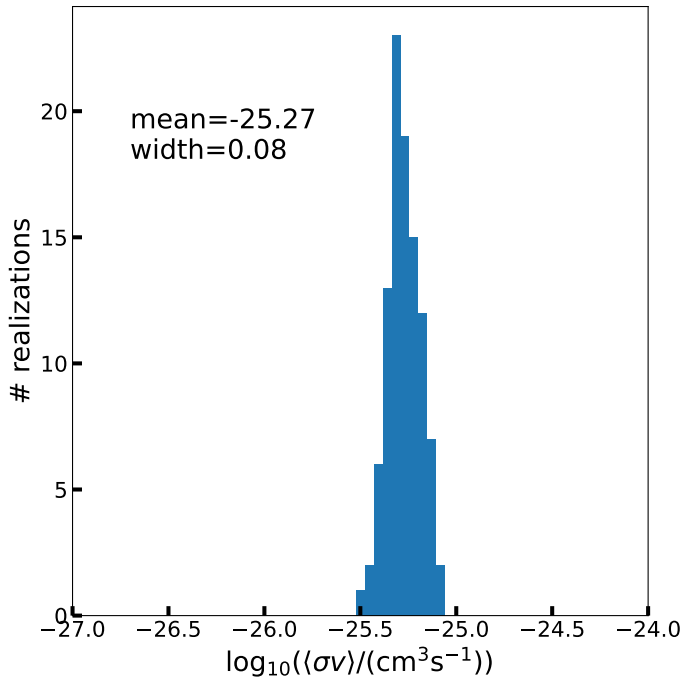

Figure 4.3: Distribution of $\log_{10}\langle\sigma v\rangle$computed with 100 realizations for background and signal count measurements for a DM particle with mass 1 TeV. The mean of the distribution is -25.27 and the standard deviation is 0.08.

A more detailed comparison between the expected limits derivation with the Asimov dataset and realizations of the true measurements is shown later in Sec. 10.3 together with examples.

4.5 Including uncertainties in the limit computation

Several sources of uncertainties can affect the derivation of the limits. For the DM analysis, the GC region is observed for the collection of the dataset. As previously explained, this region is crowded with numerous VHE sources. One strategy is to mask these known emissions and thus avoid leakage of signal in the region of interest of our analysis.

The level of Night Sky Background (NSB) can be subject to significant changes in the inner halo of the Milky Way. However, the shower template method applied for the analysis of the raw data used in this example, as described in Ref. [153], performs a dedicated treatment of the NSB. Therefore, when measuring the background, no further normalization is needed. A more detailed discussion on how the level of NSB can affect the measurements of photons is provided later in Sec. 6.4.1.

The gamma-like rate measured in the FoV depends on the gradient of the

zenith angle of the observations. For each degree of difference in the zenith angle we expect a 1% difference in the gamma-like rate. More detail about this estimation is provided for the analyses shown in this work and is reported later in Sec. 6.4.

A systematic uncertainty may arise when azimuthal symmetry is assumed in the field of view. To test this, the number of counts were computed for a given pointing position in the dataset. More detailed discussion on the test for azimuthal symmetry is provided in Sec. 6.4.3. No significant effect was observed beyond the 1%-per-degree gradient in the FoV. This is an expected effect due to the difference in the zenith angle of the observations. In the next section, we explain how to deal with this effect in more detail.

The raw data analysis in H.E.S.S. can be performed with different analysis chains. This can lead to systematic uncertainties on the energy scale of the reconstructed events. When building the energy count distributions, the systematic uncertainty on the energy scale, derived for our dataset, is 10%. This systematic uncertainty affects similarly the energy scale of the measured and expected energy count distributions, therefore is not included in the computation of the limits.

4.5.1 Residual background uncertainty

For H.E.S.S. observations we expect a 1% gradient of the residual background rate in the FoV per degree of difference between the observation zenith angles for different pointing positions. When we perform measurements in the ON and OFF regions, a difference in the zenith angles of the events measured in the two regions is measured and thus the gradient in the residual background is expected between the two regions. More details on the derivation of the difference of the zenith angle and the gradient on the residual background for some of the work presented in this thesis is shown later in Sec. 8.4. For the example shown in this chapter, the difference in the means of the ON and OFF zenith angle distributions is up to 1°. On a run-by-run basis, the measured OFF is renormalized according to the difference of the zenith angle means of the ON and OFF distributions. Then, there is still the typical width of the zenith angle distributions, which is of 1°. Therefore, a systematic uncertainty of 1% for the normalization of the measured energy count distributions is used. This systematic uncertainty can be accounted for in the likelihood function as a Gaussian nuisance parameter. With this modification, the likelihood function writes as:

$$\mathcal{L}(N_{\rm S}, N_{\rm B}|N_{\rm ON}, N_{\rm OFF}, \alpha) = \frac{[\beta(N_{\rm S}+N_{\rm B})]^{N_{\rm ON}}}{N_{\rm ON}!} e^{-\beta(N_{\rm S}+N_{\rm B})} \frac{[\beta(N'_{\rm S}+N_{\rm B})]^{N_{\rm OFF}}}{N_{\rm OFF}!} e^{-\beta(N'_{\rm S}+N_{\rm B})} e^{-\frac{(1-\beta)^2}{2\sigma_\beta^2}} \,. \quad (4.11)$$

In this, β acts as a normalization factor and σ_β is the width of the Gaussian function (see, for instance, Refs. [336, 244, 285]). β is found by maximizing the likelihood

function such that $\mathrm{d}\mathcal{L}/\mathrm{d}\beta \equiv 0$ and it writes as:

$$\beta(N_{\rm ON}, N_{\rm OFF}, N_{\rm S}, N_{\rm B}) = \frac{-\sigma_\beta^2(N_{\rm S}+N'_{\rm S})+1+\sqrt{(\sigma_\beta^2(N_{\rm S}+N'_{\rm S}+2\widehat{\widehat{N_{\rm B}}})-1)^2+4\sigma_\beta^2(N_{\rm ON}+N_{\rm OFF})}}{2}. \quad (4.12)$$

From this equation, it is clear the dependence of the definition of β on the measured statistics, which enters the expression through $N_{\rm ON}$, $N_{\rm OFF}$ and $\widehat{\widehat{N_{\rm B}}}$. The profile of β as a function of σ_β is shown in Fig. 4.4 for one specific bin of the likelihood function and for a fixed DM mass of $m_{\rm DM}$ = 1 TeV. The value of σ_β=0.01, corresponding to the 1% systematic uncertainty level is highlighted. The TS profile computed with the inclusion of the gaussian nuisance parameter for the systematic uncertainty is shown in Fig. 4.5 and compared to the TS profile computed for the standard definition of the likelihood. We show the TS profile obtained including σ_β=0.03 too. When the σ_β=0.01 is included in the computation of the TS, the obtained 95% C.L. upper limit on the free parameter is 20% less constraining. For σ_β=0.03, the upper limit is 50% less constraining.

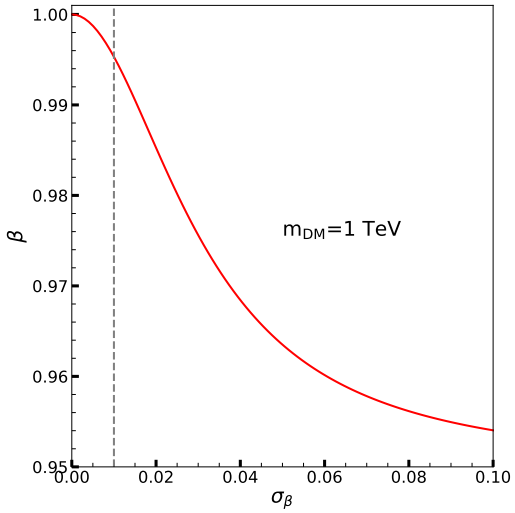

Figure 4.4: Profile of the β parameter as a function of σ_β in a specific bin of the likelihood function and for $m_{\rm DM}$ = 1 TeV. The gray dashed line highlights the value corresponding to σ_β=0.01.

4.5.2 Nuisance parameter for the J-factor statistical uncertainty

The J-factors obtained with measurements are affected by statistical and systematic uncertainties. The statistical uncertainty in the derivation of the DM distribution in the GC region can be accounted for through a nuisance parameter in the likelihood by factorizing in either Eq. 4.11 or Eq. 4.8 a nuisance parameter following a log-normal distribution. The mean value of the log-normal distribution is $\bar{J}$

and the width is σ_J (see, for instance, Refs. [14, 12]). This log-normal distributions writes as:

$$\mathcal{L}^J(J|\bar{J},\sigma_J) = \frac{1}{\sqrt{2\pi}\,\log(10)\,\sigma_J\,J}\exp\left(-\frac{(\log_{10}\mathrm{J}-\overline{\log_{10}\mathrm{J}})^2}{2\sigma_J^2}\right). \tag{4.13}$$

The measured J-factor is one Gaussian realization that follows the $\mathcal{L}^J$ distribution. We obtain the best value of J by computing the maximization of $\mathcal{L}^J$. Expected value is obtained through $\hat{J} = \bar{J}e^{-\sigma_J^2 log^2(10)}$. Then, $\hat{J}$ can be derived and used to renormalize the number of expected events from DM as $N^S \rightarrow N^S\hat{J}/\bar{J}$. The TS profile computed with the inclusion of the statistical uncertainty on the J-factor is shown in Fig. 4.5 and compared to the TS profile computed for the standard definition of the likelihood. The 95% C.L. upper limit on the free parameter is a factor 2.8 less constraining when the statistical uncertainty on the J-factor is included in the computation of the TS.

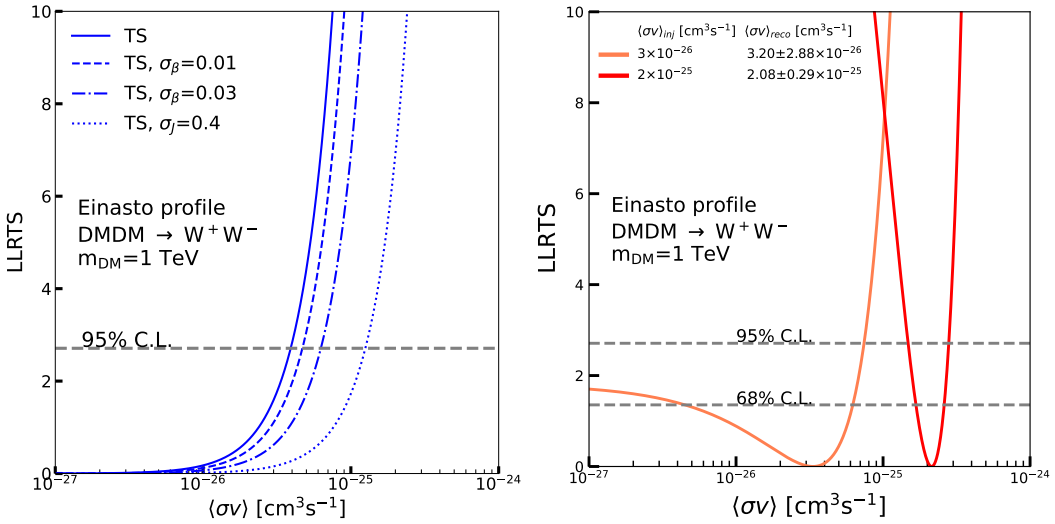

Figure 4.5: TS profiles for a fixed DM mass, annihilation channel and DM density profile. *Left panel:* the standard computation (blue solid line) is compared to the one with inclusion of the residual background uncertainty for $\sigma_\beta = 0.01$ (dashed line), for $\sigma_\beta = 0.03$ (dotted-dashed line) and the one with the statistical uncertainty on the J-factor $\sigma_\mathrm{J} = 0.4$ (dotted line). *Right panel:* TS profiles for the reconstruction of injected values of $\langle\sigma v\rangle_\mathrm{inj}$. 95% C.L. and 68% C.L. are shown for comparison with the depth of the TS profiles. Reconstructions at 68% C.L. (orange line) and more than 5 σ (red line) are shown and the reconstructed value together with the 68% containment bands are given in the legend.

4.6 Reconstruction performance on injected values of the free parameter

We inject a fake DM signal, for a given mass and a chosen value of $\langle\sigma v\rangle_{\rm inj}$. This is done in the measured OFF distributions which are assumed to be devoid of signal from DM. In this way, starting from the measured OFF and injecting $N_{\rm S}$ and $N'_{\rm S}$ we create ON and OFF distributions, respectively. This is done in order to assess the capability of our framework to recover the injected signal. We test values of $\langle\sigma v\rangle$ from 3×10^{-26} and 2×10^{-25} cm^{3}s^{-1}, for a DM mass of 1 TeV and particles annihilating in W^+W^-. We assume the DM is distributed according to the Einasto profile. The TS procedure is carried out for each injected value $\langle\sigma v\rangle_{\rm inj}$ and the reconstructed annihilation cross section $\langle\sigma v\rangle_{\rm reco}$ is computed. The resulting TS profiles are shown in the right panel of 4.5. The values of $\langle\sigma v\rangle_{\rm reco}$ and the 1 σ bands are given in the legend. For the injection of 2×10^{-25} cm^{3}s^{-1}, the signal is recovered at a 5 σ level whereas, for 3×10^{-26} cm^{3}s^{-1}, only the 68% containment bands are recovered.

4.7 Outlook for Test-Statistics-based approaches

Searching for a weak signal against background emission is usually performed with techniques as the ones described in the previous sections. In Part III of this work, we apply the log-likelihood ratio test-statistics to search for DM signals in the GC region with an H.E.S.S. II dataset in Chap. 8 and towards DM subhalo candidates observed with H.E.S.S. in Chap. 9. The same approach is also applied to characterize the TeV emission of the low-latitude Fermi Bubbles, in Chap. 7. We have shown in this chapter:

- statistical analyses with the LLRTS framework that can be used to obtain new upper limits on the free parameters of the models used to describe the searched emissions;
- how to build mock datasets;
- methods for the computation of observed and expected upper limits;
- methods for the reconstruction of an injected fake signal;
- how to implement the systematic uncertainties in the analyses.

All these points will be applied in the analyses presented in this work. In what follows, we will present an alternative and novel approach to disentangle signal and background emissions based on neural network based methods.

4.8 Neural-Network-based methods

Alternative methods to the application of the TS procedure are machine-learning-based ones such as neural networks (NNs). These are used as predictive models to search for weak emissions in background dominated regions relaxing the a-priori assumptions on the knowledge of the background emission.

4.8.1 Neural networks for signal-background separation

In several domains, NNs have been successfully applied. Recent applications in VHE astrophysics have also produced important results [108, 249]. NNs can be used for predictions on target samples, however one fundamental weakness is the inability of the traditional neural networks to quantify the prediction uncertainty. Evaluating the latter is important in many domains, ranging from basic research, reinforcement learning and anomaly detection. The quantification of uncertainty has been addressed by both frequentist and Bayesian approaches (see for instance [303] and [228]). A natural proposition following the Bayesian approach was to promote the weights of neural layers to random variables distributed as Gaussians [258]. Then, it was demonstrated that the learnt weights uncertainty improves generalization in non-linear regression problems, and can be used for exploration-exploitation trade-off in reinforcement learning [96]. The uncertainty was then also separated into two components: epistemic and aleatoric contributions (see Ref.[154]). The uncertainty on the model is encoded in the epistemic component, which would not be reduced if additional observations were included. Instead the noise due to the training of a specific sample is embedded in the aleatoric uncertainty. In physics, the two uncertainties are known as the systematic and statistical ones.

Probabilistic neural networks are known as graphical models and are derived by the treatment and inclusion of both uncertainties in the same framework. Graphical models are therefore built on the Bayesian approach and allow for incorporation of prior beliefs with respect to the model. Their flexibility permits the treatment of various processes and allows for introduction of latent degrees of freedom.

In this part of the chapter, we use Bayesian Neural Networks (BNN) as building blocks in graphical models for Gaussian random fields as the distributions from which the weights of the layers are sampled. We then demonstrate the power of synthesis of Probabilistic Graphical Models (PGM) and BNNs on a synthetic example of signal/background disaggregation. To demonstrate the approach, we test an additive mixture model: we superimpose signal and background spectra with proportions varying in space. Through the inference we can learn the proportions of the signal and background and their spectral shapes.

4.8.2 Bayesian Neural Network structure

The framework that we consider is a deep neural network composed by dense layers. One of the latter consists of an affine transformation L^k with weight $\mathcal{W}^k$ and bias $\mathcal{B}^k$, composed with an element-wise non-linear transformation σ: $h^k = L^k \circ h^{k-1} = \sigma(h^{k-1}\mathcal{W}^k + \mathcal{B}^k)$, the so-called activation function. In our experiments we set σ to be $ReLU$, defined as $ReLU(x) = \max(0, \mathrm{x})$ [28]. The examples in this part of the chapter are computed with the application of a simple deep architecture which is defined as a consecutive application (composition) by dense layers: $y = L_K \circ \cdots L_1 \circ x$, as presented in Fig. 4.6. The vector x represents the coordinates on which the transformations are applied. The vector y represents the output of the NN after all the transformations. Therefore the NN is used to map the input to an output sampled through probabilistic models.

The probabilistic interpretation of inference with neural networks is allowed by the promotion of weights and bias of each layer to random variables sampled from Normal distributions with corresponding parameters: $\mathcal{W}^k \sim N(\mu_{\mathcal{W}}, \Sigma_{\mathcal{W}})$, $\mathcal{B}^k \sim N(\mu_{\mathcal{B}}, \Sigma_{\mathcal{B}})$. We show in Fig. 4.7 an elementary Bayesian Neural Network as a graphical model representation. The BNN is composed of K layers and takes as input x composed of N samples, rendering y as output. In each layer the transformation h is performed.

The simple BNN that we are considering follows Ref. [96], where the stochastic variational inference (SVI) [206, 366] is used to obtain Gaussian posterior distributions starting from prior distributions of weights, biases and observations. The inference process is performed through the update of the loss function. The natural choice for the latter is the Evidence Lower Bound (ELBO) [271], composed by two terms: log evidence of the observable variable x with learnable parameters θ, $\log p_\theta(x)$, and the Kullback-Leibler (KL) divergence between the approximation of the posterior distribution $q_\phi(z)$, parameterized by ϕ, and the true posterior $p_\theta(z|x)$. ELBO writes as:

$$ELBO = \log p_\theta(x) - \mathrm{KL}\left(q_\phi(z)||p_\theta(z|x)\right). \tag{4.14}$$

Taking steps in ϕ produces the update of the ELBO during the inference process. These steps increase the ELBO, by the increasing of the log evidence and decreasing of the distance between the prior and the posterior. Inference results depend on the choice of the hyperparameters. These are the optimizer, the learning rate and the number of iterations. The inference is performed with the comparison of the output vector of NN y and the real observed values. The best values for the learned parameters are determined through the minimization of the loss function: this is done with the optimizer and a widely used choice for the latter is the Clipped Adaptive Moment Estimation (ADAM) [233]. The acronym ADAM is derived from adaptive moment estimation. The learning rate is the parameter used to tune the inference process; it specifies the step size at each iteration while the model searches for the minimum of the loss function. The number of iterations

determines how many times the full architecture performs the combination of operations given by all the layers. More details on the hyperparameters used for our experiments are given later.

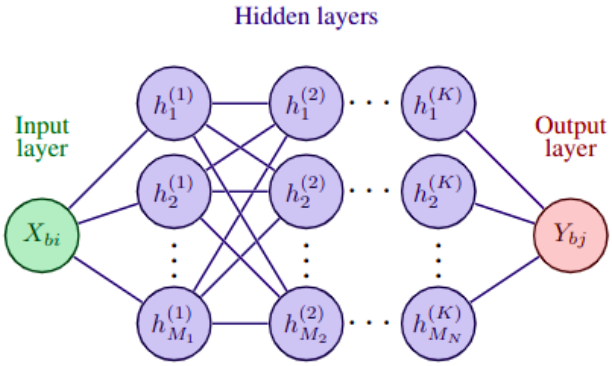

Figure 4.6: Sketch of a neural network composed of K dense layers. Input X_{bi} is a 2-dimensional array, where b is the batch index (runs over samples) and i runs over the input dimension. Output Y_{bj} is a 2-dimensional array where b is the batch index (runs over samples) and j runs over the output dimension. M_k is the dimension of kth hidden layer.

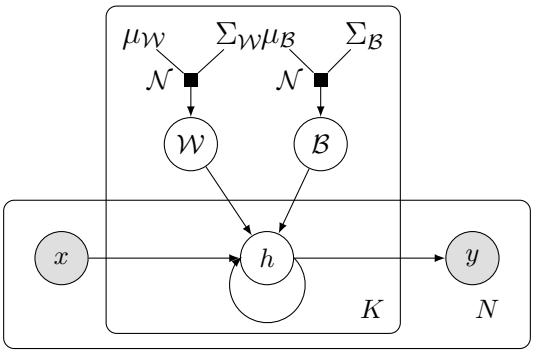

Figure 4.7: Representation of an elementary BNN as a graphical model. The observable variables (input x and output y) are given as shaded circles, the latent variables ($\mathcal{W}$, $\mathcal{B}$ and h) are shown as empty circles and the hyper-parameters ($\mu_{\mathcal{W}}$, $\sigma_{\mathcal{W}}$, $\mu_{\mathcal{B}}$ and $\Sigma_{\mathcal{B}}$) are represented by the standalone letters. The dependence between the starting and terminal vertices are given by directed arrows, the sampling from a normal distribution $\mathcal{N}$ is given by the black squares. The K BNN layers are represented by the internal plate of dimension K and the size of the data sample is given by the plate of dimension N.

4.8.3 Transformed Bayesian Neural Networks

Through the combinations of various types of distributions, we can derive non-trivial setups for the probabilistic models. We consider a Gaussian mixture model with K components. Each component is normally distributed. The mean of the Normal distribution is parameterized by real-valued parameters while the scale is taken only as positive. The overall proportions of the components in the mixture are sampled from a Dirichlet distribution $X_{\mathrm{k}} \sim Dir(\alpha)$. The latter is parameterized by a positive vector $\alpha_1, \dots \alpha_K > 0$, and X_k belong to a $K-1$ simplex: $\sum X_{\mathrm{k}} = 1$.

Therefore the transformed BNNs are adopted as defined over various ranges. For the tests in these sections we consider exponential transformations (transforms unconstrained vector of K dimensions to a positive vector of K dimensions) and stick-breaking transformations (unconstrained vector of $K-1$ dimensions into a simplex vector of K dimensions) Conceptually, the stick-breaking process consists of repeatedly breaking off and rejecting a random fraction of a "stick" with initial length 1 [300].

The transformation is applied after the last layer of the BNN, in a way that the output of the exponential transform is strictly positive and the output of the stick breaking transform produces a k-dimensional vector summing to unity (k-simplex).

In what follows, we consider the vector sampled from Bayesian neural networks as $y \sim BNN(x, (\mathcal{W}, \mathcal{B}))$. Outputs of BNN transformed as exponential and stick-breaking are denoted as BNN_{e} and BNN_{s}, respectively.

An additional transformation that may be considered is a positive normalization. For some applications it is useful to work with normalized positive random fields instead of only positive random fields. This transformation computed an approximate normalization of the BNN output give the data.

4.9 Additive Mixture

We have introduced the architectures composed by single dense unit BNN. We now turn to the implementation of a non-trivial test of the framework by creating a generative additive mixture model. Within this framework, we consider two types of coordinates: the spatial x and the spectral p coordinates. Two positive spectral functions describing the background and signal emission are considered as $g_1(p)$ and $g_2(p)$. They are mixed in the spatial coordinates by a simplex-valued $\beta(x)$. We suppose that only the sum can be observed through $f(x, p)$:

$$f(x, p) = \beta(x) g_1(p) + (1 - \beta(x)) g_2(p). \tag{4.15}$$

The problem is built such that the spectrum of signal $g_2(p)$ has to be identified in the presence of non-trivial noise $g_1(p)$. We assume that the spectral components

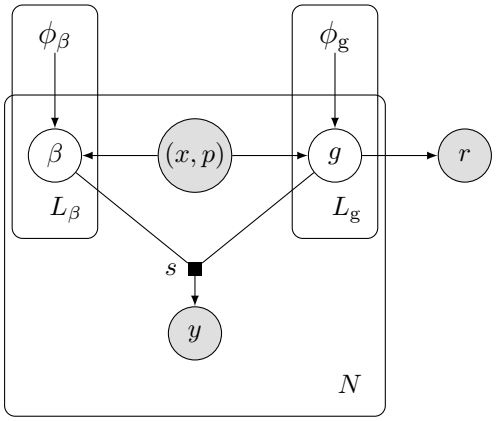

Figure 4.8: Additive mixture model rendered as a graphical model. Observable variables (input (x, p), outputs y and relative entropy r) are represented by shaded circles represent, latent variables associated with BNNs β and g are represented by empty circles, hyper-parameters of BNNs (ϕ_β, ϕ_g) are represented by standalone letters. The dependence between the starting and terminal vertices are represented by directed arrows. The convolution given by the black square s can be applied to Eq. 4.15. The conditional independence of the data sample is given by the internal plate of dimension N. Conditional independence of parameter sampling of β and g BNNs is given by the plates L_β and L_γ.

$g_l(p)$ are normalized: $\int dp g_l(p) = 1$. Then, the total sum is $f(x) = \int dp\, f(x,p)$ equal to 1 for each x.

The spectral components $g_l(p)$ assume positive-only values and we model them by an exponentially transformed BNN_e. The spatial proportion $\beta(x)$ is modeled by a Dirichlet random field $\beta(x) \sim Dir(\alpha_l(x))$, where $\alpha_l(x) = N\gamma_l(x)$ and $\gamma \sim BNN_\mathrm{s}(x)$ (stick-breaking transformed BNN).

Degeneracy in the components can arise due to the permutation symmetry: $g_1 \leftrightarrow g_2$ and $\beta \leftrightarrow 1-\beta$. We therefore set the initial value of γ_l to have an asymmetric proportion e.g $(0.99, 0.01)$, with the first component being the background and the second - the signal. We introduce another observable to avoid the inference engine from splitting the observed signal uniformly between the two components. The former is the relative entropy between the spectral components $g_1(p)$ and $g_2(p)$:

$$D_\mathrm{KL}(g_2(p) \parallel g_1(p)) = \int g_2(p) \ln(g_2(p)/g_1(p)).$$

This is set to a large number, $e.g.$, 100.

The first observed term forces the approximation of y_i by the combination of $g_l(p)$ and $\beta(x)$. The relative entropy forces the model to approximate maximally different $g_1(p)$ and $g_2(p)$, because $D_\mathrm{KL}(g_2(p) \parallel g_1(p))$ is a proxy to distance in function space.

The goal of the inference is to obtain the best possible spatial and spectral description of the mixture through the identification of the optimal model parameters ϕ_β and ϕ_g, $i.e.$, the shapes of $g_l(p)$ and the mixing proportion $\beta(x)$. The current formulation of the model does not include Bayesian treatment of the aleatoric uncertainty and observations are sampled using a small fixed variance (0.002). The additive mixture model is shown by graphical representation in Fig. 4.8.

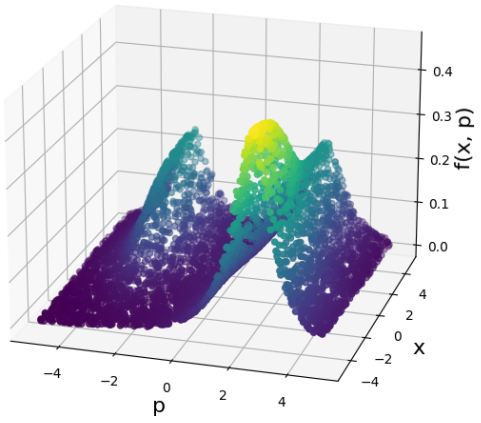

Figure 4.9: Dataset of 5000 data points generated from the mixture $f(x, p)$. The total signal is dominated by the background emission $g_1(p)$ at negative x coordinates. Positive values of x correspond to the superposition of signal and background.

4.10 Synthetic Experiments

The derivation of the BNNs and the experiments were implemented in Pyro (version 1.5.2) [88], a probabilistic programming language written in Python and based on *pytorch* [302], which enables Bayesian probabilistic modeling thanks to Monte Carlo and variational inference engines.

The experiments are performed with the optimizer fixed to the Clipped Adaptive Moment Estimation (ADAM) [233] and, unless mentioned otherwise, set the learning rate to 10^{-2}, the clipping norm to 10, and default values for the coefficients used for computing running averages of gradient and its square: (0.9, 0.999). More details on how these parameters influence the (ADAM) optimizer are provided in Ref. [233]. The BNN architecture in what follows consists of 3 hidden layers of fully connected neurons for the dimensions of $32 \times 128 \times 32$.

The dataset used for the experiment is generated from Eq. 4.15 and it is shown in Fig. 4.9.

4.10.1 Inference algorithm

The inference process to compute the ELBO loss and complete steps in the space of *guide* parameters ϕ is performed with the Pyro's stochastic variational inference (SVI) abstraction which moves along the gradients of loss function and infers the best parameters of the model ϕ_β and ϕ_g. The *guide* function corresponds to the approximation of the posterior distribution $q_\phi(z)$ shown in Eq. 4.14.

The procedure is considerable as a Bayesian update: it search for the variational parameters ϕ of the approximation of the true posterior $q_\phi(z)$. The optimization method and the parameters of the model are fixed to what was specified in the previous section.

At each epoch, the ELBO loss is computed as well as the relative values of the loss with respect to the previous iterations. Under two conditions, the former are compared for a chosen window. We apply an empiric improvement to the inference procedure. This happens when we restart it with a lower value of the learning rate (which is decreased to the half in our case) while keeping current *guide* parameters. Two cases cause the stop and restart of the inference: (i) the loss for the last S_p steps increased or (ii) the relative loss for the last S_r steps was below a certain threshold. Both thresholds S_p and S_r are fixed to 3 in the current project. We found that setting the threshold to 3 was providing the most stable inference for the model. In condition (i), the inference engine is diverging from the optimal region for sampling in the parameter space due to the stochastic nature of the sampling. This provokes the diverging of the loss function. This procedure is repeated until the inference reaches the fixed number of iterations.

4.10.2 Training of a simple individual Bayesian Neural Networks

We introduced in Sec. 4.8.3 and Sec. 4.8.2 the individual and transformed BNNs. With these either functions can be approximated or more complex models can be built. If they are components of more complex models, it can be useful to impose certain priors on their functional form, $e.g.$, we might assume some prior knowledge on the mixture composition, which cannot be observed directly. This means that latent components can be pre-trained in a way that their priors condition the output to have a desired shape. If the prior and the *guide* are built with the same functional form, this procedure resembles a Bayesian update. Then, the pre-trained *guide* parameters can improve the convergence of a more complex model when the unit BNN which priors have been pre-trained is part of the model.

For this procedure, we follow three steps: (i) a data sample mimicking the desired shape is created, (ii) a unit BNN is fitted to the generated data sample with non-informative priors; this results in pre-trained *guide* parameters, (iii) the inferred *guide* parameters are used as prior parameters and (optionally) as the parameters of the initial setup of the *guide* when part of a more complex model. In

the second step, the BNN is sampled to create outputs to match the observations. At this stage, we are not interested in the aleatoric component and we then represent it as a constant. We then use normal, log-normal and Dirichlet distributions for sampling.

Taking the example for the inference of a unit BNN that is learning the spectral shape of $g^{\star}(p) \sim e^{\frac{1}{1+p^2}} - 1$, shifted by $b = -2.5$ (and normalized to 1). The fit of this positive function is performed with an exponentially transformed BNN_{e}, because of the shape of the expected spectrum. The latter is sampled with a log-normal distribution after the last layer by convention.

The inferred distribution for the posterior of a unit BNN after the inference is shown in the upper left panel of Fig. 4.10. The loss function is shown in the upper right. Spikes are visible in the evolution of the loss function versus the epochs. These are due to the two cases that provoked the stop and restart of the inference. The cases were explained in Sec. 4.10.1. When these cases occur, our model adjusts the learning rate and proceeds in the inference. The location and scale parameters, μ and Σ respectively, for the last hidden layer and the weights component $\mathcal{W}$, are shown in the bottom panels of the same figure, as a function of the epoch.

4.10.3 Synthetic Additive Mixture

The goal is to identify two superimposed positive spectral functions and their proportions as a function of coordinates using the inference to learn the components of the additive mixture model when a minimum amount of information is provided. Our method for the additive mixture model is tested with a synthetic dataset defined by triples $\mathcal{D} = \{(x_i, p_i, f_i)\}_{i=1}^{N}$, $x_i \in \mathcal{R}$, $p_i \in \mathcal{R}$. The coordinates x_i and p_i are sampled randomly on $[-5, 5]$ and we refer to this implementation of the dataset as the Signal/Background (SB) model. The values of the function $f(x_i, p_i)$ are obtained by the generative model in Sec. 4.9 with deterministic spectral components $g_l(p)$ and proportions $\beta(x)$. In what follows we identify the background as $g_1(p)$ and the signal as $g_2(p)$. We consider (i) case A where non-informative priors are used, and (ii) case B where only $g_1(p)$ is conditioned, *i.e.* the pretraining is performed on the correspondent BNN resulting on conditioned ($\mathcal{W}$, $\mathcal{B}$) before the inference on the additive mixture. For both of them we use a previously introduced template $g^*(p)$ (normalized to 1), which we shifted by $b = 2.5$ in two directions:

$$g_1(p) = g^*(p - b) \qquad g_2(p) = g^*(p + b) \tag{4.16}$$

The first tentative is to demonstrate that the inference works for a specific choice of $\beta(x)$. We define the latter as a logistic function that equals 0.99 at $-\infty$ and 0.5 at $+\infty$. Then, our approach is tested by varying the dataset proportions, *i.e.* smaller proportions of the signal are tested. The components $\beta(x)$ and $g_l(p)$ are obtained

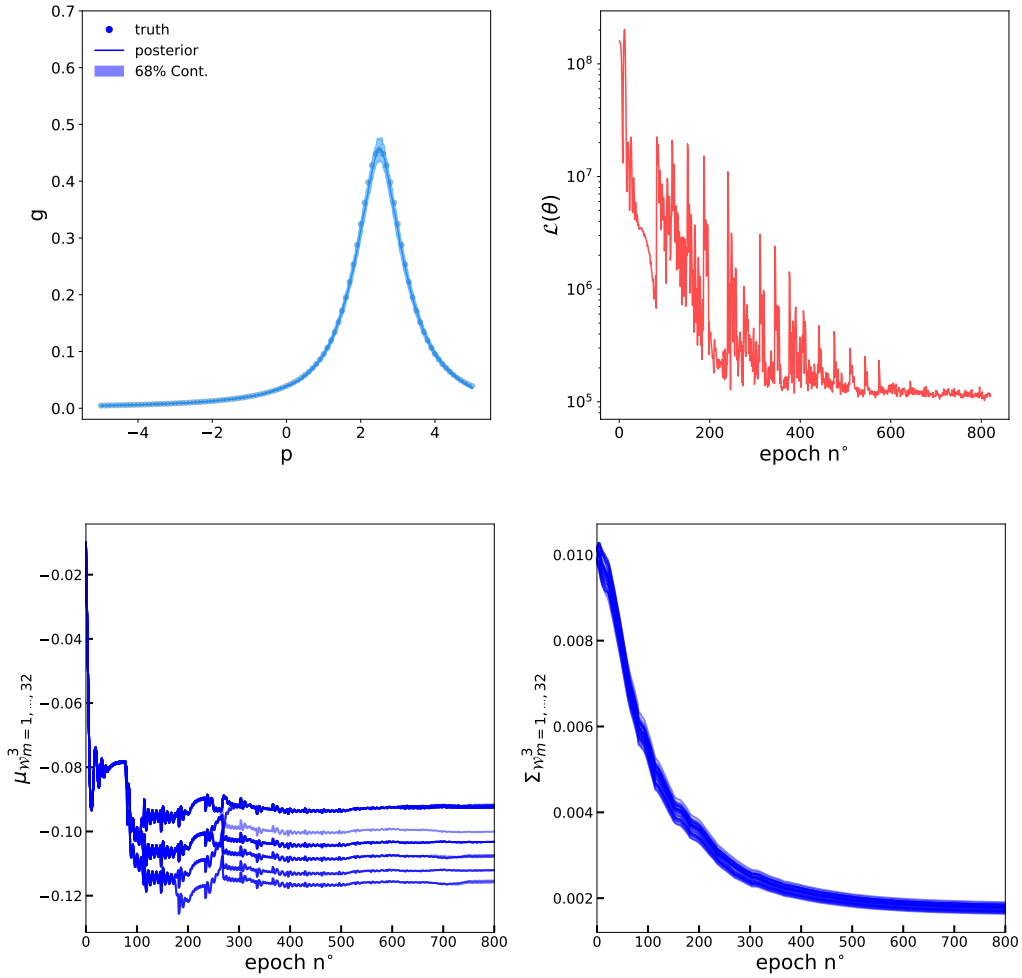

Figure 4.10: *Left-top panel:* Predicted posterior values for a unit BNN_{e} compared with the true ones. The mean posteriors is the solid line, the 68% containment bands are shown as the shaded area. Solid circles represent sampled true values. *Right-top panel:* ELBO loss function as a function of training epoch for a unit BNN. *Left-bottom panel:* Location hyperparameters of the weight distribution $\mathcal{W}$ during the inference for the 32 neurons of the last hidden layer of a unit BNN as a function of training epoch n. Their values are initialized to zeros in the beginning of SB inference. *Right-bottom panel:* Scale hyperparameters of the weight distribution $\mathcal{W}$ during the inference for the 32 neurons of the last hidden layer of a unit BNN as a function of training epoch n. Their values are initialized to 0.1 in the beginning of SB inference.

by the transformations shown in Sec. 4.9. The stick-breaking and the exponential transforms are used. Then, the transformed BNNs are hereafter referred to as

BNN_β and BNN_g, respectively. The output of both BNNs is always of dimension 2, since we obtain an output for each component. The prior distributions for ($\mathcal{W}$, $\mathcal{B}$) of each hidden layer of BNN_β and BNN_g are sampled from $\sim N(0, 0.1)$ at the beginning of the inference. The latter is performed for 700 epochs in both cases, until the model reaches convergence.

We show in the left panel of Fig. 4.11 the evolution of the location parameters of the $\mathcal{W}$ for the last hidden layer of BNN_β as a function of the epoch number. The middle panel of the same figure shows the evolution of the scale parameters. The ELBO loss function vs training epochs is shown in the right panel of the same figure. The top panel shows case A, while case B is shown in the bottom ones. For case A, the parameters converge to their final values after 500 epochs.

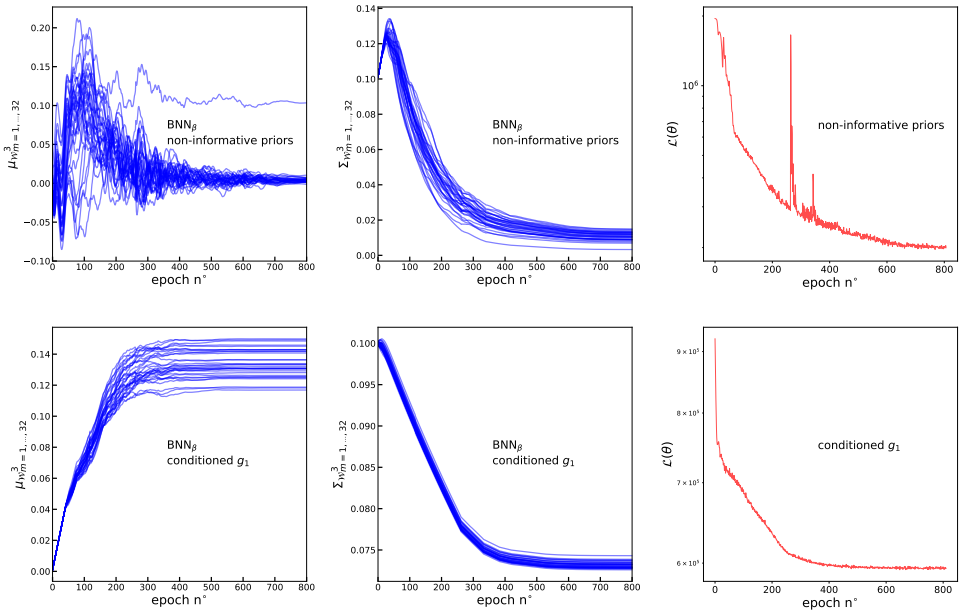

Figure 4.11: *Left panel:* Location hyperparameters of the weight distribution $\mathcal{W}$ for 32 neurons of the last hidden layer of BNN_β as a function of training epoch after the model is learnt over the additive mixture. The location parameters of $\mathcal{W}$ are initialized to zeros in the beginning of SB inference. *Middle panel:* Scale hyperparameters of the weight distribution $\mathcal{W}$ for 32 neurons of the last hidden layer of BNN_β as a function of training epoch. Scales are initialized to 0.1 in the beginning of SB inference. *Right panel:* ELBO loss function as a function of training epoch. For left, center and right panels top figures are given for the case non-informative prior (top) and the case of the prior, pre-trained on the background spectral shape $g_1(p)$ (bottom).

4.11 Results

We show here the results obtained for the inference on the SB model with $\beta(x)$ set to vary continuously from $\beta^T|_{x=-5} = 0.99$ in the background-dominated spatial region to $\beta^T|_{x=5} = 0.7$ in the region where background and signal are mixed. We show results for both cases A and B previously mentioned.

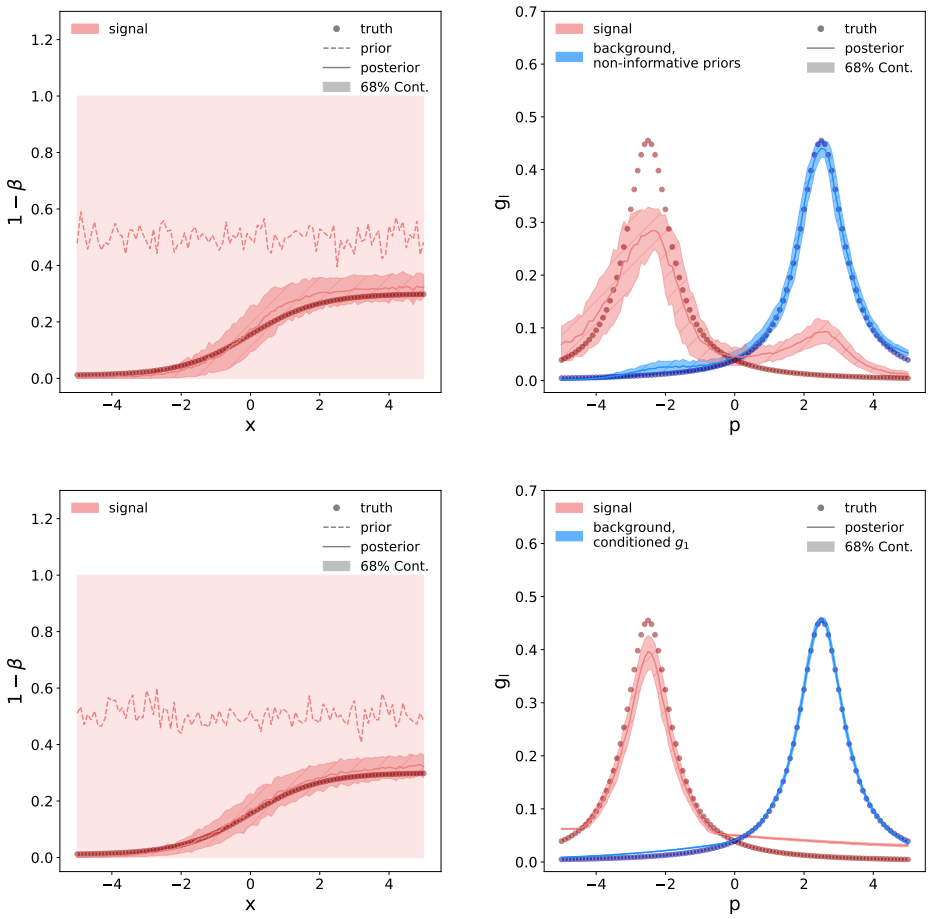

Figure 4.12: In the left panel the mixing proportion is shown from prediction of the posterior distribution compared to true values, along with 68% containment bands (shaded area), assuming true values of $\beta^T|_{x=5}$ = 0.7. The same is shown for the spectral functions $g_l(p)$ in the right panel for signal (red) and background (blue). The sampled true values are given by the solid circles in all the subplots. Predictions from prior distributions are represented by their means (dashed line) and 68% containment bands (light shaded area).

The posterior distributions obtained after the inference of 1-$\beta(x)$ and $g_l(p)$ are shown in Fig. 4.12 for case A and B in the upper and lower panels, respectively.

In both cases, the true values of 1-$\beta(x)$ are well recovered within the 68% containment bands of the model for both cases. The relative errors between the true signal fractions at $x = 5$, *i.e.* 1-$\beta^T|_{x=5}$, and the mean fractions recovered by the model are lower than 9% and 8% for case A and B, respectively. In case B, the true values of g_2 are recovered in the 95% containment bands at the peak location. However, in case A the true values of g_2 are not recovered in the 95% containment bands.

The so-called y-y plots for values recovered by the model vs true values are shown in Fig. 4.13 for case A and B in the top and bottom panels, respectively, and for the fractions 1-β and the spectral shapes g_l in the left and right panels, respectively. Uncertainty is shown as 68% containment bands. Both cases show the recovery of the true values by the model 68% containment bands. Biases from 1% to 5% are obtained for the model signal fractions in case A. For the spectral shape g_2, the bias reaches 16% when considering g_2^T values larger than 0.1. g_2^T is the true spectral shape of the signal. For smaller values, the true spectral shape is not recovered. Biases from 1% to 10% are obtained for the model signal fractions in case A. For the spectral shape g_2, the bias reaches 39% when considering g_2^T values larger than 0.1.

We run a series of experiments with several values of $\rho = \frac{\beta^T(x=5)}{(1-\beta^T(x=5))}$ in the ground truth data. This means that the ground truth background fraction value at the right boundary changes as the noise-to-signal ratio, since the spatial proportions of the background at $x = 5$ are given by $\beta^T(x = 5)$. Random seeds are used for every different experiment. In Fig. 4.14, we show the root mean square deviation (RMSD) computed between the prediction [of the corresponding constituent BNN] after the SB inference and the true value of 1-β and g_l, respectively, as a function of ρ. The RMSD is obtained as the square root of the second moment of the differences between predicted and true values in each bin. The RMSD for the background spectral shape g_1 over the whole range of ρ is small. With larger ρ, the error in identification of g_2 and 1-β increases, potentially due to the fact that the inference procedure is no longer able to distinguish a small signal from the fixed aleatoric noise.

4.12 Outlook for Neural-Networks-based approaches

In this second part of the chapter, we showed how to build a framework based on BNNs and demonstrated how it can be used to recover a weak signal in the presence of a non-trivial background. This framework is composed by BNNs as random fields, such as point distributions are composed to generate graphical models. The astrophysical motivation for this model is to learn an unknown signal in the presence of a potentially unknown background, which can be detected at various wavelengths. This problem has been recently treated by parametric statistical

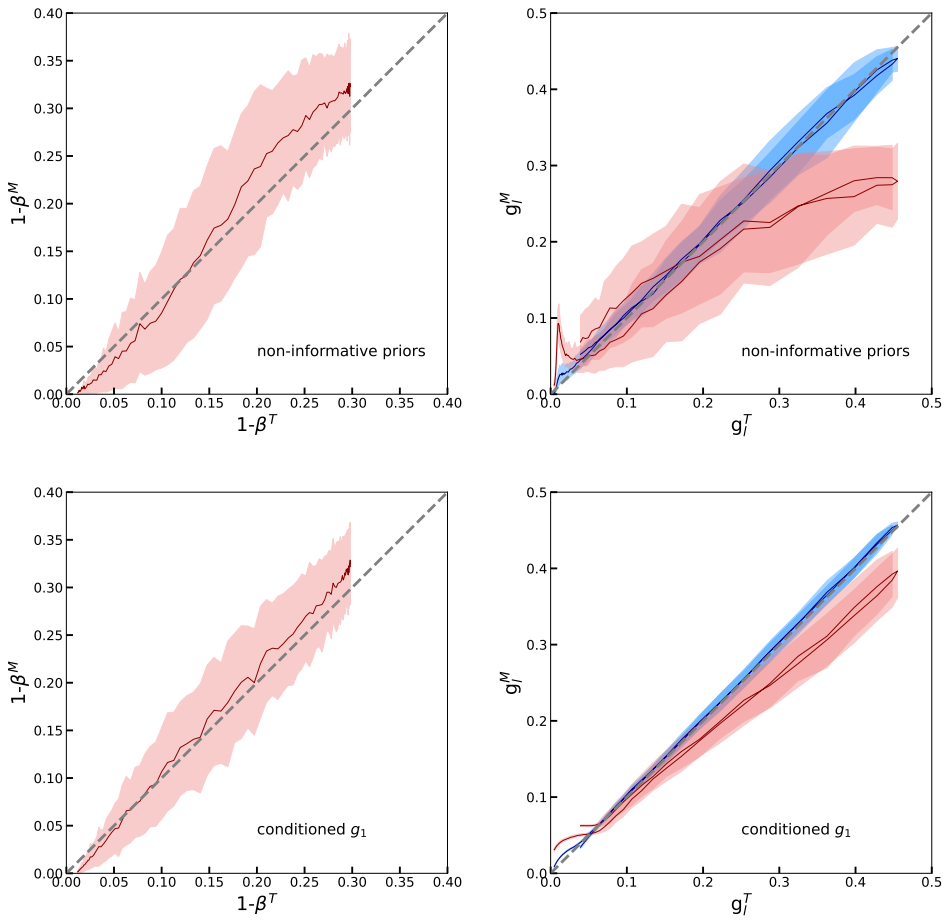

Figure 4.13: Model versus True shapes for the proportion $1-\beta$ (left panels) and spectral shapes g_l for background (blue) and signal (red) (right panels) obtained from the S-B inference. The model mean is shown as a solid line and the error bands correspond to 68% uncertainty of the model predictions. The shapes are given for the case with no prior (top panels referred as to non-informative priors) and with prior set on the background spectral shape $g_1(p)$ (bottom panels referred as to conditioned g_1). *Left panels:* Model proportion $1-\beta^M$ vs the true proportion $1-\beta^T$ together with 68% model uncertainty, respectively. *Right panels:* Model spectral shapes g_l^M vs true spectral shapes g_l^T shown together with their 68% uncertainty.

approaches and using Bayesian statistics for instance in Refs. [13, 11, 14, 10] which we also presented in the first part of this chapter. With our demonstration of the power of neural networks, we lift the problem to a new level of non-parametric inference with respect to the spectral shapes. Our approach is also Bayesian since it incorporates available extra information and can aggregate spectral information

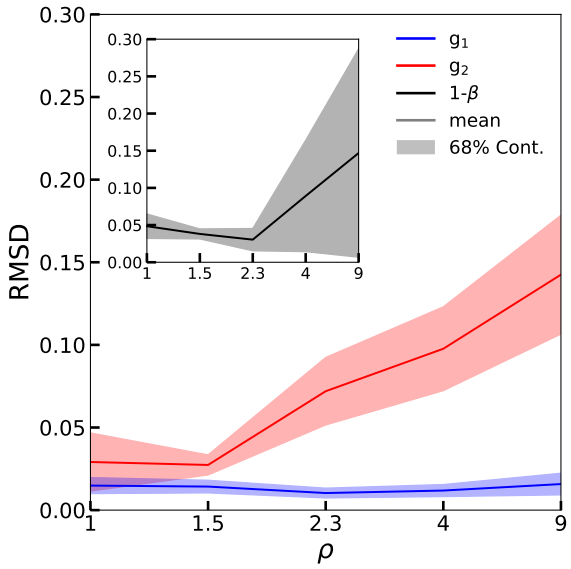

Figure 4.14: Comparison between the predictions after the SB inference and the true values for the spatial proportion of signal, 1-β, and the spectral shapes g_l given by the black, red and blue lines, respectively. The comparison is obtained by computing the RMSD as a function of the noise-to-signal ratio ρ.

by class to study sources that may belong to the same class. Several possible improvements and generalizations of the model will be addressed. The main results and outlook are:

- we have developed this new BNN based framework and applied it to separate the emission components in the synthetic dataset;
- however, the modeling of signal/background separation is built on several simplifications on the physical point of view: neither an explicit model of the measurements nor a microscopic emission model are included;
- the model is also built on space-energy factorization, assuming spatial independent energy-spectra, which is not true if the gas or radiation target density fields are strongly spatially-dependent. The gamma-ray signal expected from CR interaction in the interstellar medium would therefore follow a spatially-dependent spectral behavior;
- the considered separation is only for spatial and spectral dimensions but astrophysical and cosmological raw observations are made in the two spatial coordinates and the time: the number of spatial dimensions can be easily extended. However, the number of components in the model should be increased with caution since it decreases the stability of the inference, due to appearance of extra permutation symmetries;

- we identified only epistemic uncertainties but the background model may be viewed as a space-dependent aleatoric uncertainty and aleatoric uncertainty per se can be represented as a parameter or another unit BNN;
- we demonstrated the capability of our SB model for a limited signal-to-noise ratio region. We consider this as due to our choice of fixed aleatoric scales, however the inference with the ELBO loss function may become less stable when smaller scales are chosen.

Future and immediate applications of this model can be to search for weak gamma-ray signals, as the expected emissions from DM self-annihilation. In this case, the signal-to-noise ratio in the mixture region would be much smaller than what is considered here. In fact, we saw that the error of identification of g_2 and $1-\beta$ increases for larger values of ρ, *i.e.* smaller values of the signal-to-noise ratio. We tested in the previous section values of ρ up to 9, which corresponds to a signal-to-noise ratio of ~ 0.11. However, the expected signal from DM self-annihilation might be lower than 10^{-1} in mixture regions. More work is ongoing to adapt our framework to the search of DM signals. The Bayesian structure can also be used to learn time-variable emission, where an additional dimension is dependent on time and needs to be considered in the BNN framework. The results obtained so far with the Bayesian Neural Network framework presented in this chapter, at the moment of the writing, have been submitted to ICLR2023 [64].

Part II

Galactic Center at Very-High-Energy

Chapter 5

The Galactic Center region at Very High Energies

Contents

From the latest measurements, the center of the Milky Way is situated at 8.127 kpc away from the Sun [186]. It is a region crowded with many astrophysical sources and it has been observed at many wavelengths. Observing the GC has been crucial in the past years to understand the acceleration processes and the multitude of astrophysical objects populating the region. The observations in the VHE regime provided new information on several point-like and extended sources. We start the description of the Galactic Center region with multi-wavelength observations in Sec. 5.1. Astrophysical sources emitting at TeV energies are described in Sec. 5.2. We dedicate Sec. 5.3 to presenting some extended VHE sources. Finally, we conclude in Sec. 5.4 with the discussion on the outflows observed at VHE in the GC region.

5.1 Multi-wavelength observations of the Galactic Center

The spectral and spatial descriptions of an astrophysical object benefit from multi-wavelength observations. Its spectrum, spatial morphology and chemical properties are easier to understand if the object is detected at different frequencies. Moreover, multi-wavelength observations of a given region are useful to characterize the underlying astrophysical object related to the observed emissions. Also, information about the emission itself, the nearby radiation field and target material can be collected from different frequencies. Observing at many wavelengths helps separating nearby sources. In addition, the angular resolution of the observing instrument is fundamental, such that it is possible to associate the emission to the object producing it. The GC region is a very crowded environment and the observations of it need to disentangle the emissions from many complex sources.

Radio observations

Observations in radio waves are sensitive to frequency between 250 MHz and 300 GHz which corresponds to wavelengths between 10 km and 10 cm. These can be observed by ground telescopes since radio waves penetrate the atmosphere. With these observations, we can trace hot gas and atomic hydrogen. Radio waves can be used to study the magnetic field distribution and intensity because the synchrotron emission is emitted also in radio. They can be used for the observation and study of SNRs and their structure. The first radio emission from the GC region was detected in 1932. In Fig. 5.1, we show the image of the total intensity observation of the GC region with MeerKAT [200] at 1.28 GHz. In the sky map, SNRs are visible. The Sgr A* complex is shown at the center. Nebulae ($e.g.$ Sgr A West) and molecular clouds ($e.g.$. Sgr B, Sgr C and Sgr D) are visible too. The extent of non-thermal emission from synchrotron radiation emitted from SNRs

($e.g.$. G0.9+0.1 et G359.1-0.5) is present as well. The same emission as filaments along the Galactic magnetic field ($B \sim$ mG) can be observed too.

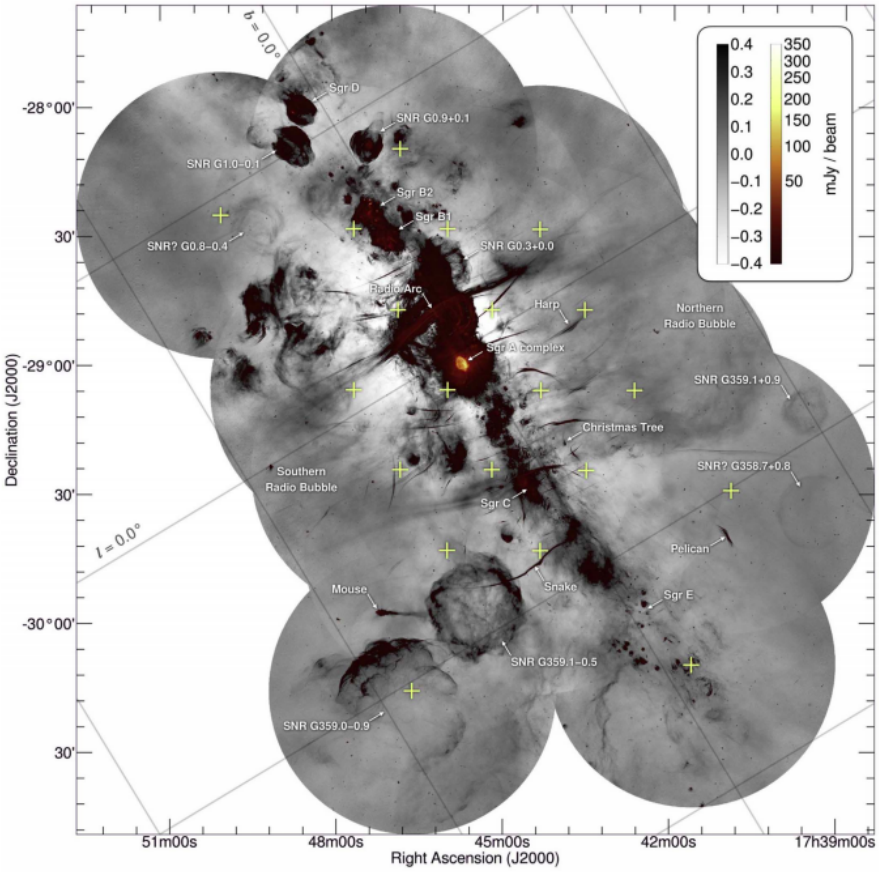

Figure 5.1: Full MeerKAT observations of the GC region, covering 6.5 square degrees. The observations were obtained with 20 pointings, shown as "+" markers. The detected sources are indicated by their name. A grid showing galactic coordinates is superimposed to the figure. More details can be found in Ref. [200], from where the image was extracted.

Observations in microwaves

In the highest frequency range for radio waves, we observe the microwaves. These correspond to wavelengths ranging from 10 cm to 1 mm. Ground telescopes can partially observe this radiation, with which we can trace the distribution of cold gas and dust. Molecular gas, as carbon monoxide (CO) and carbon monosulfide (CS), can be measured with microwaves observations. The former is a tracer of the molecular hydrogen, which is a hint for star forming regions. The Central Molecular Zone (CMZ), in the GC region, emits in microwaves.

Radiation observed in infrared

At wavelengths smaller than the microwaves, we observe Infrared (IR) radiation. This spans wavelengths from 1 mm to 700 nm, covering frequencies between 300 GHz and 428 THz. The near IR emission (below 3 μm) can penetrate the atmosphere and we can observe, through the dust cold objects. Mid and far IR (above 50 μm) can be observed from space telescopes. With this range of the IR wavelengths, we can observe cold dust, for objects like dust-covered stars, faint stars and dense arcs of dust. The telescopes observing in IR have angular resolution good enough ($e.g. \sim 2$" for Spitzer) to resolve tiny clusters of stars around the Milky Way central black hole. In Fig. 5.2, we show the map of the GC observations with the IR Spitzer space telescope for 3.6, 4.5, 5.8 and 8 μm [289]. The central region with star formation is visible, as well as massive star clusters, like the Quintuplet.

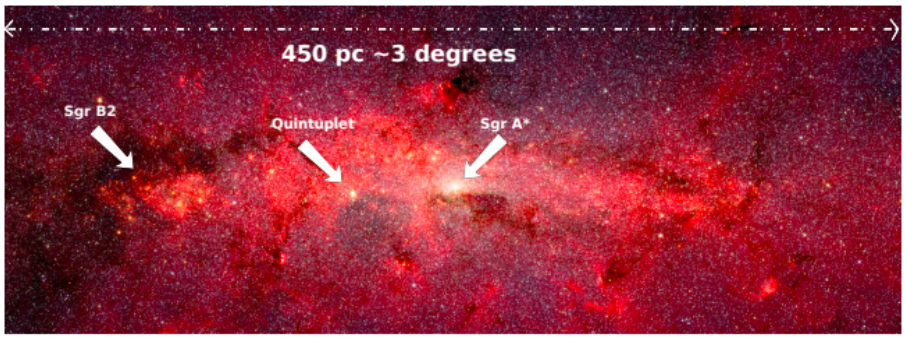

Figure 5.2: Spitzer observations of the GC region in 3.6, 4.5, 5.8 and 8 μm IR observations, showing a part of the molecular cloud Sgr B2, the Quintuplet star cluster and Sgr A*. The image was extracted from [289].

Observations in optical light and ultraviolet radiation

The optical light is observed through the atmosphere for wavelengths between 400 and 700 nm. Stars emit in this wavelength range. However, optical light does not penetrate dust-rich regions like the GC and the Galactic plane. For smaller wavelengths, *i.e.* between 10 and 400 nm, we observe ultraviolet (UV) light. The low-frequency window of the UV penetrates the atmosphere. In UV, we mainly observe young, massive, early-type (O, A and B spectral class) stars, which are the brightest ones in the GC region. The UV radiation is produced by the surrounding gas which is ionized by the star.

X-ray observations

Observations in X-rays detect light in wavelengths between 10 pm and 10 nm, with energies corresponding to 10^2 - 10^5 eV. These wavelengths do not penetrate the atmosphere, therefore must be observed from space-based telescopes. They trace hot gas and non-thermal processes (above about 10 keV) and are used to describe a wide variety of objects. In Fig. 5.3, we show two panels of the Chandra observations in X-rays [364]. The background of the image on the left panel shows a diffuse X-ray radiation. Winds of millions of degrees, accelerated by young massive stars, heat the gas which produces this radiation. With X-rays, we can trace explosions of dying stars and outflows powered by Sgr A*. The map in the left panel is built with observations at 1-4 keV (red), 4-6 keV (green) and 6-9 keV (blue). The map on the right panel is obtained from 1-4 keV observations only, with detected discrete sources being removed. The complex of Sgr A* is still visible. Dust scattering halos of bright X-ray binaries and major X-ray-bright SNRs remain too.

Gamma-ray observations

The highest energies above hundreds of MeV, are observed in gamma rays. These do not penetrate directly into the atmosphere, however they interact with it at about 10 km altitude. Therefore, we can observe gamma-rays with space based telescopes and ground based Cherenkov ones. Gamma rays trace non-thermal processes and are used to observe the objects that are known as cosmic accelerators. Exotic processes, like dark matter annihilation or decay, can produce gamma rays in the final state of the interaction. We show the GC region, as observed by H.E.S.S., in Fig. 5.4. More information about the objects emitting in TeV energies is provided in the next sections.

5.2 TeV astrophysical sources in the Galactic Center region

5.2.1 HESS J1745-290

The strong TeV emission of HESS J1745-290 was observed by H.E.S.S. close to the position of the supermassive black hole Sagittarius A* [51], lying at the gravitational center of the Galaxy. The barycenter of this VHE emission is located at l=359.94°, b=-0.04° as shown in Fig. 5.5. The supermassive black hole has a mass of 4.31×10^6 $M_\odot$. Sgr A* has been observed in many wavelengths and its variability has been measured in X-rays and IR [104]. However, no hint for variability has been detected so far in gamma-rays. We show its composite spectrum in Fig. 5.6, where the VHE emission as measured by the H.E.S.S. array is shown on the right of the spectrum [38]. The emission measured by H.E.S.S. is

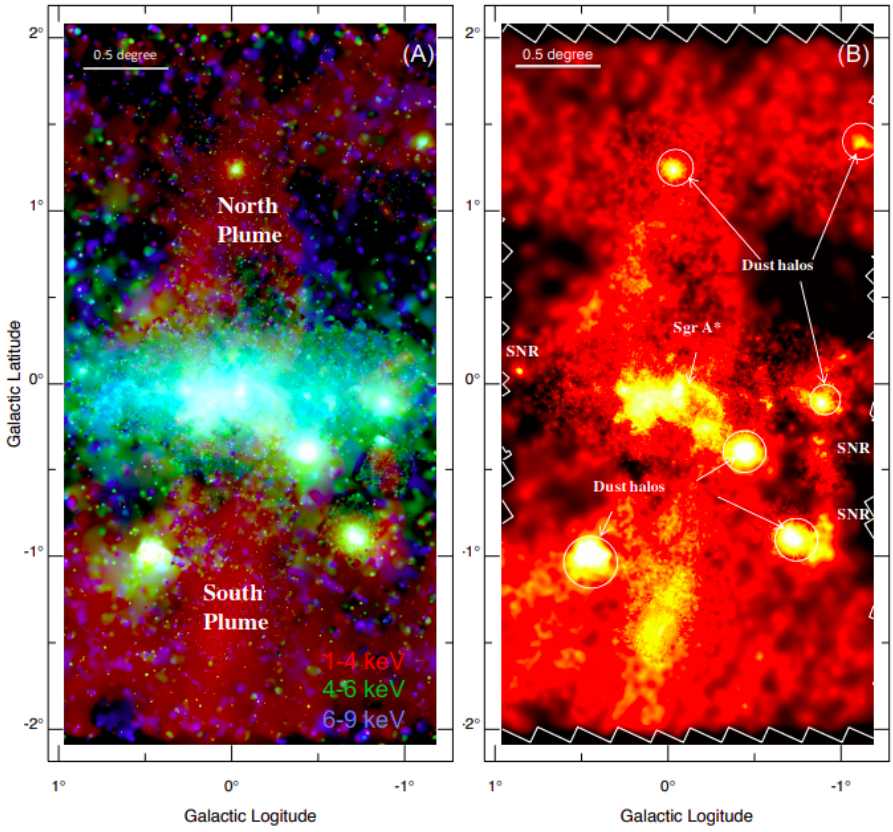

Figure 5.3: Chandra observations of the GC region. On the left panel, 3-color X-ray intensity mapping of 1-4 keV (red), 4-6 keV (green) and 6-9 keV (blue) is shown with the North and South plumes X-ray emission clearly visible. On the right panel the diffuse 1-4 keV map is shown without the detected discrete sources but with dust halos and SNR clearly visible as well as Sgr A*. Figure extracted from [364].

well reproduced with an exponential cut-off power-law. The cut-off is derived as $E_{\rm cut} = (10.7 \pm 2.0_{\rm stat} \pm 2.1_{\rm syst})$ TeV, the spectral index of the function is measured as 2.1 and the normalization results in 2.55×10^{-12}TeV^{-1}cm^{-2}s^{-1}. A smoothed broken power law can also be used to obtain a good fit. The best fit indexes are 2.02 and 2.63, the break energy is computed as 2.57 TeV and the normalization is 2.57×10^{-12}TeV^{-1}cm^{-2}s^{-1}. To explain the submillimeter emission of Sgr A*, the stochastic acceleration of electrons in the turbulent magnetic field of the region can be used. With the same argument, the IR and X-ray flaring states can be also explained. Moreover, since charged particles are accreted onto the black hole, protons could escape the field. They could accelerate and interact with the interstellar medium in the central star cluster and produce gamma rays [251]. The cutoff on the proton spectrum can be computed with $E_{\rm p,cut} \simeq E_{\rm cut}/20$, having therefore protons accelerated up to a few hundreds of TeV. The broken power

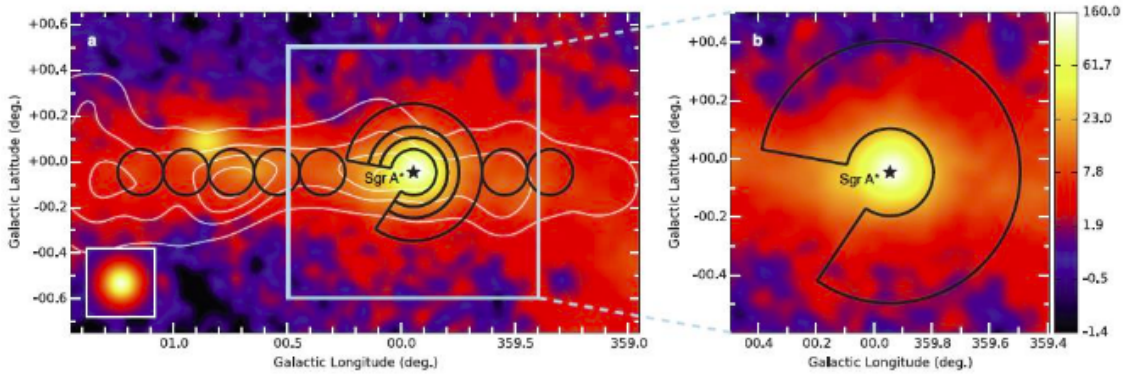

Figure 5.4: Gamma-ray observation of the GC region with H.E.S.S. [18]. Black lines used for the analysis of the CR energy density in the central zone are shown together with the white lines from CS line emission. On the right, a zoomed view of the inner $\sim$ 70 pc is shown.

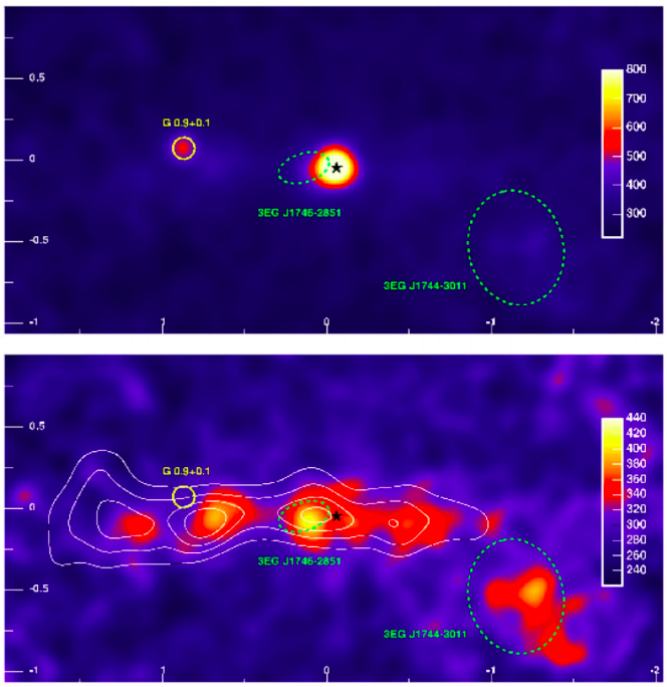

Figure 5.5: Excess map [39] from H.E.S.S. observations of the inner 200 pc of the GC region. *Top panel:* Some of the brightest sources are highlighted: the central emitter HESS J1745-303 and the PWN/SNR HESS J1747-281. *Bottom panel:* map of the Galactic ridge emission after subtraction of the bright sources. The gas dense central molecular clouds are shown as the white contours from measurement of CS emission. In this panel, the sources from the top one are removed.

law spectrum could be explained by models that predict competition between injection and escape of protons. Inverse Compton emissions from electrons accelerated up to about 100 TeV in the nearby PWN G359.95-0.04 could be also responsible for part of the TeV emission.

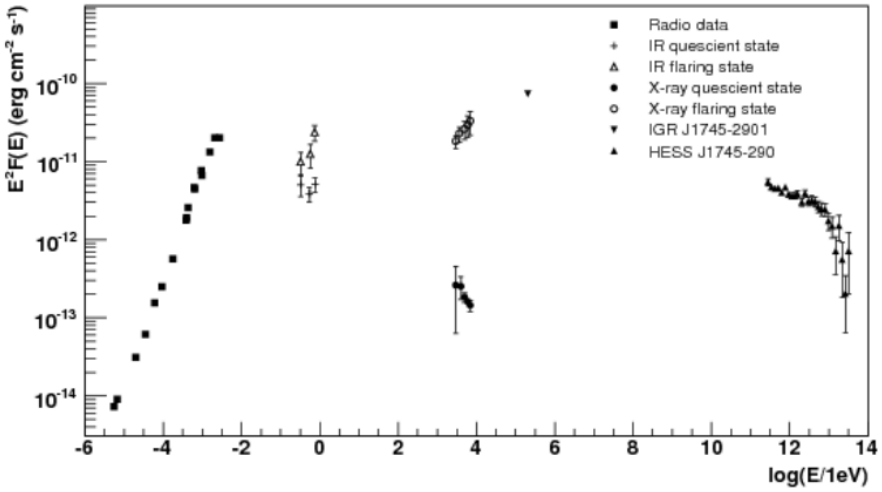

Figure 5.6: Composite spectrum of Sgr A*. The wide spectral energy distribution is obtained from spectra in radio, IR, X-rays and gamma-rays. Variable flaring states are observed in IR and X-rays. Figure extracted from Ref .[38]

5.2.2 HESS J1746-285

The source HESS J1746-285 is measured as point-like in the TeV and as the spatially closest one to the GC [9]. It has been detected at l=$0.14°$, b=$-0.11°$, above the GC ridge. The source is located in the proximity of a radio bubble that was observed in IR, connected to the young massive Quintuplet cluster. The position of the source coincides with a candidate PWN, G0.13-0.11 [364]. From the X-ray and radio emissions properties, G0.13-0.11 seems to be the result of a moving pulsar and the propagation of the wind material, regulated by the surrounding magnetic field [364]. Moreover, the spectral and luminosity properties reinforce this hypothesis. Even though this solution is the most plausible one, other possible counterparts for HESS J1746-285 exist [9].

5.2.3 HESS J1747-281

The few-degrees region around the GC hosts other bright TeV gamma-rays sources. At the position of the composite SNR/PWN G09+01, the HESS J1747-281 source has been detected in TeV [39, 181] as a point-like source. It is located at l=$0.87°$,

b=0.08°. A bright compact core surrounded by a shell is suggested by its radio spectrum. These characteristics are typical SNR features. X-rays observations identified the center of the source as a PWN [312]. Even though no pulsed emission has been detected yet in gamma rays, it could host the young radio pulsar CXOU J174722.8-280915. In Fig. 5.5, we show the position of G09+01 as a yellow circle, where the HESS J1747-281 emission is visible as measured by H.E.S.S..

5.2.4 HESS J1745-303

The TeV detection of HESS J1745-303 located the extended source at l=358.71°, b=-0.64° [168]. It was associated with the composite SNR G359.1-0.5. Through canonical SNR plasma models it is impossible to explain the complex morphology and the substructures shown by the X-rays observations. The substructures present in the vicinity of the source, may be due to radiative transitions of free electrons in He-like, Si and S ions, suggesting an over-ionization of the plasma. The insufficient density of the SNR does not support the explanation of the emission through hadronic models. However, the SNR shock can enhance the signal when the latter interacts with a molecular cloud present in the same region detected in another wavelength [91]. The source has been observed recently in X-rays [330]. The CO clouds in the vicinity of the SNR were analyzed. The spatial distribution of the CO cloud and that of the GeV/TeV emission showed no clear coincidence with each other. However, the GeV emission cannot be totally considered unrelated. In Fig. 5.7, we show the emission as observed by H.E.S.S., together with the position of the associated SNR G359.1-0.5. For reference, we also overlay other possible counterpart candidates. The excess significance levels at 4σ and 7σ from H.E.S.S. measurements are shown as black contours. The source may also be associated with 3EG J1744-3011 [179]. However, the uncertainty on its location, which is shown as a gray shaded line, is larger than the significant region of the H.E.S.S.source. The position of 3EG J1744-3011 is shown as a green dashed circle in Fig. 5.5. In the bottom panel, we show the gamma-ray emission from HESS J1745-303.

5.2.5 The H.E.S.S. Galactic plane survey

H.E.S.S. observed the Galactic plane with the four-telescopes array. The Galactic Plane Survey (GPS) [8] is an homogeneous reanalysis of the 10-year dataset. The latter includes a total of about 2700 hours, collected in Galactic longitudes between b=250° and b=65° and latitudes $\pm 3^{\circ}$. With the dataset, 48 VHE gamma-ray sources were confirmed and 16 new ones were revealed. Sources close to each other could be resolved thanks to the very good instrument angular resolution. 31 of the detected sources were classified as PWNs, SNRs and binary systems. The remaining ones are still unidentified. However, most of them are likely associated with objects observed at other wavelengths like PWNs. Complex regions,

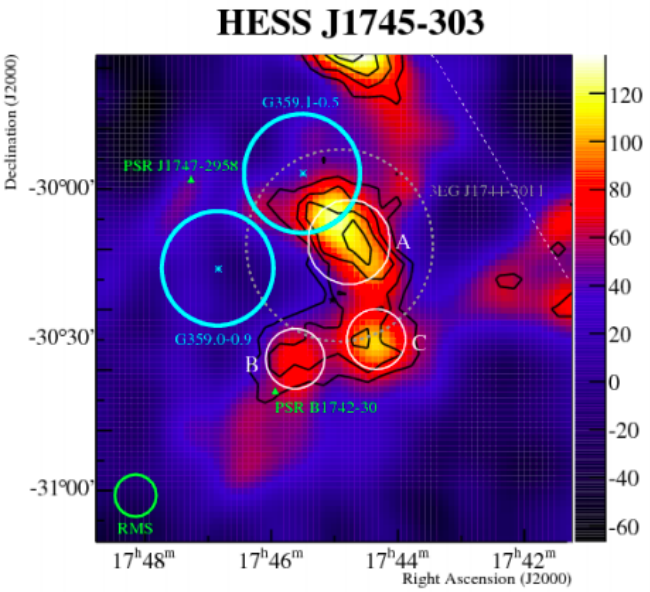

Figure 5.7: Gamma-ray sky of the emission observed from HESS 1745-303 with H.E.S.S.. The transition between the blue and the red happens at 3σ excess significance. The black contours show the 4σ and 7σ statistical significance. Possible counterparts to the emission, G359.1-0.5 and G359.0-0.9 are marked as cyan circles. Figure extracted from Ref. [168].

like shell sources and the GC region, have not been homogeneously reanalyzed for the survey. We show in Fig. 5.8 an illustration of the H.E.S.S. Galactic plane survey superimposed to the all-sky image of Planck C0(1-0) data. In the lower panels, the limits of the exposure of the survey are shown as the white contours. The Survey has little of no exposure for Galactic latitudes of $|b| > 3°$ at most locations along the Galactic plane. The image was extracted from Ref. [8], where the full source catalog, with position, size, detection significance and integrated flux above 1 TeV for each detected source available. Some of the sources from this survey are used later to define the exclusion regions used for the dark matter search.

5.3 Extended/Diffuse very-high-energy emissions

5.3.1 The Central Molecular Zone

The very dense star formation region at the center of the Galaxy is known as the Central Molecular Zone (CMZ). It is made of hot gas [283, 48]. The clouds extend for about 300 pc along the plane and are revealed by the bright CS line emissions

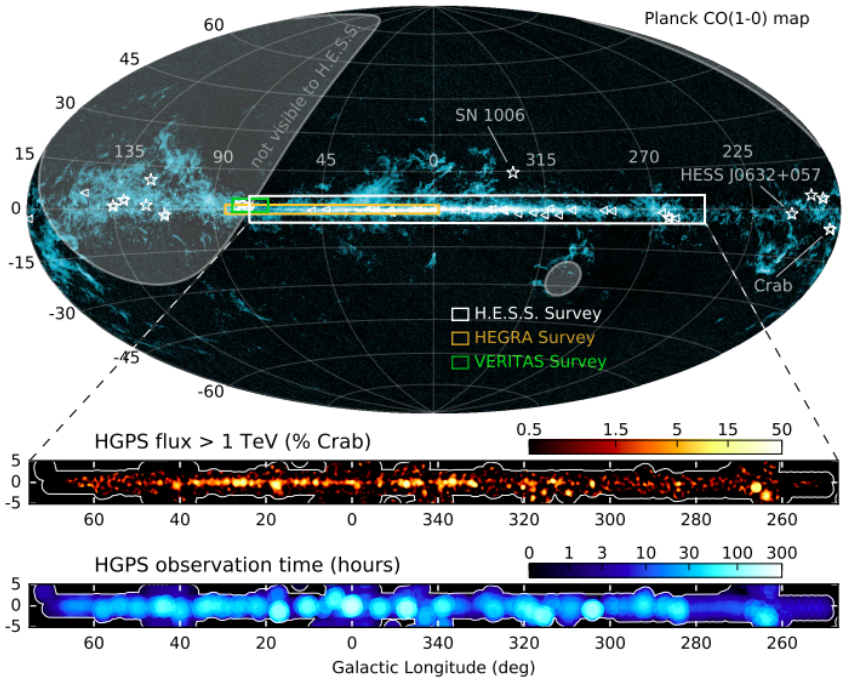

Figure 5.8: Full sky map of the Galactic plane survey performed by H.E.S.S. [8]. The all sky image of Planck CO(1-0) data is shown in the background. HEGRA and VERITAS Galactic plane surveys are shown as well. The lower panels show the HGPS γ-ray flux above 1 TeV for regions where the sensitivity is better than 10% Crab and observation time, both also in Galactic coordinates. The white contours in the lower panels delineate the boundaries of the survey region

in radio, at 1.1 mm wavelength [52]. A quantity of matter corresponding to an estimated 60 million solar masses constitutes this region, with an average density 100 times larger than outside the CMZ, *i.e.* of about hundreds of atoms per cm^3 [192]. The main structures in the CMZ region are: Sgr A* radio arc complex, Sgr B, Sgr C, and Sgr D as shown in Fig. 5.1. Observing the inner few degrees of the GC at different wavelengths revealed expanding molecular rings, arc structures and the GC lobes. These structures are fundamental to understand the processes taking place at the GC lobes. Indeed, explosive events may have generated all of the structures, but the production mechanisms are still unknown. Better knowledge of the morphology, density and velocity of the underlying gas distribution could help to further investigate them.

5.3.2 The Galactic Center ridge

The central 200 pc of the Milky Way hosts the Galactic Center ridge, a large extended VHE gamma-ray emission. H.E.S.S. observed it [9], and could reveal its

morphology thanks to the very good angular resolution. The observation showed that the GC ridge emission is spatially correlated with a complex of giant molecular clouds. In Fig. 5.5, the CS contours of the gas clouds are overlaid to the H.E.S.S. map of the GC region. This map is obtained after the subtraction of the bright point-like sources HESS J1745-290 and G0.9+0.1 in the top panel. At the bottom right of the figure, the emission from HESS J1745-303 is visible. The emission that extends along the Galactic plane for about 200 pc in longitude and 30 pc in latitude is the Ridge. To extract its spectrum, a region of $|l|<0.8^{\circ}$ and $|b|<0.3^{\circ}$ has been chosen. A power law with spectral index 2.29 well describes the emission. CRs nuclei interacting with the CMZ are likely responsible for the production of the ridge emission, due to the correlation with the CS map. The initial CRs spectrum can be recovered and is expected to have an index of about 2.3. The spectrum is hard, compared to the neighborhood with index 2.75, and could be related to the source being close to the central accelerator. This would not allow strong energy losses. The number density of CRs with multi-TeV energies exceeds the local density by a factor from 3 to 9. This measurement points towards the presence of an additional injection of CRs above the CR local flux.

5.3.3 Galactic Diffuse Emission measured by *Fermi*-LAT

The *Fermi*-LAT instrument measured a diffuse emission in the MeV-GeV energy range, known as the Galactic Diffuse Emission (GDE). This background is produced by standard astrophysical processes originating in the GC and Galactic plane. The mechanisms responsible for this emission are electrons/positrons ICS and bremsstrahlung, and pion decay. The Galactic diffuse emission has been observed since the '70s and had been already studied [350]. The most accurate studies of this emission have been possible thanks to *Fermi*-LAT [25]. With respect to the previous telescopes, the large FoV, the unprecedented sensitivity and wider energy range (spanning from MeV to hundreds of GeV), played an important role in the observations with *Fermi*-LAT. The model of the GDE is based on some assumptions: it depends strongly on the injected CRs spectrum, the modeling of the energy losses and gains (diffusion, re-acceleration, ...), CR sources and gas distribution. Moreover, the model depends on the interstellar radiation field (ISRF), the result of emission by stars, and subsequent scattering, absorption, and re-emission of the absorbed starlight by the dust in the interstellar medium (ISM). The computation of GDE models can be performed with GALPROP [362], providing the parameters for ISM and ISRF. Both leptonic and hadronic processes need to be treated to produce the GDE [284]. The distribution of VHE gamma-ray sources is traced by the ICS, which is produced in the vicinity of CR accelerators. On the other side, in gas dense regions and molecular clouds like the previously mentioned CMZ, processes like Bremsstrahlung (dominating the low energies) and pion decay (dominating the high energies) take place. The emission correlated to the gas does

not trace the CR accelerators because CRs have time to diffuse before interacting with ambient nuclei. However, it traces the distribution of gas. The few hundred kiloparsecs around the GC and along the Galactic plane host most of the sources and gas clouds. Since the emission is the result of CRs interaction with the ISM, it can be used to study the propagation of CRs and the properties of the ISM. In Fig. 5.9, we show a recent modeling of the spectra of the GDE, as extracted from *Fermi*-LAT observations [24]. This modeling was obtained with GALPROP v54.1. We used this later for the derivation of the Fermi Bubbles spectrum at low Galactic latitudes, inside the region defined for the search of the emission with H.E.S.S. observations. From the spectrum, we see that gas-correlated components (green squares) dominate the ICS one (orange dots). Moreover, the derived spectra for the Fermi Bubbles are shown.

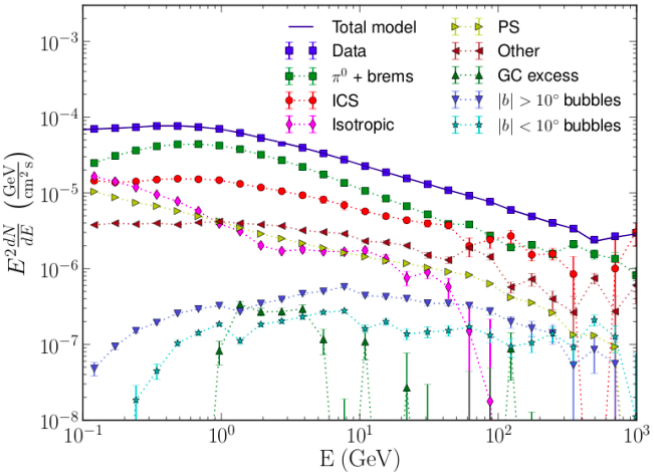

Figure 5.9: Spectra of the GDE as measured by *Fermi*-LAT and its components. The data are shown as blue squares. The contributions to the emission are shown as gas-correlated GDE emission (green squares), ICS radiation (orange dots), isotropic background (magenta diamonds), point-like sources (yellow triangles) and the GC GeV excess (green triangles). High latitude (|b|>10°) and low latitude (|b|<10°) Fermi Bubbles emissions are shown as well as indigo triangles and teal stars, respectively. Figure extracted from Ref. [24].

5.3.4 The Galactic Center Excess detected by *Fermi*-LAT

The inner 1° region of the GC showed a gamma-ray excess (GCE) in GeV *Fermi*-LAT measurements, with respect to the predictions from interstellar emission model (IEM). The DM hypothesis was one of the first interpretations. It was shown that the signal could be explained by the annihilation of DM particles with mass 30-50 GeV with a NFW profile [292] and relic cross section of the order of 10^{-26} cm^{3}s^{-1}

as predicted for thermal production. However, constraints below the relic cross section up to a few hundreds GeV had been set from previous *Fermi*-LAT measurements in conventional-background-free dwarf galaxies. This is in tension with the possible DM explanation of the GCE. The spectra used to define the hypothesis appeared strongly dependent on the chosen IEM in the updated analysis [24] with the updated 6.5 years of *Fermi*-LAT observations. The latter also included an additional population of electrons used in the modeling of the CMZ and three different point source catalogs. A more recent analysis revisited the spectrum from the GCE with 11 years of observations with *Fermi*-LAT [158] as shown in Fig. 5.10, extracted from Ref. [158]. The spectrum of the GCE has been remodeled in [24] considering the interplay with the addition of low-latitude emission from the Fermi Bubbles and is shown in Fig. 5.9 as black circles. From the debate around the nature of the GDE, a population of millisecond pulsars in the Galactic bulge was proposed as a promising hypothesis. This population would be derived by non-spherically symmetric stellar density distributions of the Galactic bulge [257].

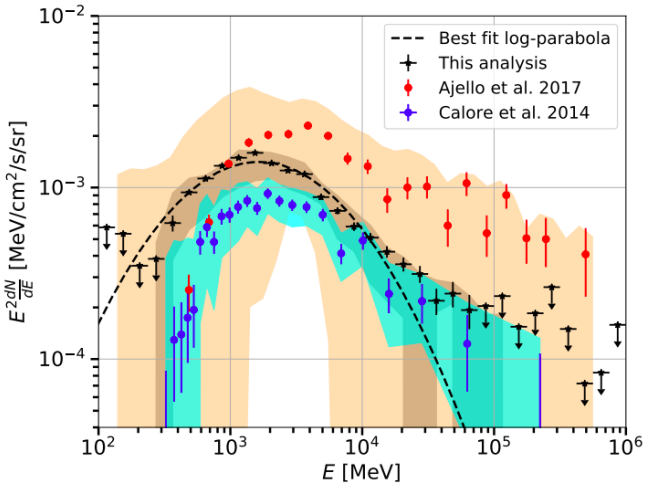

Figure 5.10: Comparison between the spectra for the GCE obtained in Ref. [158] and previous analyses. The different analysis techniques available for the computation of the IEMs produce the variation represented by the bands. The best-fit to the GCE SED, obtained with the Baseline IEM by using a log-parabola function, is displayed. Figure extracted from Ref. [158].

5.4 Outflows from the Galactic Center

5.4.1 The Galactic Center PeVatron

H.E.S.S. published the measurement of an excess of photons detected in the GC in Ref. [18]. The spectrum has been measured up to tens of TeV. The measured spectrum and the best fit of the diffuse emission in the TeV energy range are shown in the left panel of Fig. 5.11. The analysis of this source has been performed in an open-ring-shaped region of interest of size 1.4×10^{-4}sr, extending from inner radius of 0.15° to the outer one of 0.45°. A cut to exclude a part of the region has been extracted at opening angles between -10° and 56°. The excess map extracted from the H.E.S.S. paper is shown on the left panel of Fig.5.4. The right panel shows a zoom on the GC TeV diffuse emission and shows the region of interest. To describe the spectrum from the emission measured in this region, a power law with no cutoff, a photon index 2.32 and normalization 1.92×10^{-12} TeV^{-1}cm^{-2}s^{-1} is found. To explain the normalization of the spectrum, the standard diffusion coefficient of D=6×10^{29} (E/10 TeV)$^{1/3}$ cm^{2}s^{-1} is used and $\dot{Q}_p(\geq 10\text{ TeV}) \simeq 4\times10^{37}$(D/$10^{30}$ cm^{2}s^{-1}) erg s^{-1} as the required constant injection rate [18]. The two quantities are derived from numerical computations to obtain the energy spectrum of cosmic-ray protons for E > 10 TeV. To measure the radial distribution of cosmic rays in the CMZ, $\omega_{\rm CR}(E,r,t)$, the same assumption can be made. Between the tested dependencies, $\omega_{\rm CR} \propto 1/r$ is best to reproduce the data. Other scenarios could be CRs advected in a wind or from an injection from a burst. However, they are not favored by the data. The scenario with $\omega_{\rm CR} \propto 1/r$ indicates a quasi-continuum injection into the CMZ. 5.7×10^{34} erg s^{-1} of integrated luminosity is obtained above 1 TeV. Extremely energetic protons can produce gamma-rays of such a luminosity when accelerated by the central emitter. [18]. Sgr A* is argued as the most plausible supplier of protons and nuclei accelerated either in the accretion flow, or at the termination of the outflow. To obtain gamma-rays at such large energies, the acceleration of the protons must push them to PeV energies. An object that can do this is named *PeVatron*. Standard accelerators usually show a cutoff at a few TeV, instead. There have been alternatives to the PeVatron solution, suggesting for instance a SNR scenario. However, a single SNR would not produce such a large luminosity over a long timescale (> 100 yr). Alternative explanation to Sgr A* for the diffuse emission and the PeVatron are provided in Ref. [238].

5.4.2 The Fermi Bubbles

Fermi Bubbles (FBs) are giant bipolar structures of width of 40° in Galactic longitudes, extending up to 55° above and below the Galactic plane in latitude. They were observed with *Fermi*-LAT and a recent analysis derived their spectrum [24].

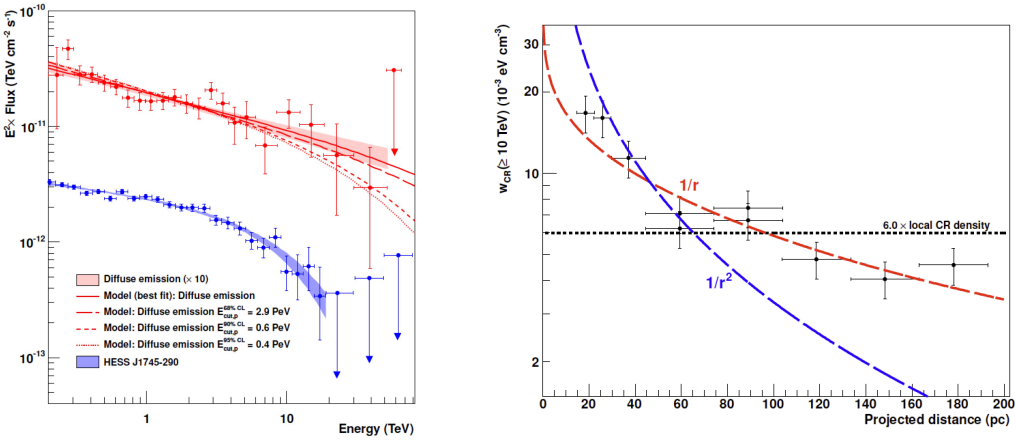

Figure 5.11: *Left panel:* Gamma-ray spectrum at TeV energies of the diffuse emission in the GC region (red) and the PeVatron, HESS J1745-290 (blue). The fit for the two spectra are shown as a power-law and an exponential cutoff power law for the diffuse emission and the PeVatron, respectively. *Right panel:* CRs distribution as a function of the projected distance to the GC. Three fits to the data are shown: 1/r (red dashed line), $1/r^2$ (blue dashed line) and homogeneous (black dotted line) radial profiles integrated along the line of sight. The 1/r profile is preferred. Figure extracted from Ref. [18].

From the high latitude observations, the spectrum extracted shows a slope of 1.9 and a cutoff at 110 GeV. In more recent analyses, the VHE FBs emission showed two components [198]. While at high latitude the FBs spectrum is quite soft, the low latitude component, *i.e.*, for $|b|<10^\circ$, seems harder and brighter. The template at low-latitude is used later for the search for the expected emission of the FBs at TeV energies in Chap 7. In Fig. 5.12 we show the FBs template used later in the search for the TeV FBs emission with H.E.S.S. observations as well as to model the background emission expected when computing H.E.S.S. sensitivity limits on the possible DM detection (see Chap. 10). The FBs emission is observed with a photon index of 1.9, therefore its association with the GDE, which shows a photon index of 2.4, is not favored. While the high-latitude FBs spectrum softens significantly above 100 GeV, this behavior is not seen at low-latitudes and no significant hint for a cutoff in the Fermi spectrum is observed. This keeps open the possibility to observe a low-latitude FBs component in TeV gamma-rays with H.E.S.S.. In Fig. 5.9 we show the spectra extracted from the Fermi article [24]. The Fermi Bubbles in $|b|<10^\circ$ and $|b|>10^\circ$ are shown as teal starts in indigo triangles, respectively. A structure similar to the Bubbles has been recently observed by eROSITA [316]. Soft-X-ray emitting bubbles extending approximately 14 kpc above and below the plane are shown in Fig.5.13. They enclose the gamma-ray emission observed by the Fermi telescope and seem to be correlated to the

Fermi Bubbles. The mechanism of their production is not clear yet. From the detection of synchrotron haze, we can assume that a radio counterpart should be present in leptonic scenarios. The emission can be reproduced by both leptonic and hadronic processes of gamma ray production [24]. In one recent analysis of the GC region with MeerKAT, one of the large coherent structures observed is the 430 pc bipolar radio bubbles which should be related to the FBs [200]. In Chap. 7 we present the most recent analysis for the search of the Fermi Bubbles emission with the H.E.S.S. Inner Galaxy Survey dataset.

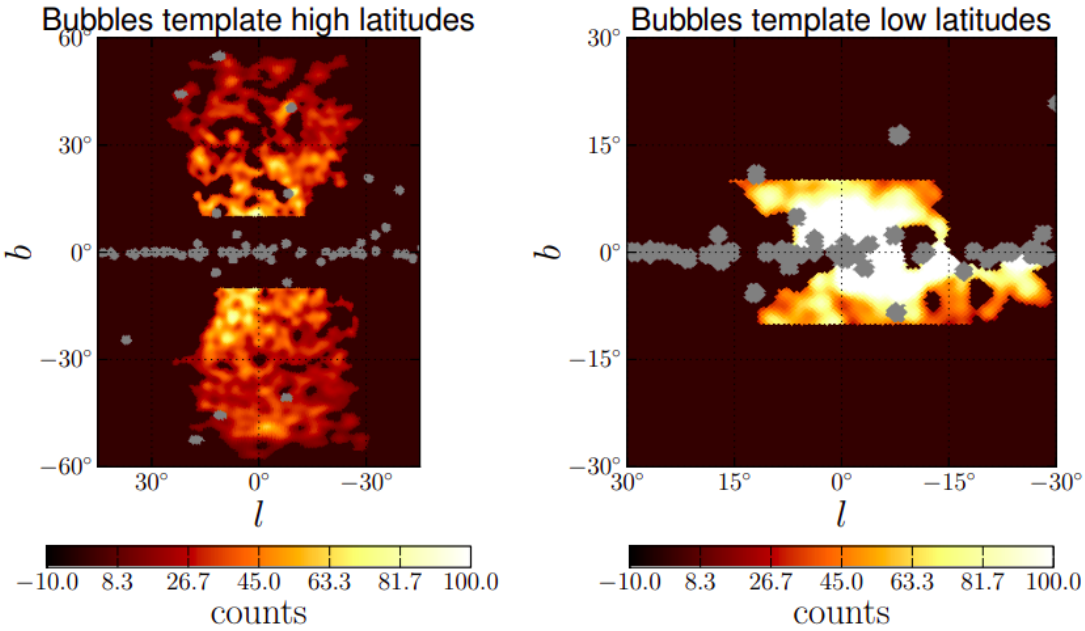

Figure 5.12: Fermi Bubbles emission template for the high-latitude and low latitude components, respectively in the left and right panels [24]. The gray masks are excluded regions corresponding to other previously detected gamma-ray sources.

5.4.3 Radio and X-ray outflows

A lobe structure was also revealed by radio and X-ray observations of the inner Milky Way halo. The former has been observed as broadly collimated outflows, ejected from the GC perpendicularly to the plane. Observations, part of a radio survey at 10 GHz, in the radio continuum with the Nobeyama Radio Observatory detected the extended lobe jet-like emissions [338]. At 1° above the plane, structures have been detected. The same features are highlighted in the survey at 5 GHz taken from the Bonn survey. Radio outflows from the GC region have been detected also by the Green Bank Telescope in a survey of the inner $4^\circ \times 1^\circ$ of the Milky Way [241]. These observations, performed at 3.5, 6, 20 and 90 cm show

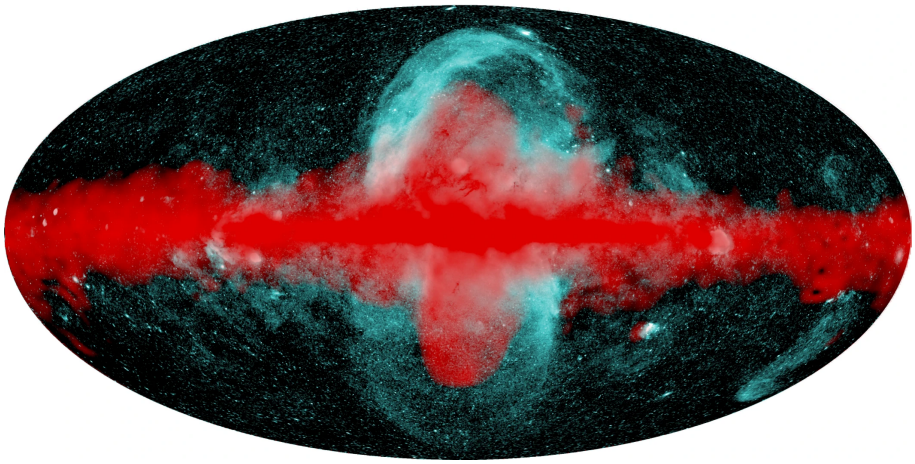

Figure 5.13: A composite view of Fermi–eROSITA Bubbles. The X-ray observations are shown as the cyan region. The gamma ray emission, as observed by Fermi, is shown in red. Figure extracted from Ref. [316]

lobes of diffuse emission that extends above the Galactic plane, coming out of the proximity of the GC. In addition, the ROSAT all-sky survey identified bursts and emission structures from the GC region. Two towering "chimneys" glowing in X-rays have been observed by Chandra, XMM-Newton and Suzaku [287], both in the Northern and Southern hemispheres. The X-ray brightness and color is comparable in the two hemispheres.

Chapter 6

The H.E.S.S. Inner Galaxy Survey

Contents

Summary

This chapter is dedicated to the description of the entire 2014-2020 H.E.S.S.-II dataset of observations of the GC region. It includes the Inner Galaxy Survey (IGS), the first ever conducted survey towards the Galactic Center region in the TeV energy range. With six years of high-quality observations collected with the full five-telescope H.E.S.S. array, the 2014-2020 dataset is used in the following chapters to search for (i) dark matter annihilation signals in Chap. 8 and (ii) the expected TeV emission at the base of the Fermi Bubbles in Chap. 7. Moreover, an IGS-like mock dataset is built in Chap. 10 to derive expected sensitivity on the detection of dark matter signal with H.E.S.S.. The full exposure map obtained so far is compared to the one from the 2004-2013 H.E.S.S.-I dataset of observations of the GC. Moreover, the evolution of the gamma-ray acceptance maps of the observed FoV during the years of the IGS is shown. The parameters for the observations of the entire six-years dataset are shown.

In Sec. 6.1 we will explain the goal and the strategy used to perform the observations of the IGS. In Sec. 6.2, we discuss the full observational dataset of the Survey, with details about the different phases of H.E.S.S. observations. Sec. 6.3 is dedicated to the parameters of the observations performed between 2014 and 2020. In the same section, excess and significance sky maps of the dataset are shown. In Sec. 6.4, we explain how we performed a thorough study on the systematic uncertainties affecting this massive dataset. A procedure to derive background models for the 2014-2020 H.E.S.S. dataset is explained in Sec. 6.5 with a few preliminary results. Finally, we draw the conclusions and some possible outlooks in the final Sec. 6.6.

6.1 Description of the Inner Galaxy Survey

6.1.1 Scientific goals of the Survey

The IGS was included in the key-science projects of H.E.S.S. from 2016. One of the goals of the IGS was to homogenize the time exposure of the region in positive Galactic Latitudes above the Galactic Center. To accomplish that goal, a grid of pointing positions have been defined. The survey aimed at covering the inner several hundred parsecs of the Galactic Center to to achieve the best sensitivity possible to the signals coming from DM annihilation and Galactic Center outflows. The largest measurable DM annihilation signal is expected from the GC region, due to its proximity and the large expected DM content. When considering a cuspy DM profile, the expected signal is lowered if observations of latitudes of few degrees above the Galactic plane are taken. However, that region is much easier to treat with respect to the very GC which is crowded by conventional astrophysical background emissions. Moreover, studies of ≤ 1 kpc DM cores can benefit from observations that extend far from the GC. Therefore, new studies can be performed to improve upon previous analyses on DM annihilation searches obtained with H.E.S.S. observations [13, 244]. The survey dataset has also been used for the search of TeV low-latitude Fermi Bubbles emission, which has already been detected at other wavelengths [24, 316] and can be studied in the TeV energy range. Moreover, the FBs emission is measured as brighter and harder at low Galactic latitude than in the other regions around the GC [24]. We can therefore use the IGS dataset to search for this emission. Analyzing the Fermi Bubbles emission can bring new insights in the studies of the acceleration processes driving the parent particle populations and the astrophysical objects present in the GC region that produce such processes. H.E.S.S. already extensively observed the Galactic plane [8] with the four-telescopes H.E.S.S.-I array. Another goal of the IGS is to deepen the knowledge of the diffuse emission coming from the Galactic plane, a background that can affect the observations at few degrees above the plane and needs to be taken into account when performing the DM and outflow searches. Both the higher latitudes of the pointing positions and the larger statistics of the H.E.S.S. phase II observations of the GC region, will be useful for studying the shape of the TeV emission from the GC and will help disentangling between different hypotheses previously mentioned.

6.1.2 Telescopes pointing positions

The observations of the IGS program have been carried out with pointing positions at Galactic latitudes up to 3° from the GC. The IGS pointing positions in Galactic coordinates are listed in Tab. 6.1. From this configuration, an almost homogeneous time exposure of the region was obtained. The Northern hemisphere

of the GC region was chosen, due to the combination of the large spatial extension of this interesting region and the limited visibility window of the GC. In addition, the Southern region of the GC hosts a larger level of NSB in an extended region, as shown in Fig. 6.1. The observational time for each of the pointing positions was chosen and requested in the observational proposal to the H.E.S.S. collaboration year-by-year. The distribution of observational time between the different pointing positions was adapted to reach an almost homogeneous time exposure between 0° and 4° in Galactic latitudes and 2° and -2° in Galactic longitudes. The pointing positions have been chosen during the years and have been arranged to form a spatial grid with fourteen components. Studies of extended distribution of dark matter in the Milky Way halo and the expected low-latitude TeV emission from the Fermi Bubbles benefit from the geometry of the grid of the IGS pointing positions. In fact the brightness surface of the low-latitude emission from the Fermi Bubbles peaks in the North to the Galactic plane [24], inside the region of maximum exposure of the H.E.S.S.-II dataset.

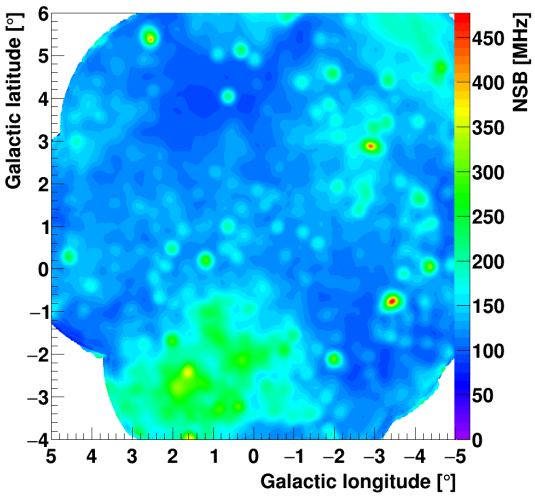

Figure 6.1: NSB map in MHz of the inner halo of the Milky Way in Galactic coordinates. The region is zoomed to show the zone where maximum exposure is obtained with the dataset of H.E.S.S.-II observations.

Pointing position name	1-4	1-5	1-6	1-7	1-8	1-9	2-5	2-6	2-7	2-8	3-5	3-6	3-7	3-8
Gal. long. [deg.]	-3.0	-1.8	-0.6	0.6	1.8	3.0	-1.8	-0.6	0.6	1.8	-1.8	-0.6	0.6	1.8
Gal. lat. [deg.]	0.8	0.8	0.8	0.8	0.8	0.8	2.0	2.0	2.0	2.0	3.2	3.2	3.2	3.2

Table 6.1: IGS pointing positions in Galactic coordinates for the 2016-2020 observations. In the first row, the names of the pointing positions are given. In the second and third rows, the Galactic longitudes and latitudes of the pointing positions are given.

6.2 Observational dataset

The full H.E.S.S. dataset of observations of the inner halo of the Milky Way includes measurements collected with both the phase I and the phase II of the H.E.S.S. array. The phase I includes observations with only the four-telescope array, whereas the fifth telescope was used too for observations during the second phase. Phase-I observations were taken between 2004 and 2013, towards pointing positions distributed around the GC. Some of these pointing positions were explicitly dedicated to the observation of the central supermassive black hole Sgr A*. This dataset consists of 254 hours of high-quality data and was used for the search of DM annihilation signals published in 2016 [244]. Phase II observations were taken between 2014 and 2020, with both pointing positions close to the GC and the IGS ones. The phase II dataset consists of 546 hours of observations, that we used to publish an update on the search for DM annihilation signals from the GC region [7], and the search for the TeV emission from the low-latitude Fermi Bubbles [286]. Both datasets are mostly constituted by 28-min data taking observational runs. The most constraining limits on the velocity weighted cross section of annihilating DM in the TeV mass range have been obtained with the 2014-2020 dataset. A combination of the two datasets is foreseen as a legacy study, in order to obtain the most constraining limits on self-annihilating DM from the GC region. For both datasets, the γ-ray events were chosen following standard quality selection criteria [33]. In the following, we will describe the two datasets singularly.

6.2.1 H.E.S.S. phase-I observations of the Galactic Center

The H.E.S.S. phase I dataset consists of 254 hours (live time) of GC observations performed between the year 2004 and 2013 included. The offset of the pointing positions w.r.t. the GC was chosen to be from 0.7 up to 1.1°. The γ-ray events were chosen following standard quality selection criteria [33]. All observations were taken under nominal darkness conditions. In addition, observational zenith angle lower than 50° was required, to minimize systematic uncertainties in the event reconstruction. The mean zenith angle obtained for the selected observations is 19°. The data were analyzed in *CT1-4 Stereo* mode, *i.e.* at least two of the smaller telescopes are required to trigger the same shower event, with a semi-analytical shower model [291]. Figure 6.2 shows the exposure map (m^2s) obtained from this dataset. The exposure is obtained by convolving the time exposure with the acceptance of the H.E.S.S. phase I instrument as used in [244]. The H.E.S.S.-I dataset shows an almost flat exposure within the inner $\sim |1.7|^\circ$ of the GC region in longitudes and latitudes.

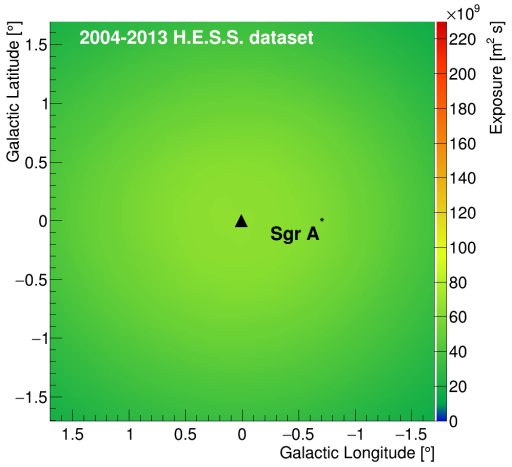

Figure 6.2: Exposure map (in m^2s) of the observational dataset of the GC region for the H.E.S.S. I [244] phase. The position of the supermassive black hole Sagittarius A* is symbolized by the black triangle.

6.2.2 H.E.S.S. phase-II observations of the inner Milky Way halo

The entire H.E.S.S. phase II dataset consists of high-quality 546 hours (live time) of observations taken towards the inner halo of the Milky Way. This dataset was collected between 2014 and 2020. The IGS started in 2016, aiming at the coverage of the GC region with significant exposure at Galactic longitudes $|l| < 5^\circ$ and latitudes b from -3° up to 6°. The total time-exposure map for the 2014-2020 dataset is shown in Fig. 6.3 in Galactic coordinates. In the right panel of the same figure, the exposure map is shown. It is obtained by convolving the time-exposure map with the acceptance of the H.E.S.S. telescopes for the observations of the IGS. The pointing positions of the IGS are shown as well. An acceptance-corrected time exposure of at least 10 hours is reached up to $b \approx$+6 $^\circ$ with the 2014-2020 dataset. The pointing positions of the IGS are shown as well. A zoomed view of the full exposure map of this dataset is shown in Fig. 6.4. For the 2014-2020 dataset, about 5 times more exposure is available due to the larger observational time and the improved sensitivity of the full five-telescopes H.E.S.S. array.

H.E.S.S. phase-II observations before the IGS

The data collected in 2014 and 2015 were dedicated to observations towards the GC region. Pointing positions for 2014 and 2015 observations were chosen for the needs of the Galactic plane survey [8] and dedicated source observations of the pulsar PSR J1723-2837 and the supermassive black hole Sagittarius A*. The 2014 and 2015 observations resulted in 50 and 84.5 hours of high quality data, respectively. The gamma-ray sky acceptances for 2014 and 2015 observations are shown

in the top left and top right panels of Fig. 6.5, respectively. The acceptance is fairly flat within 1° and degrades rapidly at larger latitudes. Observations were taken under nominal darkness condition and at zenith angles lower than 40° to minimize systematic uncertainties in the event proper reconstruction. Angular resolution of 0.06° (68% containment radius) and an energy resolution of 10% above 200 GeV are achieved. The events are reconstructed in either *CT1-5 Stereo* or *CT1-4 Stereo* mode, *i.e.* at least two telescopes are required to trigger the same shower event, with a semi-analytical shower model [291]. In this case, the best event reconstruction between an array configuration with only CT1-4 telescopes and one with CT1-4 and CT5 telescopes is chosen. After 2015, the IGS observations were also meant to compensate for the lack of exposure at larger Galactic Latitudes.

H.E.S.S. phase II Inner Galaxy Survey observations

The H.E.S.S. phase II IGS dataset includes observations collected between 2016 and 2020. In 2016, a total of 65 hours has been collected almost homogeneously on the 14 pointing positions. The 2017 observational campaign was conducted in order to homogenize the exposure on pointing positions at higher latitudes with an amount of 60 hours of observations. The three years of observations between 2018 and 2020 were focused to increase the time exposure over the 3-X pointing positions of the grid, with some observations dedicated to 2-5 and 2-8. For the last three year of IGS, 84.7, 95.5 and 106.3 hours were observed respectively. The gamma-ray sky acceptances for the observations in 2016, 2017, 2018 and 2019 are shown in the middle panels of Fig. 6.5. The procedure for the selection of the γ-ray events applied is the same that we described in the previous section. For 2014-2019 observations, the *CT1-5 Stereo* mode is used as reconstruction configuration. For 2020 observations we apply the *CT1-4 Stereo* mode, where the best event reconstruction between the array configurations with only CT1-4 telescopes is chosen. This is necessary since no lookup and spectral tables for the processing of 2020 data in *CT1-5 Stereo* mode are available for physics analysis of FlashCam in CT5. Therefore, we have to use the *CT1-4 Stereo* configuration. The total gamma-ray sky acceptances for the observations taken between 2014 and 2019 is shown in the bottom left panel of Fig. 6.5. The acceptance for the observations collected in 2020 is shown in the bottom right panel of the same figure.

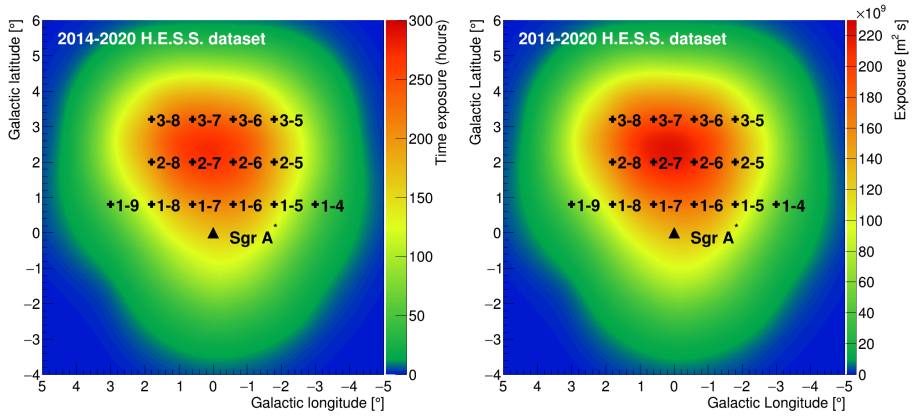

Figure 6.3: Time-exposure and exposure of the H.E.S.S. II dataset observed between 2014 and 2020 in the left and right panels, respectively. An accepted corrected time exposure of at least 10 hours is reached up to b≈+6°. The black triangle shows the position of the supermassive black hole Sagittarius A*. The black crosses show the pointing positions of the IGS observations of the dataset.

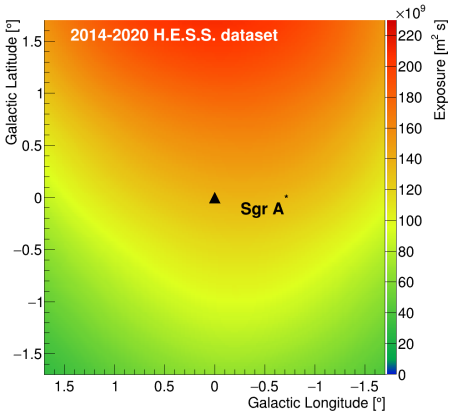

Figure 6.4: Zoomed view of the exposure map (in m^2s) of the 2014-2020 observational dataset of the GC region for the H.E.S.S. II phase as published in [7]. The position of the supermassive black hole Sagittarius A* is symbolized by the black triangle.

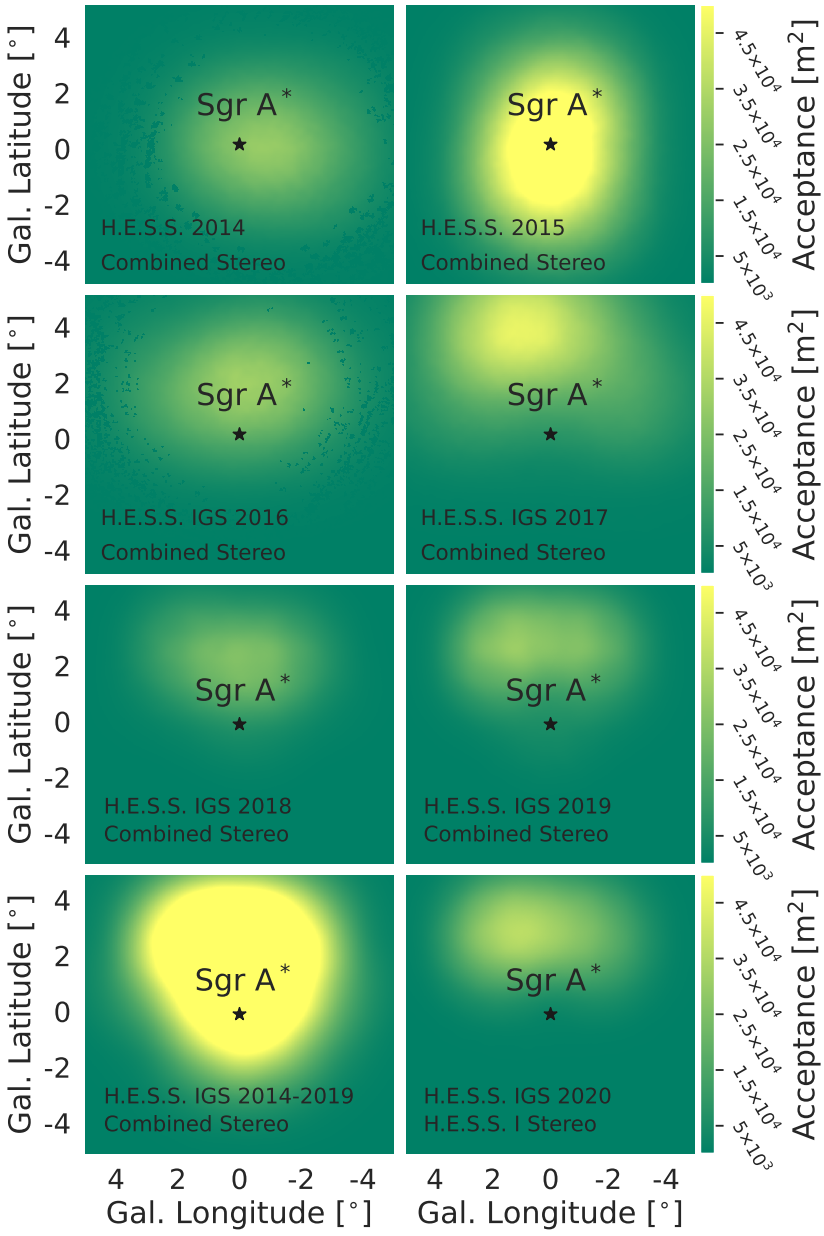

Figure 6.5: Gamma-ray sky acceptance maps in Galactic coordinates for the observations of the inner halo of the Milky Way taken between 2014 and 2020. The position of the supermassive black hole Sagittarius A* is shown by the black triangle. The first six maps show the acceptance for the observations taken between 2014 and 2019 in the *CT1-5 Stereo*, or *Combined Stereo*, mode. The bottom left panel shows the combination of the acceptance maps for the years 2014-2019. The bottom right panel shows the map for the observations taken in 2020, with the *CT1-4 Stereo*, or *H.E.S.S. I Stereo*, mode.

6.3 Low-level analysis of the 2014-2020 data taking

6.3.1 Zenith and offset distributions

After data quality selection, the 2014-2020 H.E.S.S. II dataset provides 546 hours. As of standard criterium, observations with zenith angle lower than 40° were preferred. However, they are not always possible due to the limited time window available due to numerous astrophysical objects of interest in the 17-18h right ascension band[1]. Therefore, the zenith angle of the observations ranges from 3.0° up to 60.0°, with a mean value of 18.0°. Observations carried out in 2014 and 2015 were performed on pointing positions closer to the GC, therefore the mean values of offset are 1.1° and 1.5°, respectively. For both years, a mean zenith of 19.7° was reached for the observations. After 2016, the observations were performed mostly on 2-X and 3-X pointing positions, therefore the mean offset increased. For 2016, 2017, 2018, 2019 and 2020 observations values of mean offset of 2.2°, 3.0°, 2.7°, 2.8°and 3.3° respectively are obtained. For the same years, the mean zenith values of 12.0°, 13.2°, 19.7°, 18.2°and 18.3° respectively are reached. The mean values of zenith and offset angles are summarized in Tab. 6.2 for all the years in the dataset. Year-by-year offset distributions are shown in Fig. 6.6. The mean offset for each observation is shown by the green dashed line. The bottom-right panel shows the distribution stacked from the six-years H.E.S.S. dataset collected between 2014-2020. The zenith angle distributions for each year of observations are given in Fig. 6.7. The red dashed line shows the mean zenith angle for the respective year. The bottom right panel shows the stacked distribution from the six years of observations.

Years	2014	2015	2016	2017	2018	2019	2020
Zenith [°]	19.7	19.7	12.0	13.2	19.7	18.2	18.3
Offset [°]	1.1	1.5	2.2	3.0	2.7	2.8	3.3

Table 6.2: Mean zenith and offset angles for the observational runs in each year of the 2014-2020 dataset.

6.3.2 Excess and Significance sky maps

Standard gamma-ray excess and significance maps are produced for the H.E.S.S. II dataset with the *Ring Background* method in the *CT1-4 Stereo* and *CT1-5 Stereo* modes, including the full five-telescopes array. No standard exclusion region on the known VHE sources is applied. The maps are shown in Fig. 6.8 for the zoomed

[1]Right ascension is a coordinated that together with the declination give the position of an object on the sphere of the sky. Unlike longitude, right ascension is usually measured in hours, minutes and seconds, where 24 hours corresponds to a full circle, *i.e.* 360°.

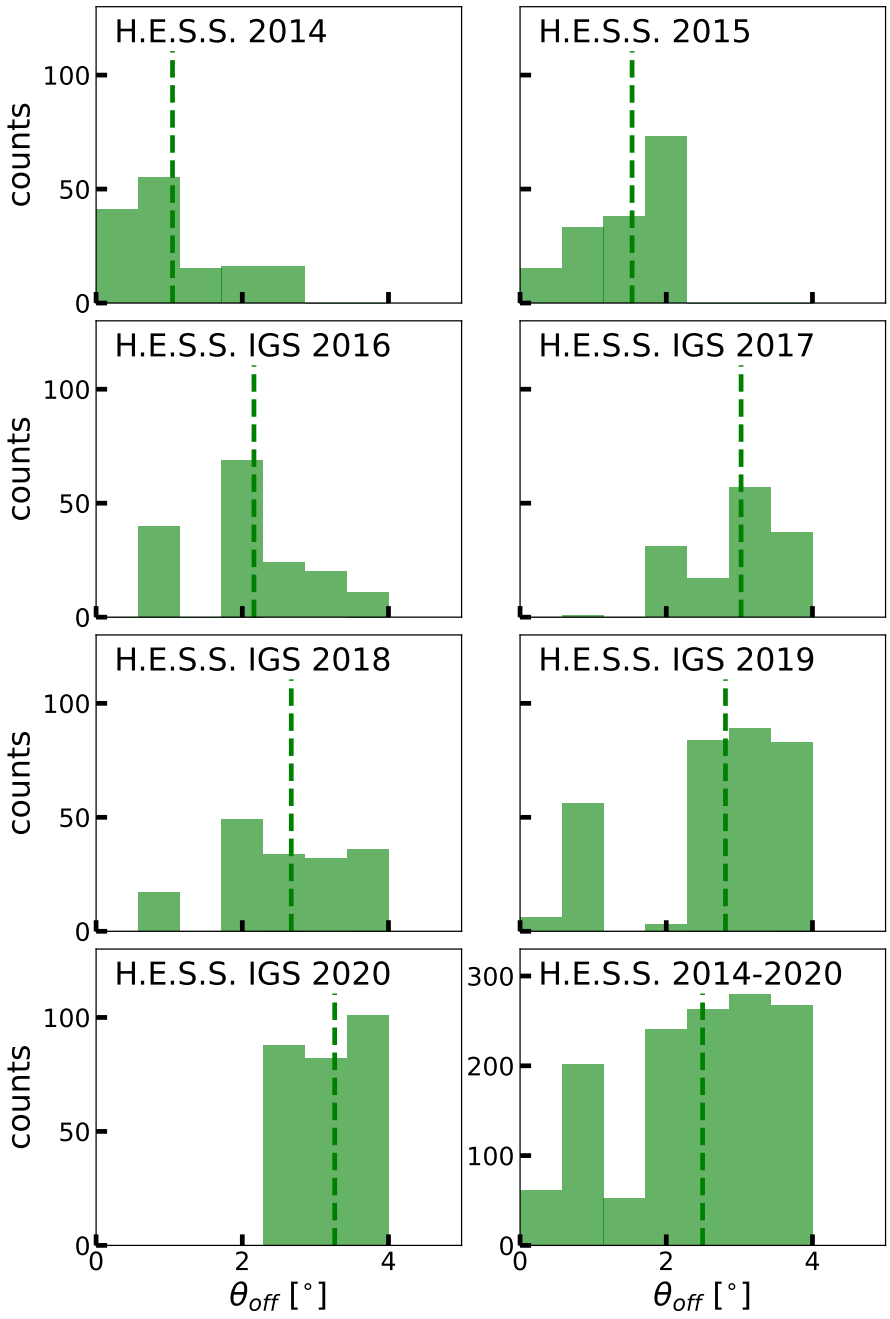

Figure 6.6: Distributions of the *offset* angles $\theta_{\rm off}$ between the nominal GC positions and the pointing position for the entire H.E.S.S. II campaign of observations of the inner halo of the Milky Way. The panels show the distributions for each year of observations and the stacked distribution from the whole 2014-2020 dataset. The green dashed line shows the mean offset angle for each distribution.

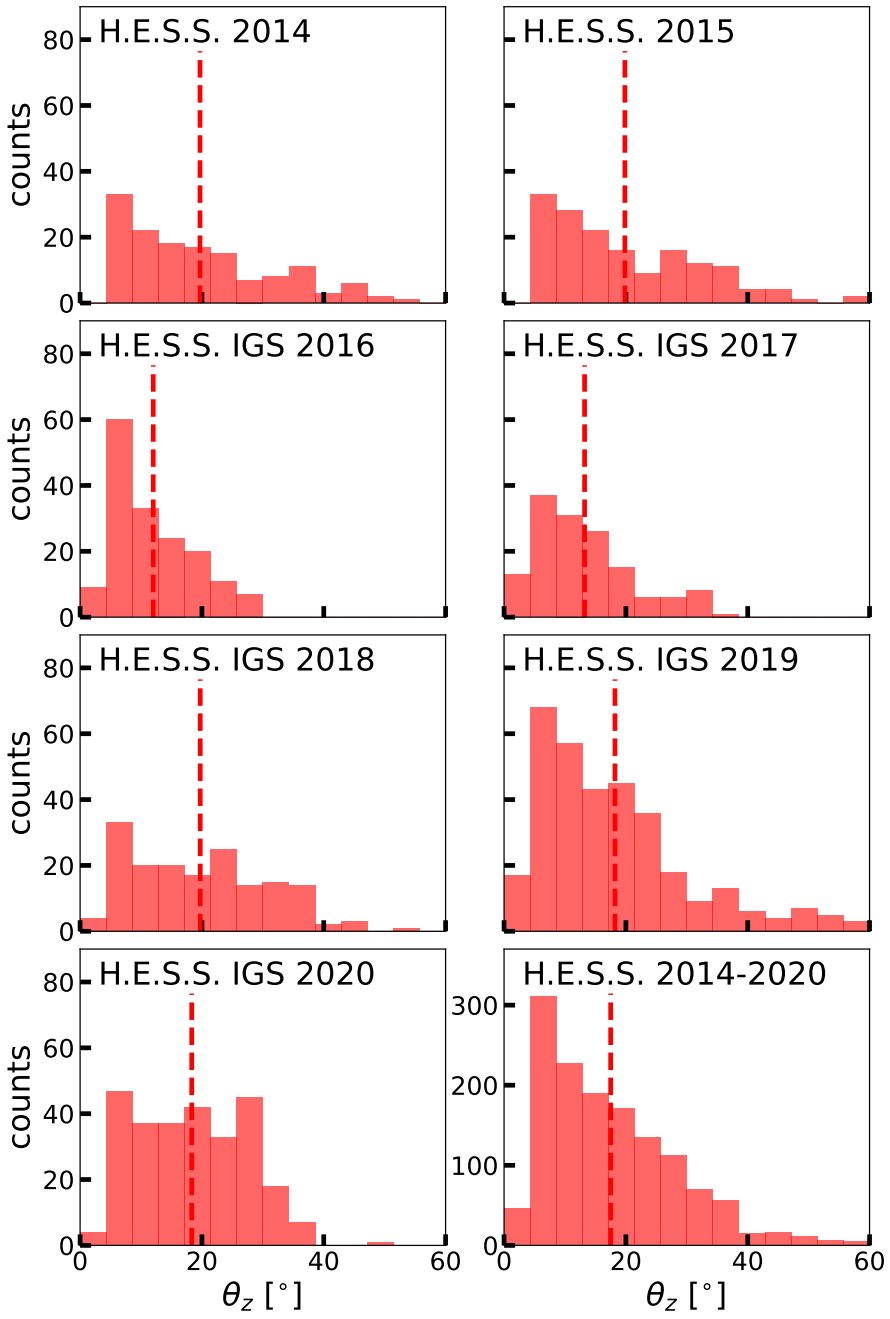

Figure 6.7: Distributions of the zenith angles θ_z for the pointing positions for the entire H.E.S.S. II campaign of observations of the inner halo of the Milky Way. The panels show the distributions for each year of observations and the stacked distribution from the whole 2014-2020 dataset. The red dashed line shows the mean zenith angle for each distribution.

region between -4° and 6° in Galactic latitudes and in |5°| in Galactic longitudes. The left panel shows the photon excess with respect to the background. The map is artificially saturated at 1000 counts. The middle panel shows the significance map in terms of standard deviations, saturated at 15 σ. Some significant hot-spots (with 4 σ significance above the background) are present in the map. The known VHE sources that stands above the background emission are HESS J1745-200 (Sgr A*), HESS J1747-281 (G09+01) and HESS J1745-30. The TeV emission from Sgr B2 is visible too. The diffuse emission can also be identified around the GC region. Known sources and hot-spots will be covered with exclusion regions during the analyses for the search for dark matter signals and Fermi Bubbles emission. During the analysis, the sources are covered with masks. No hint for a possible source detection in regions of the sky outside the masks is found.

The right panel of Fig. 6.8 shows the significance distribution obtained with the photon counts used for the production of the significance map. The distribution is fitted with a Gaussian function. The counts extracted from the pixels of the Significance map show significance values largely above the 5 σ. These are due to the high significance sources previously mentioned. However, if these sources are removed the bins of the Significance distribution are contained inside the Gaussian fit.

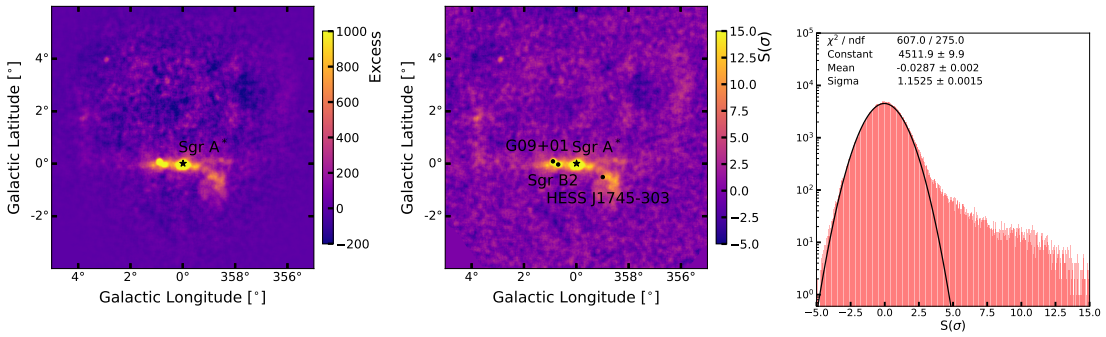

Figure 6.8: Gamma-ray excess map (left panel), significance map (middle panel) and significance distribution (right panel) for the H.E.S.S. II dataset, obtained with the *Ring Background* technique in the *CT1-5 Stereo* and *CT1-4 Stereo* modes. On the maps, no exclusion region is applied.

6.4 A study of the systematic uncertainties

The inner halo of the Milky Way is a complex environment with numerous sources emitting in the high and very-high-energy gamma-ray regimes. In this region, the level of the Night Sky Background (NSB) undergoes significant changes and this

may affect the measurement of the residual background at low energies. In the next sections we present the study to derive possible correlations between the gamma rate in the FoV and the level of NSB. We then investigate the homogeneity and isotropy of the measured residual background across the FoV, through the analysis of the distributions of the gamma-like rates measured from different pointing positions of the survey. The residual background is correlated with the zenith angle of the observations, therefore a gradient in the gamma-like rate is expected. In the next sections we also explain how we deal with this effect. A systematic uncertainty may arise when assuming imperfect azimuthal symmetry across the FoV of the telescope. We explain how we compute the number of counts as a function of the angle. Finally, we analyze the energy scale uncertainty by computing the energy shift that affect the energy reconstruction of the common events in the two H.E.S.S. analysis chains. The studies presented in this section are adapted to the configurations needed for the analyses that we performed to search for the FBs TeV emission (see Chap. 7) and DM annihilation signals (see Chap. 8). However, the procedure for the derivation of the level of systematic uncertainties is sufficiently general to hold for analyses with other datasets.

6.4.1 Night Sky Background and gamma-like rate correlation

In the FoV of the IGS dataset observations, the level of the Night Sky Background (NSB) undergoes significant changes due to the presence of the bright stars in the field of view. The NSB varies from a minimum of 25 MHz up to 400 MHz photoelectron rate per pixel in the FoV. However, the minimum and maximum values of NSB are in regions of the sky that are never covered by the region of interest of our analyses. The map of the NSB in the region has been already shown in Fig. 6.1. In the shower template analysis, a dedicated treatment of the NSB is performed as described in Ref. [153], where the contribution of the NSB is modeled in every pixel of the camera. With this analysis procedure, additional image cleaning to extract pixels illuminated by the showers is not needed. However, we want to check for possible residual NSB and gamma-like-rate correlation. For this, we define squared regions around some pointing positions of the IGS. The former are chosen with 1° side and with squared pixels of 0.1°x0.1°. We extract the values of the NSB from the pixels, we then build distributions and compute mean and RMS values for the NSB rate. From these values we find no correlations between the NSB and the background distribution for the different pointing positions considered for this test. In the left panel of Fig. 6.9 we show an example of the squared region extracted around pointing position 2-7 of the IGS dataset. In the region, the NSB varies between 110 MHz and 150 MHz. The scale of the panel has been restricted on purpose in the range between 100 MHz and 160 MHz to see the fluctuations of NSB. In the right panel of Fig. 6.9, we show the evolution of the gamma-like rate with respect to the changes in the NSB of the region. For

the analyses that we carried out with the H.E.S.S. II dataset, we extract regions of interest where the NSB varies between $\sim$ 100 MHz and 300 MHz. If we consider these two values, the gamma-like rate varies up to 1%. For all the pointing positions and the regions of interest that are used in the analyses with the 2014-2020 dataset, such a large difference in NSB rates is never reached.

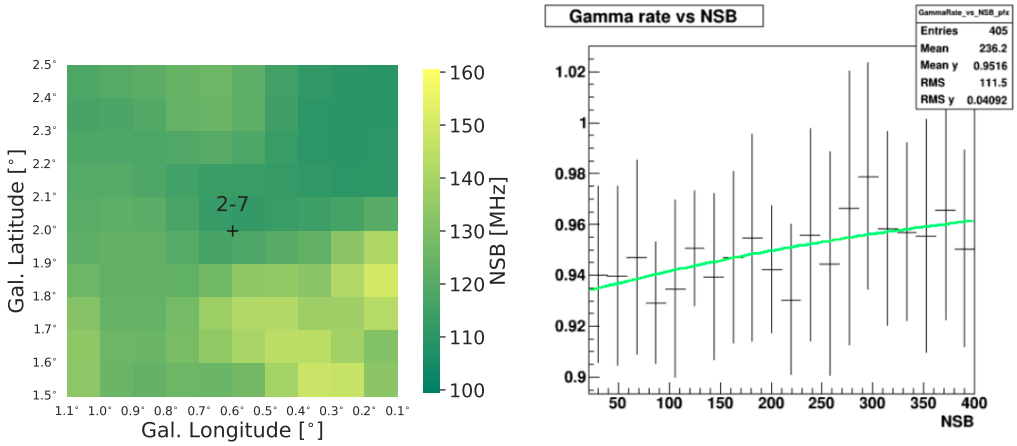

Figure 6.9: *Left panel:* Map of the NSB rate in MHz for the squared region of side 1° side and with squared pixels of 0.1°x0.1° taken around the IGS pointing position 2-7. *Right panel:* Gamma-like rate as a function of the NSB measured in the FoV of the 2014-2020 H.E.S.S. dataset. The NSB rates span from a minimum of 25 MHz up to 400 MHz, due to the high variability of the NSB of the region.

6.4.2 Zenith angle and gamma-like rate correlation

To analyze the homogeneity of the background rate across the FoV, we check the distributions of the gamma-like events for the considered dataset. For this, we extract the gamma-like number counts from the same squared regions defined in the previous section. We renormalize the counts by time exposure on a pixel-by-pixel basis and then compute mean and RMS of the distributions. The measured RMS results are larger than what is expected from statistics only. Therefore, we derive a mean value of systematics of 4% from all the regions that we considered for this study. In Fig. 6.10, we show one of the squared regions extracted around pointing position 2-7 of the IGS dataset. However, for the analyses with the IGS dataset, we can have a more precise definition of the region of interest for which we need to estimate the systematics uncertainty and we need to perform a computation valid on a run-by-run basis. Therefore, we adopt a second approach to investigate the possible inhomogeneity of the background rate across the FoV due to the gradient in the zenith angle of the observations. We investigate the corre-

lation between the difference in the zenith angles values and the gamma-like rate gradient. For this we take as an example the analysis for the dark matter search. For this analysis, we build ON regions where we search for the expected signal and control OFF regions where we measure the residual background. The ON regions are also referred to as the regions of interest (ROI). The OFF regions are built with the *Reflected Background* method, as explained later in Sec. 7.3.1 and Sec. 8.2.3. Applying this method, we reflect the ON region with respect to the pointing position and we define the OFF one. However, we know that by construction there are different values of zenith angles for events in the ON and in the OFF region. And for each degree of difference in the zenith angle across the FoV, we expect 1% gradient in the gamma-like rate. To test this, we build distributions of the zenith angles per ROI and per pointing position. The former are shown for two pointing positions and two ROIs in Fig. 6.11. The mean values of the distributions as well as the nominal zenith angle of the pointing position are shown in the figure too. From the test, we obtain a maximum difference between the mean values $\theta_{\mathrm{z,ON}}$ and $\theta_{\mathrm{z,OFF}}$ of 1°. For each run, ON and OFF distributions can be renormalized by the difference. Therefore, the gradient of gamma-like rate in the FoV is taken into account. However, the typical width of 1° of the obtained distributions introduces a systematic uncertainty. According to the expected 1% gradient for each degree of difference in the zenith angle, we consider a systematic uncertainty of 1%. This value will be applied on the normalization of the event energy distributions that are used for further analyses.

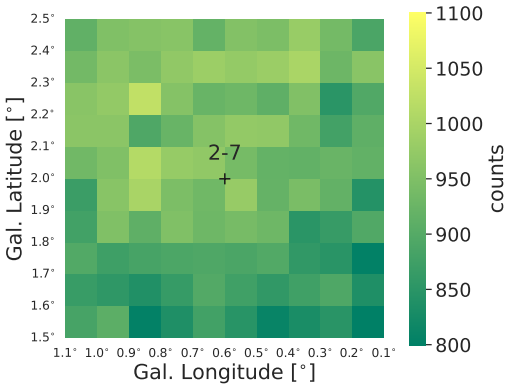

Figure 6.10: Map of the measured events from background for the squared region of side 1° side and with squared pixels of 0.1° $\times$0.1° taken around the IGS pointing position 2-7.

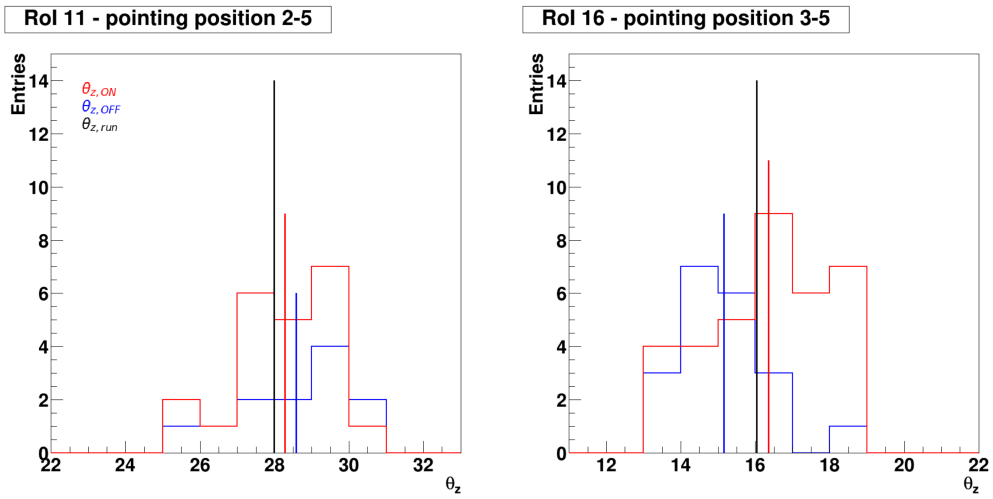

Figure 6.11: Zenith distributions obtained for the dark matter search analysis with the *Reflected Background* for two ROIs and two pointing positions. The red distribution is built from events extracted from the ON region, the blue one for the OFF region. The lines with the corresponding colors show the mean values of the distributions. The nominal zenith angle of the pointing position is shown as the black line.

6.4.3 Azimuthal symmetry in the field of view

To test the azimuthal symmetry in the FoV we consider annular regions built around some selected pointing positions. We probe different radius values but we report here the example for the ring of the region of $r_{in} = 0.7°$and $r_{out} = 0.8°$. These dimensions are the closest to the offset between the source and the pointing position, usually adopted for observations with the H.E.S.S. telescopes. One example of the ring built for the mentioned r_{in} and r_{out} is shown in the left panel of Fig. 6.12, in galactic coordinates. In this case, the IGS pointing position 2-6 is chosen. To test for azimuthal symmetry and see whether there is a preferred angle in the camera FoV, the rings are divided in 36 angular bins in which the number counts of gamma-like rates is estimated. Then, the distribution over the bins is built and the mean and RMS values are extracted. No systematic uncertainty is found apart from the expected 1% per degree of zenith angle gradient in the FoV. In the right panel of Fig. 6.12 we show the number of counts for each of the 36 angular bins. On this, we fit a function defined as $f(\alpha) = p_0 + p_1 \sin(k\alpha + p_2)$. We consider the fit for k=1, *i.e.* we test the first harmonic. From the fit, we derive p_1 as compatible with zero, which means that there is no first harmonic and the distribution of the counts over the angular bins is well in agreement with a constant. From this, we derived that there is no preferred angle in the camera FoV.

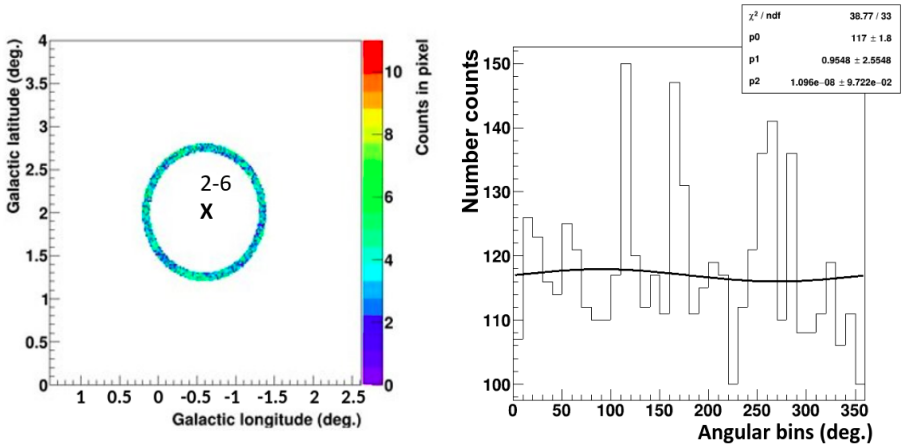

Figure 6.12: Test for azimuthal symmetry on one pointing position of the IGS dataset. *Left panel*: annular region built around pointing position 2-6 for $r_{in} = 0.7°$and $r_{out} = 0.8°$, in galactic coordinates. The color scale shows the count in each pixel of 0.02°×0.02°. *Right panel*: fit of the number counts extracted from 36 angular bins with the function defined as $f(\alpha) = p_0 + p_1 \sin(k\alpha + p_2)$. We consider the fit for k=1, *i.e.* we test the first harmonic.

6.4.4 Energy scale uncertainty

The reconstructed energies of photon events selected by the two H.E.S.S. official analysis chains do not match perfectly. The two chains have been previously explained in Sec. 2.3. We tested this discrepancy by comparing the events in our dataset reconstructed by the two chains. We take events from the whole FoV and match them through their timestamp in s and ns in the two chains. We then compute the mean of the difference between each energy value in HAP and PA, divided by the maximum value of the two. With the IGS dataset, we obtain that the systematic uncertainty on the energy scale of the energy distributions is 10%. The distribution of the difference values is shown in Fig. 6.13. However, this uncertainty affects similarly the energy scale of the measured and the expected energy count distributions. This would lead to an overall shift on the energy scale of the constraints that can be computed with the dataset. We therefore do not apply any correction for the former in the analyses that we carried out with the 2014-2020 H.E.S.S. dataset. However, the value of the width of the distributions is considered as value of systematics uncertainty.

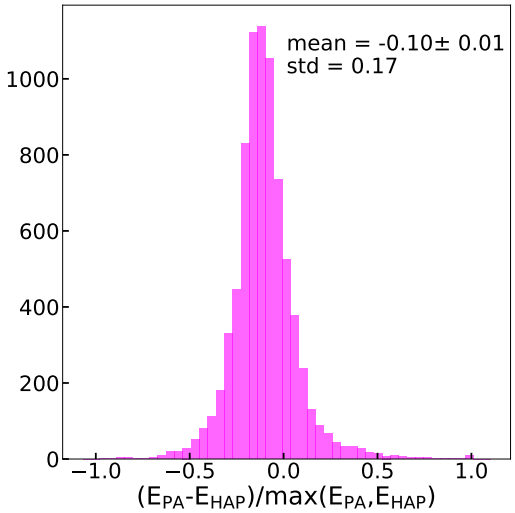

Figure 6.13: Distribution of the mean difference between the energy of the photon reconstructed in HAP and PA, divided by the maximum of the two values. The mean and the standard deviation of the distribution are given too.

6.5 First developments towards background models for the H.E.S.S. II dataset

For the analyses carried out with the 2014-2020 dataset, we build event energy distributions for ON and OFF regions, where we search for the signal and we measure the residual background. One possibility to cross-check the OFF distributions is to build background models from observations external to the dataset. For the background models, we adopt two approaches. For the first approach, we extract observations on extragalactic fields taken in the same observation conditions and build the event energy distributions. These are always distributions of gamma-like events, as extracted after the selection cuts already introduced in Sec. 2.3.4. For this, we do not need to mask any region in the chosen FoV, since we select runs on FoV with no significant detection. In particular we use observations of four unidentified Fermi objects (UFOs) with H.E.S.S. [10] and of a selection of DES dwarf spheroidal galaxies (dSphs) recently observed with H.E.S.S. [14]. For the second approach, we asked for the production of run-wise simulations for the 2014-2020 GC dataset. This approach consists in the simulation of the actual observation conditions and individual telescope configurations [208], carried out for each observational run. With this, spectrum tables for each observational run are generated. Moreover, events are simulated with the same parameters of each observational run and can be used after proper renormalizations.

6.5.1 Background models from blank-field extragalactic observations

To build a background model from extragalactic observations we select runs in zenith angle bins from the UFOs and dSphs dataset. These observations are particularly suited for the extraction of background only distributions since no significant excess is detected anywhere in the FoV. Therefore, no exclusion regions have to be applied to cover significant VHE sources. From these measurements we can extract gamma-like rate as a function of energy and offset from the pointing position and use them to predict the distributions of events as observed in the 2014-2020 H.E.S.S. GC dataset. However, the NSB of the FoV for the extra-galactic observations is different from the one measured for the GC region. As we have shown in the previous Sec.6.4.1, the NSB rate can vary in the inner halo of the Milky Way. This is not the case for the FoV of the UFOs and dSphs observations. Nevertheless, this should not affect too much the construction of the background model because the NSB level in the UFOs and dSphs FoV reaches the level of $\sim$ 150 MHz and the pointing positions are in regions where the NSB varies from $\sim$ 100 up to $\sim$ 250 MHz. As it was shown in the left panel of Fig. 6.9, a variation of NSB between $\sim$ 100 and $\sim$ 250 MHz implies a difference in the gamma-rate of $\sim$ 1% and could be included as an estimate of the systematic uncertainty.

To exploit the extragalactic observations that we selected, we perform the analysis in the *CT1-5 Stereo* mode as for the IGS dataset. We then divide the observational runs in zenith angle bins of 5° width. We compute event energy distributions for 100 energy bins logarithmically spaced between 0.1 and 70 TeV and for 100 offset bins between 0°and 10°. Each event is collected in the corresponding energy and offset bin. The offset value of each event is computed with respect to the pointing position of the run. In Fig. 6.14, we show the PDF of the event energy distributions for one selected offset bin of $\theta_{\rm off} \in [1.2°, 1.3°]$ and for the zenith bins that were covered with the observations over extragalactic fields. In Fig. 6.15, we show a comparison between the event energy distributions extracted from IGS observations and collected with the *Reflected Background* for the FBs analysis and from extragalactic observations. The distributions extracted from IGS observations are obtained by events measured from a few runs of the dataset and for some selected pointing positions. This is just an introductory example, more detailed studies are ongoing. The distributions from extragalactic observations are re-scaled for the solid angle of the ROI defined for the FBs analysis and for the livetime of the IGS runs used for the measurements of the events. The distributions are shown for the combinations of three zenith angle bins and two offset angle bins. In Tab. 6.3, we summarize the extracted $\mathrm{N}_{\rm tot,IGS}$ and $\mathrm{N}_{\rm tot,extra-gal.}$ from the distributions. $\mathrm{N}_{\rm tot}$ are extracted above a standard safe threshold for events reconstructed in *CT1-5 Stereo*, *i.e.* $E_{\rm thr} \simeq$ 200 GeV. The table also reports the percentage difference between $\mathrm{N}_{\rm tot,IGS}$ and $\mathrm{N}_{\rm tot,extra-gal.}$. The obtained percentage

difference varies between 5% and 13%, depending on the zenith and offset bins.

Zenith range	[15°, 20°[		[20°, 25°[		[25°, 30°[	
Offset range	[0.5°, 0.6°[	[2.0°, 2.1°[	[0.5°, 0.6°[	[2.0°, 2.1°[	[0.5°, 0.6°[	[2.0°, 2.1°[
$N_{\mathrm{tot,IGS}}$	347	94	254	61	50	50
$N_{\mathrm{tot,extra-gal.}}$	320	109	268	68	54	55
Percentage difference	8%	13%	5%	11%	7%	9%

Table 6.3: Total number of counts from IGS and extragalactic observations are given above the safe energy threshold. The percentage difference between the two is reported in the last row. Numbers are given for the combinations of three zenith angle bins and two offset angle bins.

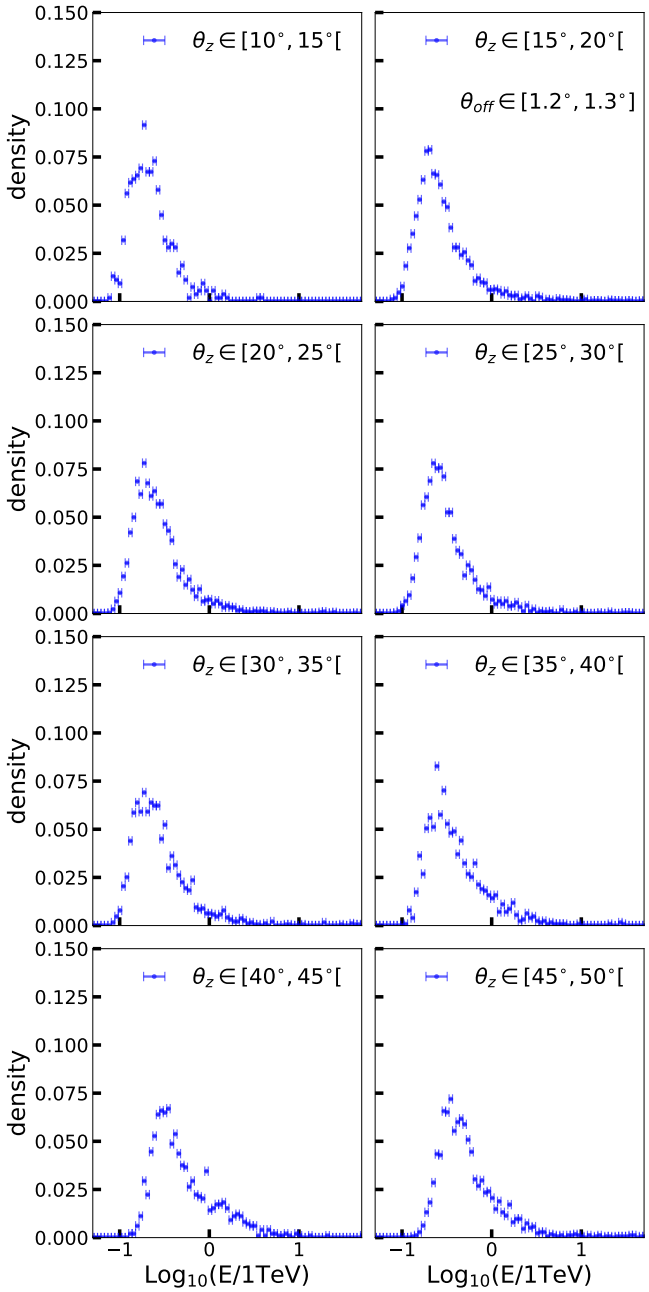

Figure 6.14: Density of the event energy distributions extracted from extra-galactic observations. The distributions are shown for some zenith angle bins and for one offset bin.

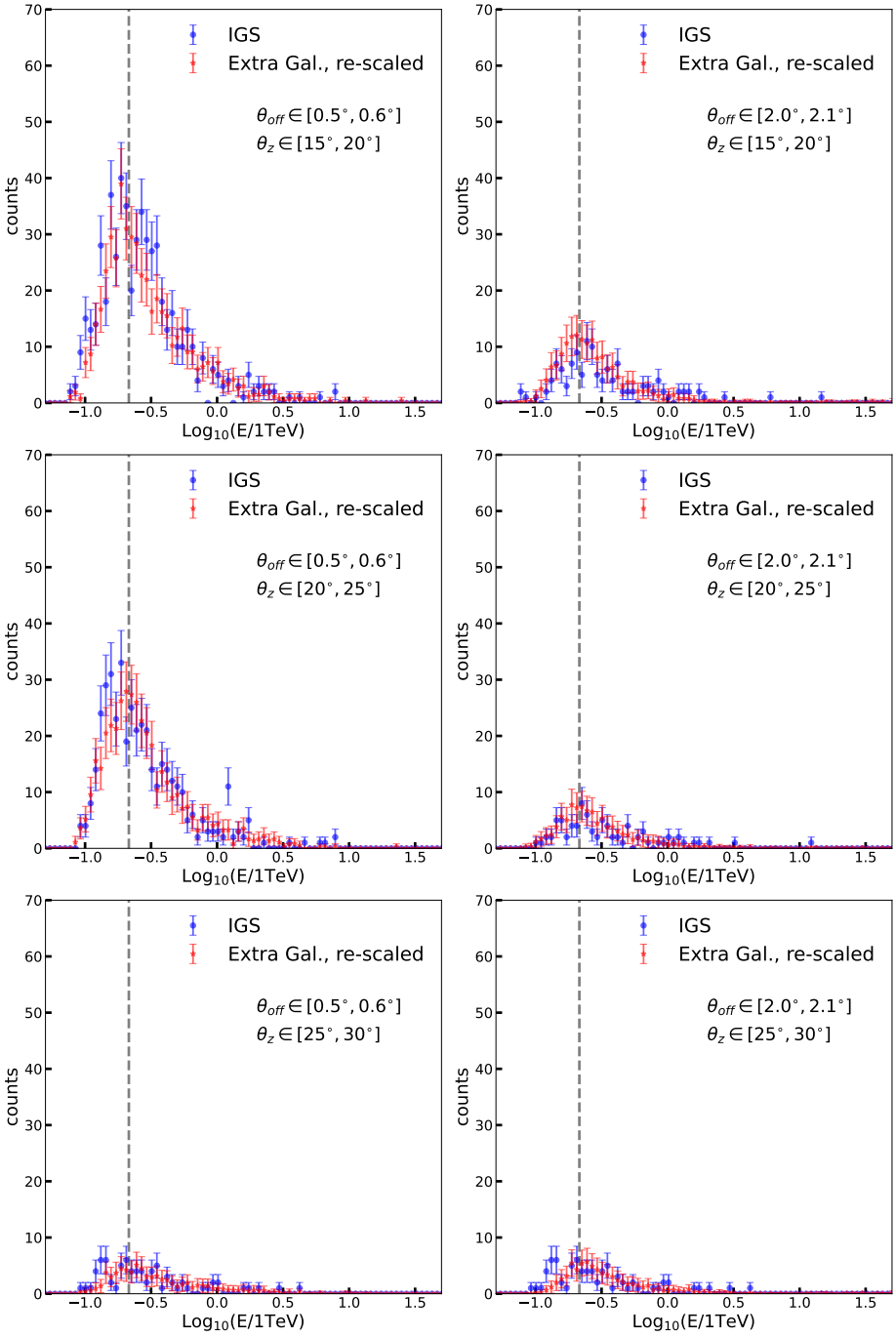

Figure 6.15: Event energy distributions extracted from IGS and re-scaled extra-galactic observations. More details about the construction of the distributions are provided in the text. The distributions are shown for the combinations of two offset angle bins and three zenith angle bins. The energy threshold is shown as the gray dashed line.

6.5.2 Background models from run-wise simulations

To build a background model from simulations we asked to process run-wise simulations (RWS) on run-by-run basis for the *CT1-5 Stereo* and *CT1-4 Stereo* modes, with the same observational conditions, status of the camera and configuration cuts that we used for the observed data analysis. The RWS are produced for the same observation conditions and telescope configuration as for the observed data: same muon efficiency, zenith angle of the observations and NSB level in the FoV of the observed region, are obtained. However, they are produced for what would be observed as for true gammas. This sets an important difference because the standard data analysis and the background model from extragalactic observations are obtained from the observation of mostly gamma-like events, since the background of misidentified cosmic rays dominates the outputs of the observations. As a standard procedure in the H.E.S.S. collaboration, RWS are produced for true gammas with power-law spectra with indexes much harder than the ones measured for observations in regions where only background is expected. This is done to simulate an artificially very hard spectrum, such to as have sufficient statistics especially in the highest energy bins. This is another difference to the measured extragalactic events.

To develop a background model from RWS events, the latter have to be renormalized by the radial acceptance expected for gamma-like events. Moreover, another renormalization is needed to take into account the much harder index used for the production. At the moment of the writing, we are exploring ways to define these renormalizations and obtain background models from RWS.

6.5.3 Comparison and application

Both approaches can be used for the construction of background models. To do so, event energy distributions in the zenith angle bins can be extracted and compared with the ones obtained from the measured H.E.S.S.-II GC dataset.

Events generated by the RWS are produced for all the runs in the 2014-2020 dataset, therefore they can be directly compared in terms of livetime even though some renormalization is needed due to the not perfect match in terms of parameters of the production of the simulations. Also, the RWS are produced with the same NSB condition as for the real 2014-2020 dataset. Once a recipe is found for the application of the renormalization for the index of the power-law and the difference in the radial acceptances, distributions of events from RWS can be built in the same zenith, offset and energy bins used for the construction of distributions from extra-galactic observations. The renormalizations are performed on an event by event basis by choosing the correct zenith, offset and energy bin at which the event belongs.

At the moment of the writing, we are working to compare measured event energy distributions obtained with the *Reflected Background*, for the standard anal-

ysis that we carried out for the search for the Fermi Bubbles emission, with the simulated ones, with events generated with the RWS and properly renormalized. The latter have to be renormalized according to the solid angle, used to collect the events in the distribution obtained with the *Reflected Background*, the livetime, the difference in the power-laws for the generation of events and the difference in the radial acceptances.

6.6 Conclusions and outlook

The observations of the inner halo of the Milky Way has been a long term key-science project of the H.E.S.S. collaboration. The IGS has been concluded in 2020 with observations up to 3.2° in Galactic latitudes. We have shown in this chapter a detailed review of the dataset and derived some important results:

- the IGS dataset has been extensively analyzed for the benefit of the analysis presented in this work but also for future usage in the H.E.S.S. Collaboration;
- the IGS dataset provides up to 5 times more time-exposure in the inner halo of the Milky Way with respect to previous H.E.S.S. I observations of the same region;
- we studied in detail many sources of systematic uncertainties;
- the estimation of the expected 1% gradient in the gamma-like rate is connected to the difference in the zenith angles of the observations;
- the typical width of zenith distributions of the observations can be used as a systematic uncertainty;
- some initial developments towards background models for H.E.S.S. II observations with extra-galactic observations and run-wise-simulations of the IGS dataset.

More hours have been granted to extend the Survey to negative latitudes, with the program called the Inner Galaxy Survey South (IGS South). The aim of the near future extended IGS observations is to reach uniformity of the exposure within several degrees around the Galactic Centre in all directions, *i.e.* not only for positive latitudes. Observations at negative latitudes will increase the still poor photon statistics measured by H.E.S.S. in that region. Moreover, a more extended exposure will be useful to study deeper the systematic uncertainties in such an extended and complex region at VHE. There will also be the possibility to train background models with more accuracy and larger statistics. Important results have been obtained with the 2014-2020 dataset and will be shown in the next chapters. The search for dark matter in the Milky Way and the search for the

expected TeV emission of the Fermi Bubbles have been long standing projects in the H.E.S.S. collaboration. The observations carried out with the IGS program and the usage of the full five-telescope array are fundamental to obtain the most constraining limits in the TeV DM particle mass range. VHE observations of the GC region with IACTs are unique for a thorough study of DM models. We present new results on this in Chap. 8. In addition, the extended exposure provided by the IGS dataset opens the possibility to study the Fermi Bubbles in the region where they are expected to be harder and brighter. We present the latest results on this in Chap. 7. At the time of the writing, the IGS South observations have started and more results will be available in the forthcoming years. Moreover, this extended dataset will play an important role in the study of the systematic uncertainties and it will be useful for future CTA datasets. Many dedicated ways of studying the uncertainties can be pursued: we showed some of these in this chapter. Run-wise simulations of the GC center observations and extra-galactic observations can be used for a thorough investigation. The IGS very-high-energy observations of the GC region are a very important entail from H.E.S.S. and are included as part of the H.E.S.S. Legacy Program. These results pave the way to more sensitive observations of the region with the CTA array, which will strengthen the limits on the results already obtained with H.E.S.S. and probably shed light over many still unanswered questions on the GC astrophysics.

Chapter 7

Search for TeV emission at the base of the Fermi Bubbles

Contents

Summary

The Fermi Bubbles (FBs) emission has been detected by the *Fermi*-LAT telescope more than a decade ago [163, 352]. Since the emission shows brighter intensity at low latitudes and no hint for a cutoff up to 1 TeV in the Fermi spectrum, we searched for the low-latitude FBs emission in the IGS dataset (see Chap. 6). In this chapter, we show the outcome of this search. Sec. 7.1 introduces the first results obtained by the Fermi telescope on the FBs emission at GeV energies. In Sec. 7.2, we define the region of interest for the search for the FBs with the H.E.S.S. IGS dataset. The dataset used for the analysis is briefly described in Sec. 7.3, together with the method used for the measurement of the background, the energy count distributions and the excess significance of the signal. Performance tests to assess the capability of our statistical framework to recover

a fake injected signal in the measured dataset are shown in Sec. 7.4. The energy-differential flux points, in the energy bins where a positive excess larger than 2 σ is found, and 95% C.L. upper limits are shown in Sec. 7.5. In the same section, we show the first derivation on constraints on the parent particle populations that can be responsible for the FBs emission. We conclude with Sec. 7.6, bringing also some possible outlook for future analyses. At the moment of the writing, the analysis shown in this chapter is being prepared for submission to *Nature* within a few months [140].

7.1 Introduction

The Fermi Bubbles (FBs) are two large lobe-like structures extending up to about 55° above and below the Galactic center (GC) that have been detected by the *Fermi*-LAT telescope [163, 352]. The high-latitude Bubbles (*i.e.* at Galactic latitudes $|b| > 10°$) morphology is consistent with a uniform distribution and they show an energy spectrum $\propto E^{-2}$ significantly softening above $\sim$ 100 GeV. The exploration of the Bubbles have been performed at other wavelengths too: the microwave haze [163, 310] or the X-ray features observed at high latitudes [316] or near the GC [311] have been measured.

The characterization of this emission has been tried by applying hadronic and leptonic models. The former requires relativistic protons/electrons injected into the medium through outflows from the region close to the GC. Both continuous or sporadic injections could have happened in the past. Possible sources for the explanation of these outflows are the supermassive black hole Sagittarius A* [187, 367, 92, 53], outflows driven by multiple core-collapse supernovae [371] or star formation near the position of Sgr A* [148].

The low-latitude FBs emission, *i.e.* $|b| < 10°$, shows brighter intensity than the high-latitude one in the *Fermi*-LAT spectrum, behaving as $\propto E^{-2}$ with no sign of cutoff and remaining hard up to $\sim$ 1 TeV [24, 198]. The *Fermi*-LAT spectrum of the Fermi Bubbles is shown for the analysis at $|b| > 10°$ and $|b| < 10°$ in Fig. 7.1, as extracted from Ref. [24]. Deep observations of the low-latitude FBs at VHE can provide fundamental insights on the understanding of the origins of the Bubbles. The formation scenario of the Bubbles could be discriminated between AGN-like burst or star-formation activity close to the GC with VHE observations.

7.2 Defining the region of interest

The definition of the region of interest (ROI) for the search of the low-latitude FBs emission is based on a *Fermi*-LAT surface brightness spatial template extracted from Ref. [198]. The ROI is hereafter also referred to as the ON region. We are limiting our analysis to the region of $|b| < 5°$ where the maximum of the IGS exposure is located, as it was shown in Sec. 6.2. The template from the *Fermi*-LAT analysis is shown in Fig. 7.2, in term of surface brightness in units of sr because the total brightness has been integrated over the total volume of the sky considered for the template. To define the ROI, we consider a threshold of 8.5 sr^{-1} on the template and take all the pixels of the Fermi template inside as ROI for the search of FBs emission with our dataset. The measurement of the background is performed with the *Reflected Background* method, which is explained more in detail later. The ROI defined with this threshold subtends a solid angle of $\Delta\Omega = 1.9\times10^{-3}$ sr. The largest value for the template emission is located at the pixel centered at (l=-1.25°,

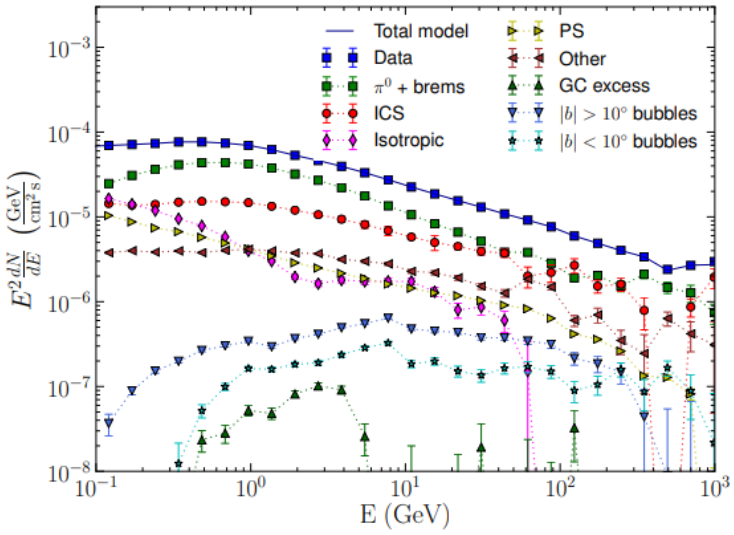

Figure 7.1: Fermi Bubbles and GC excess spectra extracted from Ref. [24]. The figure shows the various components studied in the *Fermi*-LAT analysis. The emission measured from the Bubbles in the GeV energy range by the *Fermi*-LAT experiment is shown as blue triangles and cyan stars for $|b| > 10°$and $|b| < 10°$, respectively.

b=1.75°), which is well inside the region where the IGS exposure is peaked. The contour defining the ROI is shown in Fig. 7.3 as a black dashed line. Contours for other values of the surface brightness on the template are shown as white solid lines. The color scale shows the time exposure of the dataset used for the analysis, with the brightness peak clearly inside the defined ROI.

7.3 Observations and datasets

The analysis for the search of the low-latitude FBs emission is performed with the observational dataset collected between 2014 and 2020, including the observations during the IGS period. The analysis of the data was performed in *CT1-5 Stereo* mode for the observations collected in 2014-2019 and in *CT1-4 Stereo* mode for the observations collected in 2020. This dataset was extensively described in Sec. 6.2. The technique for the selection and reconstruction of gamma-like events has been already referenced in Sec. 6.2. At least ten hours of acceptance-corrected exposure time was reached up to $b \approx$ +6°. We already showed the time-exposure map in Sec. 6.2.

The GC is a complex region, crowded with many astrophysical emitters. Such an environment includes numerous regions with detected VHE gamma-ray emissions [36, 19, 8]. Moreover, the varying night sky background has to be consid-

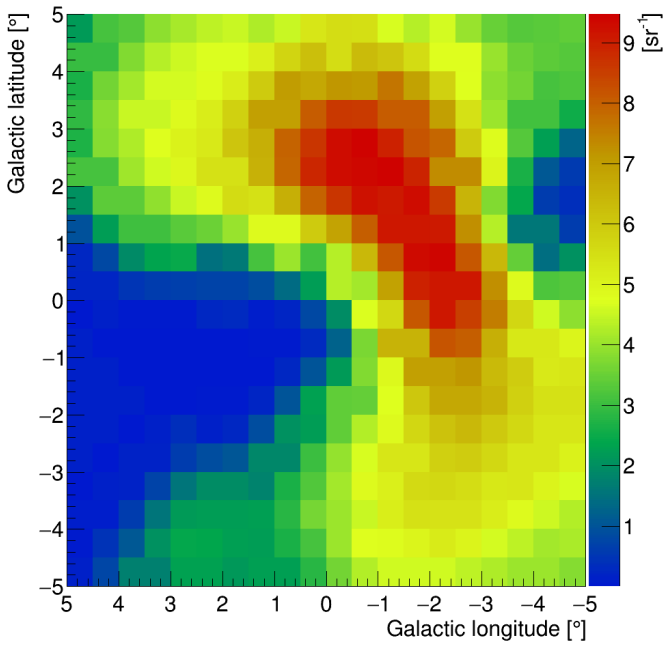

Figure 7.2: Surface brightness spatial template of the FBs emission as derived from the *Fermi*-LAT analysis [198]. The color scale is shown in units of sr^{-1}. The template emission peaks at the pixel located at (l=-1.25°, b=1.75°).

ered when observing the region [11]. The systematic uncertainties affecting the dataset have been studied in detail and extensively described in Sec. 6.4. The exclusion regions chosen to avoid leakage of VHE signals in the region used for the search for the FBs emission or for the measurement of background are shown in Fig. 7.3, superimposed on the time-exposure map of the IGS dataset. The set of masks used in the analysis includes the Galactic plane between $\pm$0.3°, the diffuse emission region around the GC [19], sources from Ref. [8], and all VHE gamma-ray sources in the field of view. 13 masks on sources from the 3FHL *Fermi*-LAT catalog are added as well [40]. The results that are shown in the chapter have been cross-checked with two independent analyses exploiting the results of an independent calibration and analysis chain [301].

The acceptance of the H.E.S.S. instrument considered for this analysis is shown in Fig. 7.4. It is built by taking the value of the acceptance for each run k, $A_{\mathrm{eff},k}(E_\gamma)$, in the dataset and computing a time averaged acceptance, using the observed time $T_{\mathrm{obs},k}$ of each run k. The spatial response of the instrument is taken into account for each run k because the acceptance term depends on the angular distance between the reconstructed event position and the pointing position of the run k. The final acceptance for this analysis is therefore also obtained as an offset averaged acceptance, the latter obtained using the offset between each spatial pixel in the H.E.S.S. ROI and the pointing position of each run k. This computation

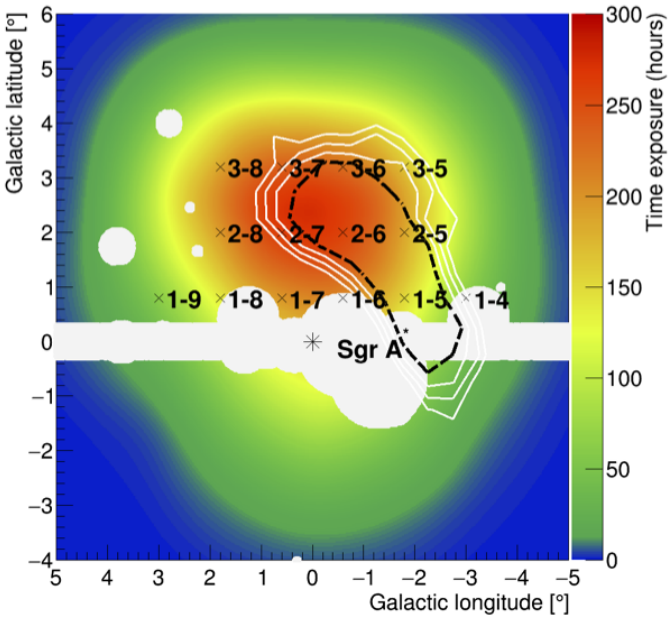

Figure 7.3: Time-exposure map of the data collected between 2014 and 2020. The position of the supermassive black hole Sagittarius A* is symbolized by the black star. The region of interest for the search of the FBs emission is shown as the black dashed contours. Other brightness contours (in sr^{-1}) on the *Fermi*-LAT spatial template are shown as the white lines. The set of masks used in the analysis is shown as the light-gray shaded area.

is also weighted by the solid angle of each pixel and the solid angle of the ROI.

For this analysis, a safe energy threshold is defined by taking the value of the energy at which the acceptance of the H.E.S.S. instrument reaches 25% of its maximum value. From this criterion, the safe energy threshold for the low-latitude FBs emission search is fixed to E_{thr} = 300 GeV.

7.3.1 Measurement of the residual background

For the determination of the residual background in the search for the FBs emission, the *Reflected Background* method is used. With this method, the measurement of the background is performed simultaneously in the same field of view as for the signal measurement on a run-by-run basis. The OFF region for the measurement of background is taken symmetrically to the ON region with respect to the pointing position, as described in Refs. [20, 13]. Therefore, the measurements from the OFF regions are performed under the same observational and instrumental conditions as the ON region. Exclusion regions are removed similarly for the ON and OFF measurements, which are therefore carried out with the same

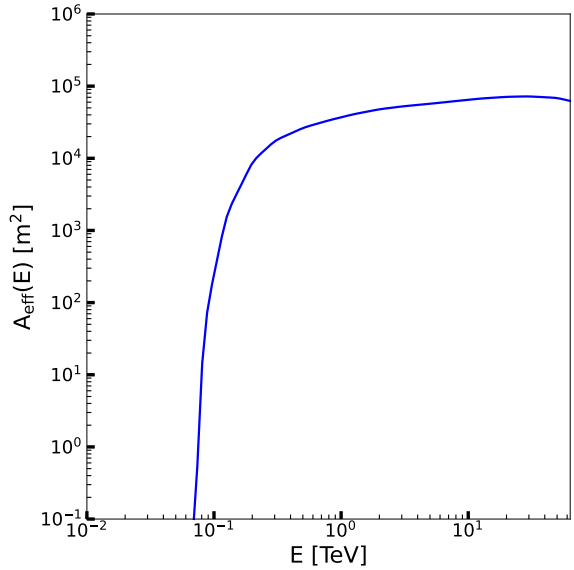

Figure 7.4: Acceptance, as a function of energy, for the FBs analysis with the 2014-2020 dataset. The acceptance is built for the combination of the *CT1-5 Stereo* and *CT1-4 Stereo* methods, as a time and offset average over the run acceptances $A_{\mathrm{eff},k}(E_\gamma)$.

solid angle size. This procedure is performed on a run-by-run basis and produces an accurate determination of the residual background. We show two examples of the measurement of background for the ROI and the pointing position (black crosses) 2-6 (l = -0.6°, b = 2.0°) and 3-8 (l = 1.8°, b = 3.2°) in Fig. 7.5. Photons with offset from the center of the camera, *i.e.* the pointing position, larger than 2.5° are excluded from the analysis. This is a safe analysis because the radial acceptance of the camera in the analysis chain that we used drops significantly after 2.5°. This effect is visible in the right panel of Fig. 7.5. The expected FBs emission is always larger in the ON region than in the OFF regions. With this method we measure the ON and OFF event energy count distributions that are shown in the next section.

7.3.2 Energy count distributions and excess significance in the region of interest

After the spectral and spatial information reconstruction of each event as a gamma-ray like is performed in *CT1-5 Stereo* or *CT1-4 Stereo* modes depending on whether the event was collected in 2014-2019 or 2020, energy count distributions are built. The distributions for the ON and OFF region, for a ROI threshold of 8.5, are shown in the left panel of Fig. 7.6. The energy threshold defined with the acceptance criterion previously explained is shown by the gray solid line. The excess significance is computed for each energy bin above the safe energy thresholds of 300

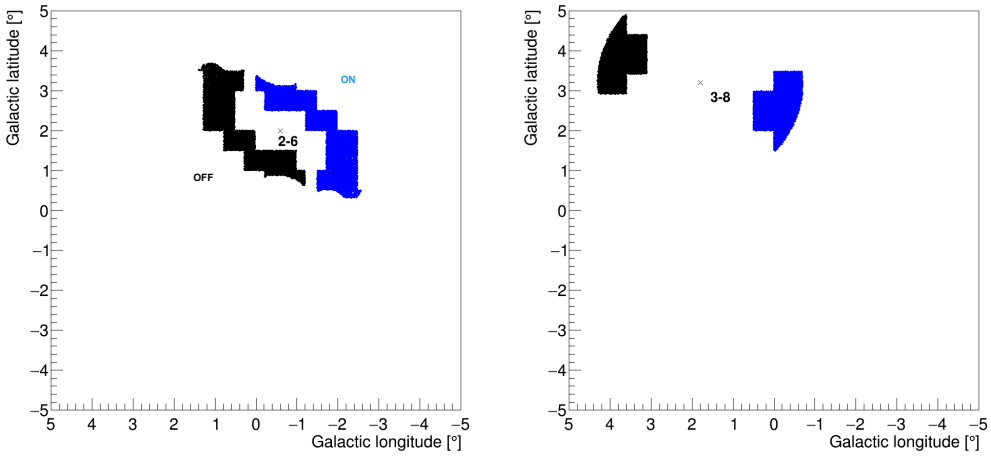

Figure 7.5: Measurement of background in Galactic coordinates for pointing positions 2-6 and 3-8 of the IGS (black crosses) and the FBs analysis. ON and OFF regions are shown as the blue and black shaded areas, respectively. The masked regions are excluded similarly in the ON and OFF regions such that these regions keep the same solid angle size and acceptance.

GeV, following the statistical approach defined in Ref. [247] and Eq. 4.10. The excess significance values for each energy bin are shown in the right panel of the same figure. Significance values are not computed for energy bins below the energy thresholds, indeed these are discarded since are dominated by systematic uncertainties and cannot be used for the analysis.

A clear positive excess is visible in the first energy bins above the threshold. The integrated value of the significance from all the energy bins above the energy threshold is $S = 9.2\,\sigma$. The excess significance are also computed for the spatial bins defined for the H.E.S.S. ROI from the *Fermi*-LAT spatial template, integrated over the spectral bins above the safe energy threshold. The positive excess is visible for some spatial bins, as shown in Fig. 7.7. The distribution of the excess significance is computed and shown in the right panel of the same figure. The mean and RMS values of significance obtained are mean $S = 1.7\,\sigma$ and std $S = 2.3\,\sigma$.

7.4 Performance tests for fake-signal injection reconstruction

In this section we show performance tests that we carried out in order to assess the capability of our framework to reconstruct a fake injected signal.

The statistical data analysis for the detection of the fake signal is based on

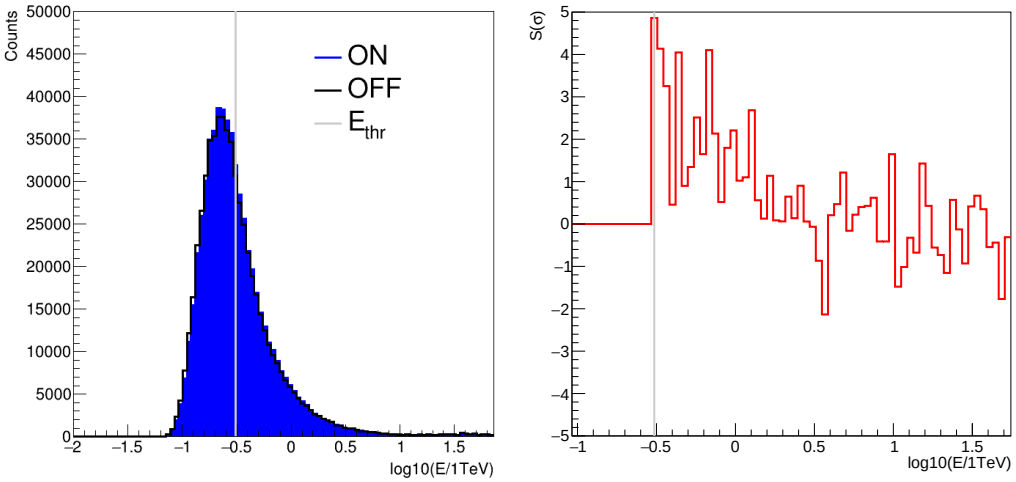

Figure 7.6: ON and OFF energy count distributions built as a function of energy with the *Reflected Background* method and for the ROI threshold of 8.5 sr^{-1}. The safe energy threshold is shown as well by the gray line. The right panel shows the excess significance in each energy bin computed with Eq. 4.10.

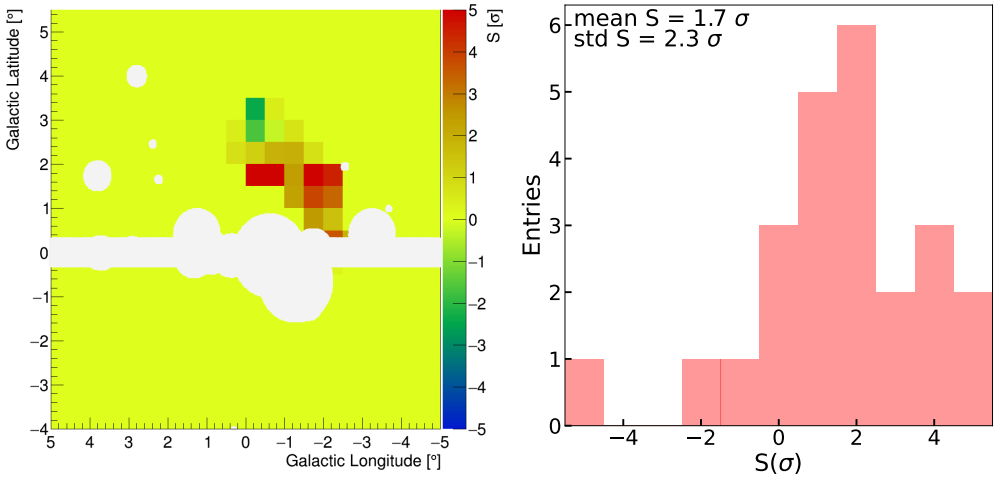

Figure 7.7: Excess significance computed with Eq. 4.10 in each spatial bin in Galactic coordinates and integrated over the spectral bins above the safe energy threshold. The masked regions are shown as the light-gray shaded area. The right panel shows the distribution of excess significance in the spatial bins.

a log-likelihood-ratio test statistics (TS) which exploits the expected spectral and spatial shapes of the signal against background in energy and spatial bins defined in the H.E.S.S. ROI. For given energy and spatial bins, the likelihood function is taken from Eq. 4.8. In the individual likelihood, the event measured in the ON and OFF regions correspond to the terms $N_{\mathrm{ON},ijk}$ and $N_{\mathrm{OFF},ijk}$, in the spectral and spatial bins i, j and k. We are considering two indices for the spatial bins because Galactic longitude and latitude are considered as spatial coordinates here. N^{B}_{ijk} is the expected number of background events in the ON region. N^{S}_{ijk} and $N^{\mathrm{S}'}_{ijk}$ are the expected number of signal events in the ON and in the OFF regions, respectively. N^{S}_{ijk} is obtained by folding the expected flux for the assumed emission model by the energy-dependent acceptance and energy resolution. The total number of events in the spatial bins j and k and spectral bin i is computed as N^{S}_{ijk}+N^{B}_{ijk}. The parameter $\alpha_{jk} = \Delta\Omega_{\mathrm{OFF}}/\Delta\Omega_{\mathrm{ON}}$ is the ratio between the solid angle of the ON region jk and its corresponding OFF region. Since in this analysis each OFF region is taken symmetrically to the ON region with respect to the pointing position, $\alpha_{jk} = 1$. We use the likelihood framework for the computation of 95%C.L. upper limits on the free parameter that we assume in the model describing the emission. The total likelihood is built either as a product over the energy bins only (1D) or as a product over energy and spatial bins in the H.E.S.S. ROI (3D).

When the fake emission is injected in the data and no significant excess is found in the ON region, constraints on the free parameter are obtained from the log-likelihood ratio TS described in [147] assuming a positive signal. In the high statistics limit, the TS follows a χ^2 distribution with one degree of freedom. The values of the free parameter for which $\mathrm{TS} = 2.71$ correspond to the 95% confidence level (C.L.) upper limits.

In order to assess the capability to detect a signal from a power-law extrapolation in the TeV energy range of the *Fermi*-LAT spectrum, we define a model for the searched low-latitude emission of the Fermi Bubbles as a power law with an exponential cut-off:

$$\Phi(E,l,b) = \Phi_0 \left(\frac{E}{1\mathrm{TeV}}\right)^{-\Gamma} \exp\left(-\frac{E}{E_{\mathrm{cut}}}\right) \times \frac{K(l,b)}{\overline{K(l,b)}}; \tag{7.1}$$

where Φ_0, Γ and E_{cut} are the normalization, spectral index and energy cutoff of the model. The factor $K(b,l)$ is the normalized surface brightness and accounts for the spatial dependency of the searched emission as derived in Ref. [40]. Using this emission model, we compute the N^{S}_{ijk} term used in Eq. 4.8. We make use of the 1D and 3D statistical methods described previously to compute upper limits on the parameters that constrain the searched emission in Eq. 7.1. In the 3D method we exploit both the morphological and the spectral information in the computation.

Assuming a different combination of the parameters characterizing the searched emission model, we make performance tests. One possibility is to test the reconstruction power on the normalization of the searched emission. We choose a

value $\Phi_{0,\mathrm{inj}}$ and we create a fake signal $\tilde{N}^{\mathrm{S}}_{ijk}$ with the model in Eq. 7.1 and inject it into the measured background $N_{\mathrm{OFF},ijk}$ to create fake energy count distributions for the ON and the OFF regions, i.e. $\tilde{N}^{\mathrm{S}}_{ijk}$+$N_{\mathrm{OFF},ijk}$ and $\tilde{N}^{\mathrm{S}'}_{ijk}$+$N_{\mathrm{OFF},ijk}$, respectively. With this setup, we run the TS procedure considering the free parameter $\Phi_{0,\mathrm{inj}}$ and $\Gamma = 1.9$ and $E_{\mathrm{cut}} = 50$ TeV fixed. We obtain 95%C.L. upper limits on the parameter tested. The LLRTS profiles for the reconstruction of an injected signal with $\Phi_{0,\mathrm{inj}}$ = 1.0$\times$10^{-9} TeV cm^{-2}s^{-1}sr^{-1} and $E_{\mathrm{cut}} = 50$ TeV are shown in Fig. 7.8. The two panels show the cases with different Γ values of the injected signal. The profiles are shown for the two ways of building the total likelihood: from the 1D and 3D individual likelihoods. For the injection with $\Gamma = 1.0$, almost 3 σ reconstruction is achieved for the 3D likelihood case, which can be seen from the depth of the well. When the index is fixed to $\Gamma = 2.2$, the reconstruction weakens to slightly more than 2 σ. The results for the reconstruction of some values of the normalization $\Phi_{0,\mathrm{inj}}$ are reported in Tab. 7.1. When injecting $\Phi_{0,\mathrm{inj}}$ = 3.0$\times$10^{-9} TeV cm^{-2} s^{-1} sr^{-1}, we obtain a sensitivity on the reconstruction power larger than 5 σ. If we set $\Gamma = 2.2$, the 1 σ bands weaken by a factor of 5%. As it can be seen from the table, for injected values of $\Phi_{0,\mathrm{inj}}$ lower than 1.0$\times$10^{-9} TeVcm^{-2} s^{-1}sr^{-1}, we cannot recover the signal. However, our framework is demonstrated capable of recovering signals with normalizations $\leq$ 1.0$\times$10^{-9} TeVcm^{-2}s^{-1}sr^{-1} which is at the level of the detected signal from the FBs with *Fermi*-LAT. Tests with the injection of a signal using two free parameters, as for instance ($\Phi_{0,\mathrm{inj}}$, Γ_{inj}) or ($\Phi_{0,\mathrm{inj}}$, $E_{\mathrm{cut,inj}}$) are performed. However, no reconstructive power is reached for Γ_{inj} or $E_{\mathrm{cut,inj}}$.

$\Phi_{0,\mathrm{inj}}$	1D reco.	3D reco.
1.0×10^{-10}	$< 7.41 \times 10^{-10}$	$< 6.61 \times 10^{-10}$
5.0$\times$10^{-10}	$< 1.15 \times 10^{-9}$	$< 1.10 \times 10^{-9}$
1.0×10^{-9}	$(1.00^{+0.62}_{-0.65}) \times 10^{-9}$	$(1.00^{+0.58}_{-0.61}) \times 10^{-9}$
3.0×10^{-9}	$(3.02^{+0.61}_{-0.68}) \times 10^{-9}$	$(3.02^{+0.61}_{-0.62}) \times 10^{-9}$

Table 7.1: Results for the performance study for injected fake signal in the measured OFF distribution of events. The first column gives the injected value of Φ_0 in TeV cm^{-2} s^{-1} sr^{-1}. Γ and E_{cut} are set to 1.9 and 50 TeV, respectively. The second and third columns provide the reconstruction values of Φ_0 in TeVcm^{-2}s^{-1}sr^{-1} obtained with the 1D and 3D methods, respectively.

7.5 Differential flux points and upper limits

The photon statistics collected in the ON and OFF regions and already shown in Fig. 7.6 is re-binned for 0.2 dex spectral bins (*i.e.* 5 spectral bins for energy decade). Then, the excess significance values are recomputed for this binning. Photon statistics and excess significance as a function of the new energy bins are

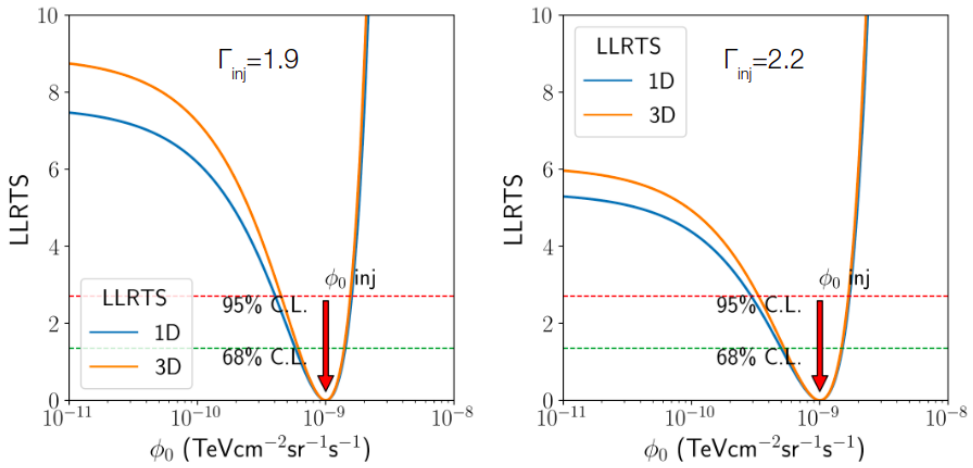

Figure 7.8: LLRTS profiles for the recovery of a fake injected signal with $\Phi_{0,\mathrm{inj}}$ = 1.0×10^{-9} TeV cm^{-2} s^{-1} sr^{-1} in the OFF distributions obtained in the FBs analysis. The fake signal is computed with Eq. 7.1. The left and right panels show the profiles for fixed indexes of Γ_{inj} = 1.9 and Γ_{inj} = 2.2, respectively. Profiles for 1D and 3D LLRTS are given as the blue and orange lines, respectively.

shown in Tab. 7.2. The positive excess is now clearly present in the first energy bins, with a significance excess of 7.6 σ and 4.5 σ for the first two energy bins.

For the first four energy bins, where we obtain statistical excess significance larger than 2 σ, we compute energy-differential observed flux points. When the obtained excess significance is lower than 2 σ, energy-differential observed flux upper limits at 95% C.L. are computed with the method explained in Ref. [326]. The current derivation of flux points and flux upper limits includes a systematic uncertainty of 20%, defined as a default conservative choice for all the energy bins. Explanations on the study of the systematic uncertainties for this analysis are given later. However, this estimate is not the final one and more studies are ongoing to have a more accurate determination of the systematic budget in each energy bin. The computation of flux upper limits and points is performed with the re-binned acceptance defined from the one already presented in Sec. 7.3, the solid angle of the ROI and the total live time for the dataset.

95%C.L. energy-differential expected flux upper limits are also derived. This is done through a set of 100 Poisson realizations of the measured background events in the OFF distributions for the 0.2 dex energy bins. For each energy bin, a Poisson realization of the measured background energy count distribution is computed independently for the ON and the OFF regions, respectively. For construction, the OFF energy count distribution already includes some of the potential FBs signal. This can be seen from the pixels on the surface brightness template that are included in the OFF regions and the Eq. 7.1. The normalized surface brightness

values of the pixels enter the equation.

For each realization of the energy count distribution in the ON and in the OFF regions, the corresponding value of the differential flux upper limit is computed according to the same method used for the observed flux upper limits and points [326]. From the mean, the 1 and 2σ standard deviation of the obtained distribution of the expected flux upper limits, the mean expected flux upper limits, the 1 and 2σ bands are derived, respectively. The 20% systematic uncertainty is included in the derivation of the mean expected limits. Systematic uncertainty dominates the mean expected limits and the containment bands over the statistical uncertainty.

In Fig. 7.9, we show the energy-differential observed flux points and upper limits together with the mean expected ones and the containment bands. The positive excess is visible at low energy right above the energy threshold. Energy-differential flux points from the *Fermi*-LAT analysis are shown too, as adapted from the analysis in Ref. [198] and re-computed for our ROI. The right panel of the same figure shows the energy-differential observed flux points and upper limits derived with the two alternative H.E.S.S. analysis chains [139]. The results with the cross-check analysis chains are in agreement, within the statistical uncertainties, with the lead chain from the energy threshold up to $\sim$ 2 TeV. Between 2 TeV and $\sim$ 40 TeV, the cross-check results are either in agreement with the lead observed flux upper limits or with the containment bands. Above 40 TeV, the cross-check analyses are in disagreement, however many systematic uncertainties affect the analyses at these energies and more studies are ongoing to obtain a refined estimation.

E_{min} [TeV]	0.30	0.46	0.71	1.11	1.73	2.70	4.22	6.57	10.25	15.99	24.93	38.89
E_{max} [TeV]	0.46	0.71	1.11	1.73	2.70	4.22	6.57	10.25	15.99	24.93	38.89	55.49
N_{ON}	127618	65962	34806	18230	9571	4913	2742	1557	998	1077	1425	1035
N_{OFF}	123800	64077	33905	17744	9466	5033	2669	1513	1039	1106	1416	1108
S(σ)	7.6	4.5	3.5	2.6	0.8	-1.2	1.0	0.8	-0.9	-0.6	0.2	-1.6

Table 7.2: For each of the energy bins for the 0.2 dex binning, the photon statistics and the excess significance are reported. In the first two rows, the minimum and maximum value enclosing the energy bins are given. The third and the fourth rows show the measured photon statistics in the ON and OFF regions, respectively, above the energy threshold. The last row reports the excess significance computed with the ON and OFF statistics applying Eq. 4.10.

7.5.1 Deriving the energy cut-off of the parent particle populations

The high-energy emission measured by *Fermi*-LAT can be explained by inverse-Compton or pion-decay, depending on the type of injected particles. Injected rel-

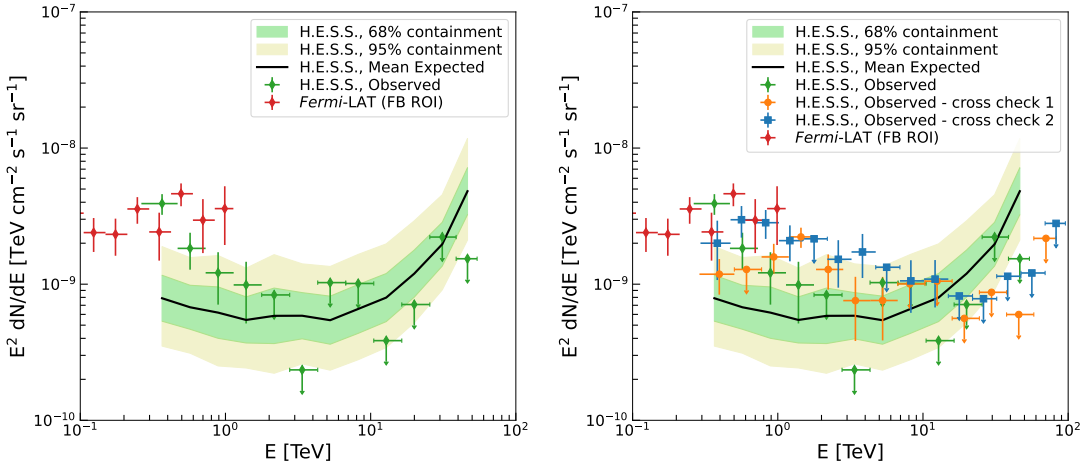

Figure 7.9: Spectral energy distribution in the H.E.S.S. ROI. Energy-differential observed flux points and upper limits from the H.E.S.S. analysis are shown in green. The positive excess is visible at low energy right above the energy threshold. Energy-differential flux points from the *Fermi*-LAT analysis are shown too, as adapted from the analysis in Ref. [198] and re-computed for our ROI. The error bars show the 1 σ statistical uncertainty. The upper limits on the energy-differential flux are computed at 95% C.L. The mean expected energy-differential flux upper limits (black line) together with the 1 σ (green) and 2 σ (yellow) containment bands are shown. The right panel shows the comparison between the observed flux points and upper limits obtained with the lead H.E.S.S. analysis and the two cross-check H.E.S.S. analyses used in this work [139].

ativistic electrons are expected to produce IC gamma-ray emission on the Interstellar Soft Radiation Fields (ISRF, see *e.g.* [314]) and/or CMB.

Photons of hadronic origin are due to decay of neutral pions, produced in inelastic interaction of injected relativistic protons with the interstellar medium. For a hadronic model, a single power-law with an index $\Gamma_p < 2.3$ can explain the inferred spectrum of CR protons. The relatively hard index means that the CR protons do not escape from a region with an energy dependent diffusion coefficient (unless the injection spectrum is $\propto E^{-2}$ and the diffusion coefficient $D(E) \propto E^{0.3}$ up to several TeV). Possible scenarii for the explanation of this origin are convective escape, confinement due to magnetic field structures, or a recent burst-like origin of the population of CR protons. The population of CRp can be explained with an energy of $\sim 7 \times 10^{52} \left(\frac{1\,\mathrm{cm}^{-3}}{n_p}\right)$ erg, where n_p is the average gas density near the GC. Explaining this amount of energy with SNRs, would require about 700 of the latter (assuming no escape, on average 10^{50} erg in CRp per SNR - 10^{51}

erg kinetic energy and 10% proton acceleration efficiency). The escape time for 6 TeV protons is about 100 kyr, considering a diffusion coefficient similar to the local one, with a value of $D \approx 10^{-26}$ cm^{2}s^{-1}.

Leptonic scenarii would require an electron spectrum with an index of $\Gamma_e = 2.8 \pm 0.1$. Above 1 GeV, the required energy in CRe is $\sim 3 \times 10^{51}$ erg, which can be produced by 3000 SNe (assuming 0.1% electron acceleration efficiency). This evaluation is up to a factor 10 uncertain due to uncertainties in the ISRF near the GC and the spectrum of electrons at low energies. Constraints on CRe from the gamma-ray data is valid only above ~ 10 GeV, consequently, the energy density of electrons can be up to a factor 10 smaller, if it is dominated by electrons around 10 GeV. The diffusive escape time and the cooling time for 3 TeV electrons (95% lower bound on exponential cutoff based on *Fermi*-LAT data) are both around 200 kyr. The electron spectrum is consistent with an injection spectrum $\propto E^{-2}$ or softer plus diffusion softening, *i.e.*, it can be produced by a stationary source of CRe, provided that the diffusion escape time is shorter than the cooling time for electrons up to ~ 3 TeV.

For the joint analysis of *Fermi*-LAT and H.E.S.S. data, we reprocess *Fermi*-LAT results for energies > 10 GeV from Ref. [198] including more years of data taken from the LAT satellite. More detail about the inclusion of the *Fermi*-LAT dataset are given in Ref. [140], which is in preparation at the moment of the writing of this thesis. The spatial template for the Fermi Bubbles we are using was produced with data from Ref. [198], for energies of 1-10 GeV. During the analysis we perform joint fit of *Fermi*-LAT and H.E.S.S. photon data with exponential cutoff spectra for simple one-zone leptonic and hadronic models.

In the leptonic scenario, an exponential cutoff distribution of electrons producing inverse Compton emission on the Interstellar Radiation field photons characteristic for the regions close to the GC [314] ($R = 0$ kpc model) is assumed. In the hadronic scenario, the pp emission is assumed to be produced in the regions of characteristic density $n = 1$ cm^{-3}, outside the CMZ. Corresponding photon spectra produced by the described populations of electrons/protons were calculated using *naima* code v.0.9.1 [368, 231, 224]. In all cases, the normalization, power-law slope and energy cut-off are considered to be free parameters.

We can compute a joint fit with *Fermi*-LAT and H.E.S.S. analysis to obtain constraints on the exponential cut-off of the tested spectra. However, systematic uncertainties affect both the *Fermi*-LAT analysis and the H.E.S.S. analysis above $\sim$ 1-2 TeV. Nevertheless, for the H.E.S.S. analysis, flux points are derived also in the energy bins above 2 TeV and used to compute the joint fit. For this derivation, the systematic uncertainty in each energy bin for the two analyses is obtained as the standard deviation between the different models. As an example of the models, in Fig. 7.9, we have shown two cross check models for the H.E.S.S. analysis. For both *Fermi*-LAT and H.E.S.S. analyses, different models are used to estimate the systematic uncertainty per energy bin. More detail about the derivation are

given in Ref. [140]. Fig. 7.10 shows the flux points and upper limits from the two analyses used for the spectral fit. The error bars are obtained through the sum in quadrature of systematic and statistical uncertainties.

The result of the fit with an exponential cutoff power law is shown as well. Values of the energy cutoffs for the three models are derived as $E_{\rm cut,photons} = 0.7^{+\infty}_{-0.6}$ TeV for an agnostic derivation of the photon spectrum, $E_{\rm cut,electrons} = 3.2^{+\infty}_{-3.0}$ TeV in case of leptonic scenario, and of $E_{\rm cut,protons} = 7.9^{+\infty}_{-7.4}$ TeV in the case of the hadronic origin of the emission. The results of the fit are not conclusive and the best fit for the energy cutoffs of the three models cannot be recovered at 2 σ level. Power-law indices for the three models are recovered at 2 σ level as $\Gamma_{\rm photons} = 2.1$ for the photon spectrum, $\Gamma_{\rm electrons} = 2.6$ in case of leptonic scenario, $\Gamma_{\rm protons} = 2.1$ for hadronic emission. The three models for exponential cutoff power law and the best fit indices and energy cutoff values are shown in Fig. 7.10. Since the energy cutoffs are not recovered we compute the reduced $\Delta\chi^2$ between tests with exponential cutoff power laws and simple power laws for the three models, defined as $\Delta\chi^2 = \chi^2_{\rm pl} - \chi^2_{\rm cutoff-pl}$. The difference in degrees of freedom is obtained considering the degrees of freedom necessary for the two computations. We obtain $\Delta\chi^2_{\rm photons} = 6.1$, $\Delta\chi^2_{\rm electrons} = 3.4$ and $\Delta\chi^2_{\rm protons} = 4.9$. The fit with a simple power law seems to be preferred for all the three models, however since the estimation of the systematic uncertainties is not yet settled this may not be the final results and more detail are given in Ref. [140]. Therefore, we can obtain constraints on the parent particle populations in form of lower limits on the energy cut-off. Moreover, the indeces of the power laws describing the models are recovered at 2 σ. We present in the following sections some of the computations performed for the derivation of the systematic uncertainties.

7.5.2 Systematic uncertainties

In this section we show in detail the study performed for the determination of the systematic uncertainty affecting the analysis for the search for the low-latitude FBs emission.

Background measurement uncertainty

As it was already explained in Sec. 6.4, the possible correlation between the NSB and the gamma-like rate in the FoV of the IGS dataset was investigated. No significant correlation is observed between the NSB and the rate in the ROI for the search for the FBs emission, therefore no correction is applied for this source of systematics.

The azimuthal symmetry of the trigger of events in the camera pixels was investigated too, as explained in Sec. 6.4. No significant effect was observed beyond the expected 1%-per-degree gradient in the FoV due to the correlation between

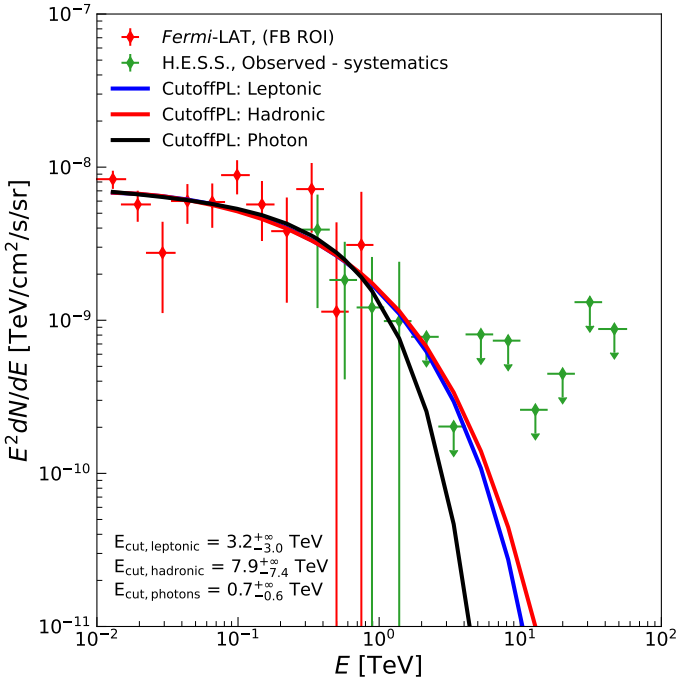

Figure 7.10: Spectral energy distribution in the H.E.S.S. ROI. Energy-differential observed flux points and upper limits from the H.E.S.S. analysis are shown in green. The positive excess is visible at low energy right above the energy threshold. Energy-differential flux points from the *Fermi*-LAT analysis are shown too, as adapted from the analysis in Ref. [198], re-computed for our ROI and with the addition of more years of observations with the LAT satellite [140]. The error bars shows the sum in quadrature of 1σ statistical and systematic uncertainties. The upper limits on the energy-differential flux are computed at 95% C.L. The best fit gamma-ray models to *Fermi*-LAT(> 10 GeV) and H.E.S.S. datasets assuming an exponential cutoff power law spectra for the injected electrons (blue) and protons (red) are shown.

the gamma-like rate and the gradient in the zenith angle values at which the observational runs are carried out. No correction is applied for this source of systematics.

A gradient of 1% is expected in the gamma-like rate across the FoV due to different zenith angles at which the observations are performed. As explained in detail in Sec. 6.4, we expect different zenith angles for events measured in the ON and the reflected OFF regions. We then build distributions of zenith angles on a run-by-run basis. The maximum difference between the mean values of $\theta_{\mathrm{z,ON}}$ and $\theta_{\mathrm{z,OFF}}$ distributions is 1°-2°. Then the ON and OFF energy count distributions are renormalized as previously explained (see Sec. 6.4). However, the typical width of the zenith distributions is between 1° and 3° for the FBs analysis. The estimate of

the systematic uncertainty is then 3%. The systematic uncertainty on the normalization of the background can be propagated in the analysis in order to quantify the effect on the differential flux upper limits. For completeness, we show a couple of zenith angle distributions for the FBs analysis in Fig. 7.11. For pointing 3-7, the mean and RMS of the ON and OFF distributions are $\bar{\theta}_{\mathrm{z,ON}} = (24.2 \pm 1.9)^{\circ}$and $\bar{\theta}_{\mathrm{z,OFF}} = (24.1 \pm 1.9)^{\circ}$. For pointing 2-5, the mean and RMS of the ON and OFF distributions are $\bar{\theta}_{\mathrm{z,ON}} = (27.1 \pm 1.8)^{\circ}$, $\bar{\theta}_{\mathrm{z,OFF}} = (27.0 \pm 1.8)^{\circ}$, respectively.

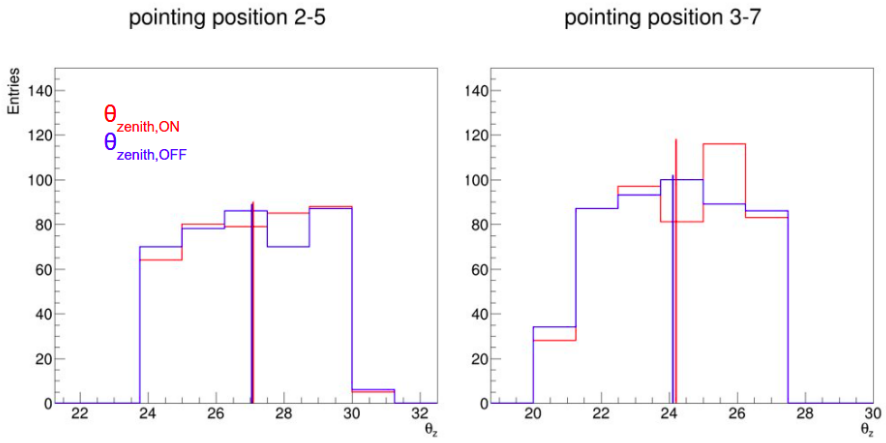

Figure 7.11: Zenith angle distributions for two pointing positions of the IGS dataset, for the FBs analysis. The distributions are built with the zenith angle values of events for one run for each pointing position. The red and blue distributions are for the ON and OFF regions, respectively. The means of the distributions are given by the solid lines of the same colors.

Subset of the IGS dataset

The analyses for the search for the low-latitude FBs emission has been cross-checked by two different analysis chains. For these, the whole dataset of the observational runs in the IGS was not available. They were therefore performed with two different subsets of it [139]. It is beyond the scope of this work to discuss in detail these two analyses, however we cross-check that the main analysis would produce the same results if carried out with these two subsets. The analysis is then computed again with the same method for the measurement of background, the same definition of the ROI by keeping the same threshold. The energy-differential observed flux upper limits are computed at 95% C.L with the same procedure. The results are shown in Fig. 7.12 for the two subsets. The positive excess in the first four energy bins is still clearly visible. Above 2 TeV there is an important level of uncertainty between the three analysis that will be discussed in more detail in the following.

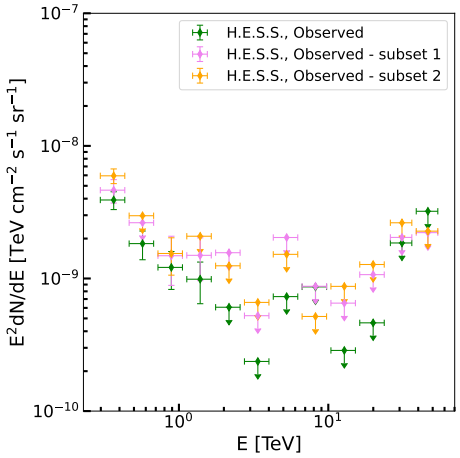

Figure 7.12: Spectral energy distribution in the H.E.S.S. ROI obtained with the main analysis chain. Energy-differential observed flux upper limits from the H.E.S.S. analysis are shown for three datasets: the whole IGS dataset and two subsets of it [139]. The positive excess is visible at low energy right above the energy threshold for all the cases. Standard analysis flux upper limits and points are shown in green. Upper limits and points computed with the subsets are shown in pink and orange, respectively.

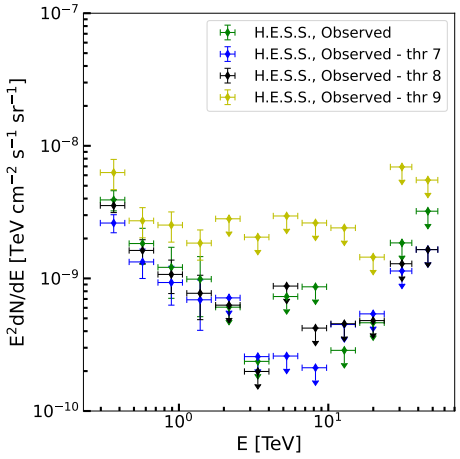

Figure 7.13: Spectral energy distribution in the H.E.S.S. ROI. Energy-differential observed flux upper limits from the H.E.S.S. analysis are shown for different definitions of the H.E.S.S. ROI, by changing the threshold used on the *Fermi*-LAT spatial template. The positive excess is visible at low energy right above the energy threshold for all the four threshold definitions. Standard analysis flux upper limits and points are shown in green. Upper limits and points computed with thresholds of 7, 8 and 9 are shown in blue, black and yellow, respectively.

Spatial template uncertainty

We test the uncertainty on the definition of the *Fermi*-LAT spatial template and the choice of the threshold for the ROI for the H.E.S.S. analysis with the tests shown in this section.

We first perform again the analysis changing the ROI by defining other three thresholds on the spatial template. We choose 7, 8 and 9. The analysis is carried out again with the same background measurement method. The energy count distributions are built and the excess significance versus energy bins are computed above the energy threshold. For the three alternative thresholds, we obtain integrated significance of $S = 8.8\,\sigma$, $9.5\,\sigma$ and $9.1\,\sigma$, respectively. The positive excess in the first four energy bins, after the re-binning for 0.2 dex, is still present for the three cases, confirming what we showed in the previous sections. We show in Fig. 7.13, the energy-differential observed flux upper limits obtained with the three thresholds compared to the standard one. The procedure for the computation of the flux upper limits is the same as defined above. The positive excess is clearly visible in the first four energy bins, confirming the emission seen by the H.E.S.S. analysis. However, above 2 TeV, the difference between the different thresholds definition is much larger and for some energy bins there is up to a factor 10 difference, clearly implying that further systematics studies are needed for the highest energy bins.

We smooth the *Fermi*-LAT spatial template by convolving it with a Gaussian kernel with 0.5° and 1° width. With these two setups, we perform the analysis again and we derive excess significance for the energy bins above the energy threshold. Integrated significance of $S = -1.0\,\sigma$ and $-2.7\,\sigma$ are obtained, respectively. The excess significance computed for the energy bins above the energy threshold for the two cases just mentioned are shown in Fig. 7.14.

We then shift the ROI for two cases: (*i*) by 1° towards more negative Galactic longitude and (*ii*) by 1° towards more positive Galactic latitudes. We perform again the analysis with these two setups and the positive excess at low energies above the threshold is no more present and integrated significance of $S = 2.5\,\sigma$ and $2.8\,\sigma$ are obtained, respectively. The excess significance computed for the energy bins above the energy threshold for the two cases just mentioned are shown in Fig. 7.14 in the bottom panels. The fluctuations of significance over the energy bins are compatible with zero.

Another test consists in reflecting the ROI with respect to the axis of 0° in Galactic longitudes. In this way the ROI is located in a region where a much smaller signal is expected from the *Fermi*-LAT spatial template. However, to perform this test we restrict the ROI considering only pixels with surface brightness larger than 9 in the *Fermi*-LAT spatial template. This is done in order to avoid that any pixel falling in the initial ROI is also inside the reflected one. With this setup the analysis is performed again and an integrated significance above the energy threshold of $S = 1.1\,\sigma$ is obtained. In Fig. 7.15, we show the excess significance computed

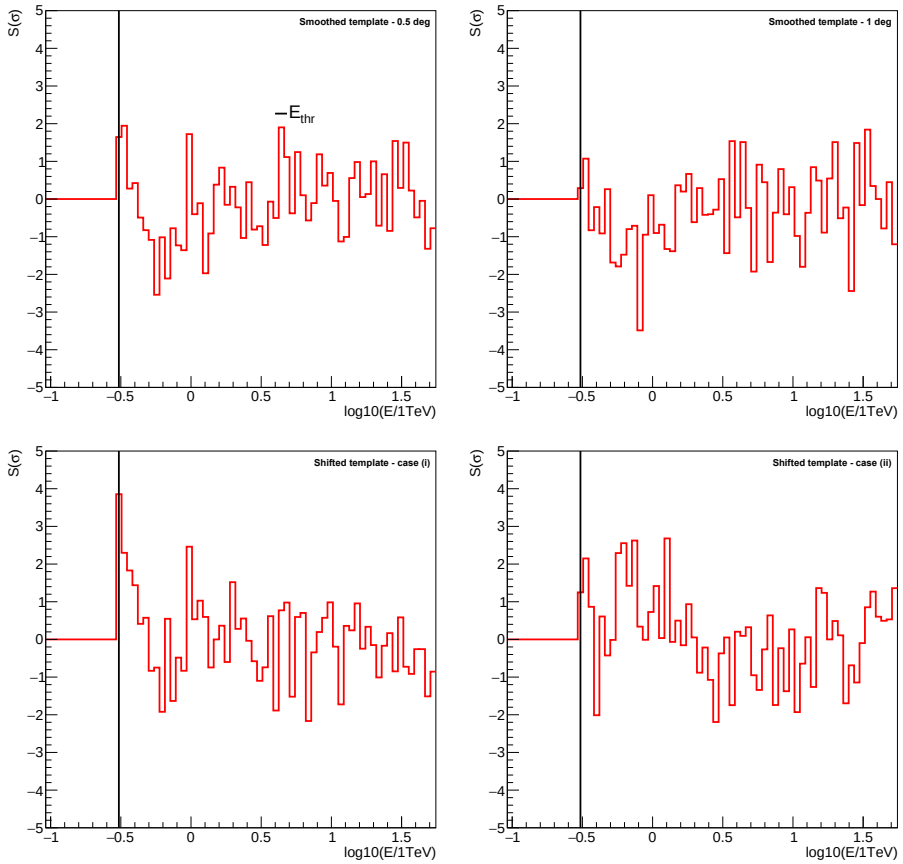

Figure 7.14: *Top panels:* Excess significance computed for the energy bins above the energy threshold for two cases of modification of the ROI: the ROI is smoothed by the convolution of the spatial template with a Gaussian kernel with 0.5° and 1° width. The left panel shows the first case, the right one the second case. *Bottom panels*: Excess significance computed for the energy bins above the energy threshold for two cases of modification of the ROI: the ROI is shifted by 1° towards more negative Galactic longitude and by 1° towards more positive Galactic latitudes. The left panel shows the first case, the right one the second case. The black line shows the energy threshold.

for the energy bins above the energy threshold, using 9 as the threshold on the spatial template. The left panel of the figure shows the result for the analysis with the original ROI, while the right one shows the results for the ROI reflected wrt the axis of 0° in Galactic longitudes. In the second case, the positive excess at low energies above the threshold is no more present. We can use this computation for a derivation of the limit of systematics affecting our analysis.

In Fig. 7.16, we show the energy-differential observed flux upper limits and points computed with the standard procedure defined so far for the analysis using

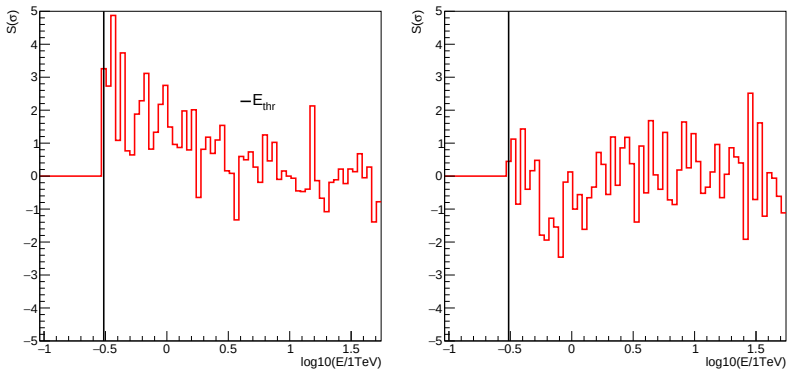

Figure 7.15: Excess significance computed for the energy bins above the energy threshold for one case of modification of the ROI: the ROI is reflected with respect to the axis of 0° in Galactic longitudes. For this test, a threshold of 9 is used on the spatial template for the definition of the ROI. The left panel shows the significance in energy bins for the original ROI defined with threshold 9. The right panel shows the significance in energy bins for the reflected ROI defined with threshold 9. The black line shows the energy threshold.

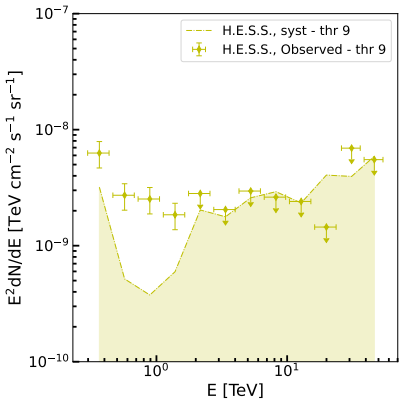

Figure 7.16: Spectral energy distribution in the H.E.S.S. ROI. Energy-differential observed flux upper limits from the H.E.S.S. analysis are shown for the definition of the H.E.S.S. ROI with threshold of 9 used on the *Fermi*-LAT spatial template. The positive excess is visible at low energy right above the energy threshold. The systematics level, shown as the yellow shaded area, for each energy bin is derived from the analysis performed with the ROI reflected with respect to the axis of 0° in Galactic longitudes but with the same definition of the threshold.

9 as the threshold on the spatial template for the ROI. The latter are shown as yellow points. The results for the analysis with the reflected ROI are shown as systematic level by a yellow shaded area. For energy bins larger than 1-2 TeV the systematic level becomes very important, implying that we need to include them in the final derivation of the FBs spectrum from the H.E.S.S. analysis.

7.6 Conclusions and outlook

In this analysis, the latest results on the search for the low-latitude FBs emission at TeV energies with the H.E.S.S. telescopes have been shown. The used IGS dataset consists of a total 546 h of live time, collected over 6 years of observations with the H.E.S.S. five-telescopes array. The main conclusions are:

- the used H.E.S.S. II dataset provides high exposure in the region where the low-latitude FBs emission is expected with the best sensitivity possible that can be reached with the H.E.S.S. array;
- a significant excess is found in the energy range from 300 GeV up to $\sim$ 2 TeV and energy-differential flux points are computed for energy bins where a significant excess above 2 σ is obtained;
- The FBs emission is detected for the four energy bins between 0.3 TeV up to 1.7 TeV as 3.7×10^{-9}, 1.8×10^{-9}, 1.3×10^{-9} and 8.8×10^{-10} TeV cm^{-2} s^{-1} sr^{-1} with a total significance of 9.2 σ above 300 GeV;
- for higher energies, 95% C.L. energy-differential flux upper limits are computed;
- this analysis highlights the capability of pointed observations with the current generation of IACTs to constrain the FBs emission;
- an agnostic derivation of the photon spectrum and hadronic/leptonic parent particle population spectra can be constrained;
- many systematic uncertainties affect the analysis for energies higher than 2 TeV and further studies are ongoing;
- nevertheless, a first inclusion of the systematic uncertainties in the *Fermi*-LAT and H.E.S.S. analyses has been shown and used for the derivation of lower limits on the energy cutoffs for the tested models;
- the joint fit on *Fermi*-LAT and H.E.S.S. analyses seems to prefer a simple power law over an exponential cutoff power law for the tested models, however this is not yet the final estimation due to other possible sources of systematics.

The several systematic uncertainties affecting the analyses have been studied and further work to include them in the final limits is ongoing to derive the total systematic budget and include it in a more accurate description of the FBs spectrum at energies above 2 TeV. One possibility has been shown and used to obtain lower limits on the energy cutoff for exponential cutoff power laws. This reflects on the derivation of the lower limits of the energy cutoff of leptonic and hadronic parent particle populations for the FBs emission. Moreover, the background models that are currently in development, as we explained in Sec. 6.5, can be used as alternative estimation of the residual background for the computation of the flux points and upper limits on the FBs emission. The spectrum between 2 and 10 TeV needs a dedicated study because a possible excess is seen in the two cross-check analysis chains shown in this work. Possible future observations of the region with CTA could improve the description of the FBs spectrum given the better energy and angular resolutions. At the time of the writing, these steps are in preparation and a publication of the final results is foreseen in a scientific journal. Preliminary results on the FBs analysis have been published in Ref. [286]. At the moment of the writing, the article is in preparation for submission to *Nature* within a few months [140].

Part III

Dark Matter search

Chapter 8

Dark Matter search with the Inner Galaxy Survey

Contents

Summary

In this chapter we present a novel search for gamma-rays from self-annihilating WIMPs in the GC region with the H.E.S.S. IGS observations (see Chap. 6). In Sec. 8.1, we provide some perspective byt showing a comparison of the current limits on the $\langle \sigma v \rangle$ of DM particles. Sec. 8.2 shows the excess and significance sky maps

obtained from the dataset, explains the procedures for the ROI definition for the search of DM, the choice of excluded regions in the FoV and the measurement of the residual background. Then, we show energy count distributions and we use them for the computation of the excess significance. We introduce how the expected signal from dark matter would look like, comparing it with the observed count distributions. In Sec. 8.3, we show the derivation of upper limits on the free parameters, since no excess compatible with DM is observed. The results are shown and compared with other experiments and with the results obtained when assuming different DM distribution profiles. In Sec. 8.4, we discuss the impact of the systematic uncertainties on the limits. We conclude in Sec. 8.5 with some outlook. This work has been published in *Physical Review Letters* [7].

8.1 Introduction

As introduced in Chap. 3, WIMPs, particles with mass and coupling strength at the electroweak scale, are among the most promising dark matter candidates. The inner halo of the Milky Way is expected to be the brightest source of gamma-ray signal from self-annihilating DM particles. To provide some perspective, Fig. 8.1 shows the main limits on the $\langle \sigma v \rangle$ of DM particles annihilating in the W^+W^- channel, assuming the DM density profile of the GC region following the Einasto parameterization. Previous limits obtained with the H.E.S.S. analysis of the 2004-2013 dataset of observations of the GC are displayed [244] together with limits from prospects of observations of the GC region with CTA [22]. For comparison with other instruments, limits from GC observations with HAWC [17] and with *Fermi*-LAT [24] are provided too.

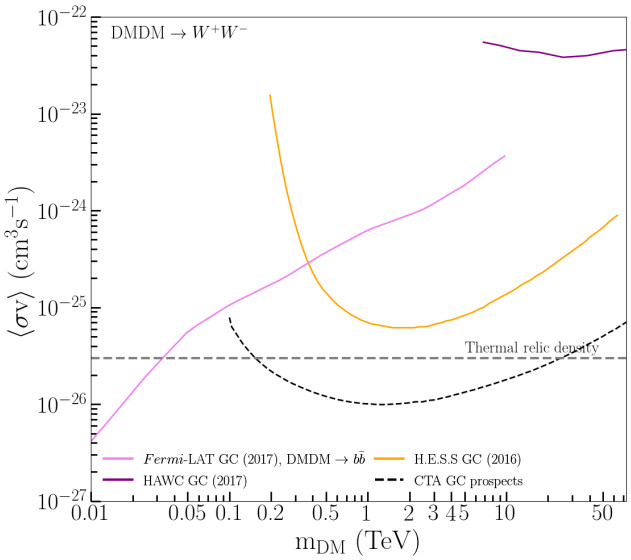

Figure 8.1: Comparison of upper limits on $\langle \sigma v \rangle$ for DM particles annihilating in the W^+W^- channel. Previous limits from H.E.S.S. observations of the GC [13] are shown as the orange line. The limits from GC observations with HAWC [17] are shown as the purple line. The limits, for the $b\bar{b}$ channel, from the observations of the GC region with the Fermi satellite are shown as the violet line [24]. Limits from prospects of observations of the GC region with CTA are shown as the black dashed line [22].

8.2 Observations and dataset

The analysis for the search of DM annihilation signals from the GC region is performed with the observational dataset collected between 2014 and 2020, includ-

ing the observations during the IGS period. The reconstruction of the events was performed in *CT1-5 Stereo* mode for the observations collected in 2014-2019 and in *CT1-4 Stereo* mode for the observations collected in 2020. This dataset was extensively described in Sec. 6.2. The technique for the selection and reconstruction of gamma-like events has been already referenced in Sec. 6.2. At least ten hours of acceptance-corrected exposure time was reached up to $b \approx +6°$. We already showed the time-exposure map in Sec. 6.2. We report it again in Fig. 8.2 to show the definition of the region of interest for our analysis.

Many astrophysical emitters populate the complex GC region. Such an environment includes numerous regions with detected VHE gamma-ray emissions [36, 19, 8]. Moreover, the varying night sky background has to be considered when observing the region [11]. The systematic uncertainties affecting the dataset have been studied in detail in Sec. 6.4. When searching for the DM signals, we define exclusion regions to avoid leakage of VHE signals in the region of interest or the region for the measurement of background. The exclusion regions used for this analysis are shown in Fig. 8.2. The set of masks includes the Galactic plane between $\pm 0.3°$, the diffuse emission region around the GC [19], sources from Ref. [8], and all VHE gamma-ray sources in the field of view. As a standard procedure, for H.E.S.S. point-like sources a circular mask of $0.25°$ is used to avoid leakage. This is chosen to be more conservative than the H.E.S.S. PSF of 0.06° at 68% containment radius. For instance, for the extended source HESS J1745-303, a conservative circular mask of 0.9° radius is applied. The results that are shown in the chapter have been cross-checked with an independent calibration and analysis chain [301].

From the convolution of the time exposure map with the acceptance of the instrument, we can obtain the exposure map of the present dataset. The acceptance versus energy, averaged over all the runs for the ROI, is shown in Fig. 8.3. The former is built considering the value of $A_{\mathrm{eff},k}(E_\gamma)$ for each run k in the dataset. The final distribution is computed as a time averaged acceptance, using the observed time $T_{\mathrm{obs},k}$ of each run k. The spatial response of the instrument is taken into account for each run k because the acceptance term depends on the angular distance between the reconstructed event position and the pointing position of the run k. For this analysis, a safe energy threshold is defined by taking the value of the energy at which the acceptance of the H.E.S.S. instrument reaches 20% of its maximum value. From this criterion, the safe energy threshold for the DM search analysis is fixed to E_{thr} = 200 GeV.

The exposure map for the 2014-2020 dataset is shown in the left panel of Fig. 8.4. To compare the present results with the previous analysis of the GC region [244], we also show a zoomed view of the exposure map of the inner degrees around Sagittarius A*. The exposure map of the observations of the GC region carried out between 2004 and 2013 is also shown. This was obtained by convolving the time exposure map of that dataset with the acceptance for the configuration of the H.E.S.S. instrument applied for those observations. For the present dataset,

about 5 times more exposure is available. This is due to the larger observational time and the improved sensitivity of the full five-telescopes H.E.S.S. array.

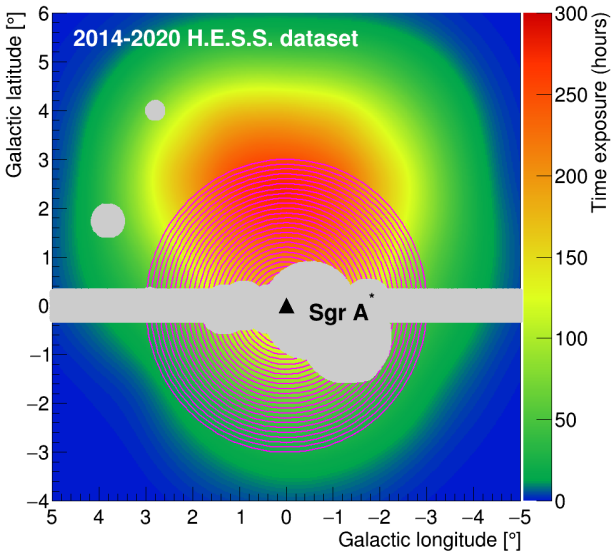

Figure 8.2: Time exposure map of the data collected between 2014 and 2020. The position of the supermassive black hole Sagittarius A* is symbolized by the black triangle. The region of interest for the search of DM signals is shown as the purple rings. The 25 annuli of width of 0.1°, centered on the nominal GC position, span inner radii from 0.5° to 2.9°. The exclusion regions used to avoid contamination from astrophysical background in the dataset are depicted as the gray-shaded area.

8.2.1 Excess and Significance sky maps

Standard gamma-ray excess and significance maps for the full five-telescopes array are produced for the 2014-2020 observational dataset using the *Ring Background* method. These have been already shown in Sec. 6.2. Here, we show the maps with the application of the standard exclusion regions from the H.E.S.S. database. No significant excess is observed anywhere in the FoV, shown on the significance map with excluded regions, except for an hotspot visible at (l, b) = (2.9°, 4.0°). The former is covered with a mask during the analysis for DM search. Specific background measurements and ROIs are defined for the DM search analysis, as it is explained in Sec. 8.2.3. The excess and significance maps, as well as the significance distribution obtained with the photon counts used for the significance map, are shown in Fig. 8.5. No source is detected in the sky outside the masks. The right panel of Fig. 8.5 shows the Significance distribution obtained with the

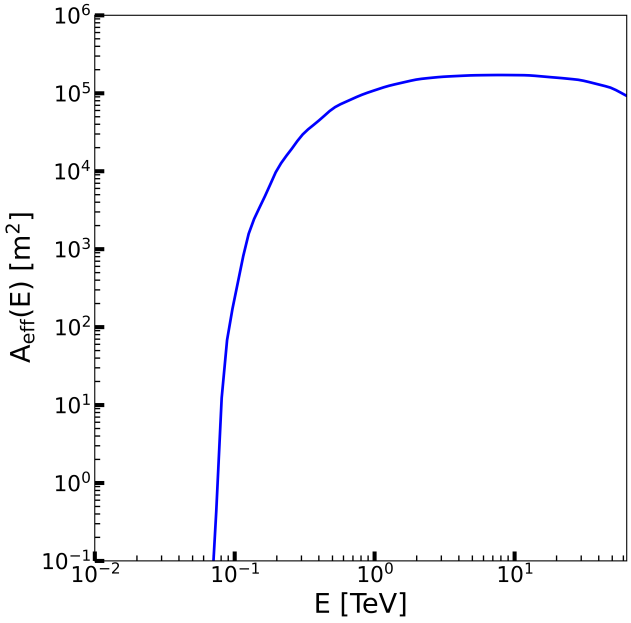

Figure 8.3: Averaged acceptance, as function of energy, for the DM analysis with the 2014-2020 dataset. The acceptance is built for the combination of the *CT1-5 Stereo* and *CT1-4 Stereo* reconstruction modes. See more details in Sec. 2.6 and in the main text.

photon counts used for the production of the significance map. The distribution is fitted with a Gaussian function. Since the VHE sources have been masked, the Significance distribution is well contained inside the Gaussian fit.

8.2.2 Definition of the region of interest and exclusion regions

The region for the search of DM signals is defined as the ROI, which is referred to as the ON region. The expected DM density profile adopted and the distribution of the pointing positions in the sky, which determined the photon statistics available for the analysis, are the main reasons for the definition of the ROI. A significant event statistics is obtained up to about 6° above the Galactic plane. This dataset was used for the search of the FBs at low latitudes, as presented in Chap 7. The same exposure was used to look for a different emission because the spatial morphologies of the FBs and the expected DM signal are very distinguishable, at least for the assumed DM models in this Chapter. In this analysis, we adopt the Einasto [341] DM density profile to describe the DM distribution for annihilating WIMPs. The expected distribution of DM peaks close to the GC. The DM distribution adopted for this analysis, described by the J-factor (see Sec. 3.5), is shown in Fig. 8.6. The color scale indicates the value of the J-factor computed

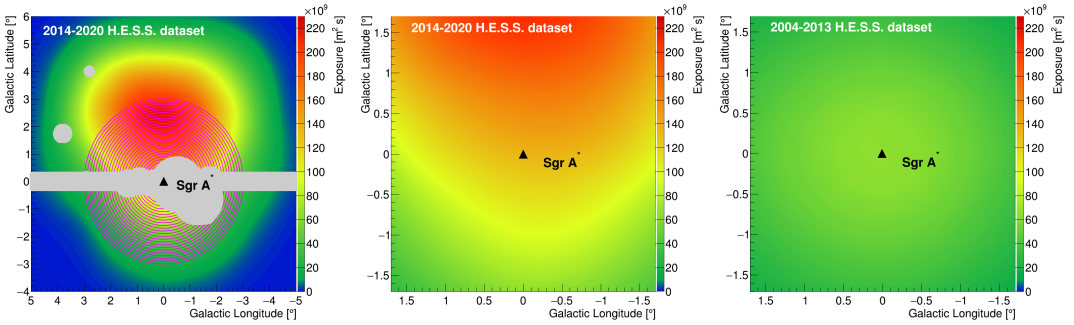

Figure 8.4: Exposure maps (in m^2s) of the observational datasets of the GC region for the H.E.S.S.-II and H.E.S.S.-I [244] phases. The position of the supermassive black hole Sagittarius A* is symbolized by the black triangle. *Left panel:* Full exposure map for the H.E.S.S. II observational dataset used in this work. The regions of interest for DM search are overlaid as solid purple lines. The exclusion regions used to avoid contamination from astrophysical background in the dataset are depicted as the gray-shaded area. *Middle panel:* Zoomed view of the exposure map obtained for the H.E.S.S.-II observational dataset. *Right panel:* Exposure map of the GC region for the H.E.S.S.-I observational dataset as used in Ref. [244].

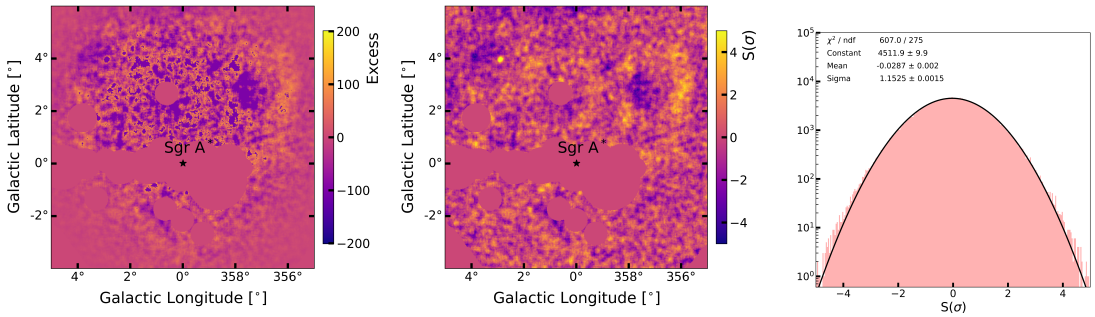

Figure 8.5: Gamma-ray excess map (left panel), significance map (middle panel) and significance distribution (right panel) for the IGS dataset, obtained with the *Ring Background* technique. On the maps, standard exclusion regions from the H.E.S.S. database are shown as zones of zero values of significance and excess. An hotspot is visible at (l, b) = (2.9°, 4.0°) in the significance map with excluded regions and is covered with a mask during the analysis.

for the Einasto profile in the pixel size of $0.02° \times 0.02°$. Given the expected spatial distribution of DM, the ROI is defined as a disk centered on the nominal GC position with a radius of 3°. In order to exploit the expected spatial morphology of the DM signals with respect to the residual background, the disk is divided into

25 ROIs defined as rings of inner radii from 0.5° to 2.9°. The width of each ring is fixed to 0.1°. The rings are shown in Fig. 8.2.

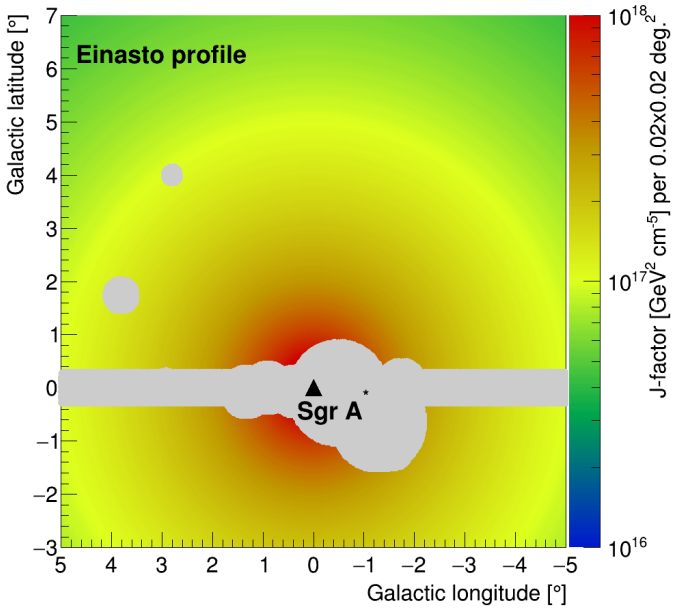

Figure 8.6: Map describing the J-factor values for the Einasto profile in Galactic coordinates. The integration of the J-factor is performed in pixels of $0.02^\circ \times 0.02^\circ$ size. The set of masks applied in the analysis to avoid astrophysical background contamination from the VHE sources in the ROIs is given by the gray-shaded area. The supermassive black hole Sagittarius A* position corresponds to the black triangle.

8.2.3 Measurement of the residual background

For the determination of the residual background in the search of DM, the *Reflected Background* method is applied (we already explained the method in Sec. 7.3). The measurement of the background is performed simultaneously in the same field of view as for the signals measurement on a run-by-run basis. The OFF region, for the measurement of background, is taken symmetrically to the ON one with respect to the pointing position, as described in Refs. [20, 13]. Therefore, the measurements from the OFF regions are performed under the same observational and instrumental conditions as the ON. Exclusion regions are removed similarly for the ON and OFF measurements, which are therefore carried out with the same solid angle size. This procedure is performed on a run-by-run basis and produces an accurate determination of the residual background. An example of measurement of background for the ROIs 7, 13 and 25 and the pointing positions

(black crosses) 2-5 (l = -1.8°, b = 2.0°) and 3-7 (l = 0.8°, b = 3.2°), respectively, is shown in Fig. 8.7. The exclusion regions are subtracted similarly in the ON and OFF regions such that the same solid angle size and acceptance are kept. The color scale indicates the same J-factor distribution which is shown in Fig. 8.6. A significant expected DM excess signals in the ON region with respect to the OFF is maintained, as it can be recovered from the ratios between the J-factor values in ON and OFF regions from the Figure. For ROI 13, with respect to the pointing positions 3-7 and 2-5, the ratios between the J-factor in the ON and OFF regions are 5 and 4, respectively.

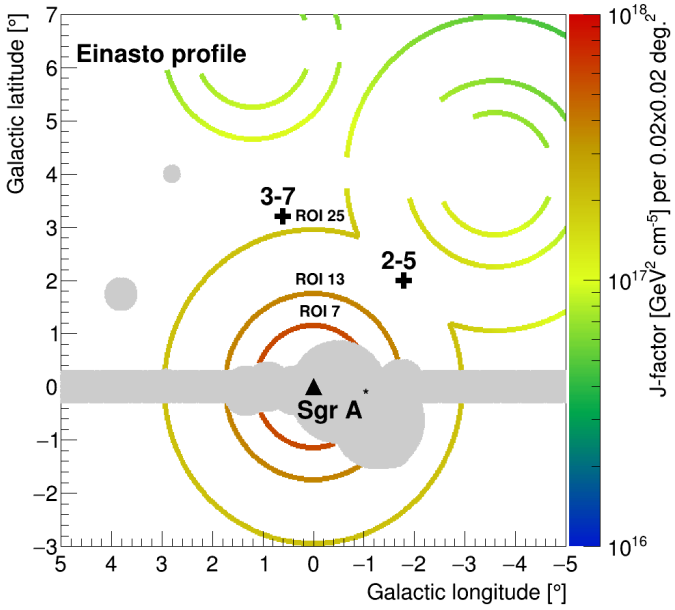

Figure 8.7: Measurement of background in Galactic coordinates for two different pointing positions of the IGS (black crosses). J-factor values are displayed for the ROIs 7, 13 and 25, respectively, together with those obtained in the corresponding OFF regions. The masked regions are excluded similarly in the ON and OFF regions such that they keep the same solid angle size and acceptance. The supermassive black hole Sagittarius A* position corresponds to the black triangle.

8.2.4 Energy count distributions

After its spectral and spatial information reconstruction as a gamma-ray like event, each event is collected depending on the ring of the ROI in which it was observed. For each ring of the defined ROI, event distributions are built as a function of energy. The distributions are shown in Fig. 8.8 for the ON and the OFF regions, respectively. The number of events is shown as the color scale, as a function of

the ROI rings, which are numbered on the Y-axis, and of reconstructed energy in TeV on the X-axis. The photon statistics in the ON and OFF regions, which was used to build the energy count distributions, for each ring of the ROI as well as the excess significance are provided in Tab. 8.1. Photon statistics and excess significance are reported for energy bins above the safe energy thresholds of 200 GeV. The excess significance is derived with Eq. 4.10. The energy-differential spectra, obtained from the event energy distributions in the ON and OFF regions for some of the ROI rings and for the combination of all of them, are shown in Fig. 8.9. The spectra shown are chosen for ROIs such that both the inner annulii of the region and the outer ones are represented. No significant excess is found in any of the ROIs. However, we explain more about the search for an excess in energy bands in the next section.

i^{th} ROI	1	2	3	4	5	6	7	8	9	10	11	12
N_{ON}	326	1830	3029	4736	6793	9144	12036	15201	16830	19530	23549	25585
N_{OFF}	298	1674	3087	4665	6699	9164	11899	15177	17242	19721	23270	25568
S(σ)	1.1	2.6	-0.7	0.7	0.8	-0.2	0.9	0.1	-2.2	-0.9	1.3	0.1
13	14	15	16	17	18	19	20	21	22	23	24	25
27571	29875	32328	35094	37292	39957	42540	42460	42282	42317	42653	43188	42879
27673	29945	32518	34774	37502	40159	42775	42939	42415	42509	42896	43011	43373
-0.4	-0.3	-0.8	1.2	-0.8	-0.7	-0.8	-1.6	-0.5	-0.7	-0.8	0.6	-1.7

Table 8.1: For each of the 25 ROIs, the photon statistics and the excess significance are reported. In the first row, the ROI number is given. The second and the third rows show the measured photon statistics in the ON and OFF regions, respectively, over the energy threshold. The fourth row reports the excess significance computed with the ON and OFF statistics applying Eq. 4.10.

8.2.5 Search for a gamma-ray excess

The search for a significant DM signals is performed with the comparison of the ON and OFF event energy distribution. The comparison is performed for each ring and the excess significance is derived using Eq. 4.10. The excess significance, in terms of σ, is reported in the third row, for each ROI, of Tab. 8.1. Significance maps for the ROI are also computed. The overall statistics in the ON and OFF region is divided in three energy bands such that comparable photon statistics is present in each one. For each energy band, a map with the value of significance obtained in each ring of the ROI is built. The maps are shown in Fig. 8.10. The significance values show no significant dependency in the first two energy bands. In the high energy band, an overall significant gamma-ray excess is found, with a formal total significance of 5.7 σ above the energy threshold. This corresponds to the p-value of 1.1×10^{-8}. This highlights an unaccounted background signal. However, the spatial and spectral morphologies of the latter are not compatible

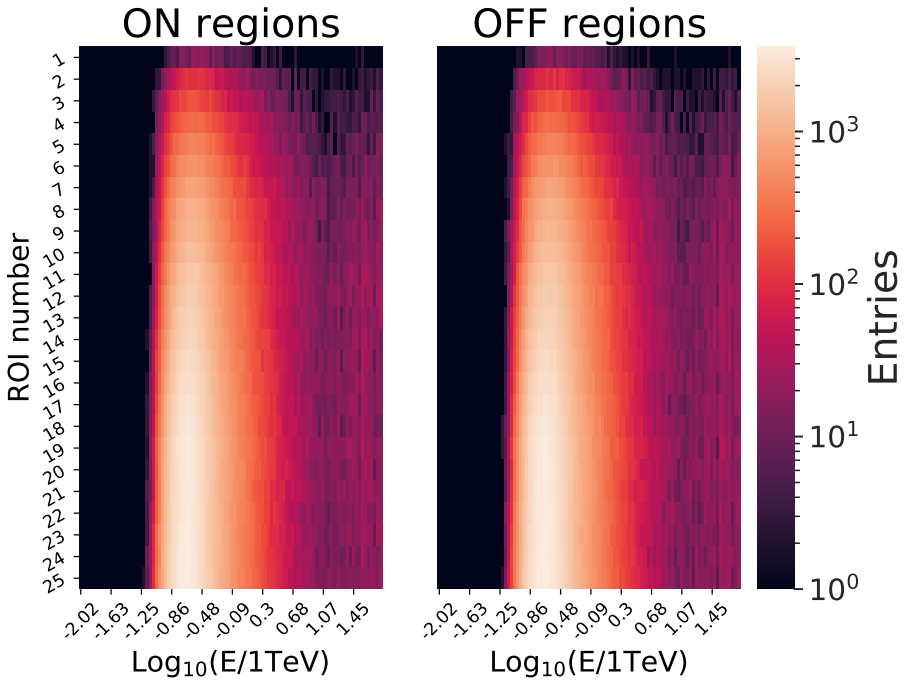

Figure 8.8: ON (left) and OFF (right) energy count distributions as a function of energy and ring of the ROI where the gamma-ray like events are measured.

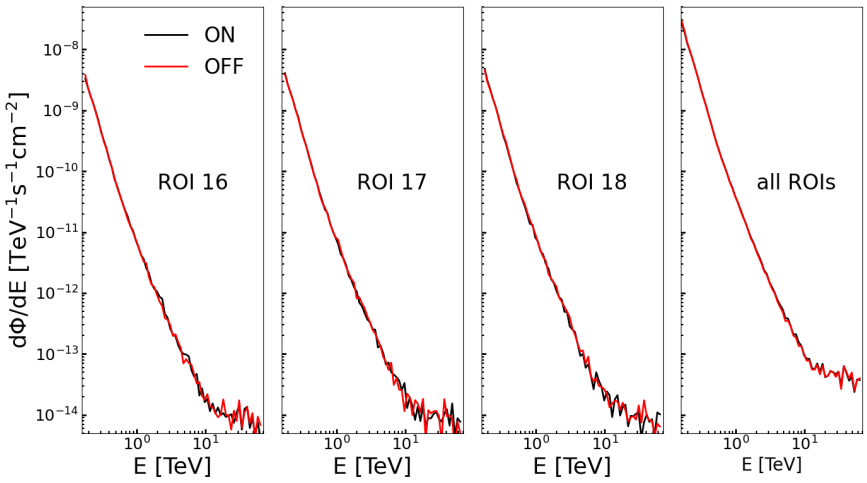

Figure 8.9: Energy-differential spectra obtained for ON (black lines) and OFF (red lines) regions for ROI 16, 17 and 18, respectively, in the first three panels. The energy-differential spectra for the ON and OFF regions of the combination of all the ROI rings are shown in the last panel.

with the ones expected from the specific searched DM model[1]. Nevertheless, the measured excess events, which enter the computations in our analysis, include this additional contribution. This produces conservative constraints since we find a positive observed excess. Therefore, the analysis is conservative as long as no expected signals from DM is detected. For some combinations, the background subtracted energy-differential spectra are shown in Fig. 8.11. The 1σ error bars are shown for each energy bin as well. For the different combinations, the spectra are compatible with zero within the 2σ error bars, at each energy value. No spectral distortion is therefore seen in any of the combinations.

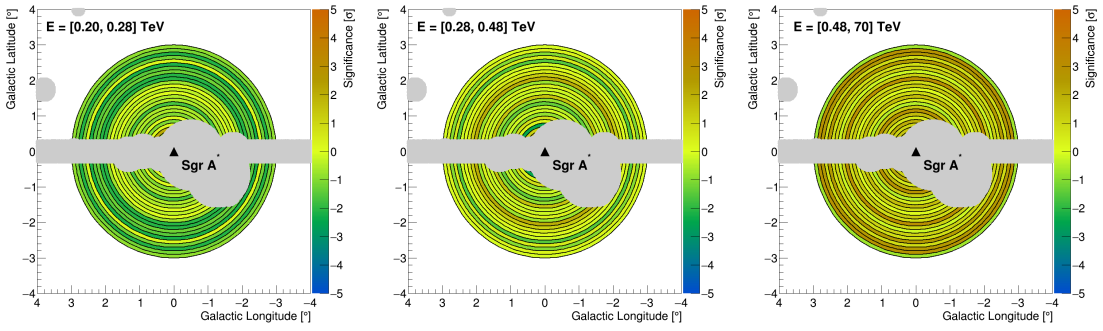

Figure 8.10: Significance maps for the ROI rings computed in three energy bands. The set of masks used in the analysis is shown as the gray-shaded area. The supermassive black hole Sagittarius A* position corresponds to the black triangle.

8.2.6 Expected signals from dark matter annihilation

The energy-differential annihilation spectrum in the W^+W^- channel convolved with the H.E.S.S. acceptance used in this analysis and energy resolution expected for the self-annihilation of DM with mass m_{DM} = 0.98 TeV[2] and $\langle\sigma v\rangle$ = 3.8$\times10^{-26}$ cm^{3}s^{-1} is shown in Fig. 8.12. It is shown for individual ROIs as well as for the combination of all ROIs. Energy-differential spectra for the corresponding ON and OFF regions, convolved with the H.E.S.S. acceptance and energy resolution, are overlaid. The spectra for the ON and OFF regions show an increase after the break at around 10 TeV. This is due to the population of events reconstructed with only the four small telescopes, which are more sensitive at larger energies. The expected number of photons for two self-annihilating DM particles can be computed, for a fixed DM particle mass and annihilation channel. We can compute the expected number of photons from annihilating DM with the energy differential flux per

[1] Alternative DM models may explain the found excess.

[2] This value is obtained from the energy bins of the acceptance $A_{\mathrm{eff}}(E)$, which are obtained as a consequence of the energy resolution of H.E.S.S. which determines the spectral binning of the instrument response functions.

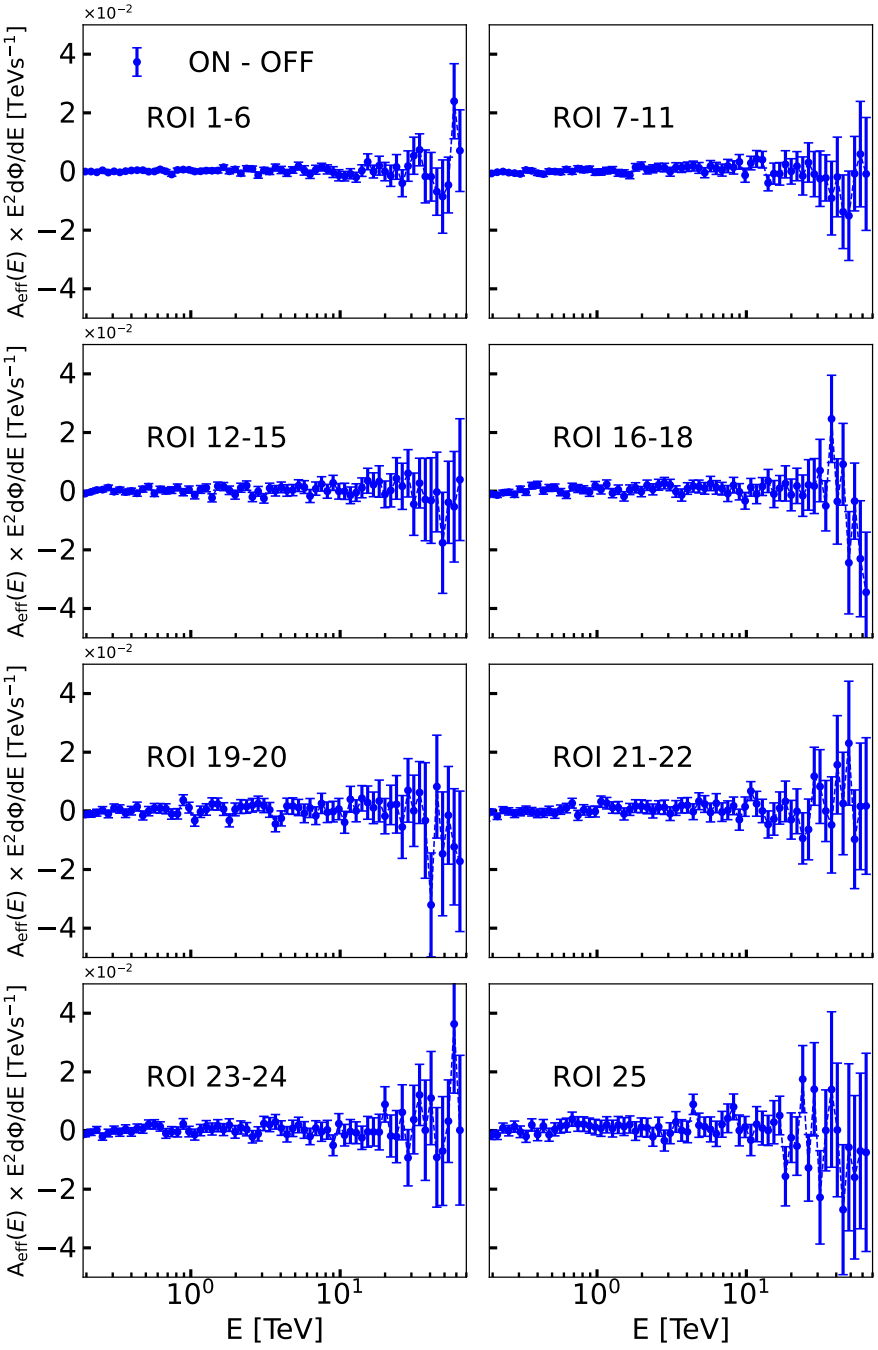

Figure 8.11: Background-subtracted energy-differential spectra in E^2, convolved with the H.E.S.S. acceptance $A_{\rm eff}(E)$. 1σ error bars are shown too. Different combinations including all the ROIs are shown.

spectral and spatial bin that we defined in Eq. 3.12. To do so, we need to include the characteristics of the instrument, like the IRFs, the effective area and the energy resolution and the observational live time. The expected number of photons from annihilating DM is computed as $N_{\rm S}$, by summing the $N_{{\rm S}k}$ over all the runs k. The finite energy resolution of the H.E.S.S. telescopes is included via the convolution of the spectrum with a Gaussian of σ/E of 10% above 200 GeV [153]. The energy resolution is expressed by $R(E_\gamma, E'_\gamma)$, relating the energy detected E'_γ to the true energy E_γ of the events. To obtain the expected number of photons we then include the J-factor $J(\Delta\Omega)$, for a ROI of solid angle $\Delta\Omega$, the energy dependent acceptance of the instrument $A_{{\rm eff},k}(E_\gamma)$ for the run k and the observational live time of the run k, $T_{{\rm obs},k}$. For each run, the information about the spatial response of the instrument is contained in the acceptance, which depends on the angular distance between the reconstructed event position and the pointing position of the run k. Then, for self-annihilating Majorana DM particles of mass $m_{\rm DM}$ in the channels f, with differential spectra dN^f_γ/dE_γ of branching ratios BR_f and with a thermally-averaged annihilation cross section $\langle\sigma v\rangle$, $N_{{\rm S}k}$ is given by:

$$N_{{\rm S}k}(\langle\sigma v\rangle) = \frac{\langle\sigma v\rangle J(\Delta\Omega)}{8\pi m^2_{\rm DM}} T_{{\rm obs},k} \int_{E_{\rm th}}^{m_{\rm DM}} \int_0^\infty \sum_f BR_f \frac{dN^f_\gamma}{dE_\gamma}(E_\gamma)\, R(E_\gamma, E'_\gamma)\, A_{{\rm eff},k}(E_\gamma)\, dE_\gamma\, dE'_\gamma\,, \quad (8.1)$$

The expected number of photons obtained with equation 8.1, for each energy bin considered in this analysis, is computed and displayed in Fig. 8.13. For illustration, we computed this for a fixed DM mass of $m_{\rm DM}$ = 3 TeV, the annihilation channel W^+W^- and annihilation cross section of $\langle\sigma v\rangle$ = 5 $\times 10^{-24}$cm^{3}s^{-1}. The peak in the distribution of DM expected events is given by the photons resulting from the annihilation of DM for the energy bin close to the DM mass of the annihilating particles.

8.2.7 Expected dark matter distribution

Some of the typical parameterizations for the DM distribution in the GC region are the Einasto and Navarro-Frenk-White (NFW) profiles. They were shown in Eq.3.4 and Eq.3.5 for the Einasto and NFW parameterizations respectively. The DM density at the Solar position is assumed as $\rho_\odot = 0.39\,{\rm GeV cm}^{-3}$ [113]. The parameters of the Einasto and NFW profiles used here, together with an alternative parameter set for the Einasto profile are provided in Tab. 8.2. These density profiles are plotted in Fig. 8.14. The ON region used for the search of DM signals, comprehensive of all the 25 ROI rings, is shown too.

For each ring in the ROI, the total J-factor values are computed. The J-factor values for the Einasto and NFW profiles are shown in Table 8.3. The second and third column provide the inner and outer radii for each ring. The solid angle is given in the fourth column. The last three columns provide the J-factor values for the three profiles tested in this analysis. The former are plotted as a function of the ROI number in Fig. 8.14. An example of the J-factor map for the Einasto profile

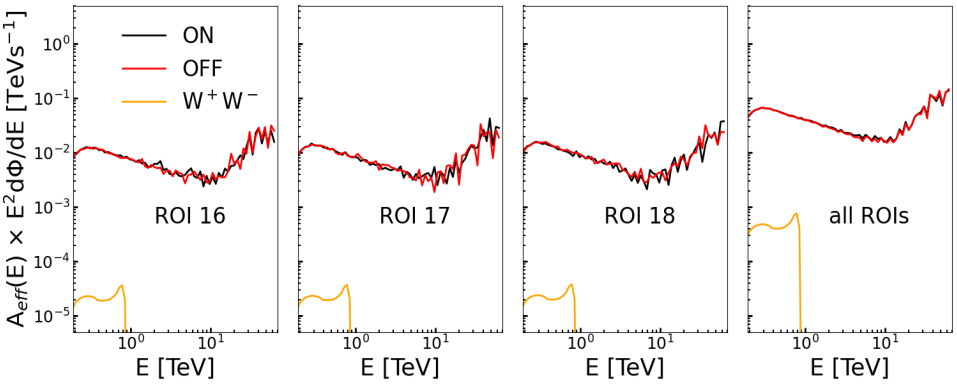

Figure 8.12: Energy-differential spectra expected expected from self-annihilating DM particles of mass m_{DM} = 0.98 TeV and $\langle\sigma v\rangle$ = 3.8×10^{-26} cm^{3}s^{-1} in the W^+W^- annihilation channel. The spectra are shown in E^2 and convolved with the H.E.S.S. response (orange line) for individual ROIs as well as for the combination of all ROIs. $A_{\mathrm{eff}}(E)$ stands for the energy-dependent acceptance of the instrument. Also plotted are the corresponding ON (black line) and OFF (red line) energy-differential spectra. The first three panels show the spectra for individual ROIs, the last panel shows the spectra for the combination of all the ROIs.

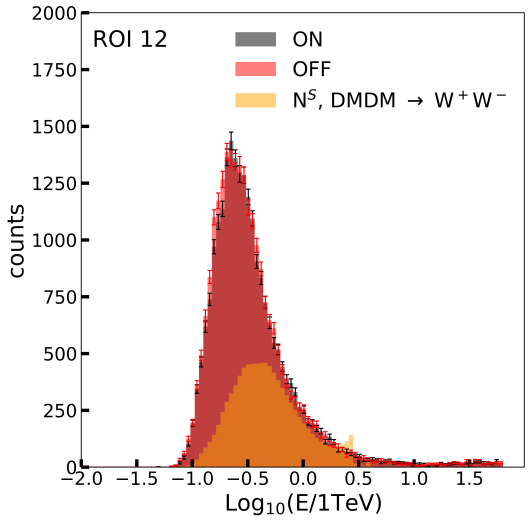

Figure 8.13: For illustration, expected DM events distribution for m_{DM} = 3 TeV, annihilation channel W^+W^- and annihilation cross section $\langle\sigma v\rangle$ = 5×10^{-24}cm^{3}s^{-1} shown as the orange distribution. For comparison, the ON and OFF event energy distributions for ROI 12 are displayed with 1σ error bars for each energy bin.

is shown in Fig. 8.6. The J-factors obtained for the Einasto parameterization as-

Profiles	Einasto	NFW	Einasto 2 [124]
$\rho_{\rm s}$ (GeVcm^{-3})	0.079	0.307	0.033
$r_{\rm s}$ (kpc)	20.0	21.0	28.4
$\alpha_{\rm s}$	0.17	/	0.17

Table 8.2: Parameters used for the DM profiles used in this analysis. The Einasto and NFW profiles are taken from Ref. [13]. The alternative normalization of the Einasto profile used is taken from [124] and referred to as "Einasto 2".

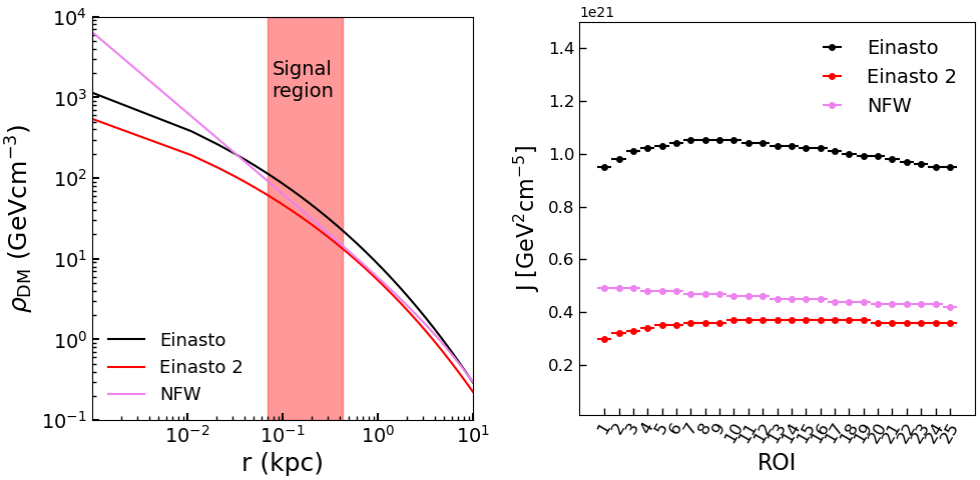

Figure 8.14: Dark matter density profiles $\rho_{\rm DM}$ versus distance r from the Galactic Center and J-factor values for each ring of the ROI. *Left panel:* Dark matter density profiles for the Einasto and NFW profile parameterizations as defined in Ref. [13]. An alternative parameterization of the Einasto profile [124] is also used and referred to as "Einasto 2". The red-shaded area corresponds to the signal region where the DM annihilation signals is searched. *Right panel:* J-factor values, obtained with the previously mentioned Einasto and NFW DM density parametrizations, are shown for each ring of the signal region.

sumes at least a factor 2 larger values than from the other two parameterizations, therefore we expect more constraining limits with the former.

i^{th} ROI	Inner radius [deg.]	Outer radius [deg.]	Solid angle $\Delta\Omega$ [10^{-4} sr]	J-factor $J(\Delta\Omega)$ [10^{20} GeV^{2}cm^{-5}]		
				Einasto	NFW	Einasto [124]
1	0.5	0.6	1.05	9.5	4.9	3.0
2	0.6	0.7	1.24	9.8	4.9	3.2
3	0.7	0.8	1.44	10.1	4.9	3.3
4	0.8	0.9	1.63	10.2	4.8	3.4
5	0.9	1.0	1.82	10.3	4.8	3.5
6	1.0	1.1	2.01	10.4	4.8	3.5
7	1.1	1.2	2.20	10.5	4.7	3.6
8	1.2	1.3	2.39	10.5	4.7	3.6
9	1.3	1.4	2.58	10.5	4.7	3.6
10	1.4	1.5	2.77	10.5	4.6	3.7
11	1.5	1.6	2.97	10.4	4.6	3.7
12	1.6	1.7	3.16	10.4	4.6	3.7
13	1.7	1.8	3.35	10.3	4.5	3.7
14	1.8	1.9	3.54	10.3	4.5	3.7
15	1.9	2.0	3.73	10.2	4.5	3.7
16	2.0	2.1	3.92	10.2	4.5	3.7
17	2.1	2.2	4.11	10.1	4.4	3.7
18	2.2	2.3	4.31	10.0	4.4	3.7
19	2.3	2.4	4.50	9.9	4.4	3.7
20	2.4	2.5	4.69	9.9	4.3	3.6
21	2.5	2.6	4.88	9.8	4.3	3.6
22	2.6	2.7	5.07	9.7	4.3	3.6
23	2.7	2.8	5.26	9.6	4.3	3.6
24	2.8	2.9	5.45	9.5	4.3	3.6
25	2.9	3.0	5.64	9.5	4.2	3.6

Table 8.3: J-factor values for the 25 rings of the ROI considered in this work, shown in units of GeV^{2}cm^{-5}. The ring number, the inner and the outer radii and the size in solid angle for each ring are given in the first four columns. The J-factor values in the rings, computed without applying the masks on the excluded regions, are given for the Einasto, an NFW [13] and an alternative Einasto [124] profiles in the fifth, sixth and seventh columns respectively.

8.3 Searching for dark matter signal

8.3.1 Limits on the annihilation cross section

Since no significant excess compatible with DM signals is found in the ROI, we derive upper limits on the $\langle\sigma v\rangle$, used in Eq. 8.1, with the framework defined in Sec. 4.4.

The statistical analysis is performed with a 2-dimensional log-likelihood ratio test statistic, which exploits the expected spectral and spatial DM signals features in 67 logarithmically-spaced energy bins and 25 spatial bins corresponding to the rings of the ROI. A safe energy threshold was defined as E_{thr} = 200 GeV. For a fixed DM mass, the likelihood function used is the same as the one defined in Sec. 4.2. For this analysis, $N_{\text{S}i,j}$ and $N_{\text{S}'i,j}$ are considered as the total number of DM events in the (i,j) bin for the ON and OFF regions, respectively. These values are computed with Eq. 8.1, where the expected DM flux is folded with the energy-dependent acceptance and energy resolution. The term dN_γ^f/dE_γ, corresponding

to the gamma-ray yield in the channel f, is computed with the Monte Carlo event collision generator PYTHIAv8.135, including final state radiative corrections [124]. To account for the systematic uncertainty in the likelihood function, a Gaussian nuisance parameter, composed by $\beta_{i,j}$ as a normalization factor and $\sigma_{\beta,i,j}$ as the width of the Gaussian function, is used (see, for instance, Refs. [336, 244, 285] and what we will explain in Sec. 8.4). The value of $\beta_{i,j}$ is found by a maximization of the likelihood function such that $\mathrm{d}\mathcal{L}_{\mathrm{i,j}}/\mathrm{d}\beta_{\mathrm{i,j}} \equiv 0$. The $\sigma_{\beta,ij}$ value used is fixed to 1%.

Since no significant excess was found in the ROI rings, we derive constraints on $\langle\sigma v\rangle$ from the log-likelihood ratio TS described in Ref. [147] and already described in Sec. 4.4, assuming a positive signal $\langle\sigma v\rangle > 0$. Given the high statistics regime, the TS follows a χ^2 distribution with one degree of freedom. With the obtained limits, values of $\langle\sigma v\rangle$ with TS higher than 2.71 are excluded at the 95% C.L..

8.3.2 Expected and observed limits

For the upper limits on $\langle\sigma v\rangle$ for self-annihilation of WIMPs with masses from 200 GeV up to 70 TeV, different annihilation channels are considered. We explored self-annihilation into the quark ($b\bar{b}$, $t\bar{t}$), gauge bosons (W^+W^-, ZZ), lepton (e^+e^-, $\mu^+\mu^-$, $\tau^+\tau^-$) and Higgs (HH) channels. The 95% C.L. observed and expected upper limits for the W^+W^- and $\tau^+\tau^-$ channels, respectively, for the above-mentioned Einasto profile are shown in Fig. 8.15. The 68% and 95% statistical containment bands are plotted as well. The observed limits are computed with the available statistics in the ON and OFF measured energy count distributions.

For the computation of the expected upper limits, 300 Poisson realizations of the background extracted from the OFF regions are performed. For each ring of the ROI and observational run, independent Poisson realizations of the measured background energy count distributions are computed for the ON and OFF regions on a run-by-run basis, respectively. The upper limits on $\langle\sigma v\rangle$ are computed according to the TS procedure for each realization of the overall energy count distribution in the ON and OFF regions. The procedure is repeated 300 times. The distribution of the computed limits is used for the derivation of the mean expected limits, the 68% and 95% statistical containment bands. These values are derived from the mean, the 1 and 2σ standard deviations of the distribution. This procedure was already described in Sec. 4.4.3.

Considering the W^+W^- channel, the obtained annihilation cross section observed upper limit for a DM particle of mass 1.5 TeV is 3.7×10^{-26} cm^{3}s^{-1}. In the $\tau^+\tau^-$ annihilation channel, the obtained upper limit is 1.2×10^{-26} cm^{3}s^{-1} for 0.7 TeV DM mass. The $\langle\sigma v\rangle$ values expected for DM particles annihilating with thermal-relic cross section [82] are crossed by the limits in the $\tau^+\tau^-$ and e^+e^- annihilation channels. With respect to the latest constraints shown in Ref. [13], we obtain an improvement factor 1.6, for a DM particle with mass of 1.5 TeV. The larger statistics of the dataset, collected from longer observational live time, and

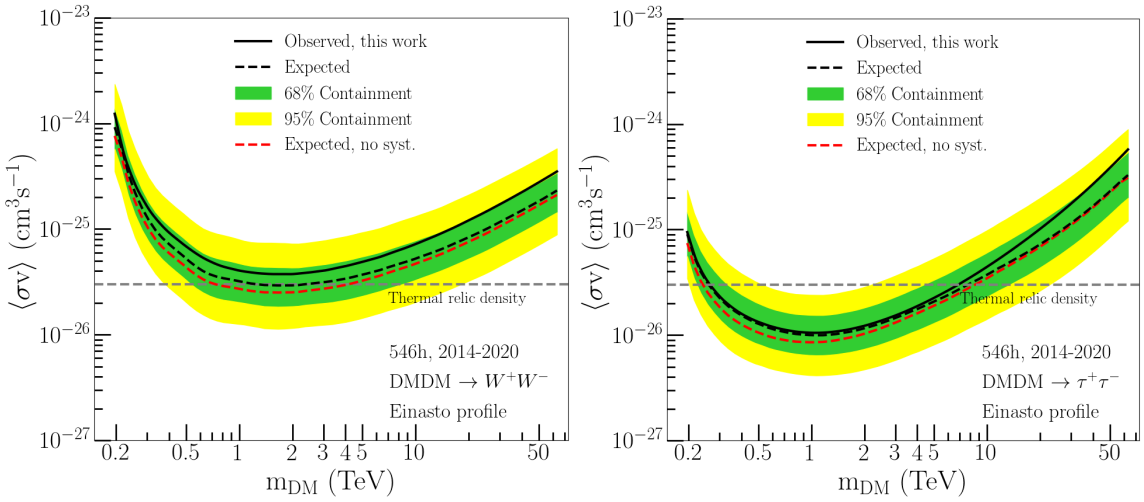

Figure 8.15: Upper limits, as a function of the DM mass m_{DM}, on $\langle\sigma v\rangle$ derived from the 2014-2020 H.E.S.S. observations, for the W^+W^- (left panel) and $\tau^+\tau^-$ (right panel) channels. The upper limits include the systematic uncertainty. Observed upper limits are shown as the black solid line. Mean expected upper limits (black dashed line) together with the 68% (green band) and 95% (yellow band) C.L. statistical containment bands are shown too. The mean expected upper limits computed without including systematic uncertainty are also shown (red dashed line). The natural scale expected for thermal-relic WIMPs is shown as the horizontal gray long-dashed line.

the deployment of the CT1-5 array of H.E.S.S. contributed to the better sensitivity of the present analysis. The limits for the channels W^+W^- and $\tau^+\tau^-$ are shown in Fig. 8.15. The analysis for the derivation of constraints on the $\langle\sigma v\rangle$ of DM particles is performed also in the $b\bar{b}$, $t\bar{t}$, ZZ, HH, e^+e^-, $\mu^+\mu^-$, and annihilation channels. The constraints for these channels are shown in Fig. 8.16.

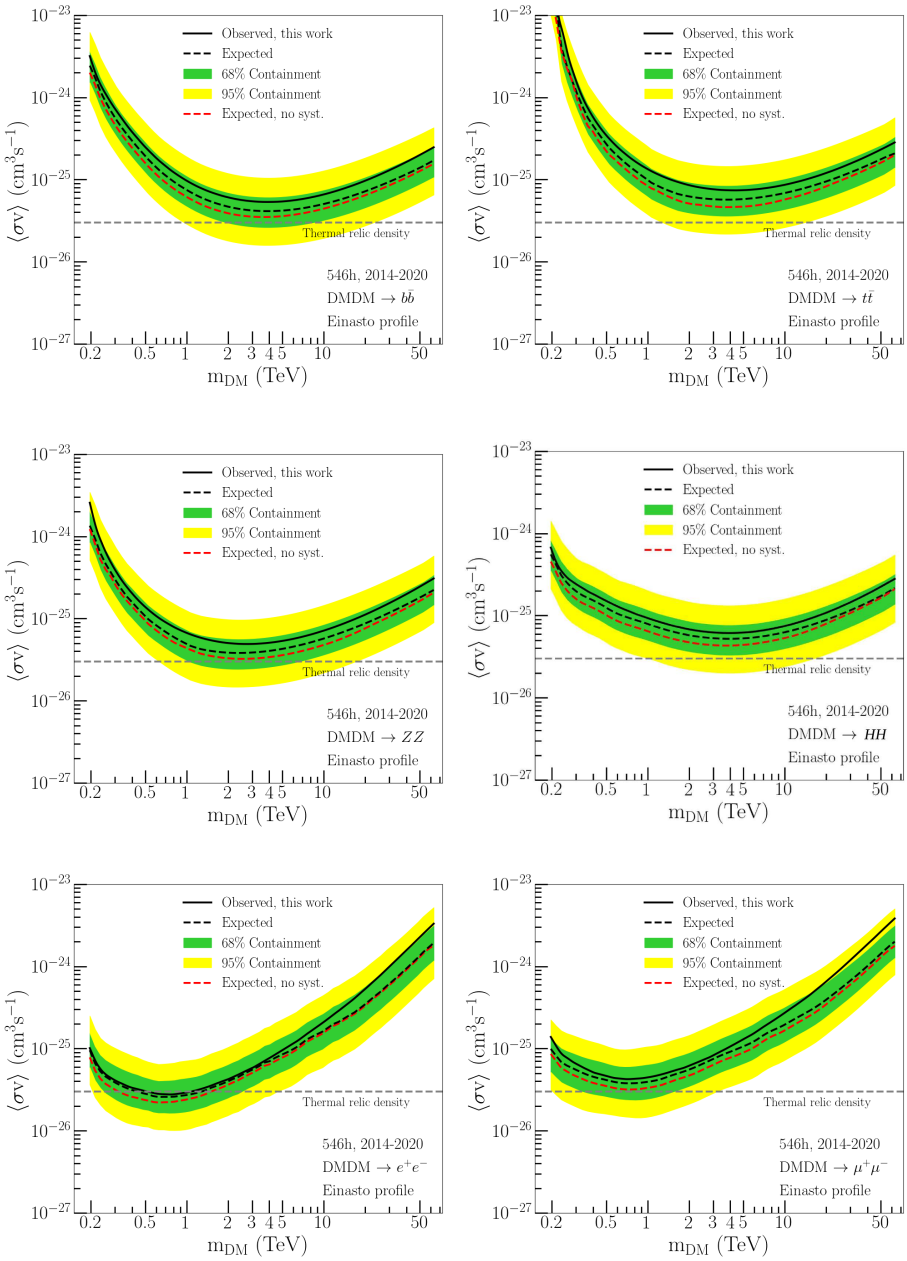

Figure 8.16: Upper limits, as a function of the DM mass $m_{\rm DM}$, on the velocity-weighted annihilation cross section $\langle\sigma v\rangle$ derived from the 2014-2020 H.E.S.S. observations. The limits are displayed for the $b\bar{b}$, $t\bar{t}$, ZZ, HH, e^+e^- and $\mu^+\mu^-$ channels, respectively. The upper limits include the systematic uncertainty. Observed upper limits are shown as the black solid line. Mean expected upper limits (black dashed line) together with the 68% (green band) and 95% (yellow band) C.L. statistical containment bands are shown too. The mean expected upper limits computed without including systematic uncertainty are also shown (red dashed line). The natural scale expected for thermal-relic WIMPs is shown as the horizontal gray long-dashed line.

8.3.3 Comparison with other experiments

The limits obtained with this analysis are the most constraining ones, for the channels presented in this analysis, in the TeV mass range. In Fig. 8.17, we show a comparison between the limits obtained with this analysis and the previous limits from H.E.S.S. observations and from other experiments in the GeV-TeV mass range, for the W^+W^- annihilation channel. The previous limits obtained with H.E.S.S. observations of the GC region were derived from a H.E.S.S. I dataset of 254 hours of observations [13]. Limits obtained with observations of the GC region with HAWC [17] and with *Fermi*-LAT [24] are shown as well. The limits obtained with *Fermi*-LAT are shown for the $b\bar{b}$ annihilation channel. *Fermi*-LAT limits from the observations of 15 dwarf galaxy satellites of the Milky Way [23] are shown too. Finally, the figure shows the limits obtained from the cosmic microwave background measured by PLANCK [29].

The limits are 1.6 times more constraining than the latest H.E.S.S. constraints [13] for a DM particle with mass of 1.5 TeV. In addition, they surpass the limits obtained with *Fermi*-LAT for particles with mass above $\sim$ 300 GeV.

8.3.4 Testing different Dark Matter profiles

The dark matter density profiles adopted in this work have been described in Sec. 8.2.7. The comparison between the limits computed with the J-factor values obtained with these profiles is shown in Fig. 8.18. Computing the limits with the NFW or the Einasto 2 parameterizations, described in Sec. 8.2.7, results in about a factor of 2.5 weaker constraints, compared to the ones obtained with the Einasto profile. If a DM density distribution was assumed as a kiloparsec-sized cored, such as the Burkert profile, the limits would be weakened by about two orders of magnitude. Instead assuming a Moore-like profile would produce limits more constraining of about a factor two.

8.4 Impact of the systematic uncertainties on the limits

A detailed study has been carried out on the systematic uncertainties affecting the 2014-2020 dataset in Sec. 6.4. For this particular analysis, the systematic uncertainty on the normalization of the energy count distributions is derived. We consider the derivation of the expected gradient in the gamma-like rate depending on the difference in the zenith angle of the observations.

For the DM analysis, the chosen ring of the ROI and each pointing position of the IGS, the difference of the mean values of the distributions of the ON and OFF event zenith angles is up to 1° depending on the zenith angle of the observational run. On a run-by-run basis, the observed gradient of the gamma-ray-like rate in

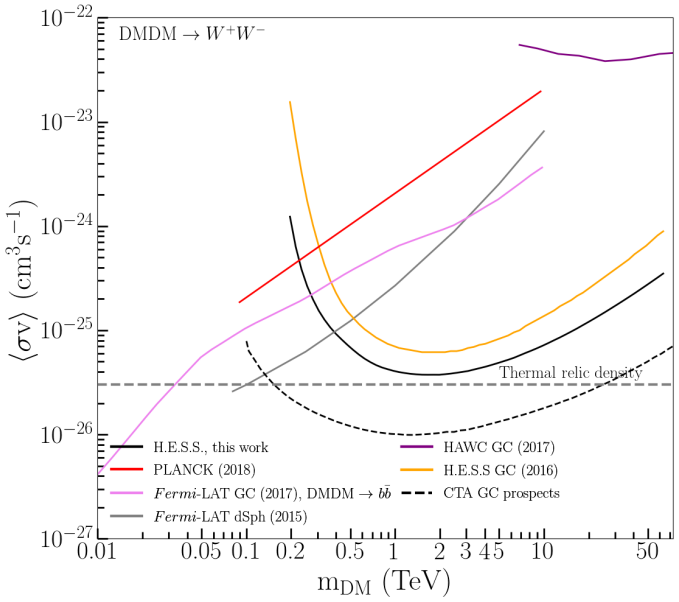

Figure 8.17: The latest H.E.S.S. constraints in the W^+W^- channel are compared with previous published limits. The previous limits from H.E.S.S. observations of the GC [13] are shown as an orange line. The limits from GC observations with HAWC [17] are shown as a purple line. The limits from the observations of 15 dwarf galaxy satellites of the Milky Way by the Fermi satellite [23] and of the GC region [24] are shown as the gray and violet lines, respectively. The limits from the GC are shown for the $b\bar{b}$ channel. Limits from the cosmic microwave background with PLANCK [29] are shown too, as the red line. . Limits from prospects of observations of the GC region with CTA are shown as the black dashed line [22]. The Einasto profile is used for all the GC limits.

the FoV is considered: the rate is renormalized according to the difference of the zenith angle mean values of the ON and OFF distributions. The typical width of 1° of the zenith angle distribution is taken into account by including a systematic uncertainty of 1% on the normalization of the measured energy count distributions. This value is included, as previously explained, as a Gaussian nuisance parameter composed by $\beta_{i,j}$ as a normalization factor and $\sigma_{\beta,ij}$ as the width of the Gaussian function. $\sigma_{\beta,ij}$ is therefore fixed to 1%. The mean expected limits are deteriorated, by the inclusion of the 1% value, from 8% to 18% depending on the DM particle mass.

No other source of systematics explained in Sec. 6.4 is included in this work.

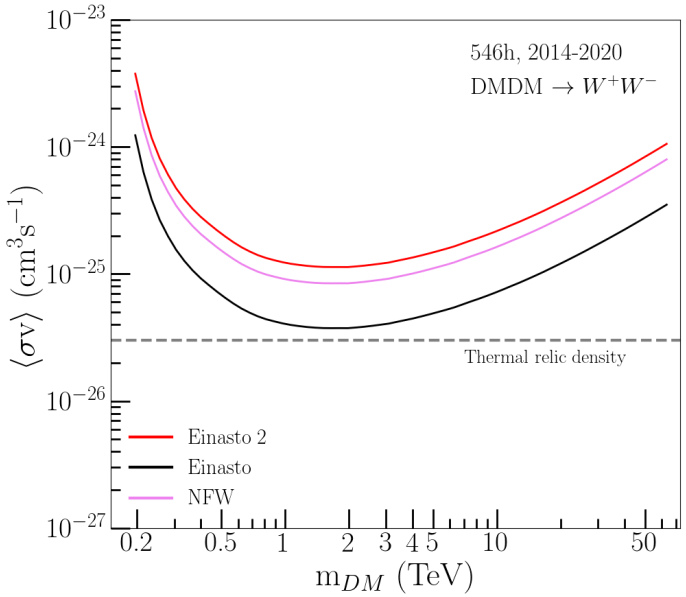

Figure 8.18: Limits on the velocity-weighted annihilation cross section $\langle\sigma v\rangle$ obtained with different parameterizations of the DM density distribution. The 95% C. L. upper limits, shown for the Einasto profile (black line), another parameterization of the Einasto profile [124] referred to as "Einasto 2" (red line), and the NFW profile (pink line), are computed for the W^+W^- channel and including the systematic uncertainty.

8.5 Conclusions and outlook

In this analysis, we obtained the latest results on a search for signals from annihilating WIMPs, from new observations of the inner halo of the Milky Way with the complete five-telescope array of H.E.S.S.. The main outcomes are:

- the used H.E.S.S. II dataset provides a factor 5 more exposure and a factor $\sim$ 1.6 more sensitivity on the DM annihilation signals from the GC region with respect to the previous H.E.S.S. I dataset;
- a significant excess is found in the high energy band of the dataset, however there is no compatibility with the spatial and spectral morphology of the searched DM signals, therefore we derive 95% C.L. upper limits on $\langle\sigma v\rangle$ of the DM particles;
- upper limits of 3.7×10^{-26} cm^{3}s^{-1} and 1.2×10^{-26} cm^{3}s^{-1} are obtained for DM particles with masses of 1.5 TeV and 0.7 TeV, for the Einasto profile and in the W^+W^- and $\tau^+\tau^-$ channels, respectively;
- the derived limits improve significantly the previous constraints, becoming

the most constraining ones so far in the TeV mass range for the explored channels;

- the natural $\langle \sigma v \rangle$ values expected for the thermal-relic WIMPs are challenged in the TeV DM mass range by the limits in the $\tau^+\tau^-$ and e^+e^- channels.

This analysis benefits from improved sensitivity due to the observations carried out with the IGS program as well as the use of the full H.E.S.S. array of five telescopes. Observations at VHE with IACTs of the Galactic Center region are unique to thoroughly study the WIMP models and provide crucial insights on TeV mass WIMPs. The IGS is an unprecedented dataset to explore the parameter space of multi-TeV DM models such as the benchmark candidates Wino and Higgsino (see Ref. [324] and references provided therein) which naturally arise in simple extensions to the Standard Model. Limits on $\langle \sigma v \rangle$ of DM particles obtained with observations from different facilities were compared in Fig. 8.17. Constraints from prospects of observations with CTA were also displayed [22]. Constraints on the DM models with the IGS observations are an important legacy of H.E.S.S. and pave the way to future analysis of observational dataset that will be collected by the Southern-site of CTA [285]. The latter will improve on the limits of the current generation of IACTs and will significantly extend the range of DM masses where the theoretically important benchmark, provided by the thermal value for the $\langle \sigma v \rangle$, can be robustly probed [22]. This work has been published in *Physical Review Letters* [7].

Chapter 9

Dark matter annihilation signals from unidentified Fermi objects

Contents

Summary

Fermi-LAT Objects with no correspondent counterparts at other wavelengths (see for instance Refs. [40, 16]) are natural candidates for DM subhalos populating the Galactic halo [226] and compelling targets for DM search beyond the classical ones such as GC and dwarf galaxies. A selection of unidentified $Fermi$-LAT Objects (UFOs), has been observed with the full five-telescope H.E.S.S. array. This chapter describes the analysis carried out with the datasets coming from 2018 and 2019 H.E.S.S. observations of a selection of the most promising UFOs. The goal is to probe their potential TeV-mass DM-induced emissions. Sec. 9.1 introduces the subject. In Sec. 9.2 the distribution of the J-factor values for DM Galactic subhalos is described. Sec. 9.3 describes the *Fermi*-LAT analysis of the selected UFOs datasets to obtain a quantitative description of how DM models can fit to the *Fermi*-LAT data. The H.E.S.S. observations and data analysis are explained in Sec. 9.4. The constraints on the parameters of the adopted DM models are described in Sec. 9.5, which specifically treats the upper limits derived with the H.E.S.S. analysis, and in Sec. 9.6, which describes the results obtained from cosmological simulations and the associated uncertainties. Finally, the conclusions are gathered in Sec. 9.7. This work has been published in *The Astrophysical Journal* [10].

9.1 Introduction

The most accredited cosmological theories explain the formation of the Universe as hierarchical, with the creation of the smallest structures happening first. Originally, DM particles collapse and form gravitationally-bound systems. These systems later merge to form the first subhalos, which subsequently form the more massive ones. After the merging history, DM halos are believed to be massive enough to retain gas, trigger star formation and give rise to the galaxies that we observe today. Nevertheless, most of the subhalos remain completely dark. Under the assumption that DM subhalos are made of WIMPs, 10^{-4} to 10^{10} $M_{\odot}$ mass subhalos are predicted to lie in DM halos of Milky-Way sized galaxies [161, 343]. The expected number density profile of subhalos is shown in Fig. 9.1, extracted from Ref.[161]. The number density profile of subhalos presents larger values than the DM density profile for large distances from the GC. The ratio between the two is also shown and represents quite well $\rho M(< r)$ of the Galaxy [161]. In the lower panel of the same figure, the profile of the subhalo concentrations is shown. The concentration increases towards the central region of the Milky Way where the low density outer parts of the subhalos are stripped by the stronger tidal force [161].

Dwarf galaxies should be hosted by the most massive subhalos ($\gtrsim 10^8$ $M_{\odot}$). Dark subhalos are predicted as compact and concentrated objects, not hosting conventional astrophysical high-energy emitters. However, when the halos are massive and/or close enough, gamma-ray fluxes produced by the annihilation processes of the constituent DM particles can be detectable with satellites and ground-based experiments, such as the current generation of IACTs [235, 348, 353, 109]. In addition, massive enough WIMPs can annihilate frequently enough and produce VHE photons detectable by the H.E.S.S. telescopes. Nonetheless, the location of these subhalos is unknown. Their search can be performed with observations of all sky with the Large Area Telescope (LAT) instrument onboard the Fermi satellite [77] or wide-field survey carried out with IACTs [35, 105]. Alternatively, one can observe unidentified *Fermi*-LAT Objects revealed by the *Fermi*-LAT observations of the whole sky [40, 16]. The datasets of the unidentified sources published by the *Fermi*-LAT collaboration have been used to search for annihilation signals from WIMPs. Fig. 9.2 was extracted from [146] and shows limits derived from the three *Fermi*-LAT catalogs for all point-like sources. The constraints were obtained for two DM particles annihilating in the $\tau^+\tau^-$ channel reaching thermal annihilation cross section [347] for DM particles with GeV masses.

The emission spectra coming from selected UFOs can be described by high-mass DM models, provided that the DM particles populating the halos have masses that lie above 100 GeV [65, 110, 146, 369, 84]. UFOs showing hard spectra in the few-ten-to-hundred GeV energy range can be identified as DM subhalos if considering DM masses sufficiently larger than 100 GeV. Therefore, such objects are

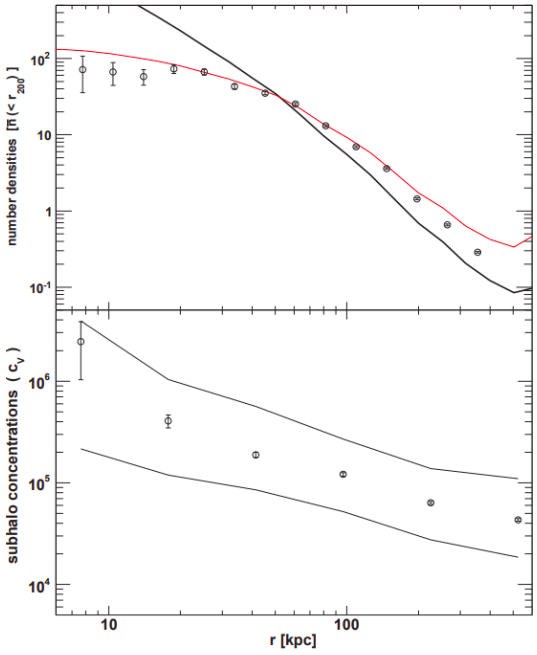

Figure 9.1: Abundance and concentrations of subhalos vs distance from the Galactic Center are plotted in the top and bottom panels, respectively. *Top panel*: the number density profile of subhalos, shown by the circles, compared to the DM halo density profile, shown by the black line. The red line shows the ratio of the two. *Bottom panel*: Subhalo concentrations median and 68% containment values shown by the circles and the black lines. The error bars indicate the statistical uncertainties in both panels. Figure extracted from [161].

excellent targets to perform searches for DM subhalos with IACTs and probe their DM origin in the TeV mass range.

9.2 Dark matter subhalos from cosmological simulations

Dark Matter halos of Milky-Way sized galaxies are populated by galactic subhalos, DM substructures predicted from cosmological N-body simulations (see, for instance, Refs. [161, 341]) and today unmerged. The mass function of the subhalos can be derived, together with a robust description of its slope and normalization, from the simulations. The function is defined as $\mathrm{dln}N/\mathrm{dln}M \propto \mathrm{M}^{-\alpha_\mathrm{m}}$, with a slope of $\simeq 1.9$ for MW-like galaxies (see, for instance, Refs. [161, 341, 182, 172]). A large number density of galactic subhalos, not hosting conventional astrophysical

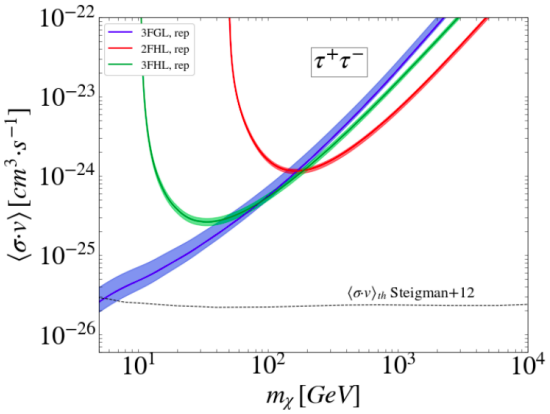

Figure 9.2: Limits on the DM annihilation cross section for the $\tau^+\tau^-$ annihilation channel with the datasets of unidentified *Fermi*-LAT objects extracted from the three *Fermi*-LAT catalogs used in Ref. [146]. The shaded bands refer to the 1σ uncertainty. The dashed line represents the thermal value of the annihilation cross section [347]. Figure extracted from [146].

sources, is expected to be present in MW-like galaxies. Even though no information is derived by observations of conventional astrophysical emitters in these subhalos, properties such as abundance of the resolved ones, radial distribution, mass and concentration can be derived from the simulations. The DM density distribution in these subhalos is believed to follow a cuspy profile, which can be built with NFW [292] or Einasto parametrizations [343]. The slope of the DM density distribution in a subhalo can be predicted only for the most massive ones, due to the limited spatial resolution of the current cosmological simulations.

9.2.1 Expected subhalo J-factor distribution in the Milky Way

Under the assumption of a profile for the DM density in subhalos, the distribution of J-factors of the galactic subhalo population $\mathrm{d}N/\mathrm{d}J$ can be derived. From the cumulative distribution $N(J) \equiv N(\geq J)$ the number of subhalos in the MW with J-factor greater or equal than some specified value can be computed. The distribution of J-factors of DM subhalos in the MW is derived with the CLUMPY code v3.0.0 [121, 99, 215]. For the realization of the DM main halo profile, 1000 simulations of a MW-like galaxy with a smooth NFW [292] are performed. The recent measurements in Ref. [114] show that the NFW profile fit well the expected DM distribution even though there are still important uncertainties connected to the derivation of the DM profile. In Chap. 8, we used the Einasto as the main profile to maintain coherence to the previous H.E.S.S. results. The parameters assumed for the NFW profile are taken from a recent study of DM distribution in the Milky

Way [114]. The parameters for the description of the subhalos, for each simulation, are chosen similar to the ones used in [217] for the "HIGH" model. The slope of the power law describing the subhalo mass function is fixed to $\alpha_{\rm m} = 1.9$ [161]; the number of objects between 10^8 and $10^{10} M_\odot$ is taken as $N_{\rm calib}$ = 300 following [343]; and the subhalo mass-concentration relation is chosen following the distance-dependent prescription of [280].

From each simulation, Galactic coordinates and the integrated values of the J-factors within 0.1° radius around the centers of gravity of the subhalos are derived. The cumulative J-factor distribution $N(\geq J)$ is shown in the upper panel of Fig. 9.3. This distribution is valid for subhalos located at Galactic latitudes $|b| > 5°$. For our analysis, we consider only subhalos located at high latitudes such that we can avoid including the diffuse emissions in the measured backgrounds. This simplifies the analysis. Moreover, the effects of tidal disruption is negligible for high latitudes subhalos. The average value of the distribution, from the 1000 realizations, is shown as the red curve. The 1σ bands are displayed as the red shaded areas. The lower panel of Fig. 9.3 shows the probability to find, in any simulation, at least one (three) subhalo(s) with a J-factor larger than the specified value as the red dashed (blue dotted) curve. The black dashed line highlights the 5% probability. The probability, on average, to find one or more subhalos with J-factor $J \geq 3 \times 10^{20}$ GeV^{2}cm^{-5} is only about 5% and it is shown by the crossing of the red dashed line with the black dashed one. The same value of the probability is found for three or more subhalos with J-factors $J \geq 1 \times 10^{20}$ GeV^{2}cm^{-5} where the blue dotted and the black dashed lines cross.

9.3 *Fermi*-LAT unidentified sources as dark matter subhalo candidates

In all-sky gamma-ray surveys, hypothetical emission in gamma-rays coming from objects detected by *Fermi*-LAT, but with no other counterparts at any other wavelengths, is expected [226]. The smoking gun trademark of DM emission is a very distinct energy cut-off at the DM mass in the detected flux, assuming the two body process of the annihilation taking place almost at rest. However, when considering DM particle masses larger than a few hundred GeV, the LAT instrument could not detect such a feature because it was too high in energy. Spectra derived from VHE observations with H.E.S.S. can cover the window and search for possible DM-induced cut-offs. To search for the best candidates through the unidentified Fermi sources, a thorough selection in the Third Catalog of High-Energy *Fermi*-LAT Sources (3FHL) [40] is performed. The 3FHL includes sources detected above 10 GeV from the first 7 years of collected data. The catalog contains 1556 objects, including point-like sources, observed with improved sensitivity and angular resolution with respect to the previous LAT catalogs at the same energies. Of the

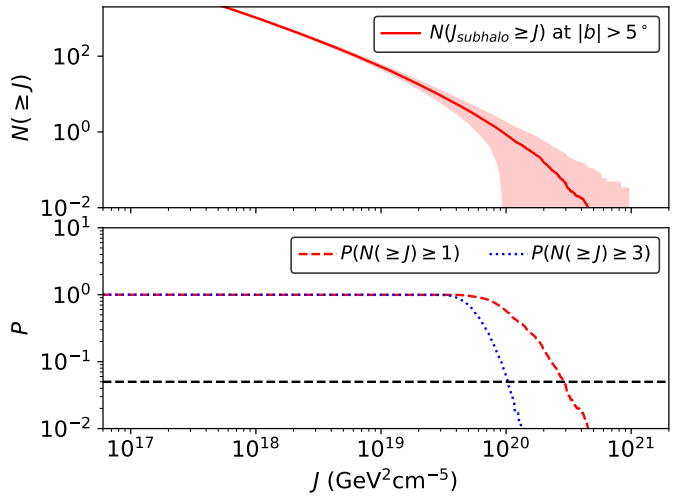

Figure 9.3: *Top panel:* Number of subhalos with J-factor exceeding a given value obtained from 1000 simulations of the subhalo population for MW-like galaxies. The average value of the cumulative distribution is shown as the red solid curve, while the 1σ statistical uncertainty is represented by the shaded areas. *Bottom panel:* Probability P to find at least one subhalo with a J-factor higher than specified (red dashed line). The blue dotted line presents the same probability for at least three suhhalos. The horizontal black dashed line shows the 5% probability. See text for more details.

sources present in the catalog, 13% [40] are unassociated or associated with a source of not known nature. The sky map of the sources in the catalog, as extracted from [40], is shown in Fig. 9.4.

9.3.1 Candidates for H.E.S.S. observations

The selection through the 3FHL catalog is performed following some criteria. The baseline criterion requires that the source is not associated with any emission at other wavelengths. Subsequently, sources too close to the Galactic plane are excluded. Afterwards, criteria to search for DM-emission like spectra are applied:

1. the unidentified sources have to be steady, *i.e.*, to not show flux variability over time according to the 3FHL catalog[1];

2. they need to exhibit a hard power-law spectral index ($\Gamma < 2$), as expected

[1]While the criterion on the variability provides steady candidates as expected for DM sources, *Fermi*-LAT photon properties at the highest energies have been checked. None of them could be attributed to flaring of nearby *Fermi*-LAT sources.

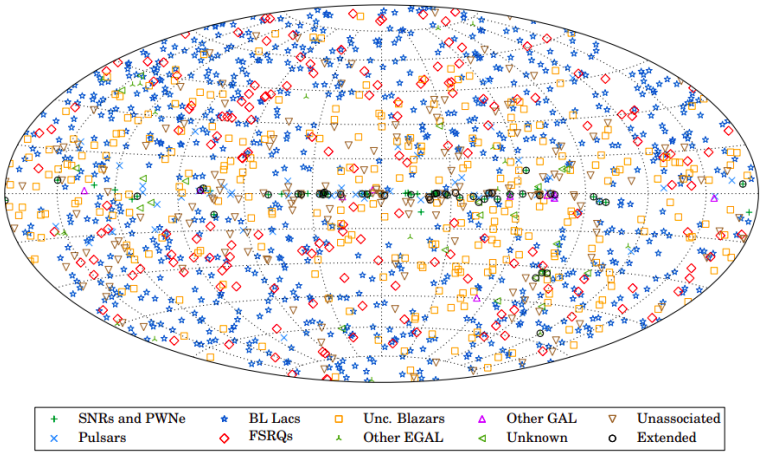

Figure 9.4: Sky map, in Galactic coordinates, showing the objects in the 3FHL catalog, as observed by *Fermi*-LAT. The legend reports the sources' most likely classification. Figure extracted from [40].

for DM-induced signals for DM masses above 100 GeV with no obvious conventional counterpart at other wavelengths.

Starting from the *Fermi*-LAT source coordinates, the possibility of counterparts in multi-wavelength (MWL) is searched. The search is performed in catalogs of MWL facilities (XMM-Newton, ROSAT, SUZAKU, CGRO, Chandra, Swift, WMAP, RXTE, Nustar, SDSS, Planck, WISE, HST) with the assumption of a searched radius around the source determined by the position uncertainty derived in the 3FHL catalog. We search for the sources far away from the Galactic plane, because the many astrophysical emitters in the plane could cover the faint emission from the searched subhalos and the latter would not survive in the Galactic disk and would be disrupted. Moreover, in this way a challenging modeling of the Galactic plane diffuse emission is avoided in the Fermi energy range. The sources that pass the criteria are six. They do not lie in a complex astrophysical environment and are relatively isolated with no high-energy gamma-ray emission within about one degree[2]. To obtain a low energy threshold, the H.E.S.S. observations are carried out at a maximum zenith angle of $45°$. The selection steps applied to the 3FHL catalog are summarized in Tab. 9.1. Following the observation proposal, observations have been granted and scheduled for four of the selected UFOs. The characteristics of the UFOs selected for observations with the H.E.S.S. telescopes are summarized in Tab. 9.2. The small number of suitable DM subhalo candidates obtained by

[2]The closest 3FHL source for 3FHL J1915.2-1323 is at 0.8° while for the other UFOs, the closest source is at distance higher than 1.7°).

Criteria	Numbers of sources
Without association	178
Far enough from the Galactic plane, cut in Galactic latitude of $\|b\| > 5^\circ$	126
Non-variable, cut in variability index (No. of Bayesian blocks in var. analysis) equal to 1	125
Maximum zenith angle at H.E.S.S. site of 45°	83
Follow a simple power law with significance for curvature $< 3\sigma$	83
Hard spectrum, cut in spectral index below 2	18
No MWL counterparts	6

Table 9.1: Selection criteria to extract DM subhalo candidates from the 3FHL catalog. For the search for multi-wavelength (MWL) counterparts, individual search radii are used ($\sim 2 - 4$ arcmin) based on the uncertainty of the Fermi position quoted in the 3FHL. The following list of MWL facilities is checked: XMM-Newton, ROSAT, SUZAKU, CGRO, Chandra, Swift, WMAP, RXTE, Nustar, SDSS, Planck, WISE, HST.

the straightforward selection is confirmation that the observation of a selection of UFOs is a viable DM search strategy for targeted observations performed by IACTs.

Name	RA [degrees]	Dec. [degrees]	TS for $E \geq 10$ GeV	Position uncertainty [arcmin]	Pivot[a] energy [GeV]	Spectral energy distribution at pivot energy [10^{-13} TeV cm^{-2}s^{-1}]	Power-law index	$\Delta\chi^2$	$E_{\rm cut}$ [GeV]
3FHL J0929.2-4110	142.3345	-41.1833	36	2.4	0.39	0.12 ± 0.01	1.37 ± 0.07	0.15	> 33
3FHL J1915.2-1323[†]	288.8182	-13.3916	23	3.0	62.8	2.1 ± 0.9	1.5 ± 0.4	0.05	> 35
3FHL J2030.2-5037	307.5901	-50.6344	40	2.6	6.3	1.9 ± 0.3	1.85 ± 0.1	0.40	> 67
3FHL J2104.5+2117[b,c]	316.1226	21.2831	58	2.2	1.56	5.3 ± 0.5	2.22 ± 0.06	0.02	> 85

Table 9.2: Selected UFOs properties and their spectral parameters. RA-Dec coordinates of the UFO sources are given in the second and third column. Test statistics (TS) values for energies above 10 GeV are provided in the fourth column. The position uncertainty is given in the fifth column. Pivot energy, spectral energy distribution at the pivot energy and best-fit power-law spectral index are given in the sixth, seventh, and eighth columns, respectively. The computed $\Delta\chi^2$ value between a pure power-law and a power law with exponential cut-off fit to the data is given in the ninth column. Finally, the lower limit on the possible energy cut-off in the energy spectrum is given at 95% C.L. in the last column. The 3FHL J1915.2-1323 source marked with † is detected only above 10 GeV. For this source, this minimum energy is considered for the values of the spectral index, pivot energy, differential flux and $\Delta\chi^2$. The minimum energy for the other sources is 0.1 GeV.

[a] The pivot energy is defined as the energy value where the ratio of differential flux over integrated flux is minimal.

[b] The spectral index in the 3FHL catalog is 1.8 [40].

[c] 3FHL J2104.5.2117 is recently associated with an AGN in the 4FGL catalog [16] with a probability of 0.4.

9.3.2 Fermi-LAT data analysis of the selected sources

For the analysis of the four UFO datasets with *Fermi*-LAT data, more than 12 years of observations are considered (from Aug. 2008 to Oct. 2020). The latest available `fermitools` v. 2.0.0 with P8R3_V3 response functions (`CLEAN` photon class)[3] are used. The energy spectra are derived applying the standard binned likelihood analysis with a 14°-radius region encompassing each of the object. The energy range is fixed between 0.1 and 1000 GeV, with eight log-equal bins. To perform the spectral analysis, spatial and spectral model descriptions of the sky region around the source of interest are fitted to the data. Moreover, in the fit region we include sources from the 4FGL-DR2 catalog [16] contained in the $14°$-radius region around the UFO position as well as components for isotropic and Galactic diffuse emissions given by the standard spatial and spectral templates `iso_P8R3_CLEAN_V2_v1.txt` and `gll_iem_v07.fits`. The spectral models are taken from the 4FGL catalog. Every parameter except the normalization is fixed to the values present in the catalog. In addition, all the sources from the 4FGL catalog up to $10°$ beyond the considered region of interest, with parameters fixed to catalog values, are included to the model. This is done to reduce the bias due to a possible presence of bright sources outside the considered region and effects that can arise as consequences of the poor PSF of the LAT at low (~ 0.1 GeV) energies. A pure power-law function is chosen to model the UFO spectra. To obtain the slope of the function, a broad energy-range fit is carried out.

To follow the recommendation of the *Fermi*-LAT collaboration, the analysis is done with energy dispersion handling enabled. Possible significant residuals between the data and the model are searched in the test-statistics (TS) maps of the considered regions. The maps are built for the $5° \times 5°$ regions around the position of each UFO. These maps show the significance ($\sim \sqrt{TS}$) w.r.t. the background model of a test point-like source with a power-law spectrum computed with a free normalization and slope fixed to -2, in each pixel. To determine the background model, the UFO source is removed and the same spatial and spectral models that we previously introduced are considered. The presence of unaccounted sources close to the UFO source position and the point-like spatial morphology of the UFO emission could be checked and verified, respectively. The TS maps, for energies larger than 10 GeV, are shown in Fig.9.5. The maps are produced in Galactic coordinates and with pixels of 0.05° size. No smoothing is applied. Position of UFO sources and nearby 4FGL sources are marked with cyan crosses and green circles, respectively. In the maps, no significant residual that could affect the *Fermi*-LAT data analysis of the UFOs is found. Therefore, the UFO sources' regions are well described by the considered models. The results of the analysis of each UFO are summarized in Tab. 9.2. From DM-induced emissions, a spectrum following a power-law with (super)-exponential energy cut-off in the TeV energy range is ex-

[3] See description of *Fermi*-LAT response functions.

pected [66]. In our case, the latter can not be significantly discriminated from a pure power-law emission due to the present availability of photon statistics in the *Fermi*-LAT dataset. The $\Delta\chi^2$ between these two models is shown in Tab. 9.2. The lower limits at 95% C.L. from the *Fermi*-LAT analysis on the energy cut-off, defined as the energy at which $\Delta\chi^2$ changes by 2.71 between power-law and exponential energy cut-off power-law models are shown in the last column of Tab. 9.2.

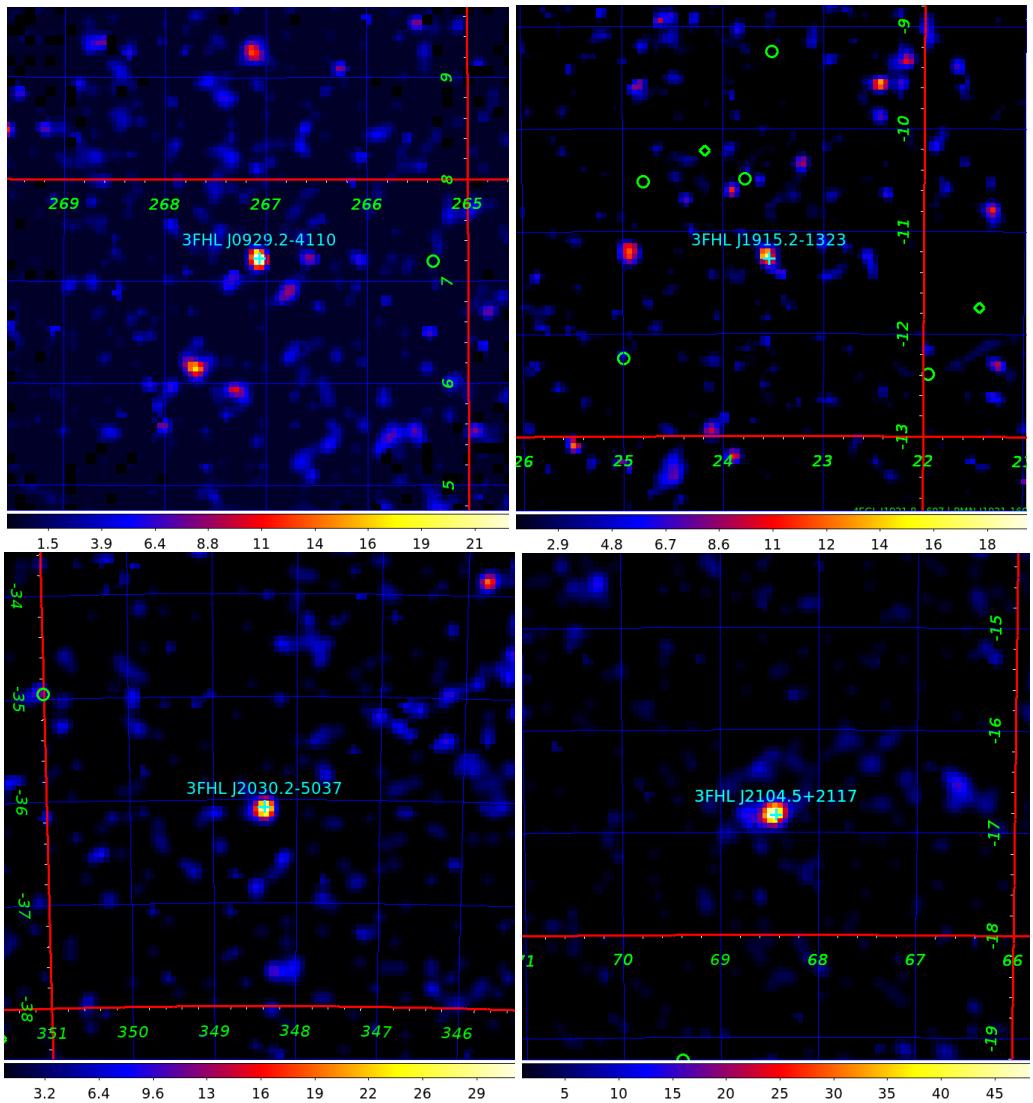

Figure 9.5: Test statistics maps displayed for energies above 10 GeV and for $5^\circ \times 5^\circ$ region around each of the considered UFOs. The maps are shown in Galactic coordinates with pixel size of 0.05°. The value of the TS is given by the color scale. The UFO source position in each map is given by the cyan cross. The positions of the nearby 4FGL sources included in the background model are given by the green cross.

9.3.3 Modeling the selected sources spectra with dark matter models

The *Fermi*-LAT flux measurements, taken from the 3FHL and the 4FGL catalogs and from the analysis described in the previous section, are shown in Fig. 9.6. When a flux point with more than 2σ significance is not obtainable, flux upper limits are shown with the same color code but with a downward arrow. DM emission models are superimposed to the *Fermi*-LAT flux measurements. Model predictions for DM masses of 1 TeV and 10 TeV, respectively, are plotted separately for the W^+W^- and $\tau^+\tau^-$ annihilation channels. Some of these can qualitatively describe the observed gamma-ray flux, obtained from the *Fermi*-LAT data analysis of the selected UFOs. For instance, the predictions shown for $m_{\rm DM}$ = 1 TeV well describes the *Fermi*-LAT data for 3FHL J0929.2-4110 in the W^+W^- and $\tau^+\tau^-$ annihilation channels. Otherwise, for 3FHL J2030.2-5037, the predictions for $m_{\rm DM}$ = 10 TeV in the W^+W^- annihilation channel do not describe the data very well, while the predictions for $m_{\rm DM}$ = 1 TeV are in better agreement. From the Figure, it is clear that some DM models can well fit the data obtained with the *Fermi*-LAT observations especially when considering the hard part of the DM spectra, which falls in good agreement with most of the *Fermi*-LAT flux measurements. However, no hint of cut-off is recognizable from the flux points and upper limits derived with the *Fermi*-LAT analysis. Therefore, observations with H.E.S.S., which has better sensitivity than the LAT at energies larger than a few hundreds of GeV, are needed to search for the smoking gun spectral characteristic of the DM models.

A quantitative assessment of how well the *Fermi*-LAT flux measurements can fit DM models is derived for each UFO. The spectra are explicitly modeled with a DM-annihilation induced spectral template[4]. The characteristic quantity of the model, when $m_{\rm DM}$ and annihilation channel are fixed, is only the overall normalization of the spectra given by $\langle\sigma v\rangle J$. To identify the range of viable parameters for DM annihilation, a scan over a large range of $\langle\sigma v\rangle J$ is performed. The adopted test-statistic (TS) is defined as a difference between best-fit log-likelihood functions for models with no DM emission ($\mathcal{L}_0$, "background only" hypothesis) and the model ($\mathcal{L}$) which includes the UFO source described by the corresponding parameter $\langle\sigma v\rangle J$: $TS = -2\log(\mathcal{L}/\mathcal{L}_0)$ [268][5]. The detection of the source corresponds to negative values of the TS, *i.e.*, adding a source with a corresponding parameter *improves* the fit in comparison to background-only hypothesis.

The results obtained for the UFO 3FHL J0929.2-4110 are shown in the left panels of Fig. 9.7, for W^+W^- (top) and $\tau^+\tau^-$ (bottom) annihilation channels, respectively. The results obtained for the other three UFO datasets, are shown in the left panel of Fig. 9.8 for the W^+W^- annihilation channel and in the right one for

[4]Provided within fermitools as `DMFitFunction` based on Ref. [221]

[5]The TS value for a source with N-parametric (spectral) model follows a χ^2 distribution with N degrees of freedom in the high statistic limit [365].

the $\tau^+\tau^-$ annihilation channel. The color scale shows the TS values for the values in the scanned range of $\langle\sigma v\rangle J$. Under the assumption that the TS follows a χ^2 distribution, when TS = -9 (resp. -25), a 3σ (resp. 5σ) significance for the detection for 1 degree of freedom is reached. The dashed cyan and orange lines show the detection region that corresponds to the improvement of TS by -9 and -25, respectively. The results for the combined dataset of three selected UFOs (3FHL J0929.2-4110; 3FHL J1915.2-1323; 3FHL J2030.2-5037) are shown in the right panels of Fig. 9.7. To obtain this, the log-likelihood profiles from individual objects, for W^+W^- (top) and $\tau^+\tau^-$ (bottom) annihilation channels, respectively, are combined. More details about the Figure are explained later in the chapter.

9.4 H.E.S.S. observations and analysis

The observations used for the analysis presented in this thesis are performed between 2018 and 2019 with the full five-telescope array and in the *wobble* observation mode. In this configuration, the telescope pointing direction is offset from the nominal target position by an angle between 0.5° and 0.7°. For the data used for the analysis, standard selection criteria [33] are applied. After the calibration of raw shower images recorded in the camera, a template-fitting technique [153] is performed to reconstruct the direction and energy of the gamma-ray events. In the template-fitting, the recorded images are compared to pre-calculated showers computed from a semi-analytical model. Above 200 GeV, energy resolution of 10% and an angular resolution of 0.06° at 68% containment radius for gamma-ray energies are achieved. The cross-checks of the results described later have been performed with an independent calibration and analysis chain yielding compatible results [301]. Each event in the dataset is chosen from the best reconstruction from three array configurations. This analysis profile is known as the *Combined Stereo* one, which has been already described in detail in Sec. 2.6. The selected UFOs are assumed to be point-like sources according to the point spread function (PSF) of *Fermi*-LAT which reaches $\sim 0.1°$ above 100 GeV. Given the H.E.S.S. PSF, the region of interest (ROI), hereafter referred to as the ON source region, is therefore defined as for point-like emission searches for H.E.S.S. and the ROI is taken as a disk of $0.12°$ radius. The results for the H.E.S.S. analysis have been cross-checked with an independent reconstruction and analysis chain [301].

9.4.1 Excess and Significance sky maps

Standard gamma-ray excess and significance maps are produced for the four UFO datasets with the *Ring Background* method, including the full five-telescopes array. The UFOs are considered as point-like sources. No significant excess is observed neither on the four targets nor anywhere else in the FoV. For the DM search analysis, specific background measurements and ROI are defined. This is explained

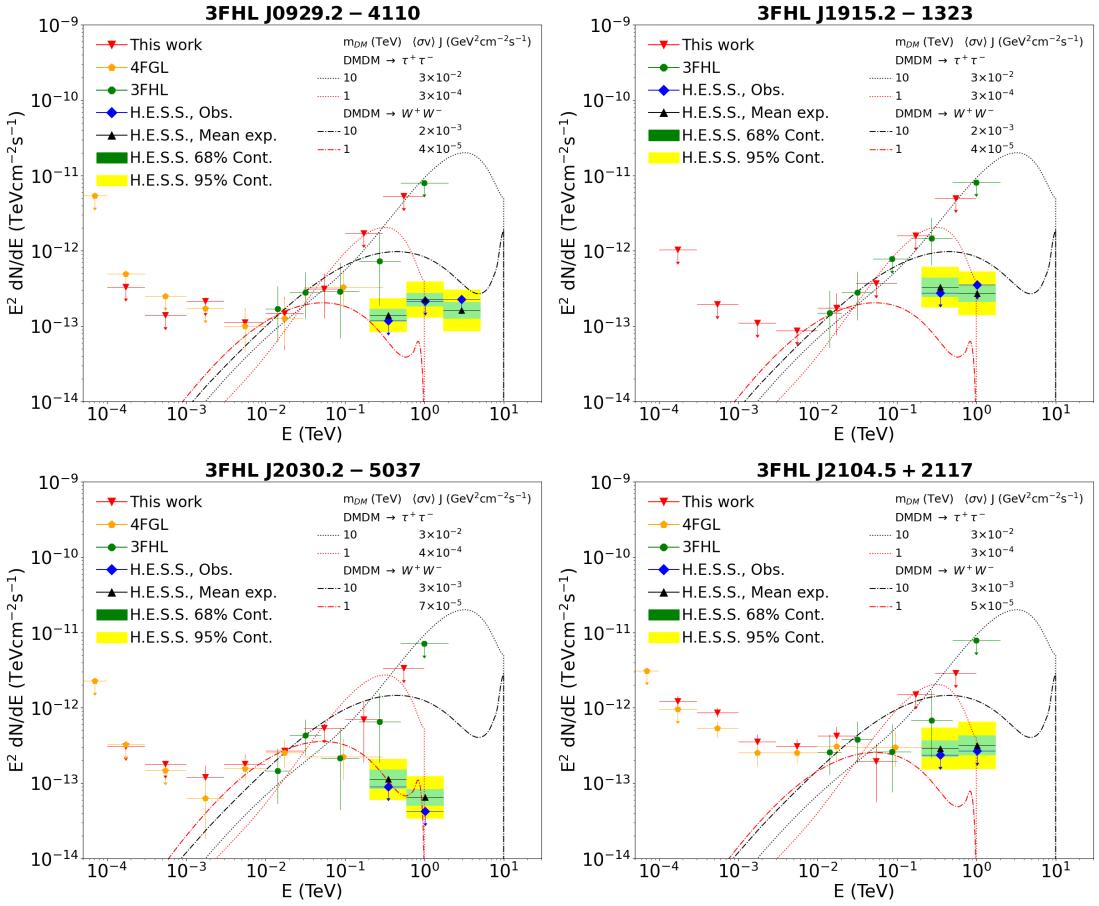

Figure 9.6: Spectral energy distributions of the selected unidentified Fermi objects observed with *Fermi*-LAT and H.E.S.S. for 3FHL J0929.2-4110 (top left), 3FHL J1915.2-1323 (top right), 3FHL J2030.2-5037 (bottom left), and 3FHL J2104.5+2117 (bottom right), respectively. The differential flux points computed in this work from the *Fermi*-LAT dataset (red dots) and taken from the 4FGL (orange dots) and from the 3FHL (green dots) catalogs [40, 16], are shown with the vertical and horizontal error bars corresponding to the 1σ statistical errors and the bin size, respectively. Flux upper limits and points (red, orange and green arrows) are given at 95% C.L.. The observed flux upper limits from H.E.S.S. observations (blue arrows) are plotted at 95% C.L., together with the mean expected flux upper limits (black) and the 1σ (green) and 2σ (yellow) containment bands. Overlaid are theoretical DM-induced fluxes for 1 TeV and 10 TeV DM masses in the W^+W^- (dash-dotted lines) and $\tau^+\tau^-$ (dotted lines) annihilation channels, respectively.

later in Sec. 9.4.2. The four excess and significance maps, as well as the significance distributions obtained with the photon counts used for the production of the significance maps, are shown in Fig. 9.9.

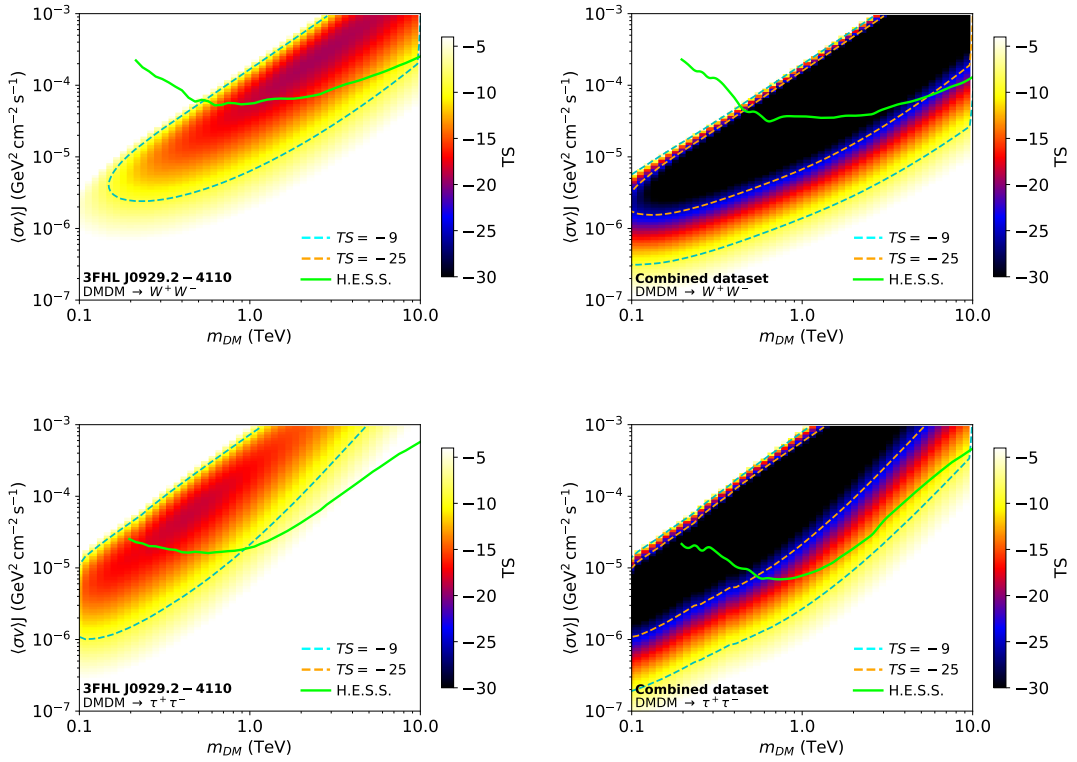

Figure 9.7: Contours of TS computed from *Fermi*-LAT datasets on the 3FHL J0929.2-4110 (left panels) and the combined UFO datasets (right panels), respectively. The contours are given in the ($\langle\sigma v\rangle J$,$\mathrm{m_{DM}}$) plane for the W^+W^- (top panels) and $\tau^+\tau^-$ (bottom panels) annihilation channel. The cyan and orange dashed lines show the -9 and -25 TS contours. Overlaid (solid green line) are H.E.S.S. upper limits displayed at 95% C.L.

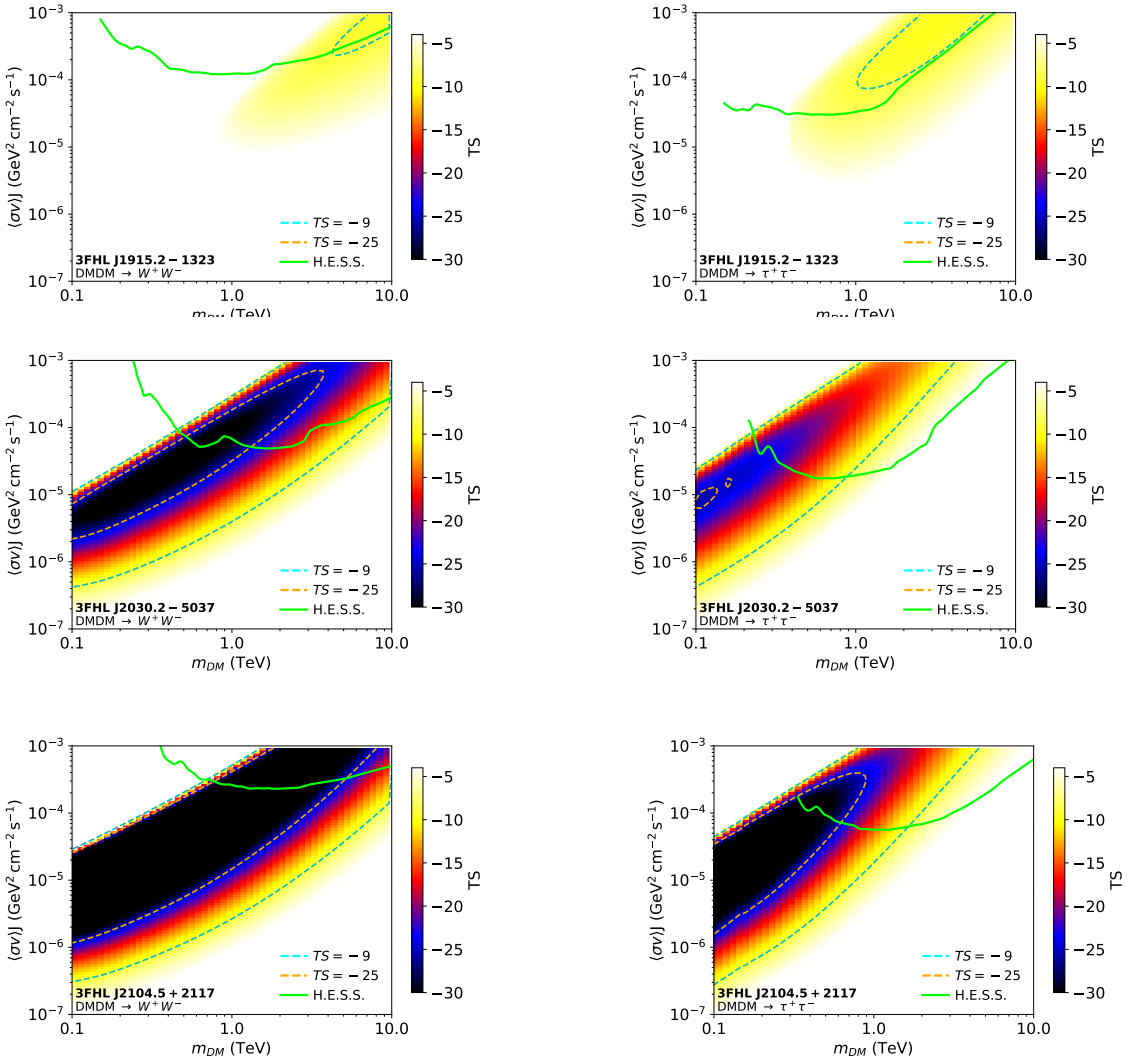

Figure 9.8: Contours of TS computed from *Fermi*-LAT datasets on the 3FHL J1915.2-1323 (top panels), 3FHL J2030.2-5037 (middle panels) and 3FHL J2104.5+2117 (bottom panels) datasets, respectively. The contours are shown in the ($\langle\sigma v\rangle J$,$\mathrm{m_{DM}}$) plane, for the W^+W^- and (left panels) and $\tau^+\tau^-$ (right panels) annihilation channel. The cyan and orange dashed lines show the -9 and -25 TS contours. Overlaid (solid green line) are H.E.S.S. upper limits displayed at 95% C.L.

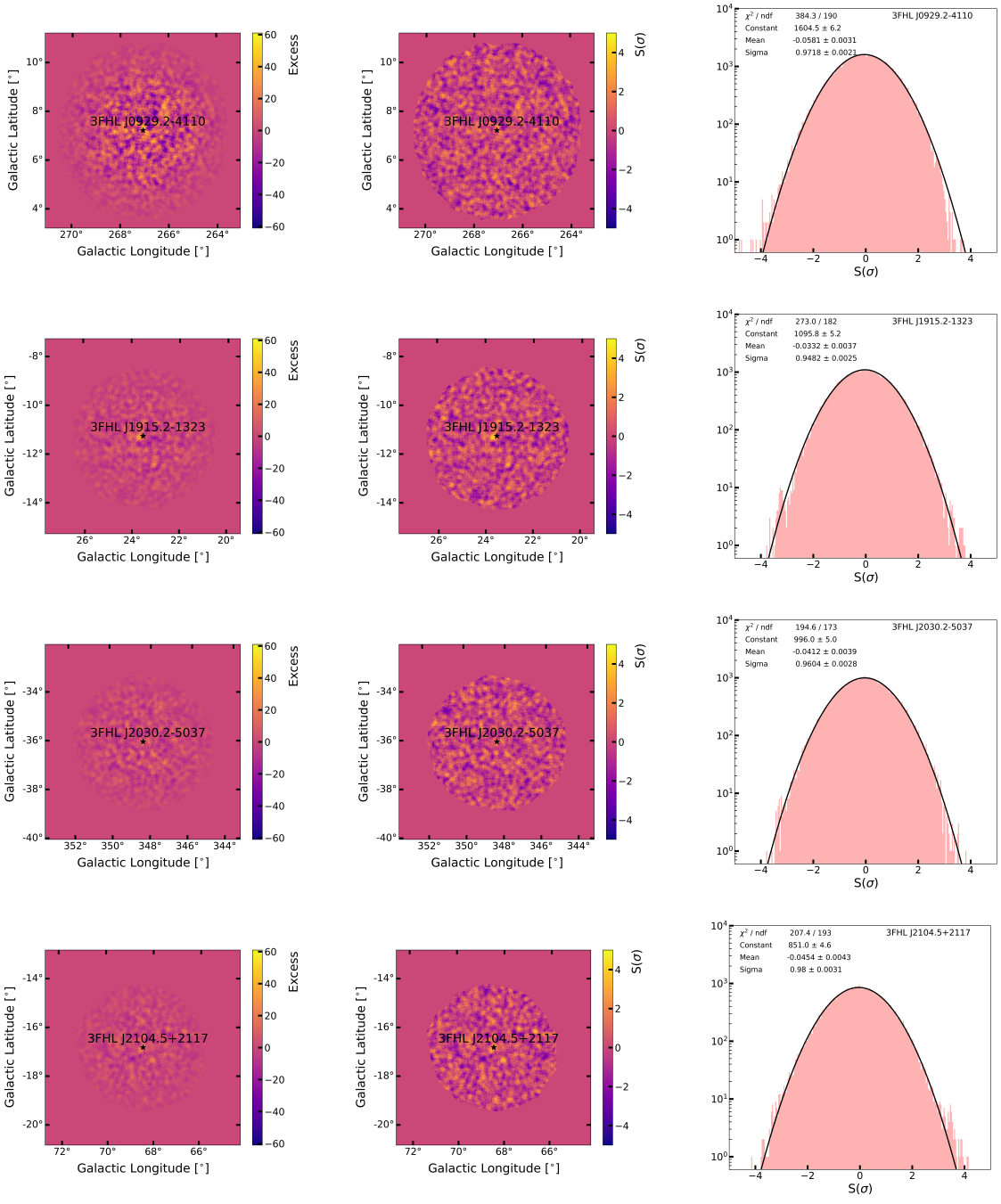

Figure 9.9: Gamma-ray excess maps (left panels), significance maps (middle panels) and significance distributions (right panels) for the four UFO datasets, obtained for point-like sources and with the *Ring Background* technique. The maps and the distributions are shown for the 3FHL J0929.2-4110, 3FHL J1915.2-1323, 3FHL J2030.2-5037 and 3FHL J2104.5+2117 datasets, respectively. No significant excess is observed anywhere in the FoV.

9.4.2 Measurement of background

For the measurement of residual background, OFF regions are defined following the *Wobble Multiple Off* technique [33], already described in Sec. 2.6. The same distance of ON and OFF regions is taken from each of the telescope pointing positions. This leads to identical acceptance values in the ON and OFF regions. To avoid any leakage from the signal region into the one where the background is searched, a disk of radius equal to twice the ON-region radius is excluded. The ratio between the solid angle size of the OFF and ON regions defines the α parameter as $\alpha = \Delta\Omega_{\mathrm{OFF}}/\Delta\Omega_{\mathrm{ON}}$. An example of the construction of the OFF regions with the *Wobble Multiple Off* technique is given in Fig. 9.10. The Figure shows the definition of the ON and OFF regions for the four UFOs. The ON region is at the centre of the FoV and is highlighted with the red circle. The OFF regions are taken at the same distance that the ON region is taken from the pointing positions, which are given by the black crosses. From the figure, it is possible to notice the excluded ring around the ON region. The colour scale shows the counts for the pixels of the corresponding panel.

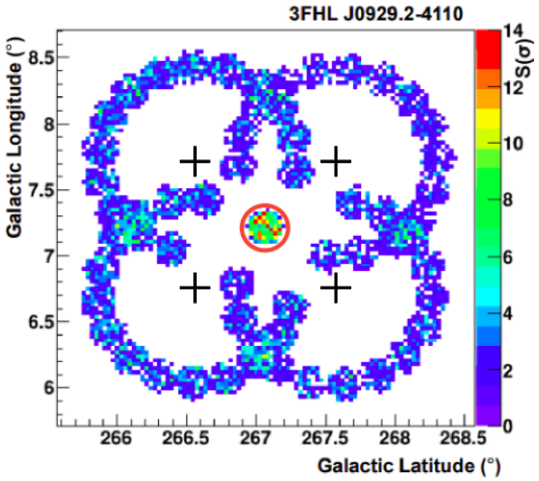

Figure 9.10: Application of the *Wobble Multiple Off* method on the FoV around the UFO 3FHL J0929.2-4110 to measure the photon count in the ON and OFF regions. The FoV is shown in Galactic coordinates. The ON region is highlighted at the center of the FoV, at the nominal position of the UFO. The OFF regions are taken at the same distance as between the ON region and the four pointing positions, which are marked by the black crosses. The colour scale shows the value of counts for each pixel in the ON and OFF regions.

9.4.3 Observed datasets and event energy distributions

With the technique described in the previous section, the statistics of the four UFO datasets is collected. The live time, the mean zenith angle of the observations, the ON and OFF counts, the α parameter averaged over all the observations and the excess significance in the ROI, derived with the H.E.S.S. observations of the UFOs, are summarized in Tab. 9.3. Then, event energy distributions are built. The distributions for the ON and OFF regions, for the four UFO datasets, are shown in Fig.9.11. The different live time between the datasets reflects the much more available statistics for the UFO 3FHL J0929.2-4110. For each of the four datasets, a safe energy threshold is defined by taking the value of the energy at which the acceptance of the H.E.S.S. instrument reaches the 20% of its maximum value. The acceptances for the four datasets are shown, in energy bins, in Fig. 9.12. The acceptances are built considering the value of $A_{\mathrm{eff},k}(E_\gamma)$ for each run k in the corresponging dataset. The final distributions are computed as a time average acceptance, using the observed time $T_{\mathrm{obs},k}$ of each run k. The spatial response of the instrument is taken into account for each run k because the acceptance term depends on the angular distance between the reconstructed event position and the pointing position of the run k. In the ON and OFF distributions, fluctuations in some energy bins are clearly visible. However, for the energy bins considered above the energy threshold, by following the statistical approach of Ref. [247], no significant gamma-ray excess is found neither in the ON source region nor anywhere else in the field of view. The photon count and the energy binning from the event energy distributions are used later for the computation of upper limits on the free parameters of the searched emission model.

Name	Live time [hours]	Mean zenith angle [degrees]	N_{ON} [counts]	N_{OFF} [counts]	$\bar{\alpha}$	Significance $[\sigma]$
3FHL J0929.2-4110	27.4	29.0	424	5884	13.9	0.1
3FHL J1915.2-1323	3.6	19.4	87	1181	13.9	0.2
3FHL J2030.2-5037	9.8	31.3	160	2192	13.9	0.1
3FHL J2104.5+2117	6.8	46.7	73	853	13.9	1.1

Table 9.3: H.E.S.S. data analysis results for each UFO. The second and third columns give the live time and mean zenith angle of the H.E.S.S. observations, respectively. Count numbers measured in the ON and OFF regions are given in the fourth and fifth columns, respectively, with the α parameter averaged over all observations, $\bar{\alpha}$, given in the sixth column. The seventh column provides the measured excess significance between the ON and OFF counts.

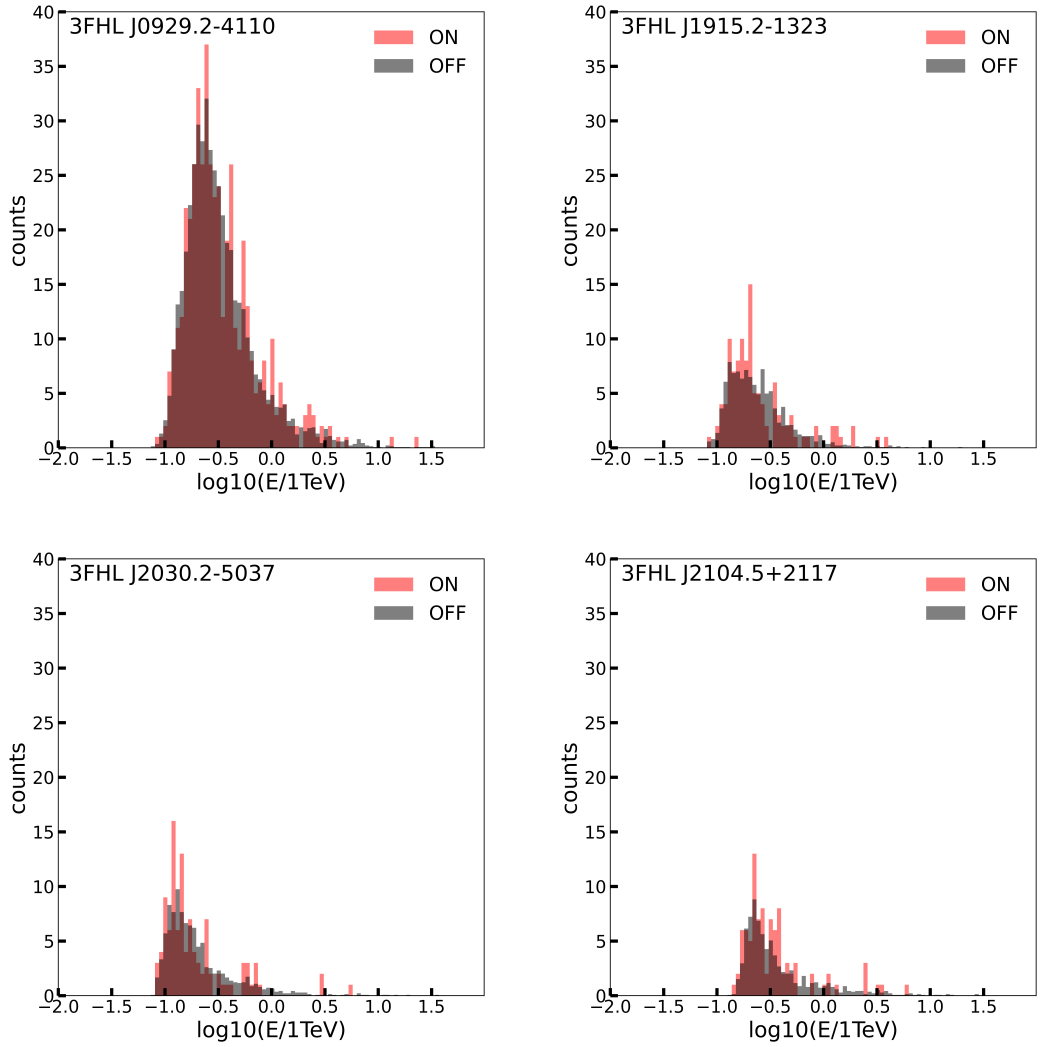

Figure 9.11: Event energy distributions for the UFOs 3FHL J0929.2-4110 (top left panel), 3FHL J1915.2-1323 (top right panel), 3FHL J2030.2-5037 (top left panel) and 3FHL J2104.5+2117 (top right panel), built with the *Wobble Multiple Off* method, are shown. The red and the black distributions are for the ON and OFF regions, respectively. Empty bins are present at high energies, this is due to lack of statistics because of the limited available time for the observations.

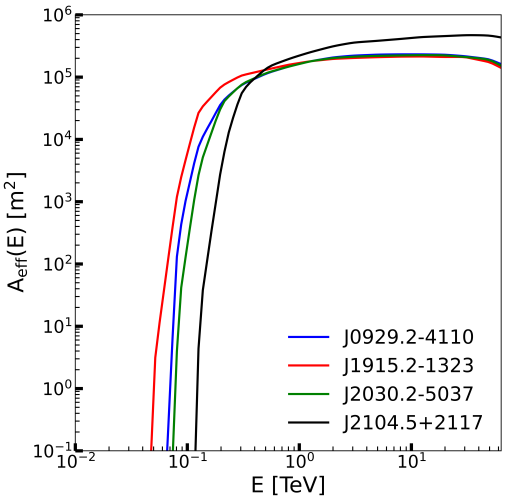

Figure 9.12: acceptances, as function of the energy, for 3FHL J0929.2-4110 (blue line), 3FHL J1915.2-1323 (red line), 3FHL J2030.2-5037 (green line) and 3FHL J2104.5+2117 (black line) are shown, respectively. The acceptances are built with the *Combined Stereo* method.

9.5 Upper limits on the dark matter emission parameters

9.5.1 $\langle\sigma v\rangle \times J$ as free parameters

The gamma-ray expected flux from annihilating DM particles including J-factor definition has been already expressed by Eq. 3.12. The distribution of DM in the observed object is described by the factor $J(\Delta\Omega)$, the J-factor. This is obtained with the integration of the square of the DM density over the line-of-sight (los) s and solid angle $\Delta\Omega$. For objects like dwarf galaxies, it is possible to measure the stellar dynamics and the distance from Earth, therefore an estimate of the J-factor can be obtained. For the UFOs, neither stellar dynamics nor distance from Earth can be measured from stellar kinematics. Consequently, the J-factor cannot be derived from this procedure. Thus, the product of $\langle\sigma v\rangle$ by the J-factor is considered as the free parameter of the emission model when upper limits are computed.

9.5.2 Upper limits computation

The spectral features from the DM annihilation signals with respect to the background only emission are searched with a binned Poisson maximum likelihood

analysis. The energy range of each UFO dataset is divided into 62 logarithmically-spaced bins from 100 GeV up to 70 TeV. The Poisson likelihood function is computed in each energy bin i, for fixed DM mass and annihilation channel, as was previously shown in equation 4.8. In the likelihood function, the term $N_{\mathrm{S}'i}$ is fixed to $N_{\mathrm{S}'i} \equiv 0$. This can be explained assuming that the UFOs are point-like sources for H.E.S.S., therefore no leakage of DM signal is expected in the background region. Since no significant excess is found in any of the selected UFOs by H.E.S.S., upper limits can be derived under the assumption that UFOs emit in gamma-ray from DM self-annihilation.

The computation of upper limits is performed through a log-likelihood ratio test statistic (LLRTS) given by Eq. 4.8. The LLRTS profiles for the four UFO datasets are shown in Fig. 9.13, for the $\tau^+\tau^-$ annihilation channel and one DM particle mass m_{DM}. Following the procedure defined in Ref. [147], upper limits are computed assuming a positive signal, *i.e.*, the term $\widehat{N_{\mathrm{S}i}}$ entering the TS is taken as $\widehat{N_{\mathrm{S}i}} > 0$. The value $\langle\sigma v\rangle J$, for which the TS value is equal to 2.71, is taken as the one-sided 95% confidence level (C.L.) upper limit on the quantity $\langle\sigma v\rangle J$. Upper limits that are obtained with the H.E.S.S. analysis are shown in Fig. 9.14. The results for the four UFOs are shown, in the W^+W^- and $\tau^+\tau^-$ annihilation channels. For most of the DM masses considered in this work, the most constraining limits are derived from the 3FHL J0929.2-4110 dataset. Constraints for a 1 TeV DM mass of $\langle\sigma v\rangle J$ = 5.5$\times$10^{-5} GeV^{2}cm^{-2}s^{-1} and 1.9$\times$10^{-5} GeV^{2}cm^{-2}s^{-1} in W^+W^- and $\tau^+\tau^-$ annihilation channels, respectively, are derived for 3FHL J0929.2-4110.

As was previously shown in Fig. 9.7, the H.E.S.S. upper limits are superimposed to the TS contours derived for the *Fermi*-LAT analysis. As explained in Sec. 9.3.3, the region inside the contours where $TS = -25$ correspond to the 5σ detection for the *Fermi*-LAT observations. These contours show the DM models that are viable according to the *Fermi*-LAT measurements. The H.E.S.S. upper limits, shown as the green curve, further constrain the available shaded regions. For the UFO 3FHL J0929.2-4110, the H.E.S.S. upper limits (showed in Fig. 9.7 on the left panel) restrict the allowed values of $\langle\sigma v\rangle J$ for the description of the DM emission in term of annihilating DM particles to be between $\langle\sigma v\rangle J$ = 5.4$\times$10^{-6} GeV^{2}cm^{-2}s^{-1} and 5.5$\times$10^{-5} GeV^{2}cm^{-2}s^{-1}, for the annihilation channel W^+W^- and a 1 TeV DM mass.

9.5.3 Combination of the datasets

The procedure needed for the computation of limits from combined datasets was already briefly introduced in Sec. 4.2.5. Here we provide more detailed and quantitative examples. With the combination of the individual datasets, the hypothesis that all the UFOs are DM subhalos, with an indeed too faint emission to be detected in the TeV energy range with the available exposure, could be tested. The combined analysis of the four H.E.S.S. UFO datasets did not show any significant overall excess. Therefore, combined upper limits on $\langle\sigma v\rangle J$ could be de-

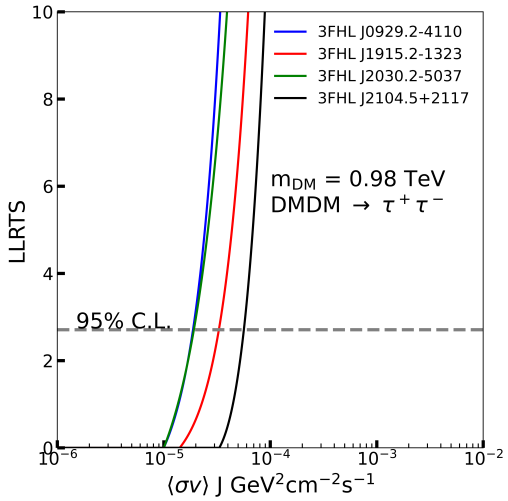

Figure 9.13: LLRTS profiles for 3FHL J0929.2-4110 (blue line), 3FHL J1915.2-1323 (red line), 3FHL J2030.2-5037 (green line) and 3FHL J2104.5+2117 (black line) are shown for the $\tau^+\tau^-$ annihilation channel and a DM particle mass of $m_{\rm DM} = 0.98$ TeV, respectively. 95% C.L. upper limits on the product of the annihilation cross section $\langle\sigma v\rangle$ and the J-factor J as a function of the DM mass $m_{\rm DM}$ are derived by taking the value of $\langle\sigma v\rangle J$ corresponding to LLRTS = 2.71.

rived versus the DM mass assuming J to be an average of the J-factor values of the individual datasets. The combined likelihood used in the TS is defined as $\mathcal{L}_{\rm comb} = \prod_{j=1}^{\rm N_{targets}} \mathcal{L}_j$, where $\mathcal{L}_j$ is the likelihood of the target j. Given the possible association with an AGN, the source 3FHL J2104.5+2117 is removed from the combination to provide conservative combined upper limits. The combined 95% C.L. upper limits on $\langle\sigma v\rangle J$ as a function of the DM mass for the W^+W^- and $\tau^+\tau^-$ annihilation channels, respectively, were already shown in the right panel of Fig. 9.7. The upper limits obtained from the combined analysis are about 10% and 20% more constraining for 1 TeV DM mass in the W^+W^- and $\tau^+\tau^-$ annihilation channel, respectively, with respect to the most constraining upper limits from the individual UFO datasets. For the W^+W^- channel and 1 TeV DM mass, the combined limits excluded values above 3.7×10^{-5} GeV^{2}cm^{-2}s^{-1}. For the $\tau^+\tau^-$ channel at the same mass, values above 8.1×10^{-6} GeV^{2}cm^{-2}s^{-1} are excluded.

9.5.4 Combination methods

We test two approaches for the combination of the UFO datasets. One of the approach consists in the sum of the statistics obtained from the observations. Therefore, the total number of measured events in the ON and OFF regions, for energy bin i, are built as $N_{{\rm ON},i,{\rm tot}} = \sum_{j=1}^{\rm N_{targets}} N_{{\rm ON},i,j}$ and $N_{{\rm OFF},i,{\rm tot}} = \sum_{j=1}^{\rm N_{targets}} N_{{\rm OFF},i,j}$,

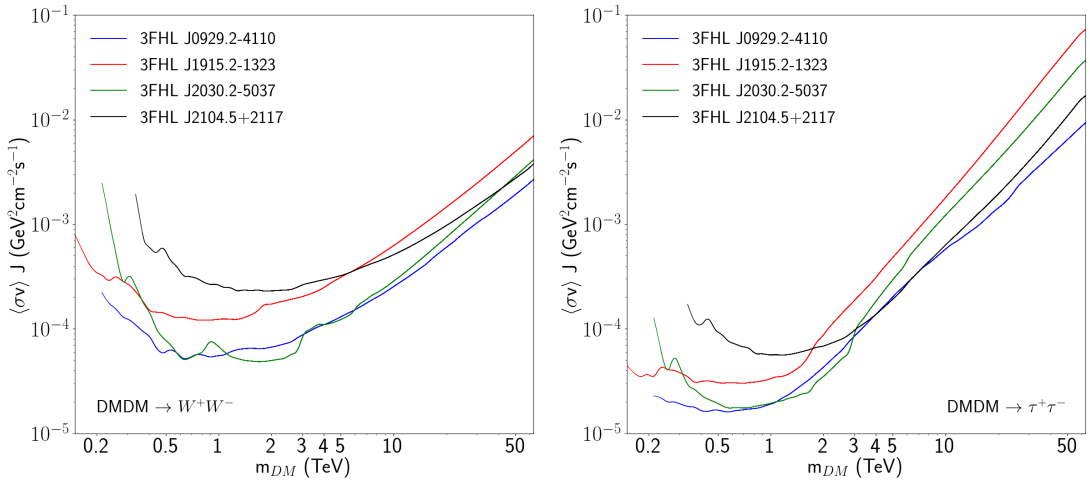

Figure 9.14: 95% C.L. upper limits on the product of the annihilation cross section $\langle\sigma v\rangle$ and the J-factor J as a function of the DM mass $m_{\rm DM}$ in the W^+W^- (left panel) and $\tau^+\tau^-$ (right panel) annihilation channels for 3FHL J0929.2-4110 (blue line), 3FHL J1915.2-1323 (red line), 3FHL J2030.2-5037 (green line), and 3FHL J2104.5+2117 (black line), respectively.

where the index j represents the UFO dataset j. The same procedure is performed for the expected number of background events $N_{{\rm B}i,{\rm tot}} = \sum_{j=1}^{\rm N_{targets}} N_{{\rm B}i,j}$. $\langle\sigma v\rangle J$ is considered as identical for each UFO since the same DM models are tested for each of the dataset. However, the J-factor could be different from one UFO to another. If the UFO J-factors are considered different, no combined limits on $\langle\sigma v\rangle J$ could be obtained. Therefore, an average value of the J-factor is considered for the computation of combined upper limits. The total number of gamma-rays expected from DM annihilation, expressed by Eq. 3.12, is obtained by summing the observed time of the individual datasets. It is then considered as $N_{{\rm S}i,{\rm tot}}$. With this setup, the total likelihood is built as the product on the 62 energy bins $\mathcal{L}_{\rm comb} = \prod_{i=1}^{62} \mathcal{L}_{i,{\rm tot}}$. However, the combination at the counts level produces some loss of information. This is due to the fact that low sensitivity is obtained when, for instance, $N_{{\rm B}i,{\rm tot}}$ and $N_{{\rm S}i,{\rm tot}}$ are computed by summing a large value for one dataset with two small values for the other two. By doing this, the possible fluctuations due to the different statistics in the datasets are smoothed out and worse sensitivity is obtained. By keeping these three datasets separated, we would not smooth the fluctuations and obtain a better level of sensitivity. Following these arguments, the combination of the three datasets is performed at the likelihood level and used for the computation of the combined upper limits. For the combination, the equation previously mentioned $\mathcal{L}_{\rm comb} = \prod_{j=1}^{\rm N_{targets}} \mathcal{L}_j$ is used. These two definition of the combined likelihood are tested to perform the LLRTS

procedure for the setting of upper limits on $\langle\sigma v\rangle J$. The LLRTS profiles obtained with the two different ways of defining the total likelihood functions $\mathcal{L}_{\rm comb}$ for a DM mass of $m_{\rm DM}$ = 0.98 TeV, are shown in Fig. 9.15. The poorer sensitivity of the analysis is clear for the combined LLRTS obtained with the sum of the measured and expected events. The LLRTS obtained with the product of the likelihood functions from the individual datasets is $\sim$ 27% more constraining at 95% C.L. on the tested free parameter $\langle\sigma v\rangle J$.

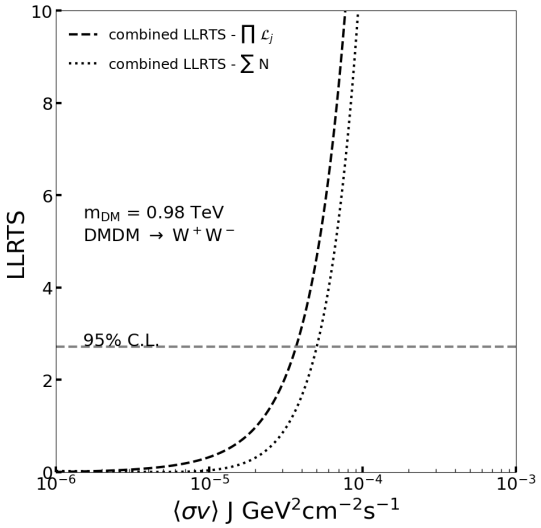

Figure 9.15: LLRTS profiles obtained from the combined UFO datasets. The source 3FHL J2104.5+2117 is removed from the combination to provide conservative combined upper limits, since its possible associations with an AGN. The profiles are shown for a DM particle mass of $m_{\rm DM}$ = 0.98 TeV and for the annihilation channel W^+W^-. The two different combination methods are shown. The dashed line shows the combination obtained with $\mathcal{L}_{\rm comb} = \prod_{j=1}^{\rm N_{targets}} \mathcal{L}_j$. The dotted line shows the combination obtained with the sum of the measured and expected events.

9.5.5 Limits on J-factor values for thermal dark matter

The J-factor values required to explain the emission measured from the UFO sources in terms of DM models could be derived if assuming the value of annihilation cross section expected for thermal WIMPs ($\langle\sigma v\rangle_{\rm th} \simeq 3\times10^{-26}$ cm^{3}s^{-1}) [347]). The upper limits on the J-factor, at 95% C.L., for the combined dataset are shown in Fig.9.16. From the figure, the constraints on the J-factor values by considering both the TS contours from the *Fermi*-LAT analysis and the green curve limits from the H.E.S.S. analysis could be derived. Considering a DM particle with mass

of 1 TeV, the J-factor values for the W^+W^- channel are constrained to be between 2.4×10^{20} and 1.3×10^{21} GeV^{2}cm^{-5}, when the DM models are considered with $TS \leq -25$ (correspondent to ≥ 5 σ confidence interval assuming TS follows χ^2 distribution). When instead a DM mass of 10 TeV is considerd, no J-factor value for DM models in the TS ≤ -25 shaded area are left available due to the H.E.S.S. constraints. For the $\tau^+\tau^-$, the H.E.S.S. limits are even more constraining. For a DM particle with mass of 300 GeV, the allowed range for the J-factor values is constrained between 1.4×10^{20} and 5.9×10^{20} GeV^{2}cm^{-5} for TS ≤ -25 DM models. More in general, the H.E.S.S. constraints limited the range of the allowed J-factor values for the W^+W^-channel to $6.1 \times 10^{19} - 2.0 \times 10^{21}$ GeV^{2}cm^{-5}, and the masses to lie in the 0.2 - 6 TeV range. In the $\tau^+\tau^-$ channel, the J-factor values are limited to the range $7.0 \times 10^{19} - 7.1 \times 10^{20}$ GeV^{2}cm^{-5}, for DM masses between 0.2 and 0.5 TeV.

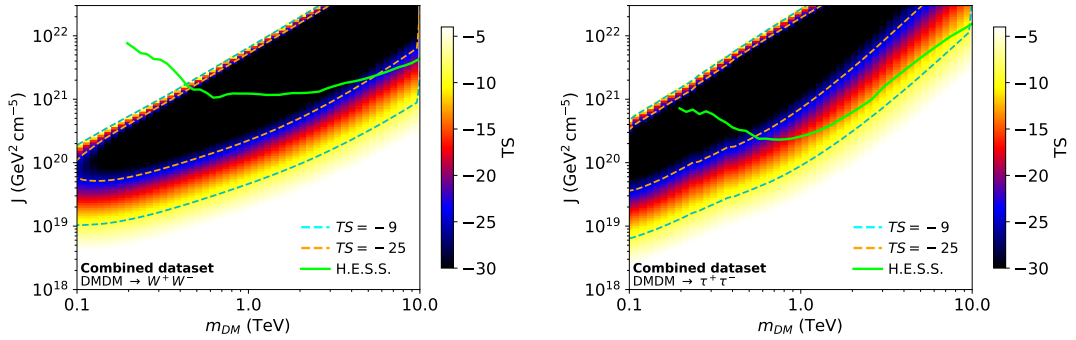

Figure 9.16: Contours of TS computed from the *Fermi*-LAT analysis of the combined UFO datasets. Under the assumption of values of $\langle\sigma v\rangle$ expected for thermal WIMPs, the contours are given in the (J,m$_{\rm DM}$) plane for the W^+W^- (left panel) and $\tau^+\tau^-$ (right panel). TS contours corresponding to TS = -9 and -25 are given by the cyan and orange dashed lines. The H.E.S.S. 95% C.L. upper limits from the combined UFO datasets are overlaid as the solid green line.

9.6 Constraints from cosmological simulations

The number of subhalos with DM distribution described by a J-factor value higher than a given value for a MW-like galaxy could be extracted from the distribution in Fig.9.3. Following the predictions from N-body cosmological simulations, the probability to have at least three subhalos with a J-factor higher than 10^{20} GeV^{2}cm^{-5}, given by the blue-dotted line in Fig. 9.3, is below 5%. The interpretation of the UFO emissions as gamma-ray from DM particle annihilation in Galactic DM subhalos could be further constrained from Fig. 9.16 to $m_{\rm DM} \lesssim 1$ TeV for

W^+W^- and $m_{\rm DM} \lesssim 0.3$ TeV for $\tau^+\tau^-$ channels. Therefore, the required high J-factor values for the DM models necessary to explain the UFO emission as from Galactic DM subhalos are unlikely. Nevertheless, there are large systematic uncertainties in the prediction of the J-factor distribution shown in Fig.9.3. These uncertainties weaken significantly the constraints from cosmological simulations, making them comparable to or weaker than the H.E.S.S. constraints in, *e.g.*, the $\tau^+\tau^-$ channel. Therefore, the only relevant constraints for robust interpretation of the UFO sources as Galactic subhalos of annihilating DM are the H.E.S.S. ones. More discussion about the uncertainties affecting the derivation of the J-factor distribution is provided in the next section.

9.6.1 Uncertainty on the simulations

The parameters for the definition of the J-factor distribution shown in Fig.9.3 were taken from the "HIGH" model in Ref. [217]. The distribution agrees very well with the results shown in Ref. [217] computed with the "HIGH" model. This model aimed at predicting the highest possible number of subhalos in a typical MW-like galaxy. When considering the predictions for the "LOW" model of [217], the real number of DM subhalos can be an order of magnitude smaller. The number of subhalos of masses between 10^8 and 10^{10} $M_\odot$ was fixed to $N_{\rm calib}$ = 300. This value can be motivated by the output of the DM-only simulations in [343]. This values can be significantly reduced by baryon feedback, up to a factor of two [281, 332]. Including baryon feedback would therefore make the highest J-factor values more unlikely. The interpretation of UFOs as DM subhalos of TeV-mass scale thermal WIMPs requires J-factor values larger than a few 10^{20} GeV^{2}cm^{-5}. This range of values is only occasionally obtained in N-body simulations of MW-type galaxies. Moreover, a large statistical variance usually affects the highest subhalo J-factor. In the "HIGH" model, a factor-of-ten uncertainty on the J-factor value for J $\gtrsim 10^{20}$ GeV^{2}cm^{-5} is expected [216][6]. The maximum value of J-factor that can be obtained in simulations depends on the adopted model. It can be increased even in comparison to the optimistic estimate of the J-factor distribution considered here as discussed below. About 10% of the total DM halo content is assumed to be in form of subhalos for the usual normalization of the subhalo mass function. For the normalization of the total DM halo density, the DM density at the location of the Sun $\rho(r_\odot) = \rho_\odot$ = 0.39 GeVcm^{-3} is usually utilized. However, uncertainties of about a factor 1.5 to 2 [322] affect this precise value. The input parameters of the simulations in the relevant ranges of interest, such as $\rho_\odot$ = 0.6 GeVcm^{-3} and the scale radius of the main DM halo $r_{\rm s}$ = 25 kpc, can be varied to increase the highest J-factor values by a factor of two. Therefore, higher J-factor values would be

[6] For predictions with the "LOW" model, since the probability to get high J-factor values would be lowered with respect to what is obtained with the "HIGH" model, the interpretation of UFOs as DM subhalos would be even more unlikely.

probed by the predicted cumulative J-factor distribution. Also, the cumulative J-factor distribution can be shifted to higher values when considering substructures in galactic subhalos (see, for instance, [203]). This would result in higher expected J-factor values for the Galactic subhalo population with typical increase factors of a few. The highest J-factor values are realized for the brightest subhalos. The latter should appear as extended sources for *Fermi*-LAT, considering its point spread function of about 0.1° above 10 GeV. This is discussed in Ref. [146]. Nevertheless, these brightest DM subhalos would still be faint gamma-ray sources with a spatial extension challenging to measure for *Fermi*-LAT. Point-like UFOs cannot be ruled out yet as potential DM subhalos and further work is needed to do so on the simulation front for predictions for subhalo angular sizes in MW-like galaxies.

Uncertainties due to parameterization of the dark matter distribution

In this work, the DM density distribution for the Milky Way halo has been chosen as following the NFW parametrization. The inner cusp of the DM profiles in Milky Way-like galaxies is softened by incorporating hydrodynamics and baryon feedback in cosmological simulations, producing a flattening of order 1 kpc [118]. However, the expected DM distribution is predicted with large uncertainties due to the effects of baryonic physics. The resolution limit of the simulations at sufficiently small distances is another important factor. Alternative Galactic mass models can be used to describe subhalo parameters for Milky Way-like galaxies [113, 269, 349, 270]. For example, the subhalo luminosity functions derived in [349] provide compatible results for different Galactic mass models. Adopting a core profile for the DM distribution would make the high DM mass exclusion of the DM models for the UFO emission even stronger. Cored profiles could be used to describe the DM distribution for DM subhalos. This would lead to lower DM concentration, which would make the subhalos more subject to tidal disruption. Therefore, the J-factor distribution would have a lower normalization and it would be shifted to lower values. The distribution of J-factor values is obtained from DM-only Via Lactea-II simulations, with WMAP cosmology. Simulations with most recent cosmological results from the Planck mission, which includes baryonic physics, could produce some changes in the predicted properties of the MW subhalos. The DM concentration of subhalos can be altered by baryon feedback and tidal effects, deriving by the presence of both DM and baryons [156, 349]. Ref. [159] provides details on how the tidal disruption of Galactic DM subhalos on the brightest subhalo is modeled. Including effects due to baryonic physics would therefore shift the J-factor distribtion to lower values. This would make the probability to find high J-factor values even smaller and constrain even more the DM-induced interpretation of the UFO emission. In addition, baryons affect the mass functions of DM halo and subhalos. The slope can be reduced by a few percent in the 10^6 - 10^9 $M_\odot$ mass range of subhalos [74]. The large J-factor subhalos rate can be altered by the changes of the slope. No cut is considered for the maximal

value of the subhalo mass during the computation of the cumulative J-factor distribution. Simulations, with the inclusion of hydrodynamics and feedback physics in addition to the gravitational effects for the expected DM distribution in both the main halo and its subhalos such as in [372], show that a significant fraction of subhalos with masses of about 10^9 $M_\odot$ is found to host no stars. However, when the subhalo mass is larger than about 10^7 $M_\odot$, the subhalos may be able to trigger star formation and actually be faint dwarf galaxies. Naturally, the values for these masses critically depend on how the baryonic physics is implemented in the simulations and how its feedback is associated. If the subhalo mass is cut over 10^7 $M_\odot$, a probability of about 0.3% is reached for the case of at least one subhalo with $J \geq 3\times10^{20}$ GeV^{2}cm^{-5}. This is a factor of about 16 lower that in the case without mass cut.

9.7 Conclusions and outlook

In this work, the unidentified sources in the 3FHL point-source catalog has been filtered using selection cuts to identify the most promising DM subhalo candidates for DM masses above a few hundreds of GeV. UFOs sources may be subhalos emitting gamma-rays from DM annihilation. Some alternative interpretations about the nature of UFOs consider them as active galactic nuclei or other type of galaxies of unknown emission at other wavelengths. Interpreting the gamma-ray emission as from pulsars or low-luminosity globular clusters hosting millisecond pulsars [276] may not describe well the UFO spectra, since the former show energy cut-offs at energies of a few GeV. The main outcomes of the chapter are:

- the four UFO datasets were collected with observations with the Fermi satellite in a 12-year observation period. Previous studies with *Fermi*-LAT datasets tested unidentified sources as DM subhalo candidates only for DM masses below 100 GeV [84, 85, 145];

- the presented analysis explores the uncharted TeV-mass thermal WIMP models for the interpretation of UFOs as DM subhalos. H.E.S.S. observed the four selected UFOs between 2018 and 2019;

- no significant signal is found in the H.E.S.S. UFO datasets and the DM models, describing the UFO emissions with high significance in the *Fermi*-LAT analysis, are strongly constrained by the H.E.S.S. flux upper limits in the TeV DM mass range for different annihilation channels;

- from model-dependent predictions from N-body simulations of the MW-like subhalo population, the DM models applied for the explanation of UFOs as Galactic subhalos require high J-factor values, which are unlikely;

- UFOs could be interpreted as subhalos of relatively light WIMPs with masses $m_{\rm DM} \lesssim 0.3$ TeV.

Previous studies shown in Ref. [146] rule out masses of few tens of GeV for canonical thermal WIMPs for the interpretation of UFOs as subhalos. For UFOs made of light WIMPs, lower J-factor values are required. However, constraints on thermal WIMPs from dwarf galaxy observations by *Fermi*-LAT [23, 44] could be in tension with these hypotheses. The prediction of the J-factor distribution are affected by the mentioned large systematic uncertainties. These make the constraints from cosmological simulations weak. Thus, the former can be considered as comparable to or weaker to the H.E.S.S. constraints in, *e.g.*, the $\tau^+\tau^-$ channel. Therefore, the model-independent H.E.S.S. constraints are the only relevant ones for robust interpretation of UFOs as Galactic subhalos of annihilating dark matter.

New constraints on expected DM emission from candidate subhalos can be obtained from new observations. The best candidate within the 3FHL catalog have been already observed and analysed by H.E.S.S.. In this analysis, we showed the best constraints that can be obtained in the TeV mass range with H.E.S.S.. Observations with CTA of new candidates or the same ones could be useful to set more constraining limits given the better energy sensitivity and energy and angular resolution that the Cherenkov Telescope Array will reach. However, given the present limits and the fact that DM models at GeV energies have been already excluded by *Fermi*-LAT measurements, analysis of DM subhalo candidates for limits on the parameters for DM self-annihilation may not be the best strategy to aim at DM detection. Moreover, the brightest subhalos in the Fermi catalogs have been already analysed and even with some years of observations with CTA the eventually observed candidate subhalos would be faint. Considering the analysis of extended subhalos, a more detailed analysis of IACTs datasets would be needed for sources that are not point-like. This work has been published in *The Astrophysical Journal* [10].

Chapter 10

The sensitivity reach of H.E.S.S. like observations to TeV Dark Matter annihilation signals

Contents

Summary

In this chapter, the sensitivity reach of H.E.S.S. like observations to signals from self-annihilating TeV DM particles is explored using mock data from H.E.S.S. II-like observations of the GC region. The most advanced calculations available for the theoretical gamma-ray annihilation yields are applied in a wide range of DM masses in order to make an estimate of the theoretical uncertainty in the sensitivity expectation. We test specific and canonical heavy dark matter models such as the Wino, the Higgsino and the Quintuplet. For the description of the DM distribution we make use of updated Milky Way mass profiles from the latest measurements of the MW rotation curve. In Sec. 10.1 we show the comparison of two gamma-ray yields, and the models for DM distribution in the Milky Way used in this work. For the background modeling, we consider realistic assumptions on the conventional TeV astrophysical backgrounds in the Galactic Center region and assign motivated uncertainties from IGS observations and analysis. We compute the H.E.S.S. sensitivity to DM annihilating in the 0.5 - 100 TeV mass range for model-independent searches as well as in the framework of the Wino, Higgsino and Quintuplet models. For the derivation of the limits we make use of the log-likelihood-ratio test statistic analysis widely described in Sec. 4.2. Sec. 10.2 shows the definition of the region of interest for the DM search, the exclusion regions on the known VHE sources and the statistical methods used for the computation of the sensitivity limits. In Sec. 10.3, we show the obtained limits and, in Sec. 10.4, we describe the uncertainties considered for this work. We conclude with Sec. 10.5 together with some outlooks. At the time of the writing, more contributions to the conventional background emissions in the GC region are being explored. At the moment of the writing, the results shown in this chapter have been submitted as an article to *Physical Review D* [282].

10.1 Theoretical expectations for Dark Matter models

The computation of the energy-differential flux of gamma rays produced by the self-annihilation of Majorana WIMPs of mass $m_{\rm DM}$ is shown in Sec. 3.8. In this section, we briefly discuss the expected gamma-ray annihilation yields from the most advanced calculations available as well as updated Milky Way mass profiles from latest mass-modeling measurements of the MW rotation curve. We use these for the derivation of the sensitivity with mock datasets of H.E.S.S.-like observations.

10.1.1 `PPPC4DMID` and `HDMSpectra` gamma ray yields

In this work we make use of two gamma-ray yields for the production of the spectra of photons expected from DM particles self-annihilating. The code for the production of the yield from `PPPC4DMID` is extracted from Ref. [124]. The other yield, `HDMSpectra`, is extracted from the public software in Ref. [55]. Being outside the scope of this work, we refer the reader to the two references for a detailed description of the theoretical studies performed for the derivation of the yields. We show in Fig. 10.1 the comparison of the spectra of photons expected from self-annihilating DM particles in the W^+W^- channel for the two gamma-ray yields `PPPC4DMID` and `HDMSpectra`. The spectra are shown for DM particles with masses $m_{\rm DM}$ = 1, 10, 50 and 100 TeV. Also shown are the gamma-ray yield for self-annihilation into the three neutrinos channels, $\nu_\mu\overline{\nu}_\mu$, $\nu_e\overline{\nu}_e$ and $\nu_\tau\overline{\nu}_\tau$ for further comparison with limits obtained with ANTARES in Sec 10.3. Final state neutrinos produced from annihilation of DM particles may emit W and Z gauge bosons which in turn would produce continuous gamma-ray spectra [321]. Examples of spectra of DM particles self-annihilating in the three channels are shown from the `HDMSpectra` yield, and for DM masses $m_{\rm DM}$ = 20, 40, 60, 80 and 100 TeV, in Fig. 10.2.

10.1.2 Canonical TeV WIMP candidates: Wino, Higgsino and Quintuplet

WIMPs are intimately associated with supersymmetry, emerging as expected DM particles from SUSY models, but the absence of evidence for this framework from collider searches may undermine the motivation for WIMPs themselves. It is true that the full motivation for the search for WIMP signatures is not what it was several years ago, the scenario remains among the most compelling. The elegance of the thermal relic cosmology is one of the driving factors: DM detaches from the primordial plasma with the correct relic abundance for $\langle\sigma v\rangle\sim 10^{-26}$ cm^3/s [347]. This is the exact level at which the late time annihilations in the Galactic Center could be detectable. Therefore, for model-independent searches it is worthwhile

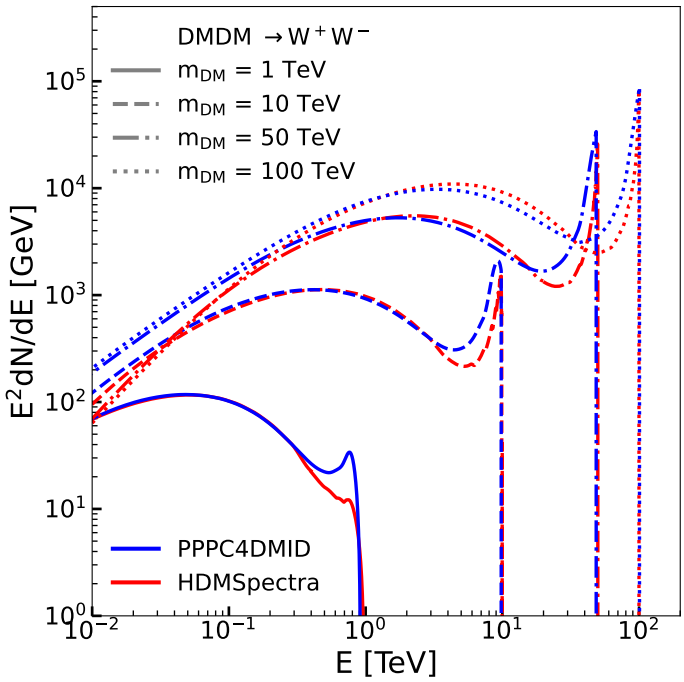

Figure 10.1: Spectra of photons expected for self-annihilating WIMPs in the W^+W^- annihilation channel for m_{DM} = 1 (solid lines), 10 (dashed lines), 50 (dashed-dotted lines) and 100 (dotted lines) TeV from the `PPPC4DMID` [124] (blue lines) and `HDMSpectra` [55] (red lines) gamma-ray yields.

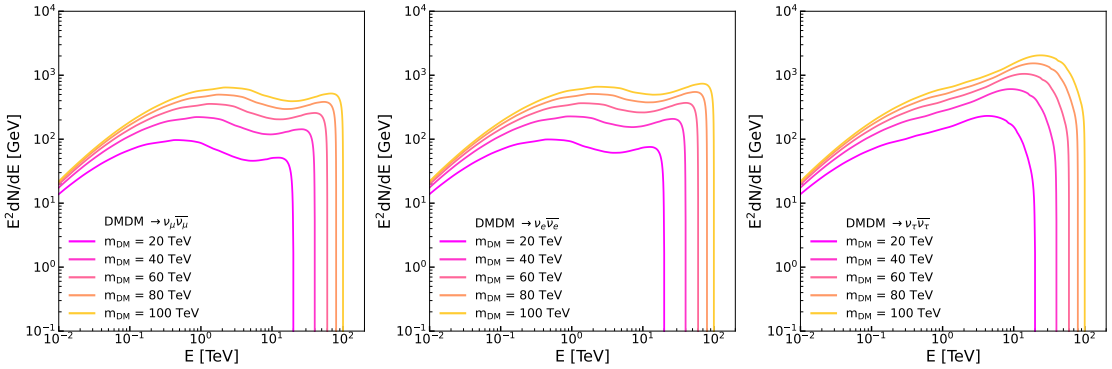

Figure 10.2: Spectra of photons expected for self-annihilating WIMPs in the $\nu_\mu\overline{\nu}_\mu$, $\nu_e\overline{\nu}_e$ and $\nu_\tau\overline{\nu}_\tau$ annihilation channels for m_{DM} = 20, 40, 60, 80 and 100 TeV from computations using the the HDMS [55] code.

to consider DM annihilation around this value of $\langle\sigma v\rangle$ for the wide range of final states.

Strong motivation is still present for having more specific realizations of the WIMP. The most simple minimal field content could be added to the Standard

Model to explain DM. This can be done with TeV scale states charged under the electroweak interaction, and including an SU(2) doublet with unit hypercharge, as well as a $\mathbf{3}$ and $\mathbf{5}$ representation of SU(2) [125, 129, 126, 128, 130, 261, 227]. These states are the Higgsino, Wino, and Quintuplet, and can explain the correct DM abundance through the thermal relic cosmology for masses of 1 ± 0.1 TeV, 2.9 ± 0.1 TeV, and 13.6 ± 0.8 TeV, respectively [129, 205, 214, 72, 277, 101]. A broad description of the detection prospects for these minimal DM candidates is provided in Refs. [101, 102]. Higgsino and Wino are also thermal DM candidates that realize supersymmetry consistently with LHC observations [47, 175, 190]. It is still unclear the real paths needed to discover DM in these scenarios (see e.g. Refs. [133, 134]), nevertheless CTA could see a signal from Higgsino [324] and this strongly motivates determining the existing IACT sensitivity.

For these reasons, we are evaluating IACT sensitivity to Higgsino, Wino, and Quintuplet in addition to model-independent derived results. As these are fully defined models, we will use a completely specified particle physics contribution to the gamma-ray yield. Indeed, by fixing the m to the already mentioned values for the thermal masses, no free parameters at all (up to the choice of the two mass splittings for the Higgsino, discussed below) is left for these models. It is still interesting to consider the full range of masses which can be covered with the IACT sensitivity in case the early Universe departed from the thermal relic cosmology. Each of these WIMPs could annihilate into a two-photon final state, which adds as a target the gamma-ray line at the DM mass. However, a full determination of the cross-section and gamma-ray yield for these models includes Sommerfeld enhancement, resummation of effects of order m/m_W, and additional channels beyond the direct annihilation to two-photons. The Wino model accounts for all these effects (for details see Refs. [58, 56, 296, 59, 297, 49, 62, 57, 70, 73]), and we make use of next-to-leading logarithmic (NLL) computation from Ref. [57]. The Quintuplet model has been recently extended with the inclusion of the same formalism and results will soon appear in the calculation of Ref. [61]. The spectra for both the Wino and Quintuplet are including line-like photons from the two-body decay, lower energy continuum photons (arising from final states such as W^+W^-), and also endpoint photons. The Higgsino model does not yet include the same computation (although see Refs. [60, 71, 69]), and therefore we apply here the approach in Ref. [324] of including the leading order (LO) computation of the line and continuum and the inclusion of Sommerfeld enhancement. Finally, for the Higgsino model we need to specify an additional parameter which is the splitting between the charged and neutral states in the spectrum, denoted δm_+ and δm_N, respectively. Two benchmarks used in Refs. [60, 324] are chosen for this purpose: for splitting one, we take $\delta m_+ = 350$ MeV and $\delta m_N = 200$ keV, saturating the limits set by direct detection, and for splitting two we invert these to $\delta m_+ =$ 480 MeV and $\delta m_N = 2$ GeV.

We show in Fig. 10.3 the theoretical spectra of photons associated with the

continuum and endpoint contributions for Winos at different m_{DM}. The spectra for lines at m_{DM} are shown too, as pure delta functions. Spectra of photons for the continuum contribution for several m_{DM} for Higgsinos in splits 1 and 2 are shown in the left and right panels of 10.4 together with the line contributions, respectively. Spectra of gamma-rays produced from self-annihilation of WIMPs in the Quintuplet model will be shown later.

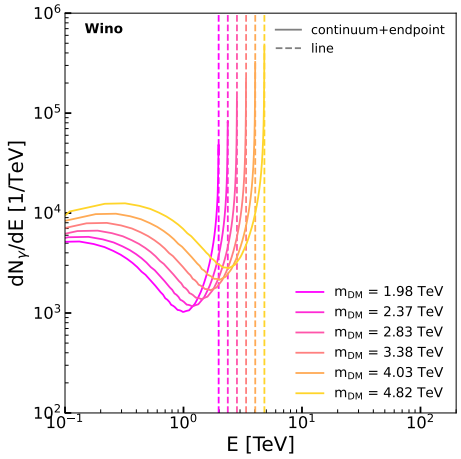

Figure 10.3: Theoretical gamma-ray yield expected for self-annihilating Winos [124]. The spectra show the continuum and endpoint contributions. The yield for lines, which are pure delta functions, are shown too (dashed lines).

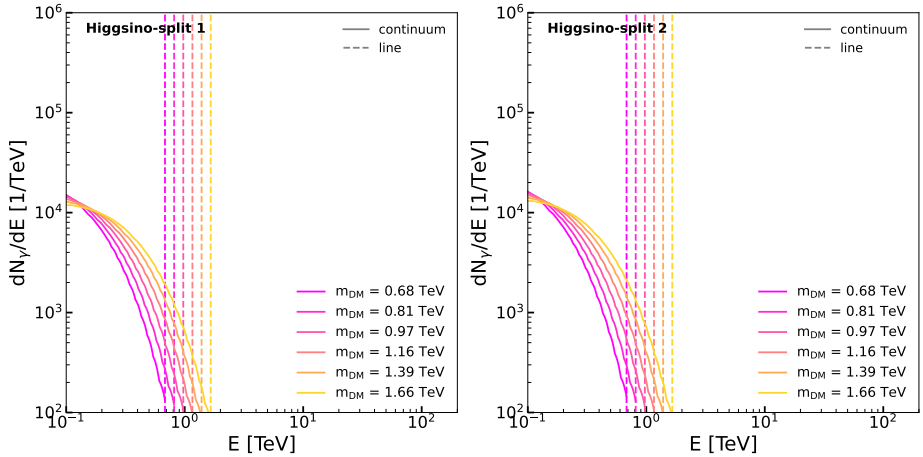

Figure 10.4: Theoretical gamma-ray yield expected for self-annihilating Higgsinos in split 1 and 2 in the left and right panels, respectively [124]. The spectra show the continuum contributions. The spectra for lines, which are pure delta functions, are shown too (dashed lines).

10.1.3 Models for the Dark Matter distribution in the Milky Way

To infer the DM distribution in the inner part of the Milky Way, two complementary approaches are commonly used. When using DM-only cosmological simulations (see, for instance, Refs. [341, 161, 344]), cuspy DM distributions are predicted. Common parameterizations for the cuspy profiles are the NFW [292] or Einasto [341] profiles. When baryonic physics and feedback processes are included in the simulations, the complexity is dramatically increased [333, 213, 315]. The DM distribution can dynamically evolve, due to the presence of complex baryonic processes in the core of Milky Way-like galaxies, in such a way that kpc-sized cores depending on the modeling of baryonic physics [281, 118] can be created. Approaches based on mass-modeling make use of gravitational measurements the mass profile of the Milky Way and the measurements of the baryonic mass components. However, large uncertainties affect the latter. Therefore, these uncertainties propagate to the DM distribution derivation [218, 313]. NFW profiles with wider than 2 kpc are disfavored in the Galactic bulge when using stellar measurements [210]. Thus, it is not easy to firmly determine the DM distribution in the inner halo of the Milky Way and there is no established consensus in the community on DM profile in the inner Galaxy. In this work, we use a recent computation of the profile of the MW mass, obtained from measurements from Gaia DR2 of the rotation curve and thorough modeling of the baryonic components in the GC region [114]. A profile of the MW, obtained by contraction due to baryons, provides a better fit to the data than the standard NFW profile [114]. Therefore, we adopt two profiles in this work, defined as NFW and contracted NFW (cNFW) parameterizations. This parameterization of the NFW profile is different from the one used in Chap. 8. The NFW profile is further modified with a core of radius $r_{\rm c}$ = 1 kpc since the adiabatically-contracted DM distribution is significantly uncertain in the inner 1 kpc of the GC due to baryonic physics and the complex interaction between feedback processes. The DM density profile is then behaving as $\rho^{\rm cNFW}(r) = \rho^{\rm cNFW}(r_{\rm c})$ for $r \leq r_{\rm c}$. In order to test the reach of sensitivity of H.E.S.S. to DM particles annihilating in neutrinos channels, we also consider an alternative parameterization of NFW as used in Ref. [43], labeled hereafter as to aNFW for simplicity, for comparison with limits derived from ANTARES data. We show the profile parameters used for the computation of the J-factors in Tab. 10.1. We extract the 1σ uncertainties for the profile parameters ($\rho_{\odot}$,$r_{\rm s}$) and we further propagate into the J-factor computation, following the determination in Ref. [114]. However, the derived 1σ uncertainties on the differential J-factors per solid angle, $\mathrm{dJ}/\mathrm{d}\Omega$ can be considered as conservative values since the correlation between the uncertainties on $\rho_{\odot}$ and $r_{\rm s}$ values are not explored in detail here. To compare these results with the previous ones obtained in Chap. 8, we also use an Einasto profile for the DM distribution, with parameterization taken from Ref. [11].

The cumulative J($< \theta$) and differential dJ/dΩ are shown in Fig. 10.5 as function of the angular distance θ from the GC for the three considered parameterizations

Parameterizations	NFW	cNFW	aNFW
$\rho_{\odot}$ [GeVcm^{-3}]	0.32	0.34	0.47
$r_{\rm s}$ [kpc]	15.5	23.8	16.1

Table 10.1: Mean profiles parameters ($\rho_{\odot}$,$r_{\rm s}$) for the NFW and cNFW parameterizations, respectively, extracted from [114]. The last column provides the ($\rho_{\odot}$, $r_{\rm s}$) parameters for the aNFW profile, extracted from Ref. [43].

together with their 1σ uncertainty.

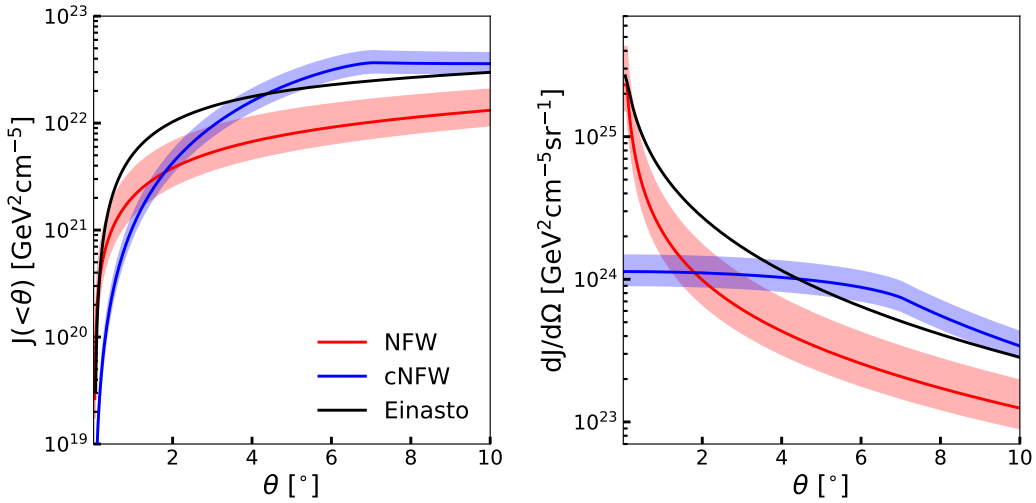

Figure 10.5: J-factor profiles for the cumulative and differential computation as function of the angular distance θ for the Einasto (black line), NFW (red line) and contracted NFW (blue line) profile parameterizations. The 1σ uncertainty band for the NFW and cNFW profiles are given as the red- and blue-shaded regions, respectively.

10.2 Prospective sensitivity search on Dark Matter signal from the Galactic Center

10.2.1 Relevant very-high-energy emissions in the Galactic Center

The GC region and the many faint and diffuse VHE emissions populating it have been already described in Chap. 5. In this work, we consider three conventional astrophysical diffuse sources, the H.E.S.S. Pevatron in the GC [18], the low-latitude

FBs emission [24, 286] and a possible contribution from millisecond pulsar (MSP) in the Galactic bulge [257] postulated to explain the "Galactic Center Excess" [257].

The current H.E.S.S. measurements for the Pevatron localize the emission in the inner $\sim$ 75 pc around the GC. The modeling of the FBs is done according to the best-fit spectrum above 100 GeV from Ref. [286] and the spatial morphology as from *Fermi*-LAT spatial template, derived from the FBs using *Fermi*-LAT observations following Ref. [198]. As we have already explained in Chap. 7, gamma rays in the *Fermi*-LAT analysis are derived up to $\sim$ 1 TeV, however the poor photon statistics above 100 GeV prevents us from performing detailed morphological studies in this energy range. Therefore, the spatial template is assumed as energy-independent. This latter assumption is conservative since any more detailed description of the template of the Bubbles would produce more constraining results on the spectrum, which would reflect a more constrained background in our analysis. Self-annihilation of WIMPs, spatially distributed as a generalized NFW profiles with inner slope of about 1.2 [212, 4, 184], is a possible explanation for the the gamma-ray excess (GCE) in the inner halo of the MW derived from *Fermi*-LAT observations (see, for instance, Refs.[211, 3, 184, 256, 41, 24]). However, from more recent studies, it emerged that non-spherically symmetric stellar density distribution of a population of millisecond pulsars in the Galactic bulge can well describe the GCE spatial morphology. Electrons are accelerated by the magnetospheres of pulsars in wind regions and could then escape the pulsar environment. They can then undergo inverse-Compton scatter on ambient radiation fields to produce VHE gamma rays. We assume the spatial morphology of the MSP emission at VHE as following the Boxy Bulge distribution described in Ref. [257]. Energetic CRs interacting with interstellar material and ambient photon fields give rise to diffuse gamma-ray emission known as the Galactic diffuse emission (GDE). The latter is the result of π_0 decay Bremsstrahlung, and inverse Compton scattering (ICS) processes. The majority of photons detected by *Fermi*-LAT [25] is constituted by GDE in the energy range from MeV up to about 1 TeV. The uncertainties inherent to models for the GDE currently limit the DM detection potential of analysis with the Fermi satellite datasets, but is not yet the case for H.E.S.S. [7]. At the time of the writing, we are working to include GDE models in the expected background to estimate the sensitivity reach of the current generation of IACTs but the shown results do not include the latter yet.

10.2.2 Definition of the region of interest

As for the previous analyses for the search for DM annihilation signal towards the GC region, we define the ROI, or ON region, as a disk centered on the dynamical center of the Milky Way, following the procedure adopted in Refs. [13, 11, 323, 7]. The same scheme for the construction of the ROIs have been described in Sec. 8.2.2. To represent the coverage of the GC region reached with the observa-

tions carried out with the H.E.S.S. Inner Galaxy Survey, we define the ROI radius up to 4°. The signal region is therefore constituted as concentric annulii with inner radius spanning from $\theta_i = 0.3°$ up to $\theta_i = 3.9°$. The ROI is further divided into 37 regions defined by the annulii to exploit the spatial and spectral characteristics of the DM signal with respect to the background. As was already explained, we use conservative masks on several regions harboring VHE sources to avoid leakage of astrophysical signal in the ROI and the challenging modeling of complex conventional astrophysical background. For this work, a box with Galactic longitudes $|l| < 1°$ and Galactic latitudes $|b| < 0.3°$ is excluded to mask VHE sources in the Galactic plane. Moreover a disk with radius of 0.8° centered at (l, b) = (-1.29°, -0.64°) for HESS J1745-303 is excluded too. Other background emissions in the region are modeled, as we explain later in the next section. We show in Fig. 10.6 the expected fluxes for ROI 2 in the left panel. We show DM fluxes for DM particles of mass of 3 TeV self-annihilating with $\langle\sigma v\rangle$ = 10^{-27}cm^{3}s^{-1}, for the NFW and cNFW DM distributions, respectively, together with relevant instrumental and astrophysical fluxes.

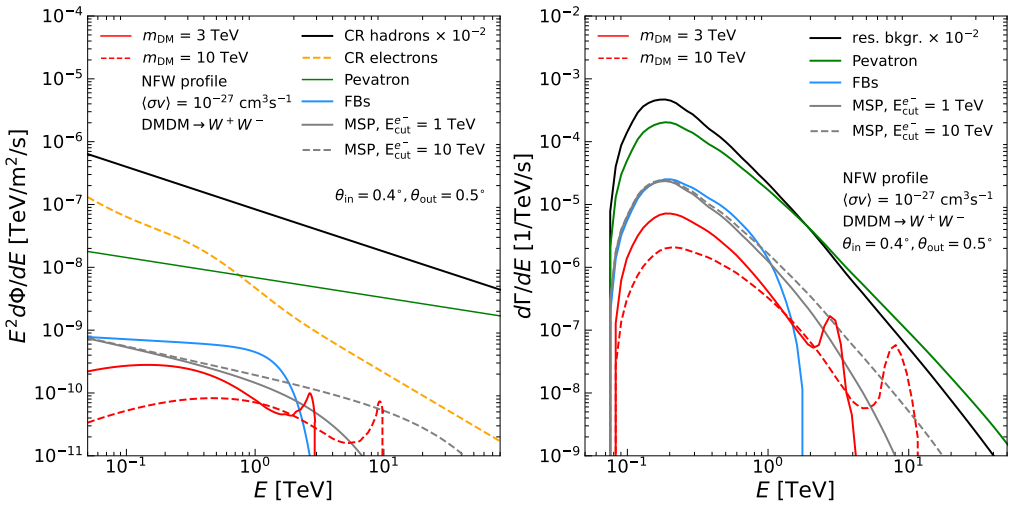

Figure 10.6: *Left panel:* Spectra of gamma-rays expected from WIMPs of mass $m_{\rm DM}$ = 3 and 10 TeV self-annihilating in the W^+W^- channel and with a velocity-weighted annihilation cross section $\langle\sigma v\rangle = 1 \times 10^{-27}$ cm^{3}s^{-1}. Cosmic ray fluxes for hadrons (proton + helium) (solid black line) and electrons (orange line) are plotted too. We show the three conventional astrophysical emissions: the diffuse fluxes from the H.E.S.S. Pevatron [19] (green line), the base of the Fermi Bubbles [286] and the expectation from the MSP-bulge population for two different values of the cut-off energy for the electron IC emission [257]. All the energy-differential gamma-ray fluxes are given for ROI 2. *Right panel:* Energy-differential count rates as a function of energy for signal and background in ROI 2.

10.2.3 Expected backgrounds and dark matter signal in the Galactic Center

We model the expected background in the region for the search of DM signal by the known sources of residual and conventional emissions.

CR protons and nuclei entering the atmosphere produce hadronic showers that can usually be discriminated against by the gamma-ray showers. Nevertheless, some hadronic showers are misidentified as gamma-ray ones, *i.e.* the rejection power is finite and this limit has to be taken into account. Then, by following Ref. [81], we define the expected number of events produced by a flux of CR protons and helium nuclei, as well as electrons and positrons. To encode the finite rejection power on protons and helium nuclei, we consider a constant rejection factor of 10 [324, 153, 79]. The reconstructed primary interaction depth on the incident particle in the atmosphere can be used to distinguish between showers initiated by electrons and positrons and by gamma-rays. As shown in Chap. 3, we can compute the number of signal events $N_{\mathrm{S}i,j}$ in the i^{th} ROI of solid angle $\Delta\Omega_i$ and j^{th} energy bin of width ΔE_j for a given DM annihilation channel and density profile. We use the equation:

$$N_{\mathrm{S},ij} = T_{\mathrm{obs},i} \int_{E_j-\Delta E_j/2}^{E_j+\Delta E_j/2} \int_{-\infty}^{+\infty} \frac{d\Phi_{\mathrm{S},ij}}{dE'}(\Delta\Omega_i, E') A^{\gamma}_{\mathrm{eff}}(E') G(E_j - E') dE' dE \,, \quad (10.1)$$

where we use Eq. 3.9. The other terms have already been defined for the case of Eq. 3.9. We use again the energy-dependent effective area for gamma rays $A^{\gamma}_{\mathrm{eff}}$, and the finite energy resolution of the instrument modeled as a Gaussian energy resolution G with σ/E = 10%. We define similarly the number of background events $N_{\mathrm{B}i,j}$ in the i^{th} ROI of solid angle $\Delta\Omega_i$. To do so we substitute $d\Phi^{\mathrm{DM}}_{\gamma,i,j}/dE \times A^{\gamma}_{\mathrm{eff}}$ by $d\Phi^{\mathrm{CR}}_{i,j}/dE \times A^{\mathrm{CR}}_{\mathrm{eff}} + d\Phi^{\mathrm{Conv}}_{\gamma,i,j}/dE \times A^{\gamma}_{\mathrm{eff}}$, where $d\Phi^{\mathrm{CR}}_{i,j}/dE$ and $d\Phi^{\mathrm{Conv}}_{i,j}/dE$ are the flux of cosmic rays and conventional gamma-ray background, respectively. The energy-dependent acceptance for the hadronic (proton, helium) CR flux is given by $A^{\mathrm{CR}}_{\mathrm{eff}}$ = $\epsilon^{CR} A^{\gamma}_{\mathrm{eff}}$, with ϵ^{CR} being the CR efficiency. The flux of photons from the residual background is modeled from protons, helium and electrons as power laws. For the first two spectra, we define the fluxes as $d\Phi(E)/dE = N \times (E/1TeV)^k$. A more complex function is adopted for the electrons: $d\Phi(E)/dE = N \times (E/1TeV)^k + L/(E\omega\sqrt{2\pi}) \exp(-(\ln(E/E_p))^2/2\omega^2)$. The parameters of the spectra are reported in Tab. 10.2.

Since a fraction of hadronic CR remains identified as gamma-rays, ϵ^{CR} is assumed to be 10% over the full energy range considered here. This allows us to reach a photon efficiency of higher than 95%[153]. We extract the gamma-ray acceptance for observations with full five-telescopes H.E.S.S. array from Ref. [209]. This ensures a realistic description of the IGS observations, largely explained in Chap. 6 and used for the analyses in Chap. 8 and 7. Refined descriptions of the instrument response function would require dedicated simulations of both the

Particle	N [1/TeV m^2 s sr]	k	L	E_p [TeV]	ω
p	0.096	-2.70			
He	0.0719	-2.64			
e	6.85×10^{-5}	-3.21	3.19×10^{-3}	0.107	0.776

Table 10.2: Parameterizations for the fluxes of CR spectra of protons, electrons and helium as extracted from Ref. [324].

instrument and the observations, which is beyond the scope of this study. An homogeneous time-exposure of 500 hours is assumed to represent what has been achieved with the IGS dataset. We define the differential count rates following Eq. 10.1, for each considered emission in ROI i, by:

$$\frac{d\Gamma_{\mathrm{S,B}ij}}{dE} = \frac{dN_{\mathrm{S,B}i,j}}{T_{\mathrm{obs},i}\, dE}\,. \tag{10.2}$$

We show in the right panel of Fig. 10.6 the rates expected from DM annihilation signal, CR, and the above mentioned conventional astrophysical emissions, *i.e.*, the PeVatron, FBs and MSPs, for ROI 2.

10.2.4 Statistical analysis method

The computation of the H.E.S.S. sensitivity to the DM signal is performed through the application of a 2D LLRTS. As already mentioned, we are using Poisson distributions in the likelihood function (see Sec. 4.4.1). The latter is built with spectral and spatial bins (i, j) for two statistically independent measurements (ON, OFF) as defined in Eq. 4.11. In what follows, we obtain the OFF number counts from simulations of the backgrounds, therefore, α_i = 1 and $N'_{\mathrm{S}i,j}$ = 0. The systematic uncertainties are included through the Gaussian nuisance factor in the likelihood function as described in Sec. 4.4. The term $\beta_{i,j}$ is applied again as a normalisation factor to the expected number of events. The width of the Gaussian function is defined as $\sigma_{\beta_{i,j}}$. $\beta_{i,j}$ is derived by the maximization of the likelihood function as $\mathrm{d}\mathcal{L}_{\mathrm{i,j}}/\mathrm{d}\beta_{\mathrm{i,j}} \equiv 0$, for a given value of $\sigma_{\beta,ij}$. We consider the uncertainty on the J-factor in the likelihood function by factorizing in Eq. 4.11 a nuisance parameter following a log-normal distribution with mean $\bar{J}$ and width σ_J as we already introduced in Sec. 4.5.2.

We derive the J-factor, $\hat{J}$, maximizing the likelihood function and use it in Eq. 4.11 to renormalize the number of expected events from DM as $N_{\mathrm{S}} \rightarrow N_{\mathrm{S}}\hat{J}/\bar{J}$. Then, the full likelihood is obtained by the product of the binned function over the spatial and spectral bins, *i.e.* $\mathcal{L} = \prod_{ij} \mathcal{L}_{i,j}\mathcal{L}_i^J$. Then, we obtain the limits on the free parameter $\langle\sigma v\rangle$ with the likelihood function $\mathcal{L}$ and the data, as function of the DM mass. We use the TS as defined in Sec. 4.2. We want to set one-sided

95% C. L. upper limits on $\langle\sigma v\rangle$, therefore we extract the values on $\langle\sigma v\rangle$ for TS = 2.71. This procedure is applied to compute the limits shown in the following. We have already discussed that we can compute the expected sensitivity by generating a large number of Monte Carlo simulations of ON and OFF measurements and determine mean expected limits and associated containment bands through the TS in Sec. 4.4. We have also discussed the alternative procedure with the Asimov dataset [147]. For the latter, we do not perform realizations of the background in the signal and background regions, but we consider the mean dataset valid for $N_{\rm ON} \equiv N_{\rm OFF}$. We use this for the computation of the mean expected sensitivity in this work. We can also use the Asimov approach to compute the containment bands of the expected sensitivity. We define the N-sigma containment band by calculating $TS = (\Phi^{-1}(0.95) \pm N)^2$, where Φ^{-1} is the inverse of the cumulative distribution function for the standard normal with μ=0 and σ=1.

10.3 Sensitivity limits

We compute the sensitivity limits, expressed as the mean expected upper limits at 95% C.L. on the annihilation cross section $\langle\sigma v\rangle$ as a function of the DM particle mass from 0.5 up to 100 TeV. We use the HDMS gamma-ray yield for the computation. However, the energy range for the binning of the event energy distributions used for the statistical analysis extends up to 70 TeV.

We will show limits computed following the Asimov approach. The percentage difference between the limits computed with the Asimov and the MC realizations approaches is shown in Fig. 10.7. This example is obtained for DM particles annihilating in the W^+W^- annihilation channel and distributed as the NFW profile used in this chapter. The mean expected limits and the 1σ containment band differs up to 5% and 4%, respectively, in the probed mass range. The small difference between mean expected limits shows that the utilized approach of the Asimov dataset, despite being a simplification with respect to the realizations approach, is solid and does not introduce distortions in the obtained limits.

10.3.1 Sensitivity to Dark Matter models

The limits for DM particles annihilating in the various channels and distributed according to the NFW and cNFW profile paramterizations of the Milky Way DM halo considered in this chapter, are shown in the left panel of Fig. 10.8. For DM particle with mass of 1.5 TeV, the limits exclude $\langle\sigma v\rangle$ down to 9.5×10^{-26}cm^{3}s^{-1} and 3.6×10^{-26}cm^{3}s^{-1} for the W^+W^- and $\tau^+\tau^-$ annihilation channels and the NFW profile, respectively. A degradation by a factor of 2.6 in the limits is obtained when adopting the cNFW parameterization. The right panel of the same figure shows the limits for DM particles annihilating in the channels $\nu_\tau\overline{\nu}_\tau$, $\nu_\mu\overline{\nu}_\mu$ and $\nu_e\overline{\nu}_e$, for the NFW parameterizations of the MW DM distribution used in Ref. [43], referred

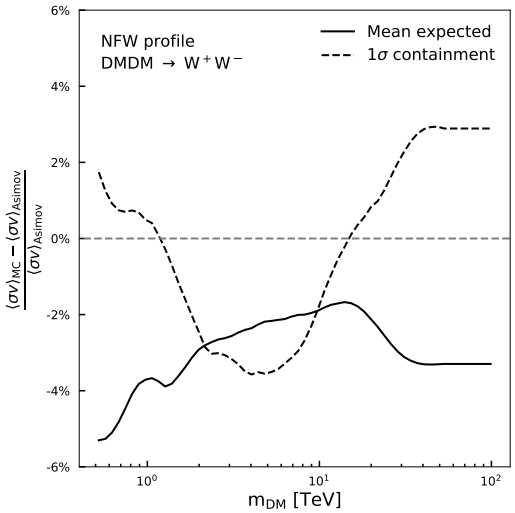

Figure 10.7: Comparison between the upper limits obtained for the Asimov and MC realizations approaches expressed as percentage differences of the mean expected upper limits (solid line) and the 1σ containment band (dashed line) on $\langle\sigma v\rangle$ (see text for more details) as a function of the DM mass $m_{\rm DM}$. The expected limits are computed at 95% C. L. on $\langle\sigma v\rangle$ for the W^+W^- channel derived for a H.E.S.S.-like mock dataset of GC observations.

as to aNFW profile in Tab. 10.1. The 90% C.L. mean expected upper limits from the ANTARES analysis in Ref. [43] for DM particles annihilating in $\nu_\mu\overline{\nu_\mu}$ are superimposed for comparison. With the obtained limits with H.E.S.S. we reinforce the statement that gamma-ray telescopes play an important role in the constraints of DM annihilating in neutrino channels [321].

Mean expected upper limits at 95% C.L. on the annihilation cross section $\langle\sigma v\rangle$ as a function of the DM particle mass from 0.5 up to 100 TeV are computed for canonical DM candidates as the Wino, the Higgsino split 1, and the Quintuplet, respectively. The difference in the limits between Higgsino split 1 and split 2 are negligible and therefore we show here only one case. The top panels of Fig. 10.9 shows the limits for the annihilating canonical DM candidates for the NFW profile. Mean expected upper limits are shown together to 1σ and 2σ containment bands. The theoretical cross sections and the thermal mass values are shown too. The bottom panels show the mean expected upper limits for the NFW and the cNFW profiles, respectively. The limits computed for the line-only spectrum are compared to the full-spectrum ones. For the Quintuplet model, the limits computed for endpoint plus line contributions are shown too. Note that for the Higgsino full-spectrum limits no endpoint contribution is available in the gamma-ray yields computation yet [324].

DM as made of Winos is excluded for both the distributions that we are using. With the assumption that Wino is either non-thermally produced or constitutes a

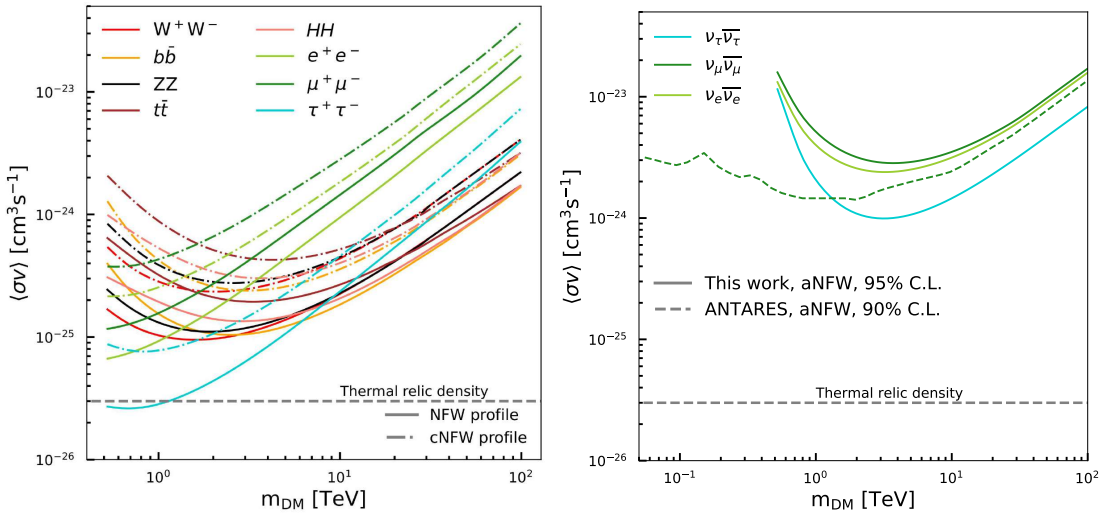

Figure 10.8: *Left panel:* Mean expected upper limits at 95% C. L. on $\langle\sigma v\rangle$ as a function of the DM mass m_{DM} for the W^+W^-, ZZ, HH, $b\bar{b}$, $\tau^+\tau^-$, $\mu^+\mu^-$, $t\bar{t}$ and e^+e^- annihilation channels for the computation of the gamma-ray yields from HDMS [55] for the NFW and cNFW profile parameterizations of the MW DM distribution and the H.E.S.S.-like mock dataset of GC observations adopted in this work. The horizontal gray long-dashed line is set to the value of the natural scale expected for the thermal-relic WIMPs. *Right panel:* Mean expected upper limits at 95% C. L. on $\langle\sigma v\rangle$ as a function of the DM mass m_{DM} for the $\nu_\tau\overline{\nu}_\tau$, $\nu_\mu\overline{\nu}_\mu$ and $\nu_e\overline{\nu}_e$ annihilation channels for the NFW parameterizations of the MW DM distribution used in Ref. [43], referred as to aNFW profile in Tab. 10.1. For comparison 90% C.L. mean expected upper limits are shown from ANTARES [43].

subset of the DM content, the masses for Wino DM can be excluded up to about 10 TeV. The current sensitivity cannot probe the thermal mass for the Higgsino DM. Due to the Sommerfeld-induced resonance for the theoretical cross section definition, the current sensitivity can reach the level of Higgsino masses of about 6.5 TeV. The continuum contribution dominates the limits for the Wino and Quintuplet models outside the resonances of $\langle\sigma v\rangle_{\mathrm{line}}$. The differential gamma-ray yield as a function of energy is shown in Fig. 10.10 for self-annihilating DM particles in the Wino, Higgsino splitting 1 and Quintuplet states, respectively. For each state, six spectra for masses close to resonances of $\langle\sigma v\rangle_{\mathrm{line}}$ are shown. The sum of contributions from continuum, endpoint and line and from endpoint and line only are shown for the Wino and Quintuplet states. For the Higgsino splitting 1 state, no endpoint contribution is available. As can be understood from Fig. 10.10, in between resonances, the limits for the Quintuplet receive a stronger contribution from the continuum and endpoint. The expected gamma-ray yield for the Quintuplet model is significantly increased in between mass resonances from state superposition contributions according to the H.E.S.S.-like energy resolution. This can improve the limits up to a factor of about ten and explains the features visi-

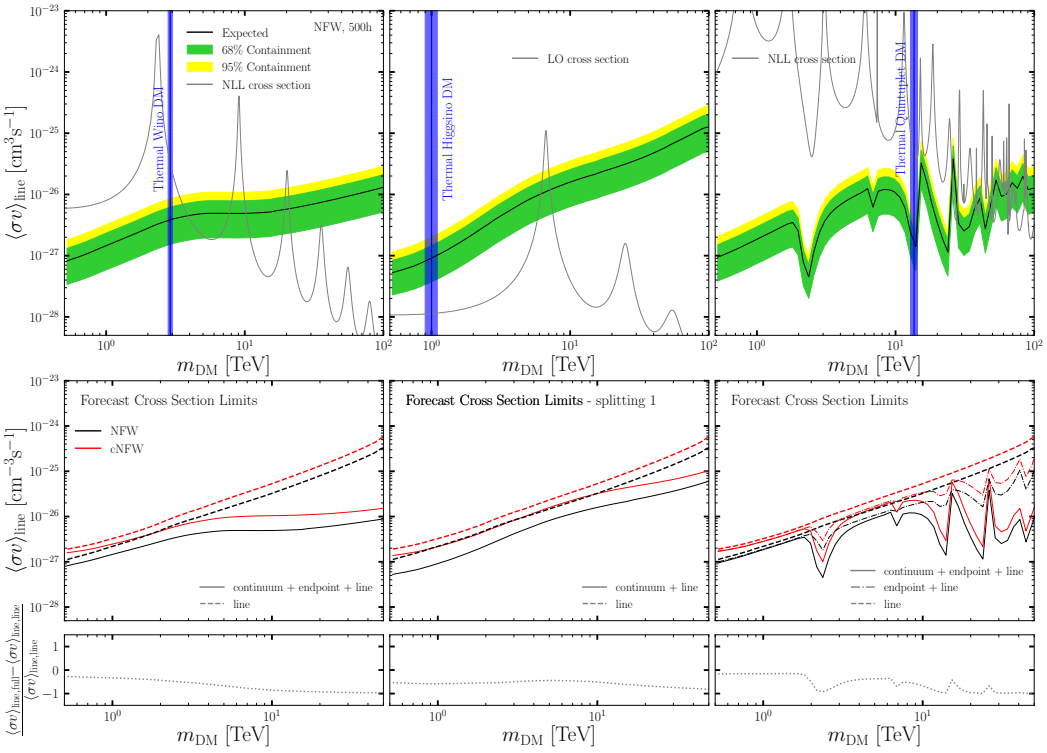

Figure 10.9: 95% C.L. expected upper limits on the annihilation cross section for Winos (left panels), Higgsino split 1 (middle panels) and Quintuplet (right panels), respectively, as a function of their mass. *Top panels*: 95% C.L. expected upper limits plotted together with the containment bands at 1σ (green band) and 2σ (yellow band) levels, for the NFW profile. The theoretical cross sections are plotted in gray. For each model, the thermal DM mass is marked as a cyan solid line with its 1σ error band. The limits are computed with the full spectrum. *Bottom panels:* percentage difference of the limits obtained between the full spectra and the line-only contribution to the gamma-ray yield, shown for the NFW (solid line) and the cNFW (dashed line), respectively. For the Quintuplet state, the limits from the contribution of endpoint and line to the gamma-ray yield are shown too.

ble for the Quintuplet limits in Fig. 10.9. The thermal Quintuplet DM is excluded within present sensitivity. A few non-thermally produced Quintuplet models are still viable above several ten TeV masses.

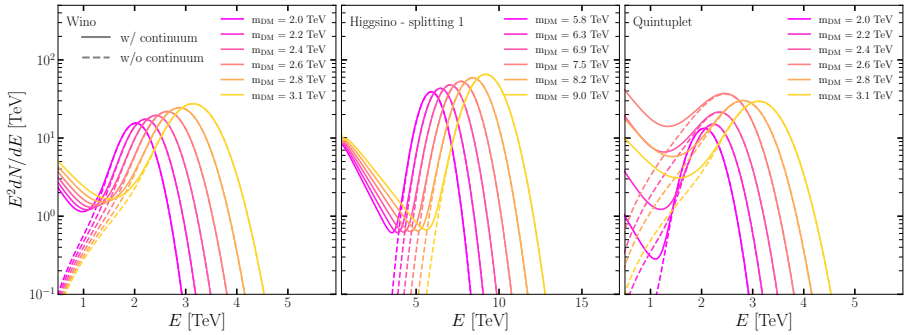

Figure 10.10: Energy-differential gamma-ray spectra expected for self-annihilating DM particles in the Wino (left panel), Higgsino splitting 1 (middle panel) and Quintuplet (right panel) states, respectively, computed with `HDMSpectra` [55]. Spectra with and without continuum are shown as solid and dashed lines, respectively. For the Wino and Quintuplet the spectra without continuum include endpoint and line contributions while for the Higgsino only the line contribution. In each model, the spectra are shown for masses close to chosen resonances.

10.4 Systematic uncertainties

10.4.1 Theoretical uncertainties

Since we computed limits for the two theoretical gamma-ray yields adopted in this work (see Sec. 10.1.1) we show the difference in the mean expected limits, for the W^+W^- annihilation channel and the NFW, cNFW and Einasto DM profiles in Fig. 10.11. The difference between the derivation with the two yields reaches 6% for a DM mass of 1 TeV, spanning from 25% up 5% to depending on the DM mass and considering the NFW profile. In the bottom panel of Fig. 10.11, the ratio between the two computations is shown for the same profile. The estimate of the J-factor uncertainties performed for the NFW and cNFW profiles in Sec. 10.1.3 is included in the sensitivity computation as explained in Sec. 10.2.4. Fig. 10.12 shows the impact of the J-factor uncertainty on the mean expected limit for the NFW DM profile parametrization considered in this work. The limits degrade by a factor of 3.2 up to 3.6, depending on the mass.

10.4.2 Background measurement uncertainties

The likelihood function can be modified to include the systematic uncertainty on the background residual determination through Eq. 4.11. To derive the systematic uncertainties affecting the background measurements we follow what is obtained forH.E.S.S. observations of the GC region as we explained in Sec. 6.4, and we then adopt a value of $\sigma_{\beta,ij}$ = 1%. We keep this value fixed since a more accurate deter-

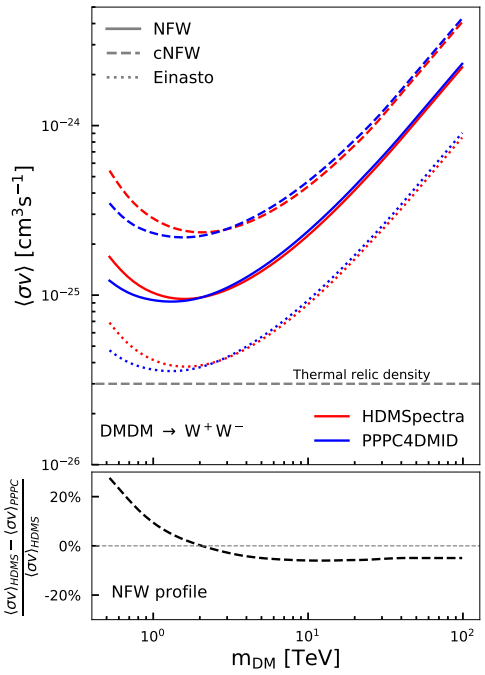

Figure 10.11: *Top panel:* Mean expected upper limits at 95% C. L. on $\langle\sigma v\rangle$ as a function of the DM mass $m_{\rm DM}$ for the W^+W^- channel derived with a H.E.S.S.-like mock dataset of GC observations for the computation of the gamma-ray yields from the `PPPC4DMID` [124] (blue line) and and `HDMSpectra` [55] (red line), respectively. The limits are shown for the NFW, cNFW and Einasto profiles. The horizontal gray long-dashed line is set to the value of the natural scale expected for the thermal-relic WIMPs. *Bottom panel:* percentage difference of the limits obtained with the two gamma-ray yields for the NFW profile.

mination of the spatial and energy dependencies of the systematic level is beyond the scope of this work. We show the limits with the inclusion of the uncertainty on the residual background in Fig. 10.12. The limits are degraded by a factor from 1.2 up to 1.4, depending on the mass.

10.4.3 Background mismodeling

We use this section for the investigation of how the uncertainties on residual and conventional backgrounds can deteriorate the reconstruction of a DM signal. For instance, the residual background determination is affected by the imperfect knowledge of the CR fluxes reaching the Earth's upper atmosphere. We consider an overall uncertainty in the measurements of the cosmic-ray fluxes. To do so, we change the indices of the power law describing the emission from fluxes of CR by $\pm$ 0.2 and we then derive new limits. We show this new derivation and the

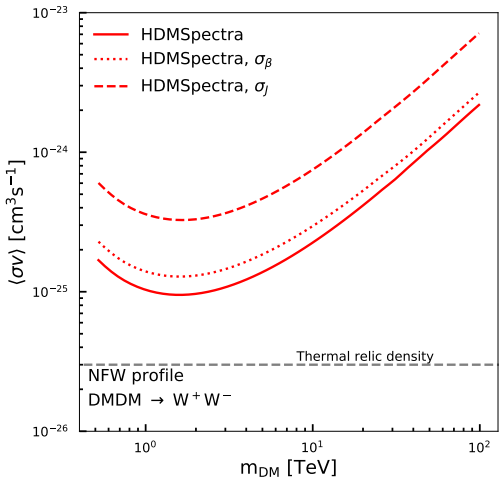

Figure 10.12: Mean expected upper limits at 95% C.L. for particles annihilating in W^+W^- for the NFW DM profile parameterization, as a function of the DM mass. Limits are shown for cases with and without inclusion of statistical uncertainties on the J-factor and systematic uncertainties on the background normalization. These are included as a log-normal and a Gaussian nuisance parameters, respectively.

comparison with the one with no uncertainties on the background determination in Fig. 10.13. We also show the ratio between the limits with and without the inclusion of the uncertainty in the bottom panel.

m_{DM}	$\langle\sigma v\rangle_{inj}$	$(\langle\sigma v\rangle^{mean}_{reco} - \langle\sigma v\rangle_{inj})/\langle\sigma v\rangle_{inj}$	Uncertainty budget		
			Statistical	Instrumental	Background mismodeling
TeV	[cm^{3}s^{-1}]	[%]	[%]	[%]	[%]
1	5×10^{-26}	$< 1\%$	84%	15%	1%
10	5×10^{-26}	$< 1\%$	91%	8%	1%

Table 10.3: Different sources of uncertainties shown as uncertainty budget in the reconstructed $\langle\sigma v\rangle$ value for DM signal injected in mock data corresponding to one $\langle\sigma v\rangle_{inj}$ value. Two cases are shown: for DM masses of 1 and 10 TeV in the W^+W^- annihilation channel. $\langle\sigma v\rangle$ are assumed to be reconstructed if min(TS)+ $1.36 \geq 0$.

We also tested a possible addition of a cutoff to the PeVatron emission, without obtaining significant changes in the limits, therefore no change is applied in this case. We test the uncertainty on the determination of emissions from FBs and MSP with the change on the indices of the power laws of $\pm$ 0.2. For this case too, the alteration does not significantly change the limits derivation. We perform a series of injection tests. We inject a fake DM signal for a DM particle with a given mass, annihilating in a given annihilation channel and distributed accord-

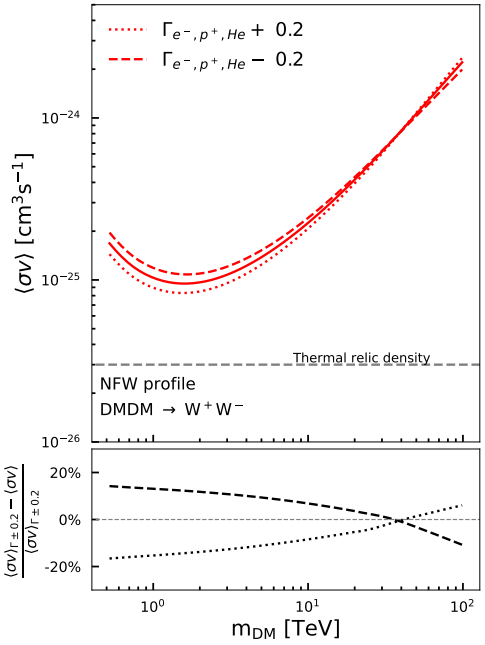

Figure 10.13: *Top panel:* 95% C. L. mean expected upper limits on the velocity-weighted annihilation cross section $\langle\sigma v\rangle$ for particles annihilating in W^+W^- for the NFW DM profile parameterization, as a function of the DM mass. The NFW profile is considered here. The horizontal gray long-dashed line is set to the value of the natural scale expected for the thermal-relic WIMPs. Limits for the changes on the indices of the power laws describing the spectra of cosmic rays by $\pm$ 0.2 are shown as the dashed and dotted lines. *Bottom panel:* percentage differences of the limits between the case with no uncertainty and the two cases shown in the top panel.

ing to a given DM profile. This signal is injected in the mock dataset composed of residual and conventional backgrounds. This is done in order to quantify the level of alteration on the performances of the injected signal due to the different uncertainties. We test values of $\langle\sigma v\rangle$ from 9×10^{-27} cm^{3}s^{-1} up to 4×10^{-25}, for DM masses of 0.98 and 9.81 TeV and particles annihilating in W^+W^-. The TS procedure is carried out for each injected value $\langle\sigma v\rangle_{\rm inj}$ and the reconstructed annihilation cross section $\langle\sigma v\rangle_{\rm reco}$ is computed. This is done for three cases: (i) we fix conventional background emissions and change the indices of the residual background power laws by $\pm$ 0.2, (ii) we fix the residual background and the MSP emission and change the FBs power law index by $\pm$ 0.2, (iii) we fixed the residual background and the FBs emission and change the MSP power law index by $\pm$ 0.2. The results for $\langle\sigma v\rangle_{\rm reco}$ and the 1σ bands are plotted in Fig 10.14. The comparison is between the standard case with no deterioration on the background emission,

and all the previously mentioned cases. Results for $m_{\rm DM}$ = 0.98 TeV are in the top panels, whereas results for $m_{\rm DM}$ = 9.81 TeV are shown in the bottom ones. The uncertainty budget is summarized in Table 10.3.

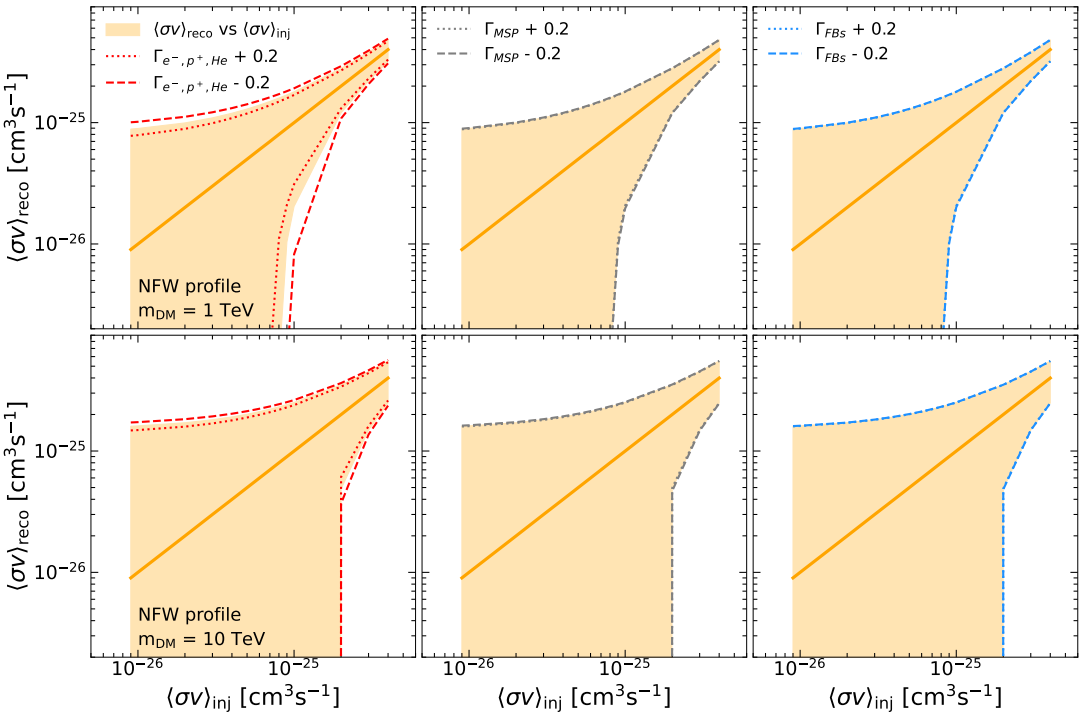

Figure 10.14: Reconstruction tests for injected values of the annihilation cross sections $\langle\sigma v\rangle_{inj}$ from 9×10^{-27} cm^{3}s^{-1} up 4×10^{-25}, for particles annihilating in W^+W^- and for masses of 0.98 and 9.81 TeV, in the top and bottom panels, respectively. The TS is performed with each injected value $\langle\sigma v\rangle_{\rm inj}$ to determine the reconstructed annihilation cross section $\langle\sigma v\rangle_{\rm reco}$ and the 1σ containment bands. The spectral emissions in the background are changed by considering three cases. *Left panels*: $\pm$ 0.2 on the indices of the residual background. *Middle panels*: $\pm$ 0.2 on the index of the MSP emission. *Right panels*: $\pm$ 0.2 on the index of the FBs emission. See text for more details.

10.5 Conclusions and outlook

In this chapter we have shown the ultimate reach in terms of sensitivity of the current generation of IACTs to DM annihilation signal. We have also shown sensitivity in terms of specific heavy DM candidates. All the sensitivity limits shown have been computed in the range between 500 GeV and 100 TeV, assuming two

distributions of DM from the most-up-to-date computations. The main results are:

- new sensitivity limits with an H.E.S.S. II realistic mock dataset of the GC region have been shown for two gamma-ray yield predictions: `PPPC4DMID` and `HDMSpectra`;
- new DM distribution profiles more accurately describing the stellar kinematics and including baryon feedback and, thus, giving a better picture of the possible DM distribution have been used;
- the limits on the cross section for DM annihilating in the $\tau^+\tau^-$ channel challenge the level of the thermal relic cross section;
- we have demonstrated that limits on neutrinos channels obtained with H.E.S.S. can be complementary to the limits obtained from neutrino-observation dedicated experiments like ANTARES;
- the most-up-to-date EFT computation of the annihilation spectra of the Wino and Quintuplet and a Sommerfeld-enhanced tree-level computation of the Higgsino spectrum have been used for the derivation of upper limits that exclude most masses for these conventional DM models;
- several sources of systematic uncertainties have been explored and their impact on the final limits has been assessed: the current sensitivity is still limited by statistical uncertainty and therefore more observations of the GC region can give new insights on annihilating DM.

At the time of the writing, more contributions to the conventional background emissions in the GC region are being explored and will be explained in detail in Ref. [282]. Further studies will be useful for a more accurate determination of the conventional backgrounds in the TeV energy range for further modeling in order to improve sensitivity prospects. The future generation of IACTs, *i.e.,* CTA, will be a unique probe for heavy DM candidates in the TeV mass range. More observations are necessary to better explore the systematic uncertainties. H.E.S.S. observations constitute a unique way to probe heavy DM candidates in the TeV mass range for signals coming from the most privileged region of the GC to detect DM annihilation signatures. Canonical DM models such as thermal Wino and Quintuplet DM can be challenged by the present sensitivity. CTA observations and analyses will improve significantly over the present limits set by H.E.S.S. and will be unique to probe the thermal Higgsino DM although the full impact will depend on the capacity to handle conventional background modeling and instrumental systematic uncertainties given the expected photon statistics. The results shown in this chapter have been submitted as an article to *Physical Review D* [282].

Conclusions

A study of the Galactic Center region and several analyses for the search for dark matter annihilation signals at Very-High-Energy, using H.E.S.S. datasets, have been presented in this thesis.

The search for signal in Very High Energy gamma-ray observations has to deal with a non-trivial residual background. Appropriate statistical methods for this task have been presented. More classical ones, like the widely known log-likelihood-ratio-test-statistics framework, are used for the analyses presented in this work. A novel approach based on Bayesian Neural network frameworks has been presented. It has been applied on a synthetic dataset with injected signal and a non-trivial background. I demonstrated how this framework can recover the spatial and spectral description of the signal when the background is dominant. Ongoing effort aims at applying this architecture on real astrophysical dataset, for instance the search for dark matter annihilation signals. At the moment of the writing, the results obtained with our Bayesian Neural network framework have been submitted to ICLR2023 [64].

The inner halo of the Milky Way is an environment full of possibilities for testing astrophysics at Very-High-Energy. Driven by this, the H.E.S.S. Collaboration extensively observed the inner few degrees around the Galactic Center with the full five-telescopes array. This dataset, known as the Inner Galaxy Survey, consists of 6 years of high-quality data for a total of 546 hours live time, collected between 2014 and 2020. It has been presented and extensively described, with details on the exposure and the parameters of the data taking. Ongoing works for the development of background models for these Galactic Center observations, using extra-galactic observations and run-wise simulations of the Inner Galaxy Survey dataset, have been introduced. One of the important emissions in the inner halo of the Milky Way is the Fermi Bubbles one. This double-lobe bubble emission, detected at low latitudes by the *Fermi*-LAT satellite, has been extensively analyzed using the Inner Galaxy Survey observations. I presented the H.E.S.S. analysis to derive the spectrum of the Bubbles and I showed the detected flux points for energies between 300 GeV and $\sim$ 2 TeV. At 1 TeV, the Fermi Bubbles emission is measured by H.E.S.S. at $\sim 1.0 \times 10^{-9}$ TeV cm^{-2} s^{-1} sr^{-1}. Constraints on the parent particle populations generating the Fermi Bubbles emission can be obtained with this analysis. Exponential cut-off power laws are tested for both leptonic and

hadronic models but the results cannot significantly define a value for the energy cut-off, therefore only lower limits can be stated. In H.E.S.S., dedicated studies are ongoing to further characterize the systematic uncertainties and better constrain the emission for energies higher than 2 TeV. At the moment of the writing, the results shown on the detection of the Fermi Bubbles are being prepared for a submission to *Nature* within a few months [140].

The Galactic Center is the most promising target to search for dark matter annihilation signals since it is the closest one and it is expected to host a large amount of dark matter. The Inner Galaxy Survey observations have been used to derive the most constraining limits, for the annihilation channels explored in this work, on $\langle \sigma v \rangle$ of the dark matter particles in the TeV mass range. Considering the channel $\chi\chi \rightarrow W^+W^-$, our limits reach 3.7×10^{-26} cm^{3}s^{-1} for a dark matter particle mass of 1.5 TeV. In the $\tau^+\tau^-$ channel, the limits reach 1.2×10^{-26} cm^{3}s^{-1} for a DM particle mass of 0.7 TeV, crossing the $\langle \sigma v \rangle$ values expected for dark matter particles annihilating with thermal-relic cross section. At 1.5 TeV dark matter mass, I obtain an improvement factor of 1.6 with respect to previous results from the 2016 H.E.S.S. analysis. The results shown on the search for dark matter annihilation signals with the Inner Galaxy Survey have been published in *Physical Review Letters* [7]. Complementary targets for the search of dark matter signals are candidate dark matter subhalos. I carried out an analysis on a selection of these subhalos among the high energy sources in the 3FHL *Fermi*-LAT catalog with no other astrophysical counterpart. For this search, upper limits for dark matter signal on the product of free parameters $\langle \sigma v \rangle \times J$, both for each individual dataset and for the combined one are derived. The emission from this selection of candidate dark matter subhalos in terms of dark matter has been excluded down to 300 GeV from the H.E.S.S. analysis. When I assume thermal dark matter, I can derive upper limits on the J-factor only. The results obtained on the search for dark matter annihilation signals from these candidates dark matter subhalos have been published in *The Astrophysical Journal* [10].

The reach in terms of sensitivity with the current generation of IACTs, and in particular with H.E.S.S., to annihilation signals from dark matter particles has been presented. For this study, I make use of a mock dataset of the Inner Galaxy Survey observations, created from expected residual background of cosmic rays and conventional background such as the emissions from a population of milli-second pulsars in the Galactic Bulge, the Fermi Bubbles and the Pevatron in the Galactic Center. The state of the art of the gamma-ray yields for the computation of the expected fluxes of photons from annihilating dark matter has been used. New derivation of the dark matter distribution in the Galactic Center, including baryon feedback and stellar kinematic computations are applied. Limits are derived for model-independent dark matter searches. The sensitivity to canonical dark matter candidates such as the Wino, Higgsino and the Quintuplet has been explored. Theoretical Wino dark matter is excluded up to 10 TeV. The current level of sensi-

tivity reaches the theoretical Higgsino cross section for masses of about 6.5 TeV, due to the Sommerfeld-induced resonance. The thermal Quintuplet DM is excluded with the present sensitivity. I widely explore how the evaluation of different uncertainties can affect the final results. At the moment of the writing, these results have been submitted to *Physical Review D* [282].

If we were to summarize the most important results shown in this work, they would be:

- important insights on a novel approach for the disentangling of a signal in a background-dominated dataset with a Bayesian Neural Network architecture have been presented;
- the Inner Galaxy Survey H.E.S.S. dataset, including the most sensitive observations available so far of the Galactic Center region at TeV energies, has been extensively analyzed and used;
- the analysis for the search for the low-latitude Fermi Bubbles showed the capability to detect and constrain this extended emission with H.E.S.S., using the Inner Galaxy Survey;
- the latter is used to obtain also the most constraining limits, in the TeV mass range, on $\langle \sigma v \rangle$ of dark matter particles annihilating in the Galactic Center region;
- other limits on $\langle \sigma v \rangle$ are obtained with H.E.S.S. observations of dark matter subhalo candidates;
- benchmarks have been established on the sensitivity to dark matter signals for the current generation of IACTs, investigating theoretical and instrumental uncertainties.

All in all, the insights derived from this work will be useful for future reference and analyses with the next generation of IACTs.

Bibliography

[1] M. Aaboud et al. “Search for new phenomena in final states with an energetic jet and large missing transverse momentum in pp collisions at $\sqrt{s} = 13$ TeV using the ATLAS detector”. In: *Phys. Rev. D* 94.3 (2016), p. 032005. doi: 10.1103/PhysRevD.94.032005. arXiv: 1604.07773 [hep-ex].

[2] M. G. Aartsen et al. “Search for annihilating dark matter in the Sun with 3 years of IceCube data”. In: *Eur. Phys. J. C* 77.3 (2017). [Erratum: Eur.Phys.J.C 79, 214 (2019)], p. 146. doi: 10.1140/epjc/s10052-017-4689-9. arXiv: 1612.05949 [astro-ph.HE].

[3] K. N. Abazajian. “The Consistency of Fermi-LAT Observations of the Galactic Center with a Millisecond Pulsar Population in the Central Stellar Cluster”. In: *JCAP* 1103 (2011), p. 010. doi: 10.1088/1475-7516/2011/03/010. arXiv: 1011.4275 [astro-ph.HE].

[4] K. N. Abazajian and M. Kaplinghat. “Detection of a Gamma-Ray Source in the Galactic Center Consistent with Extended Emission from Dark Matter Annihilation and Concentrated Astrophysical Emission”. In: *Phys. Rev.* D86 (2012). [Erratum: Phys. Rev.D87,129902(2013)], p. 083511. doi: 10.1103/PhysRevD.86.083511, 10.1103/PhysRevD.87.129902. arXiv: 1207.6047 [astro-ph.HE].

[5] B. P. Abbott et al. “Observation of Gravitational Waves from a Binary Black Hole Merger”. In: *Phys. Rev. Lett.* 116 (6 Feb. 2016), p. 061102. doi: 10.1103/PhysRevLett.116.061102. url: https://link.aps.org/doi/10.1103/PhysRevLett.116.061102.

[6] H. Abdalla et al. “H.E.S.S. Limits on Linelike Dark Matter Signatures in the 100 GeV to 2 TeV Energy Range Close to the Galactic Center”. In: *Phys. Rev. Lett.* 117.15 (2016), p. 151302. doi: 10.1103/PhysRevLett.117.151302. arXiv: 1609.08091 [astro-ph.HE].

[7] H. Abdalla et al. “Search for Dark Matter Annihilation Signals in the H.E.S.S. Inner Galaxy Survey”. In: *Phys. Rev. Lett.* 129.11 (2022), p. 111101. doi: 10.1103/PhysRevLett.129.111101. arXiv: 2207.10471 [astro-ph.HE].

[8] H. Abdalla et al. "The H.E.S.S. Galactic plane survey". In: *Astron. Astrophys.* 612 (2018), A1. doi: 10.1051/0004-6361/201732098. arXiv: 1804.02432 [astro-ph.HE].

[9] H. Abdalla et al. "Characterising the VHE diffuse emission in the central 200 parsecs of our Galaxy with H.E.S.S." In: *Astronomy & Astrophysics* 612 (Apr. 2018), A9. issn: 1432-0746. doi: 10.1051/0004-6361/201730824. url: http://dx.doi.org/10.1051/0004-6361/201730824.

[10] H. Abdalla et al. "Search for Dark Matter Annihilation Signals from Unidentified Fermi-LAT Objects with H.E.S.S." In: *Astrophys. J.* 918.1, 17 (Sept. 2021), p. 17. doi: 10.3847/1538-4357/abff59. arXiv: 2106.00551 [astro-ph.HE].

[11] H. Abdallah et al. "Search for γ-Ray Line Signals from Dark Matter Annihilations in the Inner Galactic Halo from 10 Years of Observations with H.E.S.S." In: *Phys. Rev. Lett.* 120.20 (2018), p. 201101. doi: 10.1103/PhysRevLett.120.201101. arXiv: 1805.05741 [astro-ph.HE].

[12] H. Abdallah et al. "Search for dark matter annihilation in the Wolf-Lundmark-Melotte dwarf irregular galaxy with H.E.S.S." In: *Phys. Rev. D* 103.10 (2021), p. 102002. doi: 10.1103/PhysRevD.103.102002. arXiv: 2105.04325 [astro-ph.HE].

[13] H. Abdallah et al. "Search for dark matter annihilations towards the inner Galactic halo from 10 years of observations with H.E.S.S". In: *Phys. Rev. Lett.* 117.11 (2016), p. 111301. doi: 10.1103/PhysRevLett.117.111301. arXiv: 1607.08142 [astro-ph.HE].

[14] H. Abdallah et al. "Search for dark matter signals towards a selection of recently detected DES dwarf galaxy satellites of the Milky Way with H.E.S.S." In: *Phys. Rev. D* 102.6 (2020), p. 062001. doi: 10.1103/PhysRevD.102.062001. arXiv: 2008.00688 [astro-ph.HE].

[15] J. Abdallah et al. "Simplified Models for Dark Matter Searches at the LHC". In: *Phys. Dark Univ.* 9-10 (2015), pp. 8–23. doi: 10.1016/j.dark.2015.08.001. arXiv: 1506.03116 [hep-ph].

[16] S. Abdollahi et al. "$Fermi$ Large Area Telescope Fourth Source Catalog". In: *Astrophys. J. Suppl.* 247.1 (2020), p. 33. doi: 10.3847/1538-4365/ab6bcb. arXiv: 1902.10045 [astro-ph.HE].

[17] A.U. Abeysekara et al. "A search for dark matter in the Galactic halo with HAWC". In: *JCAP* 2018.02 (2018), pp. 049–049. doi: 10.1088/1475-7516/2018/02/049. arXiv: 1710.10288 [astro-ph.HE].

[18] A. Abramowski et al. "Acceleration of petaelectronvolt protons in the Galactic Centre". In: *Nature* 531 (2016), p. 476. doi: 10.1038/nature17147. arXiv: 1603.07730 [astro-ph.HE].

[19] A. Abramowski et al. “Acceleration of petaelectronvolt protons in the Galactic Centre”. In: *Nature* 531 (2016), p. 476. doi: 10.1038/nature17147. arXiv: 1603.07730 [astro-ph.HE].

[20] A. Abramowski et al. “Search for a Dark Matter annihilation signal from the Galactic Center halo with H.E.S.S”. In: *Phys. Rev. Lett.* 106 (2011), p. 161301. doi: 10.1103/PhysRevLett.106.161301. arXiv: 1103.3266 [astro-ph.HE].

[21] V. A. Acciari et al. “Constraining Dark Matter lifetime with a deep gamma-ray survey of the Perseus Galaxy Cluster with MAGIC”. In: *Phys. Dark Univ.* 22 (2018), pp. 38–47. doi: 10.1016/j.dark.2018.08.002. arXiv: 1806.11063 [astro-ph.HE].

[22] A. Acharyya et al. “Sensitivity of the Cherenkov Telescope Array to a dark matter signal from the Galactic centre”. In: *Journal of Cosmology and Astroparticle Physics* 2021.01 (Jan. 2021), pp. 057–057. doi: 10.1088/1475-7516/2021/01/057. url: https://doi.org/10.1088/1475-7516/2021/01/057.

[23] M. Ackermann et al. “Searching for Dark Matter Annihilation from Milky Way Dwarf Spheroidal Galaxies with Six Years of Fermi Large Area Telescope Data”. In: *Phys. Rev. Lett.* 115.23 (2015), p. 231301. doi: 10.1103/PhysRevLett.115.231301. arXiv: 1503.02641 [astro-ph.HE].

[24] M. Ackermann et al. “The Fermi Galactic Center GeV Excess and Implications for Dark Matter”. In: *Astrophys. J.* 840.1 (2017), p. 43. doi: 10.3847/1538-4357/aa6cab. arXiv: 1704.03910 [astro-ph.HE].

[25] M. Ackermann et al. “*Fermi*-LAT observations of the diffuse γ-ray emission: implications for cosmic rays and the interstellar medium”. In: *The Astrophysical Journal* 750.1 (Apr. 2012), p. 3. issn: 1538-4357. doi: 10.1088/0004-637x/750/1/3. url: http://dx.doi.org/10.1088/0004-637X/750/1/3.

[26] S. Adrian-M.ez et al. “Limits on Dark Matter Annihilation in the Sun using the ANTARES Neutrino Telescope”. In: *Phys. Lett. B* 759 (2016), pp. 69–74. doi: 10.1016/j.physletb.2016.05.019. arXiv: 1603.02228 [astro-ph.HE].

[27] O. Adriani et al. “An anomalous positron abundance in cosmic rays with energies 1.5-100 GeV”. In: *Nature* 458 (2009), pp. 607–609. doi: 10.1038/nature07942. arXiv: 0810.4995 [astro-ph].

[28] A. F. Agarap. “Deep Learning using Rectified Linear Units (ReLU)”. In: *arXiv e-prints*, arXiv:1803.08375 (Mar. 2018), arXiv:1803.08375. arXiv: 1803.08375 [cs.NE].

[29] N. Aghanim et al. “Planck 2018 results. VI. Cosmological parameters”. In: *Astron. Astrophys.* 641 (2020). [Erratum: Astron.Astrophys. 652, C4 (2021)], A6. doi: 10.1051/0004-6361/201833910. arXiv: 1807.06209 [astro-ph.CO].

[30] AGILE. *AGILE - Astro-rivelatore Gamma a Immagini Leggero.* http://agile.rm.iasf.cnr.it/. 2007.

[31] M. Aguilar et al. "Composition of energy spectra and interactions, electrons, dark matter, neutrinos, muons, pions and other elementary particle detectors, cosmic ray detectors". In: *Phys. Rev. Lett.* 110.14, 141102 (Apr. 2013), p. 141102. doi: 10.1103/PhysRevLett.110.141102.

[32] F. Aharonian et al. "Observations of the Crab Nebula with H.E.S.S". In: *Astron. Astrophys.* 457 (2006), pp. 899–915. doi: 10.1051/0004-6361:20065351. arXiv: astro-ph/0607333.

[33] F. Aharonian et al. "Observations of the Crab Nebula with H.E.S.S". In: *Astron. Astrophys.* 457 (2006), pp. 899–915. doi: 10.1051/0004-6361:20065351. arXiv: astro-ph/0607333 [astro-ph].

[34] F. Aharonian. "Primary particle acceleration above 100 TeV in the shell-type Supernova Remnant RX J1713.7-3946 with deep H.E.S.S. observations". In: *Astron. Astrophys.* 464 (2007), pp. 235–243. doi: 10.1051/0004-6361:20066381. arXiv: astro-ph/0611813.

[35] F. Aharonian et al. "Search for Gamma-rays from Dark Matter annihilations around Intermediate Mass Black Holes with the H.E.S.S. experiment". In: *Phys. Rev. D* 78 (2008), p. 072008. doi: 10.1103/PhysRevD.78.072008. arXiv: 0806.2981 [astro-ph].

[36] F. Aharonian et al. "Spectrum and variability of the Galactic Center VHE gamma-ray source HESS J1745-290". In: *Astron. Astrophys.* 503 (2009), p. 817. doi: 10.1051/0004-6361/200811569. arXiv: 0906.1247 [astro-ph.GA].

[37] F. Aharonian et al. "An Exceptional Very High Energy Gamma-Ray Flare of PKS 2155-304". In: *The Astrophysical Journal* 664.2 (July 2007), pp. L71–L74. doi: 10.1086/520635. url: https://doi.org/10.1086/520635.

[38] F. Aharonian et al. "Spectrum and variability of the Galactic center VHE γ-ray source HESS J1745–290". In: *Astronomy & Astrophysics* 503.3 (July 2009), pp. 817–825. issn: 1432-0746. doi: 10.1051/0004-6361/200811569. url: http://dx.doi.org/10.1051/0004-6361/200811569.

[39] F. Aharonian et al. "Very high energy gamma rays from the composite SNR G0.9+0.1". In: *Astronomy & Astrophysics* 432.2 (Mar. 2005), pp. L25–L29. issn: 1432-0746. doi: 10.1051/0004-6361:200500022. url: http://dx.doi.org/10.1051/0004-6361:200500022.

[40] M. Ajello et al. "3FHL: The Third Catalog of Hard Fermi-LAT Sources". In: *Astrophys. J. Suppl.* 232.2 (2017), p. 18. doi: 10.3847/1538-4365/aa8221. arXiv: 1702.00664 [astro-ph.HE].

[41] M. Ajello et al. “Fermi-LAT Observations of High-Energy γ-Ray Emission Toward the Galactic Center”. In: *Astrophys. J.* 819.1 (2016), p. 44. doi: 10.3847/0004-637X/819/1/44. arXiv: 1511.02938 [astro-ph.HE].

[42] D. S. Akerib et al. “Results from a search for dark matter in the complete LUX exposure”. In: *Phys. Rev. Lett.* 118.2 (2017), p. 021303. doi: 10.1103/PhysRevLett.118.021303. arXiv: 1608.07648 [astro-ph.CO].

[43] A. Albert et al. “Results from the search for dark matter in the Milky Way with 9 years of data of the ANTARES neutrino telescope”. In: *Phys. Lett. B* 769 (2017). [Erratum: Phys.Lett.B 796, 253–255 (2019)], pp. 249–254. doi: 10.1016/j.physletb.2017.03.063. arXiv: 1612.04595 [astro-ph.HE].

[44] A. Albert et al. “Searching for Dark Matter Annihilation in Recently Discovered Milky Way Satellites with Fermi-LAT”. In: *Astrophys. J.* 834.2 (2017), p. 110. doi: 10.3847/1538-4357/834/2/110. arXiv: 1611.03184 [astro-ph.HE].

[45] C. Alcock et al. “The MACHO Project: Microlensing Results from 5.7 Years of Large Magellanic Cloud Observations”. In: *Astrophys. J.* 542.1 (Oct. 2000), pp. 281–307. doi: 10.1086/309512. arXiv: astro-ph/0001272 [astro-ph].

[46] E. Aprile et al. “XENON100 Dark Matter Results from a Combination of 477 Live Days”. In: *Phys. Rev. D* 94.12 (2016), p. 122001. doi: 10.1103/PhysRevD.94.122001. arXiv: 1609.06154 [astro-ph.CO].

[47] N. Arkani-Hamed et al. “Simply Unnatural Supersymmetry”. In: (2012). arXiv: 1212.6971 [hep-ph].

[48] L. Armillotta et al. “The life cycle of the Central Molecular Zone – I. Inflow, star formation, and winds”. In: *Monthly Notices of the Royal Astronomical Society* 490.3 (Oct. 2019), pp. 4401–4418. issn: 1365-2966. doi: 10.1093/mnras/stz2880. url: http://dx.doi.org/10.1093/mnras/stz2880.

[49] P. Asadi et al. “Capture and Decay of Electroweak WIMPonium”. In: *JCAP* 02 (2017), p. 005. doi: 10.1088/1475-7516/2017/02/005. arXiv: 1610.07617 [hep-ph].

[50] W. I. Axford, E. Leer, and G. Skadron. “The Acceleration of Cosmic Rays by Shock Waves”. In: *International Cosmic Ray Conference*. Vol. 11. International Cosmic Ray Conference. Jan. 1977, p. 132.

[51] F. K. Baganoff et al. “ChandraX-Ray Spectroscopic Imaging of Sagittarius A* and the Central Parsec of the Galaxy”. In: *The Astrophysical Journal* 591.2 (July 2003), pp. 891–915. doi: 10.1086/375145. url: https://doi.org/10.1086/375145.

[52] J. Bally et al. “The Bolocam Galactic Plane Survey: λ = 1.1 and 0.35 mm Dust Continuum Emission in the Galactic Center Region”. In: 721.1 (Sept. 2010), pp. 137–163. doi: 10.1088/0004-637X/721/1/137. arXiv: 1011.0932 [astro-ph.GA].

[53] M. V. Barkov and V. Bosch-Ramon. “Formation of large-scale magnetic structures associated with the Fermi bubbles”. In: *Astronomy & Astrophysics* 565, A65 (May 2014), A65. doi: 10.1051/0004-6361/201322743. arXiv: 1311.6722 [astro-ph.HE].

[54] B. A. Bassett and R. Hlozek. “Baryon Acoustic Oscillations”. In: (Oct. 2009). arXiv: 0910.5224 [astro-ph.CO].

[55] C. W. Bauer, N. L. Rodd, and B. R. Webber. “Dark matter spectra from the electroweak to the Planck scale”. In: *JHEP* 06 (2021), p. 121. doi: 10.1007/JHEP06(2021)121. arXiv: 2007.15001 [hep-ph].

[56] M. Bauer et al. “Soft Collinear Effective Theory for Heavy WIMP Annihilation”. In: *JHEP* 01 (2015), p. 099. doi: 10.1007/JHEP01(2015)099. arXiv: 1409.7392 [hep-ph].

[57] M. Baumgart, T. Cohen, E. Moulin, et al. “Precision Photon Spectra for Wino Annihilation”. In: *JHEP* 01 (2019), p. 036. doi: 10.1007/JHEP01(2019)036. arXiv: 1808.08956 [hep-ph].

[58] M. Baumgart, I. Z. Rothstein, and V. Vaidya. “Calculating the Annihilation Rate of Weakly Interacting Massive Particles”. In: *Phys. Rev. Lett.* 114 (2015), p. 211301. doi: 10.1103/PhysRevLett.114.211301. arXiv: 1409.4415 [hep-ph].

[59] M. Baumgart, I. Z. Rothstein, and V. Vaidya. “Constraints on Galactic Wino Densities from Gamma Ray Lines”. In: *JHEP* 04 (2015), p. 106. doi: 10.1007/JHEP04(2015)106. arXiv: 1412.8698 [hep-ph].

[60] M. Baumgart and V. Vaidya. “Semi-inclusive wino and higgsino annihilation to LL'”. In: *JHEP* 03 (2016), p. 213. doi: 10.1007/JHEP03(2016)213. arXiv: 1510.02470 [hep-ph].

[61] M. Baumgart et al. *In preparation*.

[62] M. Baumgart et al. “Resummed Photon Spectra for WIMP Annihilation”. In: (2017). arXiv: 1712.07656 [hep-ph].

[63] W. Bednarek and M. Bartosik. “Gamma-rays from the pulsar wind nebulae”. In: *Astronomy & Astrophysics* 405 (July 2003), pp. 689–702. doi: 10.1051/0004-6361:20030593. arXiv: astro-ph/0304049 [astro-ph].

[64] A. Belikov, A. Montanari, and E. Moulin. *Unsupervised Non-Parametric Signal Disaggregation Using Bayesian Neural Networks*. May 2022, submitted to ICLR2023.

[65] A. V. Belikov, D. Hooper, and M. R. Buckley. “Searching For Dark Matter Subhalos In the Fermi-LAT Second Source Catalog”. In: *Phys. Rev. D* 86 (2012), p. 043504. doi: 10.1103/PhysRevD.86.043504. arXiv: 1111.2613 [hep-ph].

[66] A. V. Belikov and J. Silk. "Superexponential Cutoff as a Probe of Annihilating Dark Matter". In: *Phys. Rev. Lett.* 111.7 (2013), p. 071302. doi: 10.1103/PhysRevLett.111.071302. arXiv: 1304.5238 [astro-ph.HE].

[67] A. R. Bell. "The acceleration of cosmic rays in shock fronts - I." In: *Mon. Not. R. Astron. Soc.* 182 (Jan. 1978), pp. 147–156. doi: 10.1093/mnras/182.2.147.

[68] W. Benbow. "The status and performance of H.E.S.S". In: *AIP Conf. Proc.* 745.1 (2005). Ed. by F. A. Aharonian, Heinz J. Volk, and Dieter Horns, pp. 611–616. doi: 10.1063/1.1878471.

[69] M. Beneke, K. Urban, and M. Vollmann. "Matching resummed endpoint and continuum γ-ray spectra from dark-matter annihilation". In: (Mar. 2022). doi: 10.1016/j.physletb.2022.137248. arXiv: 2203.01692 [hep-ph].

[70] M. Beneke et al. "Energetic γ-rays from TeV scale dark matter annihilation resummed". In: (2018). arXiv: 1805.07367 [hep-ph].

[71] M. Beneke et al. "Precise yield of high-energy photons from Higgsino dark matter annihilation". In: (2019). arXiv: 1912.02034 [hep-ph].

[72] M. Beneke et al. "Relic density of wino-like dark matter in the MSSM". In: *JHEP* 03 (2016), p. 119. doi: 10.1007/JHEP03(2016)119. arXiv: 1601.04718 [hep-ph].

[73] M. Beneke et al. "Resummed photon spectrum from dark matter annihilation for intermediate and narrow energy resolution". In: (2019). arXiv: 1903.08702 [hep-ph].

[74] A. J. Benson. "The Normalization and Slope of the Dark Matter (Sub-)Halo Mass Function on Sub-Galactic Scales". In: *Mon. Not. Roy. Astron. Soc.* 493.1 (2020), pp. 1268–1276. doi: 10.1093/mnras/staa341. arXiv: 1911.04579 [astro-ph.GA].

[75] D. Berge, S. Funk, and J. Hinton. "Background Modelling in Very-High-Energy gamma-ray Astronomy". In: *Astron. Astrophys.* 466 (2007), pp. 1219–1229. doi: 10.1051/0004-6361:20066674. arXiv: astro-ph/0610959.

[76] L. Bergström. "Nonbaryonic dark matter: Observational evidence and detection methods". In: *Rept. Prog. Phys.* 63 (2000), p. 793. doi: 10.1088/0034-4885/63/5/2r3. arXiv: hep-ph/0002126.

[77] A Berlin and D. Hooper. "Stringent Constraints on the Dark Matter Annihilation Cross Section From Subhalo Searches with the Fermi Gamma-Ray Space Telescope". In: *Phys. Rev. D* 89.1 (2014), p. 016014. doi: 10.1103/PhysRevD.89.016014. arXiv: 1309.0525 [hep-ph].

[78] R. Bernabei et al. "First model independent results from DAMA/LIBRA-phase2". In: *Universe* 4.11 (2018). Ed. by Y. Aharonov et al., p. 116. doi: 10.3390/universe4110116.

[79] K. Bernlohr. “Simulation of Imaging Atmospheric Cherenkov Telescopes with CORSIKA and sim_telarray”. In: *Astropart. Phys.* 30 (2008), pp. 149–158. doi: 10.1016/j.astropartphys.2008.07.009. arXiv: 0808.2253 [astro-ph].

[80] K Bernlöhr et al. “The optical system of the HESS imaging atmospheric Cherenkov telescopes, Part 1: Layout and components of the system”. In: *Astropart. Phys.* 20 (2003), pp. 111–128. doi: 10.1016/S0927-6505(03)00171-3. arXiv: astro-ph/0308246.

[81] K. Bernlöhr et al. “Monte Carlo design studies for the Cherenkov Telescope Array”. In: *Astroparticle Physics* 43 (Mar. 2013), pp. 171–188. doi: 10.1016/j.astropartphys.2012.10.002. arXiv: 1210.3503 [astro-ph.IM].

[82] G. Bertone, D. Hooper, and J. Silk. “Particle dark matter: Evidence, candidates and constraints”. In: *Phys. Rept.* 405 (2005), pp. 279–390. doi: 10.1016/j.physrep.2004.08.031. arXiv: hep-ph/0404175 [hep-ph].

[83] G. Bertone, D. Hooper, and J. Silk. “Particle dark matter: evidence, candidates and constraints”. In: *Physics Reports* 405.5-6 (Jan. 2005), pp. 279–390. doi: 10.1016/j.physrep.2004.08.031. url: https://doi.org/10.1016%5C%2Fj.physrep.2004.08.031.

[84] B. Bertoni, D. Hooper, and T. Linden. “Examining The Fermi-LAT Third Source Catalog In Search Of Dark Matter Subhalos”. In: *JCAP* 12 (2015), p. 035. doi: 10.1088/1475-7516/2015/12/035. arXiv: 1504.02087 [astro-ph.HE].

[85] B. Bertoni, D. Hooper, and T. Linden. “Is The Gamma-Ray Source 3FGL J2212.5+0703 A Dark Matter Subhalo?” In: *JCAP* 05 (2016), p. 049. doi: 10.1088/1475-7516/2016/05/049. arXiv: 1602.07303 [astro-ph.HE].

[86] P. Narayana Bhat et al. “The Third Fermi gbm Gamma-ray Burst Catalog: the First six Years”. In: *Astrophys. J. Suppl.* 223.2 (2016), p. 28. doi: 10.3847/0067-0049/223/2/28. arXiv: 1603.07612 [astro-ph.HE].

[87] J. Billard et al. *Direct Detection of Dark Matter – APPEC Committee Report*. 2021. doi: 10.48550/ARXIV.2104.07634. url: https://arxiv.org/abs/2104.07634.

[88] E. Bingham et al. “Pyro: Deep Universal Probabilistic Programming”. In: *J. Mach. Learn. Res.* 20 (2019), 28:1–28:6. url: http://jmlr.org/papers/v20/18-403.html.

[89] J. Binney and S. Tremaine. *Galactic Dynamics: Second Edition*. 2008.

[90] S. Bird et al. “Did LIGO Detect Dark Matter?” In: *Phys. Rev. Lett.* 116 (20 May 2016), p. 201301. doi: 10.1103/PhysRevLett.116.201301. url: https://link.aps.org/doi/10.1103/PhysRevLett.116.201301.

[91] Bitran, M. et al. “A large scale CO survey of the Galactic center region”. In: *Astron. Astrophys. Suppl. Ser.* 125.1 (1997), pp. 99–138. doi: 10.1051/aas:1997214. url: https://doi.org/10.1051/aas:1997214.

[92] J. Bland-Hawthorn et al. “Fossil Imprint of a Powerful Flare at the Galactic Center along the Magellanic Stream”. In: *Astrophys. J.* 778.1, 58 (Nov. 2013), p. 58. doi: 10.1088/0004-637X/778/1/58. arXiv: 1309.5455 [astro-ph.GA].

[93] R. Blandford, D. Meier, and A. Readhead. “Relativistic Jets from Active Galactic Nuclei”. In: *Ann. Rev. Astron. Astrophys.* 57 (2019), pp. 467–509. doi: 10.1146/annurev-astro-081817-051948. arXiv: 1812.06025 [astro-ph.HE].

[94] R. Blandford, P. Simeon, and Y. Yuan. “Cosmic Ray Origins: An Introduction”. In: *Nucl. Phys. B Proc. Suppl.* 256-257 (2014). Ed. by Omar Tibolla et al., pp. 9–22. doi: 10.1016/j.nuclphysbps.2014.10.002. arXiv: 1409.2589 [astro-ph.HE].

[95] G. R. Blumenthal and R. J. Gould. “Bremsstrahlung, Synchrotron Radiation, and Compton Scattering of High-Energy Electrons Traversing Dilute Gases”. In: *Rev. Mod. Phys.* 42 (2 Apr. 1970), pp. 237–270. doi: 10.1103/RevModPhys.42.237. url: https://link.aps.org/doi/10.1103/RevModPhys.42.237.

[96] C. Blundell et al. “Weight Uncertainty in Neural Networks”. In: *Proceedings of the 32nd International Conference on International Conference on Machine Learning - Volume 37*. ICML’15. Lille, France: JMLR.org, 2015, pp. 1613–1622.

[97] C. Bœhm et al. “How high is the neutrino floor?” In: *Journal of Cosmology and Astroparticle Physics* 2019.01 (Jan. 2019), pp. 043–043. doi: 10.1088/1475-7516/2019/01/043. url: https://doi.org/10.1088%5C%2F1475-7516%5C%2F2019%5C%2F01%5C%2F043.

[98] J. Bolmont et al. “Search for Lorentz Invariance Violation effects with PKS 2155-304 flaring period in 2006 by H.E.S.S”. In: *44th Rencontres de Moriond on Very High Energy Phenomena in the Universe*. 2009, pp. 133–136. arXiv: 0904.3184 [gr-qc].

[99] V. Bonnivard et al. “CLUMPY: Jeans analysis, γ-ray and ν fluxes from dark matter (sub-)structures”. In: *Computer Physics Communications* 200 (Mar. 2016), pp. 336–349. doi: 10.1016/j.cpc.2015.11.012. arXiv: 1506.07628 [astro-ph.CO].

[100] S. Boran et al. “GW170817 Falsifies Dark Matter Emulators”. In: *Phys. Rev. D* 97.4 (2018), p. 041501. doi: 10.1103/PhysRevD.97.041501. arXiv: 1710.06168 [astro-ph.HE].

[101] S. Bottaro et al. “Closing the window on WIMP Dark Matter”. In: *Eur. Phys. J. C* 82.1 (2022), p. 31. doi: 10.1140/epjc/s10052-021-09917-9. arXiv: 2107.09688 [hep-ph].

[102] S. Bottaro et al. “The last Complex WIMPs standing”. In: (May 2022). arXiv: 2205.04486 [hep-ph].

[103] A. Boveia and C. Doglioni. “Dark Matter Searches at Colliders”. In: *Ann. Rev. Nucl. Part. Sci.* 68 (2018), pp. 429–459. doi: 10.1146/annurev-nucl-101917-021008. arXiv: 1810.12238 [hep-ex].

[104] H. Boyce et al. “Simultaneous X-Ray and Infrared Observations of Sagittarius A*’s Variability”. In: *The Astrophysical Journal* 871.2 (Jan. 2019), p. 161. issn: 1538-4357. doi: 10.3847/1538-4357/aaf71f. url: http://dx.doi.org/10.3847/1538-4357/aaf71f.

[105] P. Brun et al. “Searches for dark matter subhaloes with wide-field Cherenkov telescope surveys”. In: *Phys. Rev. D* 83 (2011), p. 015003. doi: 10.1103/PhysRevD.83.015003. arXiv: 1012.4766 [astro-ph.HE].

[106] J. S. Bullock. “Notes on the Missing Satellites Problem”. In: *arXiv e-prints*, arXiv:1009.4505 (Sept. 2010), arXiv:1009.4505. arXiv: 1009.4505 [astro-ph.CO].

[107] A. Burkert. “The Structure of dark matter halos in dwarf galaxies”. In: *Astrophys. J. Lett.* 447 (1995), p. L25. doi: 10.1086/309560. arXiv: astro-ph/9504041.

[108] A. Butter et al. “Classification of Fermi-LAT blazars with Bayesian neural networks”. In: *JCAP* 04.04 (2022), p. 023. doi: 10.1088/1475-7516/2022/04/023. arXiv: 2112.01403 [astro-ph.HE].

[109] C. Calcaneo-Roldan and B. Moore. “The Surface brightness of dark matter: Unique signatures of neutralino annihilation in the galactic halo”. In: *Phys. Rev. D* 62 (2000), p. 123005. doi: 10.1103/PhysRevD.62.123005. arXiv: astro-ph/0010056.

[110] F. Calore et al. “Realistic estimation for the detectability of dark matter subhalos with Fermi-LAT”. In: *Phys. Rev. D* 96.6 (2017), p. 063009. doi: 10.1103/PhysRevD.96.063009. arXiv: 1611.03503 [astro-ph.HE].

[111] Zhen Cao et al. “Ultrahigh-energy photons up to 1.4 petaelectronvolts from 12 γ-ray Galactic sources”. In: *Nature* 594.7861 (May 2021), pp. 33–36. doi: 10.1038/s41586-021-03498-z.

[112] B. Carr, F. Kuhnel, and M. Sandstad. “Primordial Black Holes as Dark Matter”. In: *Phys. Rev. D* 94.8 (2016), p. 083504. doi: 10.1103/PhysRevD.94.083504. arXiv: 1607.06077 [astro-ph.CO].

[113] R. Catena and P. Ullio. “A novel determination of the local dark matter density”. In: *JCAP* 08 (2010), p. 004. doi: 10.1088/1475-7516/2010/08/004. arXiv: 0907.0018 [astro-ph.CO].

[114] M. Cautun et al. “The milky way total mass profile as inferred from Gaia DR2”. In: *Mont. Not. Royal Astr. Soc.* 494.3 (Apr. 2020), pp. 4291–4313. doi: 10.1093/mnras/staa1017. arXiv: 1911.04557 [astro-ph.GA].

[115] J. A. R. Cembranos, V. Gammaldi, and A. L. Maroto. “Spectral study of the HESS J1745-290 gamma-ray source as dark matter signal”. In: *JCAP* 2013.4, 051 (Apr. 2013), p. 051. doi: 10.1088/1475-7516/2013/04/051. arXiv: 1302.6871 [astro-ph.CO].

[116] R. Chalme-Calvet, M. de Naurois, and J. -P. Tavernet. “Muon efficiency of the H.E.S.S. telescope”. In: *arXiv e-prints*, arXiv:1403.4550 (Mar. 2014), arXiv:1403.4550. arXiv: 1403.4550 [astro-ph.IM].

[117] R. Chalmé-Calvet. “Étalonnage du cinquième télescope de l’expérience H.E.S.S. et observation du Centre Galactique au delà de 30 GeV”. Theses. Université Pierre et Marie Curie - Paris VI, Nov. 2015. url: https://tel.archives-ouvertes.fr/tel-01307151.

[118] T. K. Chan et al. “The impact of baryonic physics on the structure of dark matter haloes: the view from the FIRE cosmological simulations”. In: *Mon. Not. Roy. Astron. Soc.* 454.3 (2015), pp. 2981–3001. doi: 10.1093/mnras/stv2165. arXiv: 1507.02282 [astro-ph.GA].

[119] S. Chandrasekhar. “XLVIII. The density of white dwarf stars”. In: *Journal of Astrophysics and Astronomy* 15 (1931), pp. 105–109.

[120] G. F. Chapline. “Cosmological effects of primordial black holes”. In: *Nature* 253.5489 (Jan. 1975), pp. 251–252. doi: 10.1038/253251a0.

[121] A. Charbonnier, C. Combet, and D. Maurin. “CLUMPY: A code for γ-ray signals from dark matter structures”. In: *Computer Physics Communications* 183.3 (Mar. 2012), pp. 656–668. doi: 10.1016/j.cpc.2011.10.017. arXiv: 1201.4728 [astro-ph.HE].

[122] A. Charbonnier et al. “Dark matter profiles and annihilation in dwarf spheroidal galaxies: prospectives for present and future γ-ray observatories - I. The classical dwarf spheroidal galaxies”. In: *Mont. Not. Royal Astr. Soc.* 418.3 (Dec. 2011), pp. 1526–1556. doi: 10.1111/j.1365-2966.2011.19387.x. arXiv: 1104.0412 [astro-ph.HE].

[123] P. Ciafaloni et al. “On the Importance of Electroweak Corrections for Majorana Dark Matter Indirect Detection”. In: *JCAP* 06 (2011), p. 018. doi: 10.1088/1475-7516/2011/06/018. arXiv: 1104.2996 [hep-ph].

[124] M. Cirelli et al. “PPPC 4 DM ID: A Poor Particle Physicist Cookbook for Dark Matter Indirect Detection”. In: *JCAP* 1103 (2011), p. 051. doi: 10.1088/1475-7516/2012/10/E01,10.1088/1475-7516/2011/03/051. arXiv: 1012.4515 [hep-ph].

[125] M. Cirelli, N. Fornengo, and A. Strumia. “Minimal dark matter”. In: *Nucl. Phys.* B753 (2006), pp. 178–194. doi: 10.1016/j.nuclphysb.2006.07.012. arXiv: hep-ph/0512090 [hep-ph].

[126] M. Cirelli, R. Franceschini, and A. Strumia. “Minimal Dark Matter predictions for galactic positrons, anti-protons, photons”. In: *Nucl. Phys.* B800 (2008), pp. 204–220. doi: 10.1016/j.nuclphysb.2008.03.013. arXiv: 0802.3378 [hep-ph].

[127] M. Cirelli and P. Panci. “Inverse Compton constraints on the Dark Matter e+e- excesses”. In: *Nucl. Phys. B* 821 (2009), pp. 399–416. doi: 10.1016/j.nuclphysb.2009.06.034. arXiv: 0904.3830 [astro-ph.CO].

[128] M. Cirelli and A. Strumia. “Minimal Dark Matter: Model and results”. In: *New J. Phys.* 11 (2009), p. 105005. doi: 10.1088/1367-2630/11/10/105005. arXiv: 0903.3381 [hep-ph].

[129] M. Cirelli, A. Strumia, and M. Tamburini. “Cosmology and Astrophysics of Minimal Dark Matter”. In: *Nucl. Phys.* B787 (2007), pp. 152–175. doi: 10.1016/j.nuclphysb.2007.07.023. arXiv: 0706.4071 [hep-ph].

[130] M. Cirelli et al. “Gamma ray tests of Minimal Dark Matter”. In: *JCAP* 1510.10 (2015), p. 026. doi: 10.1088/1475-7516/2015/10/026. arXiv: 1507.05519 [hep-ph].

[131] S. Clesse and J. Garcıa-Bellido. “The clustering of massive Primordial Black Holes as Dark Matter: measuring their mass distribution with Advanced LIGO”. In: *Phys. Dark Univ.* 15 (2017), pp. 142–147. doi: 10.1016/j.dark.2016.10.002. arXiv: 1603.05234 [astro-ph.CO].

[132] D. Clowe et al. “A Direct Empirical Proof of the Existence of Dark Matter”. In: *The Astrophysical Journal* 648.2 (Aug. 2006), pp. L109–L113. doi: 10.1086/508162. url: https://doi.org/10.1086%2F508162.

[133] R. T. Co, B. Sheff, and J. D. Wells. “Race to find split Higgsino dark matter”. In: *Phys. Rev. D* 105.3 (2022), p. 035012. doi: 10.1103/PhysRevD.105.035012. arXiv: 2105.12142 [hep-ph].

[134] R. T. Co et al. “Discovery potential for split supersymmetry with thermal dark matter”. In: (June 2022). arXiv: 2206.11912 [hep-ph].

[135] A. Coc and E. Vangioni. “Primordial nucleosynthesis”. In: *International Journal of Modern Physics E* 26.08 (Aug. 2017), p. 1741002. doi: 10.1142/s0218301317410026. url: https://doi.org/10.1142%5C%2Fs0218301317410026.

[136] H.E.S.S. Collaboration. *Data Quality Cuts in the H.E.S.S. database. Internal H.E.S.S. Collaboration web pages.* 2022.

[137] H.E.S.S. Collaboration. *Day shift duties in the H.E.S.S. Collaboration. Internal H.E.S.S. Collaboration web pages.* 2022.

[138] H.E.S.S. Collaboration. *H.E.S.S.* 2002. url: https://www.mpi-hd.mpg.de/hfm/HESS/pages/about/.

[139] H.E.S.S. Collaboration. *HAP reconstruction analysis chain. Internal H.E.S.S. Collaboration web pages.* 2022.

[140] H.E.S.S. Collaboration. *Search for the low-latitude Fermi Bubbles emission in the Inner Galaxy Survey*. June 2022, in preparation.

[141] H.E.S.S. Collaboration. *Total observation time during the H.E.S.S. II phase. Internal H.E.S.S. Collaboration web pages.* 2022.

[142] CMS Collaboration. *Search for dark matter in final states with an energetic jet, or a hadronically decaying W or Z boson using 12.9 fb^{-1} of data at $\sqrt{s}$ = 13 TeV.* https://cds.cern.ch/record/2205746/files/EXO-16-037-pas.pdf.

[143] J. Conrad and O. Reimer. "Indirect dark matter searches in gamma and cosmic rays". In: *Nature Phys.* 13.3 (2017), pp. 224–231. doi: 10.1038/nphys4049. arXiv: 1705.11165 [astro-ph.HE].

[144] R. Cornils et al. "The optical system of the HESS imaging atmospheric Cherenkov telescopes, Part 2: Mirror alignment and point spread function". In: *Astropart. Phys.* 20 (2003), pp. 129–143. doi: 10.1016/S0927-6505(03)00172-5. arXiv: astro-ph/0308247.

[145] J. Coronado-Blazquez et al. "Unidentified Gamma-ray Sources as Targets for Indirect Dark Matter Detection with the Fermi-Large Area Telescope". In: *JCAP* 07 (2019), p. 020. doi: 10.1088/1475-7516/2019/07/020. arXiv: 1906.11896 [astro-ph.HE].

[146] J. Coronado-Blázquez et al. "Spectral and spatial analysis of the dark matter subhalo candidates among Fermi Large Area Telescope unidentified sources". In: (Oct. 2019). doi: 10.1088/1475-7516/2019/11/045. arXiv: 1910.14429 [astro-ph.HE].

[147] G. Cowan et al. "Asymptotic formulae for likelihood-based tests of new physics". In: *European Physical Journal C* 71 (2011), p. 1554. doi: 10.1140/epjc/s10052-011-1554-0. eprint: 1007.1727 (physics.data-an).

[148] R. M. Crocker and F. Aharonian. "Fermi Bubbles: Giant, Multibillion-Year-Old Reservoirs of Galactic Center Cosmic Rays". In: *Phys. Rev. Lett.* 106 (10 Mar. 2011), p. 101102. doi: 10.1103/PhysRevLett.106.101102. url: https://link.aps.org/doi/10.1103/PhysRevLett.106.101102.

[149] Darren J. Croton. "Damn You, Little h! (Or, Real-World Applications of the Hubble Constant Using Observed and Simulated Data)". In: *Publications of the Astronomical Society of Australia* 30 (2013), e052. doi: 10.1017/pasa.2013.31.

[150] A. Cuoco, M. Krämer, and M. Korsmeier. "Novel Dark Matter Constraints from Antiprotons in Light of AMS-02". In: *Phys. Rev. Lett.* 118.19 (2017), p. 191102. doi: 10.1103/PhysRevLett.118.191102. arXiv: 1610.03071 [astro-ph.HE].

[151] Thompson D. et al. *Exploring the extreme universe with the Fermi Gamma-Ray Space Telescope*. https://physicstoday.scitation.org/doi/10.1063/PT.3.1787. 2012.

[152] *Dark Sectors and New, Light, Weakly-Coupled Particles*. 2013. doi: 10.48550/ARXIV.1311.0029. url: https://arxiv.org/abs/1311.0029.

[153] M. de Naurois and L. Rolland. "A high performance likelihood reconstruction of γ-rays for imaging atmospheric Cherenkov telescopes". In: *Astropart. Phys.* 32 (Dec. 2009), pp. 231–252. doi: 10.1016/j.astropartphys.2009.09.001. arXiv: 0907.2610 [astro-ph.IM].

[154] S. Depeweg et al. "Decomposition of Uncertainty in Bayesian Deep Learning for Efficient and Risk-sensitive Learning". In: *arXiv e-prints*, arXiv:1710.07283 (Oct. 2017), arXiv:1710.07283. arXiv: 1710.07283 [stat.ML].

[155] N. Deruelle and J.-P. Uzan. "605The Lambda-CDM model of the hot Big Bang". In: *Relativity in Modern Physics*. Oxford University Press, Aug. 2018. isbn: 9780198786399. doi: 10.1093/oso/9780198786399.003.0059. eprint: https://academic.oup.com/book/0/chapter/369328301/chapter-pdf/45462909/oso-9780198786399-chapter-59.pdf. url: https://doi.org/10.1093/oso/9780198786399.003.0059.

[156] G. Despali and S. Vegetti. "The impact of baryonic physics on the subhalo mass function and implications for gravitational lensing". In: *Mon. Not. Roy. Astron. Soc.* 469.2 (2017), pp. 1997–2010. doi: 10.1093/mnras/stx966. arXiv: 1608.06938 [astro-ph.GA].

[157] Devin, J. et al. "Impact of H.E.S.S. Lidar profiles on Crab Nebula data". In: *EPJ Web Conf.* 197 (2019), p. 01001. doi: 10.1051/epjconf/201919701001. url: https://doi.org/10.1051/epjconf/201919701001.

[158] M. Di Mauro. "Characteristics of the Galactic Center excess measured with 11 years of Fermi -LAT data". In: *Physical Review D* 103.6 (Mar. 2021). issn: 2470-0029. doi: 10.1103/physrevd.103.063029. url: http://dx.doi.org/10.1103/PhysRevD.103.063029.

[159] M. Di Mauro, M. Stref, and F. Calore. "Investigating the detection of dark matter subhalos as extended sources with Fermi-LAT". In: *Phys. Rev. D* 102.10 (2020), p. 103010. doi: 10.1103/PhysRevD.102.103010. arXiv: 2007.08535 [astro-ph.HE].

[160] G. Di Sciascio. “The LHAASO experiment: from Gamma-Ray Astronomy to Cosmic Rays”. In: *Nucl. Part. Phys. Proc.* 279-281 (2016). Ed. by Gabriella Cataldi, Ivan De Mitri, and Daniele Martello, pp. 166–173. doi: 10.1016/j.nuclphysbps.2016.10.024. arXiv: 1602.07600 [astro-ph.HE].

[161] J. Diemand et al. “Clumps and streams in the local dark matter distribution”. In: *Nature* 454 (2008), pp. 735–738. doi: 10.1038/nature07153. arXiv: 0805.1244 [astro-ph].

[162] A. Djannati-Ataı et al. “Probing Vela pulsar down to 20 GeV with H.E.S.S. II observations”. In: *6th International Symposium on High Energy Gamma-Ray Astronomy*. Vol. 1792. American Institute of Physics Conference Series. Jan. 2017, 040028, p. 040028. doi: 10.1063/1.4968932.

[163] G. Dobler et al. “The Fermi Haze: A Gamma-ray Counterpart to the Microwave Haze”. In: *Astrophys. J.* 717.2 (July 2010), pp. 825–842. doi: 10.1088/0004-637X/717/2/825. arXiv: 0910.4583 [astro-ph.HE].

[164] A Dolgov. “Massive sterile neutrinos as warm dark matter”. In: *Astroparticle Physics* 16.3 (Jan. 2002), pp. 339–344. doi: 10.1016/s0927-6505(01)00115-3. url: https://doi.org/10.1016%5C%2Fs0927-6505%5C%2801%5C%2900115-3.

[165] A. R. Duffy et al. “Impact of baryon physics on dark matter structures: a detailed simulation study of halo density profiles”. In: *Mont. Not. Royal Astr. Soc.* 405.4 (July 2010), pp. 2161–2178. doi: 10.1111/j.1365-2966.2010.16613.x. arXiv: 1001.3447 [astro-ph.CO].

[166] L. D Duffy and K. van Bibber. “Axions as dark matter particles”. In: *New Journal of Physics* 11.10 (Oct. 2009), p. 105008. doi: 10.1088/1367-2630/11/10/105008. url: https://doi.org/10.1088%5C%2F1367-2630%5C%2F11%2F10%2F105008.

[167] A. Einstein. “The Foundation of the General Theory of Relativity”. In: *Annalen Phys.* 49.7 (1916). Ed. by Jong-Ping Hsu and D. Fine, pp. 769–822. doi: 10.1002/andp.19163540702.

[168] F., Aharonian et al. “Exploring a SNR/molecular cloud association within HESS J1745-303”. In: *A&A* 483.2 (2008), pp. 509–517. doi: 10.1051/0004-6361:20079230. url: https://doi.org/10.1051/0004-6361:20079230.

[169] FACT. *HFACT - The First G-APD Cherenkov Telescope.* https://www.isdc.unige.ch/fact/. 2003.

[170] E. Fermi. “On the Origin of the Cosmic Radiation”. In: *Phys. Rev.* 75 (8 Apr. 1949), pp. 1169–1174. doi: 10.1103/PhysRev.75.1169. url: https://link.aps.org/doi/10.1103/PhysRev.75.1169.

[171] Fermi-LAT. *Fermi Gamma-Ray Space Telescope.* https://fgst.slac.stanford.edu/WhatIsLAT.asp. 2007.

[172] D. Fiacconi et al. “Young and turbulent: the early life of massive galaxy progenitors”. In: *Mon. Not. Roy. Astron. Soc.* 467.4 (2017), pp. 4080–4100. doi: 10.1093/mnras/stx335. arXiv: 1609.09499 [astro-ph.GA].

[173] B. D. Fields, K. Freese, and D. S. Graff. “Chemical Abundance Constraints on White Dwarfs as Halo Dark Matter”. In: *The Astrophysical Journal* 534.1 (May 2000), pp. 265–276. doi: 10.1086/308727. url: https://doi.org/10.1086/308727.

[174] *Formation of the large-scale structure in the Universe: filaments.* http://cosmicweb.uchicago.edu/filaments.html. Accessed: 2010-09-30.

[175] P. J. Fox, Graham D. Kribs, and Adam M. “Split Dirac Supersymmetry: An Ultraviolet Completion of Higgsino Dark Matter”. In: *Phys. Rev.* D90.7 (2014), p. 075006. doi: 10.1103/PhysRevD.90.075006. arXiv: 1405.3692 [hep-ph].

[176] P. J. Fox et al. “Missing energy signatures of dark matter at the LHC”. In: *Physical Review D* 85.5 (Mar. 2012). doi: 10.1103/physrevd.85.056011. url: https://doi.org/10.1103%2Fphysrevd.85.056011.

[177] A. Franceschini and G. Rodighiero. “The extragalactic background light revisited and the cosmic photon-photon opacity”. In: *Astron. Astrophys.* 603 (2017), A34. doi: 10.1051/0004-6361/201629684. arXiv: 1705.10256 [astro-ph.HE].

[178] A. Friedmann. “Über die Krümmung des Raumes”. In: *Zeitschrift fur Physik* 10 (Jan. 1922), pp. 377–386. doi: 10.1007/BF01332580.

[179] S. Funk et al. “The GeV-TeV Connection in Galactic γ-ray Sources”. In: *Astrophys. J.* 679.2 (May 2008), pp. 1299–1314. doi: 10.1086/587129. arXiv: 0710.1584 [astro-ph].

[180] S. Gabici. “Gamma-Ray Emission from Supernova Remnants and Surrounding Molecular Clouds”. In: *AIP Conf. Proc.* 1792.1 (2017), p. 020002. doi: 10.1063/1.4968887. arXiv: 1610.06234 [astro-ph.HE].

[181] Y. A. Gallant. “Associations of very high energy gamma-ray sources discovered by H.E.S.S. with pulsar wind nebulae”. In: *Astrophysics and Space Science* 309.1–4 (Apr. 2007), pp. 197–202. issn: 1572-946X. doi: 10.1007/s10509-007-9430-y. url: http://dx.doi.org/10.1007/s10509-007-9430-y.

[182] L. Gao et al. “The Phoenix Project: the Dark Side of Rich Galaxy Clusters”. In: *Mon. Not. Roy. Astron. Soc.* 425 (2012), p. 2169. doi: 10.1111/j.1365-2966.2012.21564.x. arXiv: 1201.1940 [astro-ph.CO].

[183] G. Giavitto et al. “A major electronics upgrade for the H.E.S.S. Cherenkov telescopes 1-4”. In: *34th International Cosmic Ray Conference*. Vol. ICRC2015. The Hague, Netherlands, July 2015, p. 996. doi: 10.22323/1.236.0996. url: https://hal.archives-ouvertes.fr/hal-03627388.

[184] C. Gordon and O. Macias. "Dark Matter and Pulsar Model Constraints from Galactic Center Fermi-LAT Gamma Ray Observations". In: *Phys. Rev.* D88.8 (2013). [Erratum: Phys. Rev.D89,no.4,049901(2014)], p. 083521. doi: 10.1103/PhysRevD.88.083521,10.1103/PhysRevD.89.049901. arXiv: 1306.5725 [astro-ph.HE].

[185] GRAVITY Collaboration et al. "Detection of the gravitational redshift in the orbit of the star S2 near the Galactic centre massive black hole ". In: *A&A* 615 (2018), p. L15. doi: 10.1051/0004-6361/201833718. url: https://doi.org/10.1051/0004-6361/201833718.

[186] Gravity Collaboration et al. "Detection of the gravitational redshift in the orbit of the star S2 near the Galactic centre massive black hole". In: *Astronomy & Astrophysics* 615, L15 (July 2018), p. L15. doi: 10.1051/0004-6361/201833718. arXiv: 1807.09409 [astro-ph.GA].

[187] Fulai Guo and W. G. Mathews. "The Fermi Bubbles. I. Possible Evidence for Recent AGN Jet Activity in the Galaxy". In: *Astrophys. J.* 756.2, 181 (Sept. 2012), p. 181. doi: 10.1088/0004-637X/756/2/181. arXiv: 1103.0055 [astro-ph.HE].

[188] J. Guy. "Premiers résultats de l'expérience HESS et étude du potentiel de détection de matière noire supersymétrique". Theses. Université Pierre et Marie Curie - Paris VI, May 2003. url: https://tel.archives-ouvertes.fr/tel-00003488.

[189] H.E.S.S. Collaboration et al. "First ground-based measurement of sub-20 GeV to 100 GeV s from the Vela pulsar with H.E.S.S. II". In: *A&A* 620 (2018), A66. doi: 10.1051/0004-6361/201732153. url: https://doi.org/10.1051/0004-6361/201732153.

[190] L. J. Hall, Y. Nomura, and S. Shirai. "Spread Supersymmetry with Wino LSP: Gluino and Dark Matter Signals". In: *JHEP* 01 (2013), p. 036. doi: 10.1007/JHEP01(2013)036. arXiv: 1210.2395 [hep-ph].

[191] F. Halzen et al. "Gamma rays and energetic particles from primordial black holes". In: 353.6347 (Oct. 1991), pp. 807–815. doi: 10.1038/353807a0.

[192] H. Perry Hatchfield et al. "CMZoom. II. Catalog of Compact Submillimeter Dust Continuum Sources in the Milky Way's Central Molecular Zone". In: 251.1, 14 (Nov. 2020), p. 14. doi: 10.3847/1538-4365/abb610. arXiv: 2009.05052 [astro-ph.GA].

[193] HAWC. *HAWC - The High-Altitude Water Cherenkov Gamma-Ray Observatory.* https://www.hawc-observatory.org/. 2022.

[194] S. Hawking. "Gravitationally collapsed objects of very low mass". In: *Mont. Not. Royal Astr. Soc.* 152 (Jan. 1971), p. 75. doi: 10.1093/mnras/152.1.75.

[195] S. W. Hawking. “Black hole explosions?” In: *Nature* 248.5443 (Mar. 1974), pp. 30–31. doi: 10.1038/248030a0.

[196] S. W. Hawking. “Particle Creation by Black Holes”. In: *Commun. Math. Phys.* 43 (1975). Ed. by G. W. Gibbons and S. W. Hawking. [Erratum: Commun.Math.Phys. 46, 206 (1976)], pp. 199–220. doi: 10.1007/BF02345020.

[197] A. Heger et al. “How Massive Single Stars End Their Life”. In: *Astrophys. J.* 591.1 (July 2003), pp. 288–300. doi: 10.1086/375341. arXiv: astro-ph/0212469 [astro-ph].

[198] L. Herold and D. Malyshev. “Hard and bright gamma-ray emission at the base of the Fermi bubbles”. In: *Astron. Astrophys.* 625 (2019), A110. doi: 10.1051/0004-6361/201834670. arXiv: 1904.01454 [astro-ph.HE].

[199] V. F. Hess. “Über Beobachtungen der durchdringenden Strahlung bei sieben Freiballonfahrten”. In: *Phys. Z.* 13 (1912), pp. 1084–1091.

[200] I. Heywood et al. “The 1.28 GHz MeerKAT Galactic Center Mosaic”. In: *The Astrophysical Journal* 925.2 (Feb. 2022), p. 165. issn: 1538-4357. doi: 10.3847/1538-4357/ac449a. url: http://dx.doi.org/10.3847/1538-4357/ac449a.

[201] A. M. Hillas. “Cerenkov Light Images of EAS Produced by Primary Gamma Rays and by Nuclei”. In: *19th International Cosmic Ray Conference (ICRC19), Volume 3*. Vol. 3. International Cosmic Ray Conference. Aug. 1985, p. 445.

[202] A. M. Hillas. “Differences between gamma-ray and hadronic showers”. In: *Space Sci. Rev.* 75 (1996). Ed. by H. J. Volk and F. A. Aharonian, pp. 17–30. doi: 10.1007/BF00195021.

[203] N. Hiroshima, S. Ando, and T. Ishiyama. “Modeling evolution of dark matter substructure and annihilation boost”. In: *Phys. Rev. D* 97.12 (2018), p. 123002. doi: 10.1103/PhysRevD.97.123002. arXiv: 1803.07691 [astro-ph.CO].

[204] J. Hisano et al. “Non-perturbative effect on thermal relic abundance of dark matter”. In: *Physics Letters B* 646.1 (Mar. 2007), pp. 34–38. doi: 10.1016/j.physletb.2007.01.012. url: https://doi.org/10.1016%5C%2Fj.physletb.2007.01.012.

[205] J. Hisano et al. “Non-perturbative effect on thermal relic abundance of dark matter”. In: *Phys. Lett.* B646 (2007), pp. 34–38. doi: 10.1016/j.physletb.2007.01.012. arXiv: hep-ph/0610249 [hep-ph].

[206] M. Hoffman et al. *Stochastic Variational Inference*. 2013. arXiv: 1206.7051 [stat.ML].

[207] W. Hofmann. “Status of the High Energy Stereoscopic System (H.E.S.S.) project”. In: *27th International Cosmic Ray Conference*. Aug. 2001.

[208] M. Holler et al. “A run-wise simulation and analysis framework for Imaging Atmospheric Cherenkov Telescope arrays”. In: *Astroparticle Physics* 123 (2020), p. 102491. issn: 0927-6505. doi: https://doi.org/10.1016/j.astropartphys.2020.102491. url: https://www.sciencedirect.com/science/article/pii/S0927650520300633.

[209] M. Holler et al. “Photon Reconstruction for H.E.S.S. Using a Semi-Analytical Model”. In: *PoS* ICRC2015 (2016), p. 980. doi: 10.22323/1.236.0980. arXiv: 1509.02896 [astro-ph.IM].

[210] D. Hooper. “The Density of Dark Matter in the Galactic Bulge and Implications for Indirect Detection”. In: *Phys. Dark Univ.* 15 (2017), pp. 53–56. doi: 10.1016/j.dark.2016.11.005. arXiv: 1608.00003 [astro-ph.HE].

[211] D. Hooper and L. Goodenough. “Dark Matter Annihilation in The Galactic Center As Seen by the Fermi Gamma Ray Space Telescope”. In: *Phys. Lett.* B697 (2011), pp. 412–428. doi: 10.1016/j.physletb.2011.02.029. arXiv: 1010.2752 [hep-ph].

[212] D. Hooper and T. Linden. “On The Origin Of The Gamma Rays From The Galactic Center”. In: *Phys. Rev.* D84 (2011), p. 123005. doi: 10.1103/PhysRevD.84.123005. arXiv: 1110.0006 [astro-ph.HE].

[213] P. F. Hopkins et al. “FIRE-2 simulations: physics versus numerics in galaxy formation”. In: *Monthly Notices of the Royal Astronomical Society* 480.1 (June 2018), pp. 800–863. issn: 0035-8711. doi: 10.1093/mnras/sty1690. eprint: https://academic.oup.com/mnras/article-pdf/480/1/800/25368704/sty1690.pdf. url: https://doi.org/10.1093/mnras/sty1690.

[214] A. Hryczuk, R. Iengo, and P. Ullio. “Relic densities including Sommerfeld enhancements in the MSSM”. In: *JHEP* 03 (2011), p. 069. doi: 10.1007/JHEP03(2011)069. arXiv: 1010.2172 [hep-ph].

[215] M. Hütten, C. Combet, and D. Maurin. “CLUMPY v3: γ-ray and ν signals from dark matter at all scales”. In: *Computer Physics Communications* 235 (Feb. 2019), pp. 336–345. doi: 10.1016/j.cpc.2018.10.001. arXiv: 1806.08639 [astro-ph.CO].

[216] M. Hütten et al. “γ-ray and ν Searches for Dark-Matter Subhalos in the Milky Way with a Baryonic Potential”. In: *Galaxies* 7.2 (May 2019), p. 60. doi: 10.3390/galaxies7020060. arXiv: 1904.10935 [astro-ph.HE].

[217] M. Hütten et al. “Dark matter substructure modelling and sensitivity of the Cherenkov Telescope Array to Galactic dark halos”. In: *JCAP* 2016.9, 047 (Sept. 2016), p. 047. doi: 10.1088/1475-7516/2016/09/047. arXiv: 1606.04898 [astro-ph.HE].

[218] F. Iocco, M. Pato, and G. Bertone. “Evidence for dark matter in the inner Milky Way”. In: *Nature Phys.* 11 (2015), pp. 245–248. doi: 10.1038/nphys3237. arXiv: 1502.03821 [astro-ph.GA].

[219] S. Jeff. *The Bremsstrahlung, Synchrotron and Compton effects as emission processes in Astrophysics.* http://www.jeffstanger.net/Astronomy/emissionprocesses.html. 2005.

[220] T. E. Jeltema, J. Kehayias, and S. Profumo. “Gamma Rays from Clusters and Groups of Galaxies: Cosmic Rays versus Dark Matter”. In: *Phys. Rev. D* 80 (2009), p. 023005. doi: 10.1103/PhysRevD.80.023005. arXiv: 0812.0597 [astro-ph].

[221] T. E. Jeltema and S. Profumo. “Fitting the gamma-ray spectrum from dark matter with DMFIT: GLAST and the galactic center region”. In: *JCAP* 2008.11, 003 (Nov. 2008), p. 003. doi: 10.1088/1475-7516/2008/11/003. arXiv: 0808.2641 [astro-ph].

[222] G. Jungman, M. Kamionkowski, and K. Griest. “Supersymmetric dark matter”. In: *Phys. Rept.* 267 (Mar. 1996), pp. 195–373. doi: 10.1016/0370-1573(95)00058-5. arXiv: hep-ph/9506380 [hep-ph].

[223] M. Kachelriess. “Lecture notes on high energy cosmic rays”. In: (Jan. 2008). arXiv: 0801.4376 [astro-ph].

[224] E. Kafexhiu et al. “Parametrization of gamma-ray production cross sections for p p interactions in a broad proton energy range from the kinematic threshold to PeV energies”. In: *Phys. Rev. Lett. D* 90.12, 123014 (Dec. 2014), p. 123014. doi: 10.1103/PhysRevD.90.123014. arXiv: 1406.7369 [astro-ph.HE].

[225] Th. Kaluza. “Zum Unitätsproblem der Physik”. In: *Sitzungsber. Preuss. Akad. Wiss. Berlin (Math. Phys.)* 1921 (1921), pp. 966–972. doi: 10.1142/S0218271818700017. arXiv: 1803.08616 [physics.hist-ph].

[226] M. Kamionkowski, S. M. Koushiappas, and M. Kuhlen. “Galactic Substructure and Dark Matter Annihilation in the Milky Way Halo”. In: *Phys. Rev. D* 81 (2010), p. 043532. doi: 10.1103/PhysRevD.81.043532. arXiv: 1001.3144 [astro-ph.GA].

[227] J. Kearney, N. Orlofsky, and A. Pierce. “Z boson mediated dark matter beyond the effective theory”. In: *Phys. Rev.* D95.3 (2017), p. 035020. doi: 10.1103/PhysRevD.95.035020. arXiv: 1611.05048 [hep-ph].

[228] A. Kendall and Y. Gal. “What Uncertainties Do We Need in Bayesian Deep Learning for Computer Vision?” In: *arXiv e-prints*, arXiv:1703.04977 (Mar. 2017), arXiv:1703.04977. arXiv: 1703.04977 [cs.CV].

[229] W. O. Kermack and W. H. McCrea. “On Milne’s theory of world structure”. In: *Mont. Not. Royal Astr. Soc.* 93 (May 1933), pp. 519–529. doi: 10.1093/mnras/93.7.519.

[230] M. P. Kertzman and G. H. Sembroski. “Computer simulation methods for investigating the detection characteristics of TeV air Cherenkov telescopes”. In: *Nucl. Instrum. Meth. A* 343 (1994), pp. 629–643. doi: 10.1016/0168-9002(94)90247-X.

[231] D. Khangulyan, F. A. Aharonian, and S. R. Kelner. “Simple Analytical Approximations for Treatment of Inverse Compton Scattering of Relativistic Electrons in the Blackbody Radiation Field”. In: *Astrophys. J.* 783.2, 100 (Mar. 2014), p. 100. doi: 10.1088/0004-637X/783/2/100. arXiv: 1310.7971 [astro-ph.HE].

[232] M. Yu. Khlopov. “Primordial Black Holes”. In: *Res. Astron. Astrophys.* 10 (2010), pp. 495–528. doi: 10.1088/1674-4527/10/6/001. arXiv: 0801.0116 [astro-ph].

[233] D. P. Kingma and J. Ba. “Adam: A Method for Stochastic Optimization”. In: *arXiv e-prints*, arXiv:1412.6980 (Dec. 2014), arXiv:1412.6980. arXiv: 1412.6980 [cs.LG].

[234] E. W. Kolb and R. Slansky. “Dimensional Reduction in the Early Universe: Where Have the Massive Particles Gone?” In: *Phys. Lett. B* 135 (1984), p. 378. doi: 10.1016/0370-2693(84)90298-3.

[235] S. M. Koushiappas, A. R. Zentner, and T. P. Walker. “The observability of gamma-rays from neutralino annihilations in Milky Way substructure”. In: *Phys. Rev. D* 69 (2004), p. 043501. doi: 10.1103/PhysRevD.69.043501. arXiv: astro-ph/0309464.

[236] F. Krayzel et al. “Improved sensitivity of H.E.S.S.-II through the fifth telescope focus system”. In: *33rd International Cosmic Ray Conference (ICRC2013)*. In Proceedings of the 33rd International Cosmic Ray Conference (ICRC2013), Rio de Janeiro (Brazil). Rio de Janeiro, Brazil, July 2013. url: http://hal.in2p3.fr/in2p3-00907589.

[237] T. Lacroix et al. “Connecting the new H.E.S.S. diffuse emission at the Galactic Center with the Fermi GeV excess: A combination of millisecond pulsars and heavy dark matter?” In: *Physical Review D* 94.12 (2016), p. 123008. doi: 10.1103/PhysRevD.94.123008. url: https://hal.archives-ouvertes.fr/hal-01554323.

[238] T. Lacroix et al. “Connecting the new H.E.S.S. diffuse emission at the Galactic Center with the Fermi GeV excess: A combination of millisecond pulsars and heavy dark matter?” In: 94.12, 123008 (Dec. 2016), p. 123008. doi: 10.1103/PhysRevD.94.123008. arXiv: 1603.05977 [astro-ph.HE].

[239] K. R. Lang. *NASA's Cosmos - The Material Between the Stars.* https://ase.tufts.edu/cosmos/view_images.asp?id=50. 2010.

[240] M. Lattanzi and J. I. Silk. "Can the WIMP annihilation boost factor be boosted by the Sommerfeld enhancement?" In: *Phys. Rev. D* 79 (2009), p. 083523. doi: 10.1103/PhysRevD.79.083523. arXiv: 0812.0360 [astro-ph].

[241] C. J. Law et al. "Green Bank Telescope Multiwavelength Survey of the Galactic Center Region". In: *The Astrophysical Journal Supplement Series* 177.1 (May 2008), pp. 255–274. issn: 1538-4365. doi: 10.1086/533587. url: http://dx.doi.org/10.1086/533587.

[242] O. Le Blanc et al. "Towards f inal characteris ation and performance of the GCT prototype telescope structure for the Cherenkov Telescope Array". In: *35th International Cosmic Ray Conference (ICRC2017)*. Vol. 301. International Cosmic Ray Conference. Jan. 2017, 836, p. 836. arXiv: 1709.03954 [astro-ph.IM].

[243] V. Lefranc. "Recherche de matière noire, observation du centre galactique avec H.E.S.S.et modernisation des caméras de H.E.S.S. I". Theses. Université Paris-Saclay, May 2016. url: https://tel.archives-ouvertes.fr/tel-01374541.

[244] V. Lefranc et al. "Prospects for Annihilating Dark Matter in the inner Galactic halo by the Cherenkov Telescope Array". In: *Phys. Rev.* D91.12 (2015), p. 122003. doi: 10.1103/PhysRevD.91.122003. arXiv: 1502.05064 [astro-ph.HE].

[245] G. Lemaıtre. "Un Univers homogène de masse constante et de rayon croissant rendant compte de la vitesse radiale des nébuleuses extra-galactiques". In: *Annales de la Société Scientifique de Bruxelles* 47 (Jan. 1927), pp. 49–59.

[246] J. D. Lewin and P. F. Smith. "Review of mathematics, numerical factors, and corrections for dark matter experiments based on elastic nuclear recoil". In: *Astropart. Phys.* 6 (1996), pp. 87–112. doi: 10.1016/S0927-6505(96)00047-3.

[247] T.-P. Li and Y.-Q. Ma. "Analysis methods for results in gamma-ray astronomy". In: *Astrophys. J.* 272 (Sept. 1983), pp. 317–324. doi: 10.1086/161295.

[248] S. Liem et al. "Effective field theory of dark matter: a global analysis". In: *JHEP* 09 (2016), p. 077. doi: 10.1007/JHEP09(2016)077. arXiv: 1603.05994 [hep-ph].

[249] F. List et al. "Galactic Center Excess in a New Light: Disentangling the γ-Ray Sky with Bayesian Graph Convolutional Neural Networks". In: *Phys. Rev. Lett.* 125 (24 Dec. 2020), p. 241102. doi: 10.1103/PhysRevLett.125.241102. url: https://link.aps.org/doi/10.1103/PhysRevLett.125.241102.

[250] Hu Liu. "Study of Longitudinal Development of Cosmic-Ray Induced Air Showers with LHAASO-WFCTA". In: *Proceedings of 37th International Cosmic Ray Conference — PoS(ICRC2021)*. Vol. 395. 2021, p. 245. doi: 10.22323/1.395.0245.

[251] Siming Liu et al. "Stochastic Acceleration in the Galactic Center HESS Source". In: *The Astrophysical Journal* 647.2 (Aug. 2006), pp. 1099–1105. doi: 10.1086/505171. url: https://doi.org/10.1086/505171.

[252] M. S. Longair. *High energy astrophysics. Vol.2: Stars, the galaxy and the interstellar medium*. Vol. 2. 1994.

[253] M. Lorentz and P. Brun. "Limits on Lorentz invariance violation at the Planck energy scale from H.E.S.S. spectral analysis of the blazar Mrk 501". In: *EPJ Web Conf.* 136 (2017). Ed. by A. Morselli, A. Capone, and G. Rodriguez Fernandez, p. 03018. doi: 10.1051/epjconf/201713603018. arXiv: 1606.08600 [astro-ph.HE].

[254] Bustamante M. et al. *High energy cosmic-ray acceleration*. https://cds.cern.ch/record/1249755/files/p533.pdf. 2010.

[255] J. H. MacGibbon, B. J. Carr, and D. N. Page. "Do Evaporating Black Holes Form Photospheres?" In: *Phys. Rev. D* 78 (2008), p. 064043. doi: 10.1103/PhysRevD.78.064043. arXiv: 0709.2380 [astro-ph].

[256] O. Macias and C. Gordon. "Contribution of cosmic rays interacting with molecular clouds to the Galactic Center gamma-ray excess". In: *Phys. Rev. D* 89.6 (2014), p. 063515. doi: 10.1103/PhysRevD.89.063515. arXiv: 1312.6671 [astro-ph.HE].

[257] O. Macias et al. "Cherenkov Telescope Array sensitivity to the putative millisecond pulsar population responsible for the Galactic Centre excess". In: *Mon. Not. Roy. Astron. Soc.* 506.2 (2021), pp. 1741–1760. doi: 10.1093/mnras/stab1450. arXiv: 2102.05648 [astro-ph.HE].

[258] D. J. C. MacKay. "A Practical Bayesian Framework for Backpropagation Networks". In: *Neural Computation* 4.3 (May 1992), pp. 448–472. issn: 0899-7667. doi: 10.1162/neco.1992.4.3.448. eprint: https://direct.mit.edu/neco/article-pdf/4/3/448/812348/neco.1992.4.3.448.pdf. url: https://doi.org/10.1162/neco.1992.4.3.448.

[259] MAGIC. *First time detection of a GRB at sub-TeV energies; MAGIC detects the GRB 190114C*. https://astronomerstelegram.org/?read=12390. 2019.

[260] MAGIC. *MAGIC - Major Atmospheric Gamma-ray Imaging Cherenkov Telescope*. http://www.magic.iac.es/. 2003.

[261] R. Mahbubani and L. Senatore. "The Minimal model for dark matter and unification". In: *Phys. Rev.* D73 (2006), p. 043510. doi: 10.1103/PhysRevD.73.043510. arXiv: hep-ph/0510064 [hep-ph].

[262] L. Maraschi, G. Ghisellini, and A. Celotti. “On the broad band energy distribution of blazars.” In: *Multi-Wavelength Continuum Emission of AGN*. Ed. by T. Courvoisier and A. Blecha. Vol. 159. Jan. 1994, pp. 221–232.

[263] A. Marciano. *WIMP Dark Matter Searches With the ATLAS Detector at the LHC*. https://www.frontiersin.org/articles/10.3389/fphy.2019.00075/full. 2019.

[264] M. Markevitch. *Chandra observation of the most interesting cluster in the Universe*. 2005. doi: 10.48550/ARXIV.ASTRO-PH/0511345. url: https://arxiv.org/abs/astro-ph/0511345.

[265] M. Markevitch et al. “Direct Constraints on the Dark Matter Self-Interaction Cross Section from the Merging Galaxy Cluster 1E 0657-56”. In: *The Astrophysical Journal* 606.2 (May 2004), pp. 819–824. doi: 10.1086/383178. url: https://doi.org/10.1086%2F383178.

[266] University of Maryland. *Rotation-Powered Pulsars*. 2018. url: https://www.astro.umd.edu/~miller/teaching/astr498/lecture18.pdf.

[267] R. Massey, T. Kitching, and J. Richard. “The dark matter of gravitational lensing”. In: *Rept. Prog. Phys.* 73 (2010), p. 086901. doi: 10.1088/0034-4885/73/8/086901. arXiv: 1001.1739 [astro-ph.CO].

[268] J. R. Mattox et al. “The Likelihood Analysis of EGRET Data”. In: *Astrophys. J.* 461 (Apr. 1996), p. 396. doi: 10.1086/177068.

[269] P. J. McMillan. “Mass models of the Milky Way”. In: *Mont. Not. Royal Astr. Soc.* 414.3 (May 2011), pp. 2446–2457. doi: 10.1111/j.1365-2966.2011.18564.x. arXiv: 1102.4340 [astro-ph.GA].

[270] P. J. McMillan. “The mass distribution and gravitational potential of the Milky Way”. In: *Mont. Not. Royal Astr. Soc.* 465.1 (Feb. 2017), pp. 76–94. doi: 10.1093/mnras/stw2759. arXiv: 1608.00971 [astro-ph.GA].

[271] P. Mehta et al. “A high-bias, low-variance introduction to Machine Learning for physicists”. In: *Physics Reports* 810 (May 2019), pp. 1–124. doi: 10.1016/j.physrep.2019.03.001. arXiv: 1803.08823 [physics.comp-ph].

[272] A. Merle. “keV neutrino model building”. In: *International Journal of Modern Physics D* 22.10 (Aug. 2013), p. 1330020. doi: 10.1142/s0218271813300206. url: https://doi.org/10.1142%5C%2Fs0218271813300206.

[273] M. et al. Meyer. *Future constraints of dark matter effective field theories and simplified models with the Cherenkov Telescope Array.* https://indico.cern.ch/event/623880/contributions/2523949/attachments/1438677/2213569/mmeyer_cta_eft.pdf.

[274] M. Milgrom. “A modification of the Newtonian dynamics as a possible alternative to the hidden mass hypothesis.” In: *Astrophys. J.* 270 (July 1983), pp. 365–370. doi: 10.1086/161130.

[275] R. A. Millikan and G. H. Cameron. "The Origin of the Cosmic Rays". In: *Phys. Rev.* 32 (4 Oct. 1928), pp. 533–557. doi: 10.1103/PhysRev.32.533. url: https://link.aps.org/doi/10.1103/PhysRev.32.533.

[276] N. Mirabal et al. "3FGL Demographics Outside the Galactic Plane using Supervised Machine Learning: Pulsar and Dark Matter Subhalo Interpretations". In: *Astrophys. J.* 825.1 (2016), p. 69. doi: 10.3847/0004-637X/825/1/69. arXiv: 1605.00711 [astro-ph.HE].

[277] A. Mitridate et al. "Cosmological Implications of Dark Matter Bound States". In: *JCAP* 1705.05 (2017), p. 006. doi: 10.1088/1475-7516/2017/05/006. arXiv: 1702.01141 [hep-ph].

[278] R N Mohapatra et al. "Theory of neutrinos: a white paper". In: *Reports on Progress in Physics* 70.11 (Oct. 2007), pp. 1757–1867. doi: 10.1088/0034-4885/70/11/r02. url: https://doi.org/10.1088%2F0034-4885%2F70%2F11%2Fr02.

[279] Á. Moliné et al. "Characterization of subhalo structural properties and implications for dark matter annihilation signals". In: *Mon. Not. Roy. Astron. Soc.* 466.4 (2017), pp. 4974–4990. doi: 10.1093/mnras/stx026. arXiv: 1603.04057 [astro-ph.CO].

[280] Á. Moliné et al. "Characterization of subhalo structural properties and implications for dark matter annihilation signals". In: *Mont. Not. Royal Astr. Soc.* 466.4 (Apr. 2017), pp. 4974–4990. doi: 10.1093/mnras/stx026. arXiv: 1603.04057 [astro-ph.CO].

[281] P. Mollitor, E. Nezri, and R. Teyssier. "Baryonic and dark matter distribution in cosmological simulations of spiral galaxies". In: *Mon. Not. Roy. Astron. Soc.* 447.2 (2015), pp. 1353–1369. doi: 10.1093/mnras/stu2466. arXiv: 1405.4318 [astro-ph.GA].

[282] A. Montanari, E. Moulin, and N. L. Rodd. "Towards the ultimate reach of current Imaging Atmospheric Cherenkov Telescopes to TeV Dark Matter". In: (Oct. 2022). arXiv: 2210.03140 [astro-ph.HE].

[283] M. Morris and E. Serabyn. "The Galactic Center Environment". In: *Annual Review of Astronomy and Astrophysics* 34 (Jan. 1996), pp. 645–702. doi: 10.1146/annurev.astro.34.1.645.

[284] I. V. Moskalenko and A. W. Strong. "Production and Propagation of Cosmic-Ray Positrons and Electrons". In: *The Astrophysical Journal* 493.2 (Feb. 1998), pp. 694–707. issn: 1538-4357. doi: 10.1086/305152. url: http://dx.doi.org/10.1086/305152.

[285] E. Moulin et al. "Science with the Cherenkov Telescope Array: Dark Matter Programme". In: *Science with the Cherenkov Telescope Array*. World Scientific, 2019, pp. 45–81. doi: 10.1142/9789813270091_0004.

[286] E. Moulin et al. “Search for TeV emission from the Fermi Bubbles at low Galactic latitudes with H.E.S.S. inner Galaxy survey observations”. In: *PoS* ICRC2021 (2021), p. 791. arXiv: 2108.10028 [astro-ph.HE].

[287] S. Nakashima et al. “Discovery of the recombining plasma in the South of the Galactic Center: a relic of the past Galactic Center activity?” In: *The Astrophysical Journal* 773.1 (May 2013), p. 20. issn: 1538-4357. doi: 10.1088/0004-637x/773/1/20. url: http://dx.doi.org/10.1088/0004-637X/773/1/20.

[288] NASA. *The Cosmic Distance scale*. 2020. url: https://imagine.gsfc.nasa.gov/features/cosmic/nearest_star_info.html.

[289] NASASpitzer. *Spitzer View of the Center of the Milky Way*. https://www.spitzer.caltech.edu/image/ssc2006-02a1-spitzer-view-of-the-center-of-the-milky-way. 2006.

[290] C. L. Naumann et al. “New electronics for the Cherenkov Telescope Array (NECTAr)”. In: *Nucl. Instrum. Meth. A* 695 (2012). Ed. by P. Bourgeois et al., pp. 44–51. doi: 10.1016/j.nima.2011.11.008.

[291] M. de Naurois and L. Rolland. “A high performance likelihood reconstruction of γ-rays for imaging atmospheric Cherenkov telescopes”. In: *Astroparticle Physics* 32.5 (Dec. 2009), pp. 231–252. issn: 0927-6505. doi: 10.1016/j.astropartphys.2009.09.001. url: http://dx.doi.org/10.1016/j.astropartphys.2009.09.001.

[292] J. F. Navarro, C. S. Frenk, and S. D. M. White. “A Universal density profile from hierarchical clustering”. In: *Astrophys. J.* 490 (1997), pp. 493–508. doi: 10.1086/304888. arXiv: astro-ph/9611107 [astro-ph].

[293] *New Hubble image of galaxy cluster Abell 1689*. https://esahubble.org/news/heic1317/. Accessed: 2010-09-30.

[294] H. P. Nilles. “Supersymmetry, Supergravity and Particle Physics”. In: *Phys. Rept.* 110 (1984), pp. 1–162. doi: 10.1016/0370-1573(84)90008-5.

[295] A. V. Olinto. “Ultrahigh-energy cosmic rays: The Theoretical challenge”. In: *Phys. Rept.* 333 (2000), pp. 329–348. doi: 10.1016/S0370-1573(00)00028-4. arXiv: astro-ph/0002006.

[296] G. Ovanesyan, T. R. Slatyer, and I. W. Stewart. “Heavy Dark Matter Annihilation from Effective Field Theory”. In: *Phys. Rev. Lett.* 114.21 (2015), p. 211302. doi: 10.1103/PhysRevLett.114.211302. arXiv: 1409.8294 [hep-ph].

[297] G. Ovanesyan et al. “One-loop correction to heavy dark matter annihilation”. In: *Phys. Rev.* D95.5 (2017), p. 055001. doi: 10.1103/PhysRevD.95.055001. arXiv: 1612.04814 [hep-ph].

[298] D. Pacini. “La radiazione penetrante alla superficie ed in seno alle acque”. In: *Il Nuovo Cimento* 3.1 (Dec. 1912), pp. 93–100. doi: 10.1007/BF02957440. arXiv: 1002.1810 [physics.hist-ph].

[299] D. N. Page. “Particle emission rates from a black hole: Massless particles from an uncharged, nonrotating hole”. In: *Phys. Rev. D* 13 (2 Jan. 1976), pp. 198–206. doi: 10.1103/PhysRevD.13.198. url: https://link.aps.org/doi/10.1103/PhysRevD.13.198.

[300] J. Paisley, D. Blei, and M. I. Jordan. “The Stick-Breaking Construction of the Beta Process as a Poisson Process”. In: *arXiv e-prints*, arXiv:1109.0343 (Sept. 2011), arXiv:1109.0343. arXiv: 1109.0343 [math.ST].

[301] R. D. Parsons and J. A. Hinton. “A Monte Carlo Template based analysis for Air-Cherenkov Arrays”. In: *Astropart. Phys.* 56 (2014), pp. 26–34. doi: 10.1016/j.astropartphys.2014.03.002. arXiv: 1403.2993 [astro-ph.IM].

[302] A. Paszke et al. “PyTorch: An Imperative Style, High-Performance Deep Learning Library”. In: *Advances in Neural Information Processing Systems 32*. Curran Associates, Inc., 2019, pp. 8024–8035. url: http://papers.neurips.cc/paper/9015-pytorch-an-imperative-style-high-performance-deep-learning-library.pdf.

[303] T. Pearce et al. “High-Quality Prediction Intervals for Deep Learning: A Distribution-Free, Ensembled Approach”. In: *arXiv e-prints*, arXiv:1802.07167 (Feb. 2018), arXiv:1802.07167. arXiv: 1802.07167 [stat.ML].

[304] R. D. Peccei and H. R. Quinn. “CP Conservation in the Presence of Instantons”. In: *Phys. Rev. Lett.* 38 (1977), pp. 1440–1443. doi: 10.1103/PhysRevLett.38.1440.

[305] M. Pecimotika. “Transmittance Simulations for the Atmosphere with Clouds”. PhD thesis. Nov. 2018. doi: 10.13140/RG.2.2.34140.95361/1.

[306] P. J. E. Peebles. *The large-scale structure of the universe*. 1980.

[307] J. Penarrubia, J. F. Navarro, and A. W. McConnachie. “The Tidal Evolution of Local Group Dwarf Spheroidals”. In: *Astrophys. J.* 673 (2008), p. 226. doi: 10.1086/523686. arXiv: 0708.3087 [astro-ph].

[308] A. A. Penzias and R. W. Wilson. “A Measurement of Excess Antenna Temperature at 4080 Mc/s.” In: *Astrophys. J.* 142 (July 1965), pp. 419–421. doi: 10.1086/148307.

[309] “Planck 2018 results. VI. Cosmological parameters”. In: *Astronomy & Astrophysics* 641 (Sept. 2020), A6. doi: 10.1051/0004-6361/201833910. url: https://doi.org/10.48550/arXiv.1807.06209.

[310] Planck Collaboration et al. “Planck intermediate results. IX. Detection of the Galactic haze with Planck”. In: *Astronomy & Astrophysics* 554, A139 (May 2013), A139. doi: 10.1051/0004-6361/201220271. arXiv: 1208.5483 [astro-ph.GA].

[311] G. Ponti et al. “An X-ray chimney extending hundreds of parsecs above and below the Galactic Centre”. In: *Nature* 567.7748 (Mar. 2019), pp. 347–350. doi: 10.1038/s41586-019-1009-6. arXiv: 1904.05969 [astro-ph.HE].

[312] D. Porquet, A. Decourchelle, and R. S. Warwick. “XMM-Newton spectral analysis of the Pulsar Wind Nebula within the composite SNR-G0.9+0.1”. In: *Astronomy & Astrophysics* 401 (Apr. 2003), pp. 197–203. doi: 10.1051/0004-6361:20021670. arXiv: astro-ph/0211426 [astro-ph].

[313] M. Portail et al. “Dynamical modelling of the galactic bulge and bar: the Milky Way’s pattern speed, stellar and dark matter mass distribution”. In: *Mon. Not. Roy. Astron. Soc.* 465.2 (2017), pp. 1621–1644. doi: 10.1093/mnras/stw2819. arXiv: 1608.07954 [astro-ph.GA].

[314] T. A. Porter et al. “Inverse Compton Origin of the Hard X-Ray and Soft Gamma-Ray Emission from the Galactic Ridge”. In: *Astrophys. J.* 682.1 (July 2008), pp. 400–407. doi: 10.1086/589615. arXiv: 0804.1774 [astro-ph].

[315] J. Prada et al. “Dark matter halo shapes in the Auriga simulations”. In: *Mont. Not. Royal Astr. Soc.* 490.4 (Dec. 2019), pp. 4877–4888. doi: 10.1093/mnras/stz2873. arXiv: 1910.04045 [astro-ph.GA].

[316] P. Predehl et al. “Detection of large-scale X-ray bubbles in the Milky Way halo”. In: *Nature* 588.7837 (Dec. 2020), pp. 227–231. issn: 1476-4687. doi: 10.1038/s41586-020-2979-0. url: http://dx.doi.org/10.1038/s41586-020-2979-0.

[317] J. R. Primack. *Dark Matter and Structure Formation in the Universe*. 1997. doi: 10.48550/ARXIV.ASTRO-PH/9707285. url: https://arxiv.org/abs/astro-ph/9707285.

[318] J. R. Primack and M. A. K. Gross. “Hot dark matter in cosmology”. In: (July 2000). Ed. by D. O. Caldwell, pp. 287–308. arXiv: astro-ph/0007165.

[319] S. Profumo. “Hunting the lightest lightest neutralinos”. In: *Phys. Rev. D* 78 (2008), p. 023507. doi: 10.1103/PhysRevD.78.023507. arXiv: 0806.2150 [hep-ph].

[320] S. Profumo and T. E. Jeltema. “Extragalactic Inverse Compton Light from Dark Matter Annihilation and the Pamela Positron Excess”. In: *JCAP* 07 (2009), p. 020. doi: 10.1088/1475-7516/2009/07/020. arXiv: 0906.0001 [astro-ph.CO].

[321] F. S. Queiroz, C. E. Yaguna, and C. Weniger. “Gamma-ray Limits on Neutrino Lines”. In: *JCAP* 05 (2016), p. 050. doi: 10.1088/1475-7516/2016/05/050. arXiv: 1602.05966 [hep-ph].

[322] J.I. Read. “The Local Dark Matter Density”. In: *J. Phys. G* 41 (2014), p. 063101. doi: 10.1088/0954-3899/41/6/063101. arXiv: 1404.1938 [astro-ph.GA].

[323] L. Rinchiuso et al. “Hunting for Heavy Winos in the Galactic Center”. In: *Phys. Rev.* D98.12 (2018), p. 123014. doi: 10.1103/PhysRevD.98.123014. arXiv: 1808.04388 [astro-ph.HE].

[324] L. Rinchiuso et al. “Prospects for detecting heavy WIMP dark matter with the Cherenkov Telescope Array: The Wino and Higgsino”. In: *Phys. Rev. D* 103.2 (2021), p. 023011. doi: 10.1103/PhysRevD.103.023011. arXiv: 2008.00692 [astro-ph.HE].

[325] H. P. Robertson. “Kinematics and World-Structure. 3”. In: *Astrophys. J.* 83 (1936), pp. 257–271. doi: 10.1086/143726.

[326] W. A. Rolke, A. M. López, and J. Conrad. “Limits and confidence intervals in the presence of nuisance parameters”. In: *Nuclear Instruments and Methods in Physics Research Section A: Accelerators, Spectrometers, Detectors and Associated Equipment* 551.2-3 (Oct. 2005), pp. 493–503. issn: 0168-9002. doi: 10.1016/j.nima.2005.05.068. url: http://dx.doi.org/10.1016/j.nima.2005.05.068.

[327] V. C. Rubin and Jr. Ford W. K. “Rotation of the Andromeda Nebula from a Spectroscopic Survey of Emission Regions”. In: *Astrophys. J.* 159 (Feb. 1970), p. 379. doi: 10.1086/150317.

[328] E. L. Ruiz-Velasco and the H.E.S.S. Collaboration. *Discovery of Late-Time VHE Emission from a Gamma-ray Burst Afterglow by H.E.S.S.* 2019.

[329] G. B. Rybicki and A. P. Lightman. *Radiative Processes in Astrophysics*. 1986.

[330] Hiromasa S. et al. “Uniform Distribution of the Extremely Overionized Plasma Associated with the Supernova Remnant G359.1-0.5”. In: *The Astrophysical Journal* 893.2 (Apr. 2020), p. 147. doi: 10.3847/1538-4357/ab80ba. url: https://doi.org/10.3847/1538-4357/ab80ba.

[331] P. Salucci. “The mass distribution in spiral galaxies”. In: *IAU Symp.* 244 (2008). Ed. by J. I. Davies and M. J. Disney, pp. 53–62. doi: 10.1017/S174392130701383X. arXiv: 0707.4370 [astro-ph].

[332] T. Sawala et al. “The APOSTLE simulations: solutions to the Local Group’s cosmic puzzles”. In: *Mon. Not. Roy. Astron. Soc.* 457.2 (2016), pp. 1931–1943. doi: 10.1093/mnras/stw145. arXiv: 1511.01098 [astro-ph.GA].

[333] T. Sawala et al. “The APOSTLE simulations: solutions to the Local Group’s cosmic puzzles”. In: *Monthly Notices of the Royal Astronomical Society* 457.2 (Feb. 2016), pp. 1931–1943. issn: 0035-8711. doi: 10.1093/mnras/stw145. eprint: https://academic.oup.com/mnras/article-pdf/457/2/1931/2930798/stw145.pdf. url: https://doi.org/10.1093/mnras/stw145.

[334] M. Seglar-Arroyo and F. Schüssler. "Gravitational wave alert follow-up strategy in the H.E.S.S. multi-messenger framework". In: *52nd Rencontres de Moriond on Very High Energy Phenomena in the Universe*. 2017, pp. 175–182. arXiv: 1705.10138 [astro-ph.IM].

[335] P. D. Serpico. "Astrophysical models for the origin of the positron 'excess'". In: *Astropart. Phys.* 39-40 (2012), pp. 2–11. doi: 10.1016/j.astropartphys.2011.08.007. arXiv: 1108.4827 [astro-ph.HE].

[336] H. Silverwood et al. "A realistic assessment of the CTA sensitivity to dark matter annihilation". In: *JCAP* 03 (2015), p. 055. doi: 10.1088/1475-7516/2015/03/055. arXiv: 1408.4131 [astro-ph.HE].

[337] G. F. Smoot et al. "Structure in the COBE Differential Microwave Radiometer First-Year Maps". In: *Astrophys. J. Lett.* 396 (Sept. 1992), p. L1. doi: 10.1086/186504.

[338] Y. Sofue. "The galactic center lobe." In: *Publ. Astron. Soc. Japan* 37 (Jan. 1985), pp. 697–713.

[339] A. Sommerfeld. "Über die Beugung und Bremsung der Elektronen". In: *Annalen der Physik* 403 (Mar. 2006), pp. 257–330. doi: 10.1002/andp.19314030302.

[340] V. Springel, C. S. Frenk, and S. D. M. White. "The large-scale structure of the Universe". In: *Nature* 440 (2006), p. 1137. doi: 10.1038/nature04805. arXiv: astro-ph/0604561.

[341] V. Springel, S. D. M. White, C. S. Frenk, et al. "A blueprint for detecting supersymmetric dark matter in the Galactic halo". In: *Nature* 456 (2008), pp. 73–76. arXiv: 0809.0894 [astro-ph].

[342] V. Springel et al. "Simulations of the formation, evolution and clustering of galaxies and quasars". In: *Nature* 435.7042 (May 2005), pp. 629–636. doi: 10.1038/nature03597. arXiv: astro-ph/0504097 [astro-ph].

[343] V. Springel et al. "The Aquarius Project: the subhalos of galactic halos". In: *Mon. Not. Roy. Astron. Soc.* 391 (2008), pp. 1685–1711. doi: 10.1111/j.1365-2966.2008.14066.x. arXiv: 0809.0898 [astro-ph].

[344] J. Stadel et al. "Quantifying the heart of darkness with GHALO – a multibillion particle simulation of a galactic halo". In: *Monthly Notices of the Royal Astronomical Society: Letters* 398.1 (Sept. 2009), pp. L21–L25. issn: 1745-3925. doi: 10.1111/j.1745-3933.2009.00699.x. eprint: https://academic.oup.com/mnrasl/article-pdf/398/1/L21/8202677/398-1-L21.pdf. url: https://doi.org/10.1111/j.1745-3933.2009.00699.x.

[345] A. A. Starobinsky. "A New Type of Isotropic Cosmological Models Without Singularity". In: *Phys. Lett. B* 91 (1980). Ed. by I. M. Khalatnikov and V. P. Mineev, pp. 99–102. doi: 10.1016/0370-2693(80)90670-X.

[346] F. W. Stecker. “Neutral-Pion Gamma Rays from the Galaxy and the Interstellar Gas Content”. In: *Astrophys. J.* 185 (Oct. 1973), pp. 499–504. doi: 10.1086/152435.

[347] G. Steigman, B. Dasgupta, and J. F. Beacom. “Precise Relic WIMP Abundance and its Impact on Searches for Dark Matter Annihilation”. In: *Phys. Rev.* D86 (2012), p. 023506. doi: 10.1103/PhysRevD.86.023506. arXiv: 1204.3622 [hep-ph].

[348] F. Stoehr et al. “Dark matter annihilation in the halo of the Milky Way”. In: *Mon. Not. Roy. Astron. Soc.* 345 (2003), p. 1313. doi: 10.1046/j.1365-2966.2003.07052.x. arXiv: astro-ph/0307026.

[349] M. Stref and J. Lavalle. “Modeling dark matter subhalos in a constrained galaxy: Global mass and boosted annihilation profiles”. In: *Phys. Rev. D* 95.6 (2017), p. 063003. doi: 10.1103/PhysRevD.95.063003. arXiv: 1610.02233 [astro-ph.CO].

[350] A. W. Strong, I. V. Moskalenko, and V. S. Ptuskin. “Cosmic-Ray Propagation and Interactions in the Galaxy”. In: *Annual Review of Nuclear and Particle Science* 57.1 (Nov. 2007), pp. 285–327. issn: 1545-4134. doi: 10.1146/annurev.nucl.57.090506.123011. url: http://dx.doi.org/10.1146/annurev.nucl.57.090506.123011.

[351] Meng Su and D. P. Finkbeiner. “Strong Evidence for Gamma-ray Line Emission from the Inner Galaxy”. In: (June 2012). arXiv: 1206.1616 [astro-ph.HE].

[352] Meng Su, Tracy R. Slatyer, and Douglas P. Finkbeiner. “Giant Gamma-ray Bubbles from Fermi-LAT: Active Galactic Nucleus Activity or Bipolar Galactic Wind?” In: *Astrophys. J.* 724.2 (Dec. 2010), pp. 1044–1082. doi: 10.1088/0004-637X/724/2/1044. arXiv: 1005.5480 [astro-ph.HE].

[353] A. Tasitsiomi and A. V. Olinto. “The Detectability of neutralino clumps via atmospheric Cherenkov telescopes”. In: *Phys. Rev. D* 66 (2002), p. 083006. doi: 10.1103/PhysRevD.66.083006. arXiv: astro-ph/0206040.

[354] T. Tavernier et al. “Limits on primordial black hole evaporation from H.E.S.S. observations”. In: *PoS* ICRC2021 (2021), p. 518. doi: 10.22323/1.395.0518.

[355] T. Tavernier, J.-F. Glicenstein, and F. Brun. “Search for Primordial Black Hole evaporations with H.E.S.S”. In: *PoS* ICRC2019 (2020), p. 804. doi: 10.22323/1.358.0804. arXiv: 1909.01620 [astro-ph.HE].

[356] “The 2dF Galaxy Redshift Survey: spectra and redshifts”. In: *Monthly Notices of the Royal Astronomical Society* 328.4 (Dec. 2001), pp. 1039–1063. doi: 10.1046/j.1365-8711.2001.04902.x. url: https://doi.org/10.1046%5C%2Fj.1365-8711.2001.04902.x.

[357] *The Baryonic Density*. https://ned.ipac.caltech.edu/level5/Sept02/Roos/Roos4.html. Accessed: 2010-09-30.

[358] "The Sloan Digital Sky Survey: Technical Summary". In: *Astron. J.* 120.3 (Sept. 2000), pp. 1579–1587. doi: 10.1086/301513. arXiv: astro-ph/0006396 [astro-ph].

[359] G. Vacanti et al. "Muon ring images with an atmospheric Cherenkov telescope". In: *Astropart. Phys.* 2 (1994), pp. 1–11. doi: 10.1016/0927-6505(94)90012-4.

[360] T. S. van Albada et al. "Distribution of dark matter in the spiral galaxy NGC 3198." In: *Astrophys. J.* 295 (Aug. 1985), pp. 305–313. doi: 10.1086/163375.

[361] VERITAS. *VERITAS - Very Energetic Radiation Imaging Telescope Array System.* https://veritas.sao.arizona.edu/. 2003.

[362] A.E. Vladimirov et al. "GALPROP WebRun: An internet-based service for calculating galactic cosmic ray propagation and associated photon emissions". In: *Computer Physics Communications* 182.5 (May 2011), pp. 1156–1161. issn: 0010-4655. doi: 10.1016/j.cpc.2011.01.017. url: http://dx.doi.org/10.1016/j.cpc.2011.01.017.

[363] H. J. Völk and K. Bernlöhr. "Imaging Very High Energy Gamma-Ray Telescopes". In: *Exper. Astron.* 25 (2009), pp. 173–191. doi: 10.1007/s10686-009-9151-z. arXiv: 0812.4198 [astro-ph].

[364] Q. D. Wang. "Chandra large-scale mapping of the Galactic Centre: probing high-energy structures around the central molecular zone". In: *Monthly Notices of the Royal Astronomical Society* 504.2 (Apr. 2021), pp. 1609–1618. issn: 1365-2966. doi: 10.1093/mnras/stab801. url: http://dx.doi.org/10.1093/mnras/stab801.

[365] S. S. Wilks. "The Large-Sample Distribution of the Likelihood Ratio for Testing Composite Hypotheses". In: *The Annals of Mathematical Statistics* 9.1 (1938), pp. 60–62. issn: 00034851. url: http://www.jstor.org/stable/2957648.

[366] D. Wingate and T. Weber. "Automated Variational Inference in Probabilistic Programming". In: *arXiv e-prints*, arXiv:1301.1299 (Jan. 2013), arXiv:1301.1299. arXiv: 1301.1299 [stat.ML].

[367] Rui-zhi Yang, F. Aharonian, and R. Crocker. "The Fermi bubbles revisited". In: *Astronomy & Astrophysics* 567, A19 (July 2014), A19. doi: 10.1051/0004-6361/201423562. arXiv: 1402.0403 [astro-ph.HE].

[368] V. Zabalza. "naima: a Python package for inference of relativistic particle energy distributions from observed nonthermal spectra". In: *Proc. of International Cosmic Ray Conference 2015* (2015), p. 922. eprint: 1509.03319.

[369] H. S. Zechlin et al. "Dark matter subhaloes as gamma-ray sources and candidates in the first Fermi-LAT catalogue". In: *Astron. Astrophys.* 538 (2012), A93. doi: 10.1051/0004-6361/201117655. arXiv: 1111.3514 [astro-ph.HE].

[370] Ya. B. Zel'dovich and I. D. Novikov. "The Hypothesis of Cores Retarded during Expansion and the Hot Cosmological Model". In: 10 (Feb. 1967), p. 602.

[371] Mengfei Zhang, Zhiyuan Li, and M. R. Morris. "A Supernova-driven, Magnetically Collimated Outflow as the Origin of the Galactic Center Radio Bubbles". In: *Astrophys. J.* 913.1, 68 (May 2021), p. 68. doi: 10.3847/1538-4357/abf927. arXiv: 2101.10741 [astro-ph.GA].

[372] Q. Zhu et al. "Baryonic impact on the dark matter distribution in Milky Way-sized galaxies and their satellites". In: *Mon. Not. Roy. Astron. Soc.* 458.2 (2016), pp. 1559–1580. doi: 10.1093/mnras/stw374. arXiv: 1506.05537 [astro-ph.CO].

[373] F. Zwicky. "On the Masses of Nebulae and of Clusters of Nebulae". In: *Astrophys. J.* 86 (Oct. 1937), p. 217. doi: 10.1086/143864.

[374] P. A. Zyla et al. "Review of Particle Physics". In: *PTEP* 2020.8 (2020), p. 083C01. doi: 10.1093/ptep/ptaa104.